AN INVESTIGATION

OF

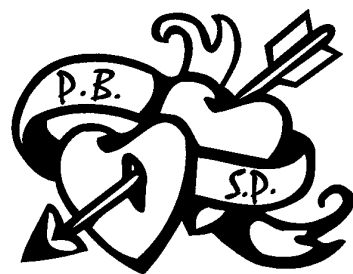## DUSTY PLASMAS

A DISSERTATION SUBMITTED TO THE

UNIVERSITY OF OXFORD

IN PARTIAL FULFILMENT OF THE REQUIREMENTS

FOR THE DEGREE OF

DOCTOR OF PHILOSOPHY

BY

EDWARD B. TOMME

MERTON COLLEGE

HILLARY TERM 2000

20000627 143

REPORT DOCUMENTATION PAGE

Form Approved
OMB No. 0704-0188

1. AGENCY USE ONLY *(Leave blank)*	2. REPORT DATE 6.Jun.00	3. REPORT TYPE AND DATES COVERED DISSERTATION

4. TITLE AND SUBTITLE
AN INVESTIGATION OF DUSTY PLASMAS

5. FUNDING NUMBERS

6. AUTHOR(S)
MAJ TOMME EDWARD B

7. PERFORMING ORGANIZATION NAME(S) AND ADDRESS(ES)
UNIVERSITY OF TEXAS AUSTIN

8. PERFORMING ORGANIZATION REPORT NUMBER

9. SPONSORING/MONITORING AGENCY NAME(S) AND ADDRESS(ES)
THE DEPARTMENT OF THE AIR FORCE
AFIT/CIA, BLDG 125
2950 P STREET
WPAFB OH 45433

10. SPONSORING/MONITORING AGENCY REPORT NUMBER

FY00-200

11. SUPPLEMENTARY NOTES

12a. DISTRIBUTION AVAILABILITY STATEMENT
Unlimited distribution
In Accordance With AFI 35-205/AFIT Sup 1

12b. DISTRIBUTION CODE

13. ABSTRACT *(Maximum 200 words)*

14. SUBJECT TERMS

15. NUMBER OF PAGES
183

16. PRICE CODE

17. SECURITY CLASSIFICATION OF REPORT	18. SECURITY CLASSIFICATION OF THIS PAGE	19. SECURITY CLASSIFICATION OF ABSTRACT	20. LIMITATION OF ABSTRACT

ACKNOWLEDGEMENTS

For some who seek to see the forest, the problem lies not in the trees but in the leaves.

— Tracey Tomme

An Investigation of Dusty Plasmas
Edward B. Tomme, Merton College
Doctor of Philosophy, Hillary Term 2000

ABSTRACT

This thesis constitutes a study of micron-sized particle behaviour in low-pressure radio frequency (RF) laboratory plasmas and of the plasma sheath in which these particles were suspended.

A summary of the theoretical aspects of dust in a plasma includes reviews of the mechanisms behind the formation of the plasma sheath, development of a novel approach to the determination of the limiting RF amplitude at which the sheath will collapse, and a discussion of charging theories for isolated probes in the plasma and plasma sheath. Forces that act on dust suspended in the plasma sheath, including forces on isolated dust grains and the interparticulate forces within plasma crystals are then addressed.

A novel theory of damped dust oscillations in the plasma sheath is developed. The existence of a harmonic potential well is postulated to explain the suspension of the dust. It is shown that the analysis of dust trajectories can lead to the determination of a number of dust parameters, including the drag force and charge on the dust. However the theory requires knowledge of the potential function in the sheath to obtain quantitative results.

A numerical model is then developed to obtain the potential functions required by the oscillation theory. It describes a collisionless to moderately collisional plasma sheath driven by low to moderate RF amplitudes at frequencies between the electron and ion plasma frequencies. Output from the model includes the potential, field, charge density, carrier densities, and ion speed as functions of height above the electrode. Parameter variation is shown to affect the model output in the expected manner. The numerical model shows that the potential function was very nearly parabolic over the entire sheath. Analysis of eight independent models demonstrates that this parabolic result was general.

Finally, the experimental apparatus and procedure used to determine the dust charge and drag on suspended dust of a variety of sizes are fully described. Two methods for charge determination are discussed, one involving analysis of damped dust oscillations and the other involving the balance of forces on the dust. Results are shown to agree well with each other, with those of other researchers, and with theory.

TABLE OF CONTENTS

LIST OF FIGURES

LIST OF TABLES

LISTS OF SYMBOLS AND ABBREVIATIONS

SYMBOLS

(Note: the subscripts d, e, i, and n on a symbol indicate dust, electrons, ions, or neutrals, respectively. Unless noted otherwise, the subscripts 0, eq, p, and s on a symbol denotes the value at a reference point, the equilibrium height, the probe surface, or the sheath edge, respectively. Unless otherwise stated in the text, MKSA units are assumed. Symbols displayed in numbered equations are in *italics*, while symbols displayed within paragraph text are in Times New Roman.)

ROMAN SYMBOLS

A	Area	j	Current Density
a	Dust Radius	K	Curvature of a Generic Parabola
$\bar{c}$	Average Speed	k_B	Boltzmann's Constant
c_{mp}	Most Probable Speed	L	Plasma Dimension
c_{rms}	Root Mean Squared Speed	$L\{f_0\}$	Inelastic Collision Integral
D	Diffusion Coefficient	M	Mach Number
E	Total Energy	m	Mass
e	Elementary Charge	n	Number Density
F	Force	P	Pressure
f	Frequency	Q_d	Dust Charge
f_p	Plasma Frequency	r	Radial Position
g	Gravitational Acceleration	r_g	Intergrain Spacing
h	Impact Parameter	T	Temperature
I	Current	t	Time
$I_0(x)$	Zero-Order Modified Bessel Function	U	Potential Energy
J	Angular Momentum	u	Normalised Speed
J_a	Asymptotic Angular Momentum	v	Velocity
J_c	Critical Angular Momentum	Z	Charge Number
$J_0(x)$	Zero-Order Bessel Function	z	Linear Position, Height

GREEK SYMBOLS

α	Collisionality Coefficient	θ	Angle
α_d	Dust Properties Coefficient	κ	Restoring (Spring) Constant
α_i	Franklin and Snell Ionisation Ratio	λ	Mean Free Path
β	Suspending Gas Properties Coefficient	λ_D	Debye Length
Γ	Coulomb Coupling Coefficient	λ_0	Wavelength
γ	Drag Coefficient	μ	Mobility Coefficient
δ	Millikan Coefficient	ν_i	Ionisation Frequency
δ_i	Franklin and Snell Collision Ratio	ξ	Normalised Distance
$\mathcal{E}$	Electric Field	ρ	Mass Density, Charge Density
ε_0	Permittivity of Free Space	σ	Collision Cross Section
η	Normalised Potential	τ	Damping Time Coefficient
η_{fp}	Normalised Floating Potential	ϕ	Electric Potential
η_{rf}	Normalised RF Amplitude	ω	Angular Frequency
η_{sb}	Normalised Self-Bias Potential	ω_p	Plasma Angular Frequency

ABBREVIATIONS

ABR	Allen-Boyd-Reynolds Radial Motion Theory
AMU	Atomic Mass Units
AC	Alternating Current
CCD	Charge-Coupled Device
DC	Direct Current
EEDF	Electron Energy Distribution Function
EPSRC	Engineering and Physical Sciences Research Council
JET	Joint European Torus
MF	Melamine Formaldehyde
OML	Orbital Motion Limited Theory
OXDUPLAG	Oxford University Dusty Plasma Group
PIC	Particle in Cell
RF	Radio Frequency
UKAEA	United Kingdom Atomic Energy Authority

1. Introduction

As sciences go, the field of plasma physics is relatively new. The fundamental work in the field was done by, among others, Schottky, Child, and Langmuir in the early 20th century. Much of what they proposed in their landmark papers [*e.g.* Child, 1911; Schottky, 1924; Langmuir, 1929] has remained intact with very little modification to this day. Plasma physics rapidly became an important field of study for such seemingly disparate disciplines as astrophysics, condensed-matter physics, aerodynamics, and lithography. It seems almost ironic that plasma, the fourth and by far the most prevalent state of matter in the universe, is perhaps the least studied and least understood.

The study of dusty plasmas is an even more recently developed field. As the name implies, dusty plasmas are gases of charged particles that have embedded within them sub-micron- to millimetre-sized particles [Garscadden, 1991]. Figure 1 depicts how some of these different types of particles may be classified, and emphasises the particle sizes studied as a part of this thesis. As non-intuitive as plasmas may seem at first glance, dusty plasmas may be even more so. Like plasmas, dusty plasmas also seem to appear in a huge variety of disciplines from astrophysics to electrical
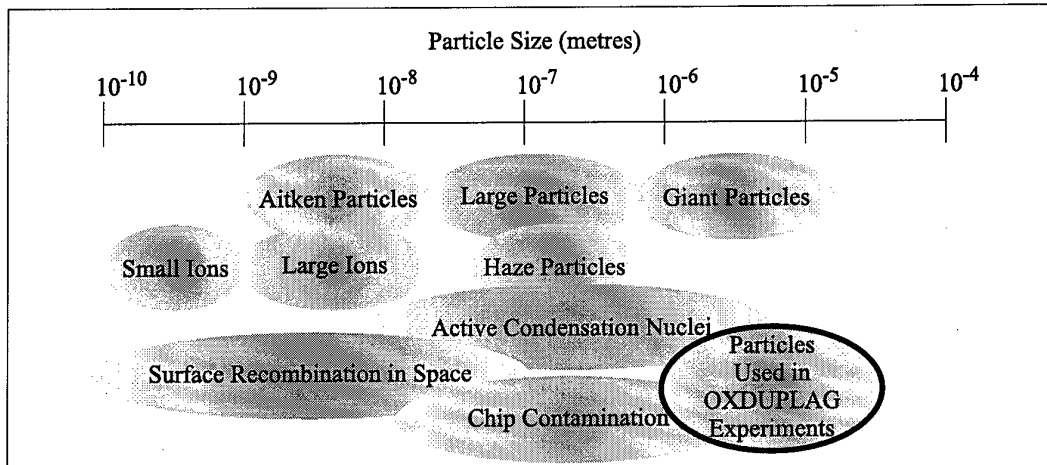
Figure 1: Compendium of Particulates in Plasmas. This figure, adapted from Garscadden [1991], shows commonly used nomenclature for dust in plasmas. The range of sizes of dust used in Oxford University Dusty Plasma Group [OXDUPLAG] experiments is indicated at the lower right of the figure.

engineering. A better understanding of these types of plasmas shows promise for solving a number of scientific and engineering problems.

1.1 WHY STUDY DUSTY PLASMAS?

As mentioned above, dusty plasmas seem ubiquitous. They are found on a vast variety of scale lengths in nature, in the laboratory, and in industry. They affect observations of distant quasars and cause untold damage to microchips. They also may soon see use in the teaching arena as a study aid for some technical subjects. In the remainder of this introductory chapter, we will look a little more closely at where one can find dusty plasmas and why it is important to understand them.

Natural dusty plasmas fill the universe. Interstellar clouds form features in astronomical photographs of nebulae and galaxies and obscure direct views of our own galactic centre except in very small frequency bands [McDonnel, 1978]. Most stars, including our own, possess circumstellar clouds left over from stellar system formation. Space probes have determined that fragmentation of comets is the probable mechanism
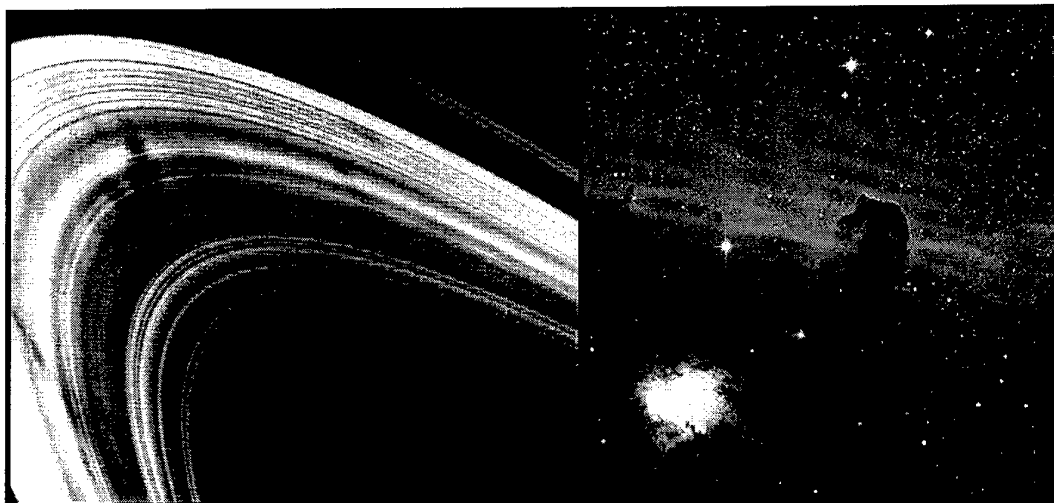
Figure 2: Cosmic Dusty Plasmas. The less luminous, blotchy spoke structure of the rings of Saturn is evident in the left image. The right frame shows absorption and reflection nebulae in the vicinity of the Horse Head Nebula in Orion. (Images courtesy of NASA.)

behind most interplanetary dust [deAngelis, 1992]. Even the complex spoke structure of planetary rings [Goertz, 1989], shown in Figure 2, and particle transport processes observed in those rings [Morfill *et al.*, 1980] may be explained by dusty plasma interactions. The study of these dusty plasmas may help lead to a better understanding of cosmological events. Around our own planet, the magnetosphere and ionosphere are filled with particulate matter that influences the many forms of electromagnetic communication and information gathering that passes through these regions. For example, the reflection of radar and radio waves from the ionosphere is influenced by ionospheric dust, a significant source of spurious reception or imprecise targeting [Havnes *et al.*, 1992a; La Hoz, 1992].

Scientific and industrial plasmas have their own share of dust-related phenomena. Industrial plasmas are used to etch circuits for the microelectronics market. Although the exact numbers are closely held proprietary secrets, dust contamination is currently estimated to ruin up to a third of semiconductor wafers produced [Coleman, 1998]. Even in the cleanest rooms ever devised by man, dust is produced as a by-
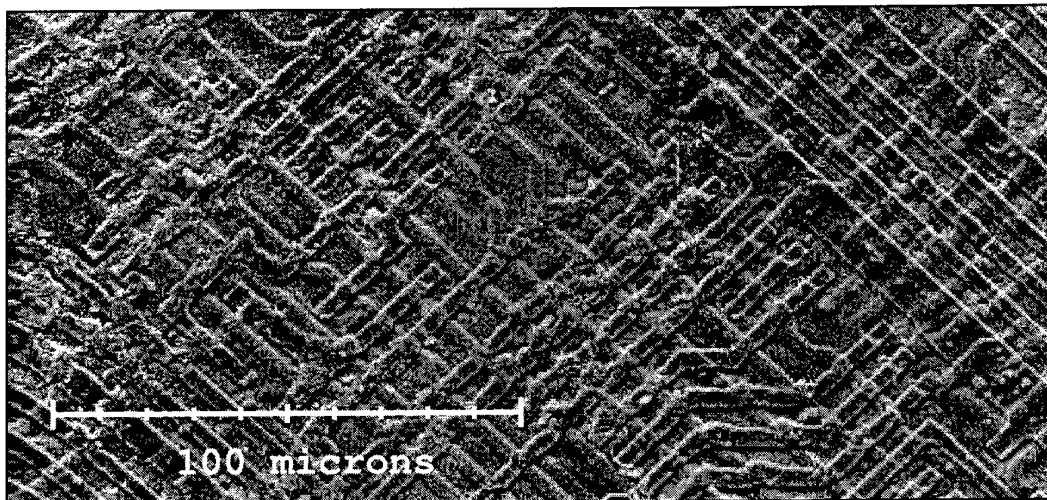
Figure 3: A Plasma-Processed Microchip. In this image, courtesy of the State University of New York, Stony Brook, a semiconductor wafer that has undergone processing in a plasma shows feature sizes of approximately 3.5 microns. Current processing limits have reduced the minimum feature size to the order of 1/10th of a micron. The trend toward dramatic reductions in possible feature sizes shows no sign of abating, implying that the sizes of contaminant dust particles that must be controlled to reduce spoilage will decrease correspondingly.

product of semiconductor etching or is grown through chemical reactions within the processing plasma [Huang *et al.*, 1996]. The elimination or control of this dust is obviously worth billions to the industry, and is currently the subject of intense research [Selwyn, 1996]. Figure 3 shows a typical etched semiconductor. As the features created on these devices decrease in size, smaller and smaller dust particles will be able to significantly affect their operation, requiring even better understanding and control of the dust elimination process.

Dust is also an unwanted by-product of some nuclear fusion experiments. In one tokamak reactor, several kilograms or more of hazardous dust could be produced per year [Piet *et al.*, 1997]. Removal of this dust currently involves shutting down the system for lengthy periods and manually collecting the dust. This process not only causes inefficient use of expensive equipment, but also exposes personnel to the dust. Development of methods for non-intrusive dust removal will obviously be of benefit both for technical and occupational health reasons.

The consequences of dust in a plasma are not all negative, however. Many researchers are currently engaged in experiments that use suspended particulates in plasmas to enhance processing goals. For example, the deposition of dust during the manufacture of nanostructured silicon can accelerate the crystallisation process [Bertran *et al.*, 1998], lower the number of crystal defects [Stoffels *et al.*, 1998] and lead to the production of more efficient solar cells [Kroesen *et al.*, 1998]. Kersten *et al.* [1998a, 1988b] have demonstrated the deposition of layers of aluminium on suspended iron particles in a plasma, while Swinkels *et al.* [1998] and Stoffels *et al.* [1999] have been able to etch suspended particles to achieve a desired size.

Finally, dusty plasmas can be used as pedagogical and theoretical tools in technical training. Plasma crystals mimic the form of two-dimensional solid-state crystals quite closely. Demonstrations in condensed matter and materials science courses that now use bubble tanks and colloidal suspensions could be done more effectively with plasma crystals. Plasma crystals react millions of times more rapidly than colloidal suspensions and allow accurate simulation of many more phenomena than do bubble tanks [Maddox, 1994]. Phenomena discussed later in this thesis that are completely unknown in colloidal suspensions have already been demonstrated in dusty plasmas.

Thus, there is a wealth of reasons for the study of dusty plasmas: furthering theoretical knowledge of some of the largest and smallest length scales in the universe; decreasing waste and increasing profits in the semiconductor industry; and promoting safety and efficiency in the development of fusion power. However, before these

benefits can be reaped, one must begin to understand the purely scientific side of the dusty plasma phenomenon.

1.2 THESIS OVERVIEW

Small particles present in plasmas tend to acquire a negative charge due to the higher mobility of electrons in the plasma. In terrestrial plasmas, negatively charged particles of sufficient size fall under the influence of gravity toward lower regions of the plasma until they reach the plasma sheath. In the sheath, the electric field from the negatively self-biased electrode begins to repel the dust. Under certain conditions, this repulsion is sufficient to cause the dust to suspend above the lower electrode. At this point, the particles encounter a balance between upward and downward forces, or in other words, they encounter a minimum in the potential well formed by the sum of these forces.

As a dust particle in a terrestrial plasma falls from the plasma into the sheath and enters the potential well, its trajectory oscillates about an equilibrium height. A number of quantities related to the dust particles and their plasma/sheath environment may be deduced using the oscillatory motion of the dust particle as a diagnostic. The purpose of this thesis is to demonstrate how such a diagnostic may be used.

In order to explain the oscillatory motion and how it may be used to deduce plasma and dust parameters, it is necessary to have a brief introduction to plasma and dusty plasma theory. The second chapter of this thesis will provide such a review, concentrating on the theory of the sheath and theories concerning the charging of particles in a plasma environment. Novel methods for calculating the sheath collapse

voltage will be developed there. Also presented in that chapter is a review of the forces acting on dust suspended in a plasma sheath, including novel approaches to the subjects of attractive forces and other interaction forces between particles in dusty plasmas.

The specific theory developed to explain dust oscillations in the plasma sheath will be put forward in chapter three. In that chapter, a review of applicable damped harmonic motion theory will demonstrate the simple model used to successfully describe the results of complex dust oscillation experiments. Next, a theory that uses dust trajectory parameters to estimate the charge on a dust particle at its equilibrium height will be presented.

The next chapter will then discuss the development of a simple model of a collisional radio frequency (RF) plasma sheath needed for the charge estimation theory. Although not as sophisticated as some models from the literature, it will be demonstrated that the model output closely mirrors observed changes to experimental plasmas when model and experiment are given different parameters. The fifth chapter will thoroughly examine eight representative numerical models from the literature and will compare them to the model developed for this thesis. It will be shown that a heretofore-unrecognised common factor pervades the results of each of these sheath models, namely, that the electric potential in the sheath follows a parabolic spatial profile to a high degree of accuracy.

In the sixth chapter, experimental results from trajectory analyses for a number of dust particles with different masses at different pressures will be presented. These results will show that the technique developed here yields results for the dust charge of the same magnitude as those of other researchers and strongly supports the parabolic

sheath potential profile postulated in the preceding chapters. The concluding chapter will propose a few ideas for furthering the work presented in this thesis.

Again, the main thrust of this thesis is to use theoretical and numerical techniques, many of which were developed for this tome, to investigate properties of dust in the plasma sheath environment. The next chapter will begin this process by reviewing some of the applicable theories from the literature concerning sheaths and particles in plasmas.

2. DUST IN THE PLASMA SHEATH

Dust in the plasma sheath is a complex subject. This study of dust in the plasma sheath begins with a review of some of the more pertinent theory, included here as a ready reference for subsequent chapters. Some of the material presented in this chapter, such as the potential energy formulation of the orbital motion theory (page 29), has been covered in some detail in the literature. However, it is felt that the presentation style in this chapter could help to provide a clearer mental picture of that complex concept than exists in other works. While some subjects presented in this chapter, such as charging theory, differ from previously published work only in presentation style, there are a number of new topics included herein. For example, the discussion of forces on dust in a plasma, including original considerations of bombardment forces (page 52) and intergrain forces in plasma crystals (page 58), is a novel twist on a much-quoted subject, as is the development of a simple relationship between the RF amplitude at which the sheath collapses and the ion mass (page 18).

As will be shown, objects are almost never really in contact with a true plasma. Plasmas have been defined as quasineutral, partially or fully ionised gases that exhibit collective behaviour [Chen, 1984]. The shielding of a plasma from objects is required in order to allow its quasineutral character to exist for long times over large distances.

The transition region between the quasineutral plasma and a boundary is known as the plasma sheath. In this region, strong fields develop, repelling all but the most energetic electrons and resulting in a space-charge region consisting almost entirely of ions with directed velocities much higher than their random thermal velocities. For the experiments detailed later in this thesis, a thorough understanding of the sheath region is critical; the dust studied in those trials is levitated in the sheath region.

Dust itself is no exception to the rule that no object ever touches a plasma. Even these small particles are effectively shielded from the plasma. In order to interpret the results of experiments on dust in plasmas properly, one thus needs to understand the basis for this shielding. To facilitate this understanding, the physical basis behind the plasma sheath will first be reviewed. How objects in plasmas acquire their shielding charges will then be examined, beginning with general probe charging theory and then proceeding on to the subject of dust charging itself. Next to be explored will be the changes required of these charging theories when the object is suspended in a larger shielding region, the plasma sheath that shields the bulk of the plasma from its container. Finally, forces that act upon dust suspended in the plasma sheath will be examined, both for dust in a plasma and for dusty plasmas.

A note on terminology: deAngelis [1992] has proposed that the term "dusty plasma" be reserved for plasmas in which the average distance between dust grains is smaller than the effective shielding distance, while the converse situation is referred to as "dust in a plasma." That convention will be followed in this thesis. The distinction between dusty plasmas and dust in a plasma is quite important. Dust in a dusty plasma is highly coupled, with information being transmitted between dust grains through their

incompletely shielded electric fields. The dust in a dusty plasma also becomes a

significant electron sink, which can radically alter the local plasma parameters.

Analysis of dust in a plasma is much less complex, and the properties of individual

grains may be more easily inferred. In contrast to many experiments from the literature

cited later, the experiments on dust oscillation reported in this thesis were performed on

dust in a plasma.

2.1 BASIC PLASMA PARAMETERS

Although much of this thesis concerns theoretical and numerical work, its

primary goal is the explanation of experimental results. The results of the experiments

depend strongly upon the control parameters of the experiments. Plasmas are typically

characterised by a number of independent parameters, among them particle

temperatures, particle densities, and method of plasma creation (RF or DC (direct

current), capacitively or inductively coupled, etc.). Unless stated otherwise, this thesis

will concentrate on capacitively coupled RF plasmas.

The simplifying assumption of massive ions will also be employed throughout

this thesis. In other words, the electrons in the RF plasmas studied here are assumed to

be the only particles that will respond to the instantaneous electric field. All other

(more massive) particles will only respond to average fields. It can be shown [e.g.

Chen, 1984] that a component x of a plasma will have a natural frequency closely

approximated by

$$(1) \qquad \omega_{px} \cong \sqrt{\frac{n_x Z_x^{\,2} e^2}{m_x \varepsilon_0}}$$

where e is the elementary charge, ε_0 is the permittivity of free space, and n, m, and Z are

the number density, mass, and number of elementary charges on component x,

respectively. This natural frequency, ω_{px}, is called the plasma frequency for particles of

type x. The nearest component in mass to the electron would be a hydrogen ion, which

would oscillate at approximately $1/\sqrt{2000}^{th}$ of the electron plasma frequency, or

$\omega_{pi} = 0.023\omega_{pe}$, where the subscripts i and e refer to ions and electrons, respectively.

For argon, the plasma frequency ratio is even smaller, with $\omega_{pi} = 0.0037\omega_{pe}$. These

small fractions will be employed to support the massive ion approximation. The

frequency range where this approximation for ion and electron motion is valid is given

by

$$(2) \qquad \omega_{pi} \ll \omega \ll \omega_{pe},$$

where ω is the frequency of the RF source used to create the plasma. Fields oscillating

at less than ω_{pi} will allow ions to respond to the instantaneous field, while fields

oscillating at much greater than ω_{pe} will affect neither electrons nor ions.

A few of the parameters commonly used to describe plasmas have now been

detailed. Table 1 lists the specific values of many of these calculated parameters based

upon temperatures and pressures commonly used in the Oxford University Dusty

Plasma Group's (OXDUPLAG) reactor. In this table, P is the pressure, k_B is the

Boltzmann constant, T is the temperature, f is the cyclic frequency, λ_D is the Debye

length, λ_0 is the wavelength, and λ is the mean free path. The variables $\bar{c}$, c_{mp}, and

c_{rms} represent the average (thermal), most probable, and root-mean-squared speeds of

P (Torr / Pa)	1.0 / 133		0.1 / 13.3		0.01 / 1.33		0.001 / 0.133	
$k_B T_e$ (eV)	2	4	2	4	2	4	2	4
n_n (m^{-3})	$3.2 \cdot 10^{22}$	$3.2 \cdot 10^{22}$	$3.2 \cdot 10^{21}$	$3.2 \cdot 10^{21}$	$3.2 \cdot 10^{20}$	$3.2 \cdot 10^{20}$	$3.2 \cdot 10^{19}$	$3.2 \cdot 10^{19}$
$c_{mp,e}$ (m/sec)	$8.4 \cdot 10^{5}$	$1.2 \cdot 10^{6}$	$8.4 \cdot 10^{5}$	$1.2 \cdot 10^{6}$	$8.4 \cdot 10^{5}$	$1.2 \cdot 10^{6}$	$8.4 \cdot 10^{5}$	$1.2 \cdot 10^{6}$
$\bar{c}_e$ (m/sec)	$9.5 \cdot 10^{5}$	$1.3 \cdot 10^{6}$	$9.5 \cdot 10^{5}$	$1.3 \cdot 10^{6}$	$9.5 \cdot 10^{5}$	$1.3 \cdot 10^{6}$	$9.5 \cdot 10^{5}$	$1.3 \cdot 10^{6}$
$c_{rms,e}$ (m/sec)	$1.0 \cdot 10^{6}$	$1.5 \cdot 10^{6}$	$1.0 \cdot 10^{6}$	$1.5 \cdot 10^{6}$	$1.0 \cdot 10^{6}$	$1.5 \cdot 10^{6}$	$1.0 \cdot 10^{6}$	$1.5 \cdot 10^{6}$

Ionisation Fraction (n_0/n_n): $1 \cdot 10^{-8}$

	2	4	2	4	2	4	2	4
n_e (m^{-3})	$3.2 \cdot 10^{14}$	$3.2 \cdot 10^{14}$	$3.2 \cdot 10^{13}$	$3.2 \cdot 10^{13}$	$3.2 \cdot 10^{12}$	$3.2 \cdot 10^{12}$	$3.2 \cdot 10^{11}$	$3.2 \cdot 10^{11}$
λ_{Di} (μm)	67	67	210	210	670	670	2100	2100
f_{pi} (MHz)	0.59	0.59	0.19	0.19	0.059	0.059	0.019	0.019
λ_{De} (mm)	0.59	0.83	1.9	2.6	5.8	8.3	19	26
f_{pe} (MHz)	160	160	51	51	16	16		

Ionisation Fraction (n_0/n_n): $1 \cdot 10^{-7}$

	2	4	2	4	2	4	2	4
n_e (m^{-3})	$3.2 \cdot 10^{15}$	$3.2 \cdot 10^{15}$	$3.2 \cdot 10^{14}$	$3.2 \cdot 10^{14}$	$3.2 \cdot 10^{13}$	$3.2 \cdot 10^{13}$	$3.2 \cdot 10^{12}$	$3.2 \cdot 10^{12}$
λ_{Di} (μm)	21	21	67	67	210	210	670	670
f_{pi} (MHz)	1.9	1.9	0.59	0.59	0.19	0.19	0.059	0.059
λ_{De} (mm)	0.19	0.26	0.59	0.83	1.9	2.6	5.9	8.3
f_{pe} (MHz)	510	510	160	160	51	51	16	16

Ionisation Fraction (n_0/n_n): $1 \cdot 10^{-6}$

	2	4	2	4	2	4	2	4
n_e (m^{-3})	$3.2 \cdot 10^{16}$	$3.2 \cdot 10^{16}$	$3.2 \cdot 10^{15}$	$3.2 \cdot 10^{15}$	$3.2 \cdot 10^{14}$	$3.2 \cdot 10^{14}$	$3.2 \cdot 10^{13}$	$3.2 \cdot 10^{13}$
λ_{Di} (μm)	6.7	6.7	21	21	67	67	210	210
f_{pi} (MHz)	5.9	5.9	1.9	1.9	0.59	0.59	0.19	0.19
λ_{De} (mm)	0.059	0.083	0.19	0.26	0.59	0.83	1.9	2.6
f_{pe} (MHz)	1600	1600	510	510	160	160	51	51

f (MHz)		
13.56		
ω (rad/sec)	T (ns)	λ_0 (m)
$85.20 \cdot 10^{6}$	73.75	22.05

P (Torr / Pa)	1.0 / 133	0.1 / 13.3	0.01 / 1.33	0.001 / 0.13
$\lambda_{i\text{-}n}$ (ion-neutral) (mm)	0.0069	0.069	0.69	6.9

$c_{mp,i}$ (m/sec)	$\bar{c}_i$ (m/sec)	$c_{rms,i}$ (m/sec)
$3.5 \cdot 10^{2}$	$4.0 \cdot 10^{2}$	$4.3 \cdot 10^{2}$

Table 1: Typical Plasma Parameters for the OXDUPLAG Reactor. All values were calculated using standard textbook equations employing assumptions stated in the text.

the particles indicated. One purpose of this table is to demonstrate that the experiments described later in this thesis are performed under conditions where the assumption of equation (2) concerning the excitation frequency is valid.

Equations used to calculate Table 1 entries are those commonly found in basic plasma texts [*e.g.* Swift and Schwar, 1970; Chapman, 1980; Chen, 1984]. Mean free path calculations are based on a hard sphere model using a 5Å atomic radius. All table entries are calculated using room-temperature argon ions and neutrals, and all data for ions assume a single ionisation. Data in lightly shaded cells indicates regions where the 13.56 MHz plasma excitation frequency used by OXDUPLAG is within an order of magnitude of either the ion or electron plasma frequencies. Data in darkly shaded cells indicates regions where one of the plasma frequencies does not allow the assumed relation $\omega_{pi} \ll 13.56\mathrm{MHz} \ll \omega_{pe}$ to be true.

2.2 THE PLASMA SHEATH

Before a specific discussion of dust in plasmas is undertaken, one must first understand what happens to any object that encounters a plasma. To do this, a concept similar to Debye screening must be examined to explain the spatial variation of potentials the plasma uses to shield itself from large fields.

2.2.1 POTENTIALS WITHIN PLASMAS

An isolated object inserted into a plasma will constantly be bombarded by the charged particles that make up the plasma. As the electrons in the plasma are much more mobile (higher velocity for the same energy) and much more responsive to perturbing fields, they initially tend to bombard the object at a higher rate. This excess

electron bombardment results in a negative net charge on the object. Eventually the negatively charged object begins to repel electrons and to attract ions until the ion and electron fluxes to the object equalise.

Around any such object, the plasma's quasineutrality approximation can no longer be used. There now exists a space charge region where $n_i \gg n_e$. The exact nature of the spatial variations of these carrier densities is a matter of debate ongoing within the literature; for example, the discussion later in this chapter concerning the different theories of charging relates to this debate. In fact, two succeeding chapters of this thesis will discuss the subject of how carrier densities vary from the plasma to its boundary. For now, however, it will only be noted that such a space-charge region exists; the region will be called a *plasma sheath*.

The plasma sheath may be seen as a dark region surrounding an object in a plasma, especially in the boundary regions between the plasma and its containing vessel in the case of laboratory plasmas. This sheath is dark due to the electron deficit of the space charge region. Plasmas glow as a result of free electron collisions with bound electrons in the neutral atoms of the gas. Many of these collisions do not result in ionisation but instead excite the bound electrons from the lower energy states. (Single-event excitation collisions in ground state argon atoms occur between 11.57 eV and 15.76 eV [Weast *et al.*, 1989]; lower energies fail to reach the first excitation potential and higher energies ionise the atom.) As they relax, the excited atoms emit characteristic photons. With fewer electrons to cause such excitation, the sheath region appears dark in comparison to the plasma.

2.2.2 THE SPATIAL EXTENT OF THE SHEATH

Now that a few of the reasons behind sheath formation have been briefly discussed, it remains to examine its spatial extent. In their original work, Langmuir [1923] and his assistants assumed that the entire potential drop from the floating potential to the plasma potential occurred across the sheath, implying that the plasma was entirely field-free. In later work, they did develop theories that involved potential penetration into the plasma [Tonks and Langmuir, 1929]. However, it was Bohm [1949] who first concisely stated a criterion for the location of the transition from the quasineutral plasma to the space-charge sheath region.

By assuming negligible sheath ionisation, a negligible electric field at the sheath edge, and monoenergetic ions mixed with Maxwellian electrons, Bohm was able to determine that in order to form a sheath, positive ions must possess a certain minimum energy. If his criterion is rewritten in terms of the ion speed, the following relationship for the Bohm speed, c_{Bohm}, is obtained:

$$(3) \qquad c_{Bohm} \geq \sqrt{k_B T_e / m_i} \,.$$

The significance of this equation is that it says the ions must be at least supersonic in the sheath. This minimum velocity requirement implies that a field must exist in the plasma to accelerate the ions, so fields on the order of $k_B T_e / 2e$ must exist within a quasineutral plasma. Riemann [1992] and Allen and Skorik [1993] have subsequently shown that the Bohm criterion applies to RF as well as DC plasmas as long as $\omega_{rf} \ll \omega_{pe}$. It must also be noted that Franklin and Snell [2000] have shown that the Bohm criterion for the

plasma sheath boundary does not apply for a large fraction of collisional plasmas. More will be discussed on that subject later in this chapter and in the chapter of this thesis dealing with the parabolic nature of the plasma sheath potential.

In an RF plasma, the boundary sheath region is typically much more pronounced than in similar DC plasmas. The reason for the greater spatial extent of the sheath is due to the near-collapse (or complete collapse) of the sheath during portions of the RF cycle. Consider a typical RF plasma system where the oscillator is protected from the plasma by a matching network [*e.g.* Chapman, 1980]. In such a system, only AC currents are allowed to flow, as the matching network generally includes a blocking capacitor that prevents the flow of DC currents. The potential between the plasma and the electrode is typically a sinusoidally varying RF signal offset by a DC amount, the *DC self-bias*, arising from the higher electron mobility, as discussed above. When the RF signal is near its maximum positive level, the instantaneous potential difference between the electrode and plasma is nearly zero. This low potential allows previously repelled electrons to flood the electrode, causing its potential to become more negative. This negative charging is not countered during the portion of the RF cycle when the signal is near its maximum negative potential due to the potential-driven exponential decrease in the number of Boltzmann electrons and the massive ion assumption.

If this situation continued unchanged, the electron and ion currents would not be equal and DC current would flow in the system; such current is not allowed due to the presence of the blocking capacitor in the system. The way this current is automatically eliminated is by the increase in the DC self-bias. The extra negative charge on the electrode subsequently repels more electrons and attracts more ions until

once again the fluxes equalise. The extra self-bias potential required to eliminate the flow of DC currents thus increases the size of the boundary sheath. The increase in self-bias (and increase in spatial extent of the boundary sheath) is a function of RF amplitude [Boschi and Magistrelli, 1963], although the spatial increase is a complicated function of the self-bias voltage.

As alluded to above, for some RF parameters, the sheath does indeed collapse. The collapse occurs when the electron current to the electrode enters the saturation region. Braithwaite *et al.* [1985] show that electron saturation is reached when the inequality $\phi_{sb} + \phi_{rf} < 0$ no longer holds. Here, ϕ_{rf} is the amplitude of the applied RF voltage and ϕ_{sb} is the DC self-bias voltage. This inequality may be rewritten as a relationship between the sheath-collapse RF amplitude and the ion mass,

$$(4) \qquad I_0\left(\frac{e\phi_{rf}}{k_B T_e}\right)\exp\left(-\frac{e\phi_{rf}}{k_B T_e}\right) > \left(2\pi m_e\Big/m_i\right)^{\frac{1}{2}},$$

where $I_0(x)$ is the modified zero-order Bessel function.

2.2.2.1 Calculation of the Sheath Collapse Potential

In an analysis performed for this thesis, a relationship for the RF amplitude at which the sheath collapses and the mass number of the plasma ions has been found. As equation (4) has no simple analytical solution, it was numerically solved for several ion masses as shown in Table 2. It was impractical to directly calculate the saturation potential for ions with masses greater than nitrogen, as the value of the Bessel function exceeds the floating-point capacity of the computer for those values. Figure 4 shows a

Ion	Hydrogen	Helium	Lithium	Beryllium	Boron	Carbon	Nitrogen
Mass (AMU)	1.0080	4.0026	6.94	9.012	10.81	12.011	14.007
Breakdown Potential $\left(e\phi_{rf} / k_B T_e \right)$	47.2 ± 0.1	186.6 ± 0.1	323.4 ± 1.5	419.8 ± 0.4	503.5 ± 1.5	559.4 ± 0.5	652.4 ± 0.5

Table 2: The Electron Saturation Potential for Selected Ions. The indicated breakdown voltages are the point where the expression in equation (5) first becomes invalid.

plot of these data, along with a linear fit. As can be seen, the fit is exceptionally good, having a linear correlation coefficient of 0.999999999996 (significant digit considerations notwithstanding). From these results, the function that relates the normalised RF amplitude above which the sheath collapses and the mass of the ions making up the plasma is

$$(5) \qquad \frac{e}{k_B T_e} \phi_{rf}(m_i) = \left(46.6 \frac{m_i}{m_p} + 0.252 \right)$$

Braithwaite *et al.* [1985] estimate that for argon, the normalised sheath collapse potential is approximately 1700. Extrapolating the results from the above equation, that voltage is 1860, a difference of only 8% from their estimate. The asymptotic expansion of the Bessel function in question is [Abramowitz and Stegun, 1965]

$$(6) \qquad I_0(z) = \frac{e^z}{\sqrt{2\pi z}} \left(1 + \frac{1}{8z} + \frac{9}{2!(8z)^2} + \frac{225}{3!(8z)^2} + \dots \right).$$

Anticipating a large value of z, only the first term of this expression is substituted into equation (4), resulting in a normalised potential of 1853 for argon, less than one percent different from the result of equation (5) (for this potential, the insignificant second term of the expansion is over 5 decades below the first). The similarity between the results
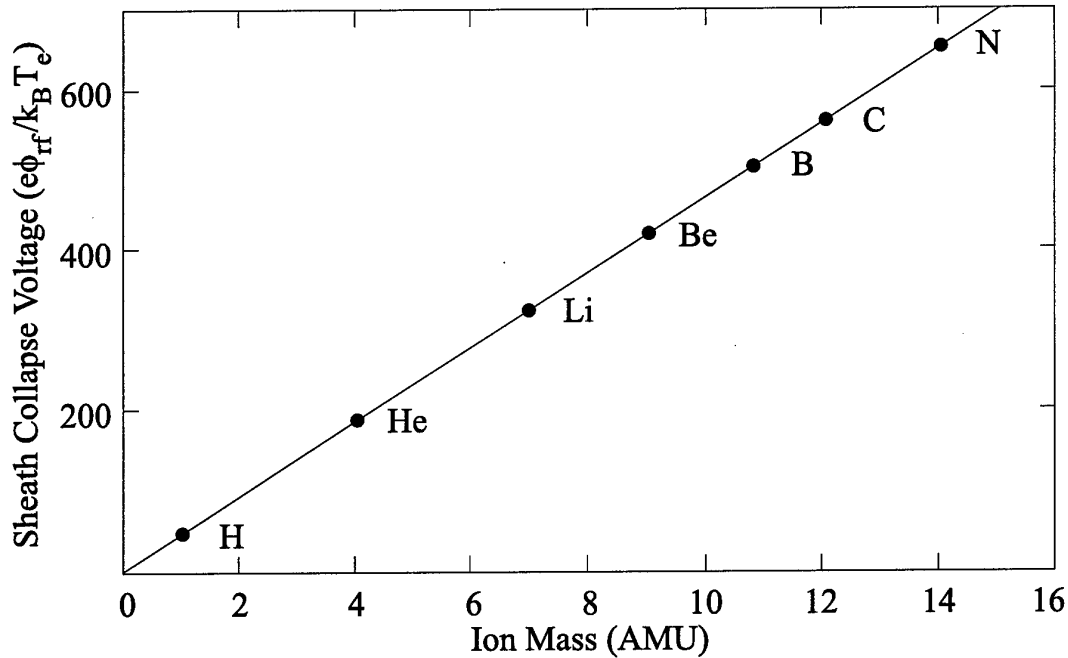
Figure 4: Sheath Collapse Voltage as a Function of Ion Mass. This figure shows the highly linear relationship between the normalised sheath collapse voltage and the ion mass for ions with low atomic numbers. Error bars are too small to be shown at this scale. The fitting function is given by equation (5), and the correlation of the data is perfect to 10 significant digits. Sheath collapse potentials for ions with masses greater than that of nitrogen may not be readily calculated due to floating point limitations of the processors used in the procedure; however, the extreme linearity of the function lends credence to extrapolation attempts.

of equations (5) and (6), the Braithwaite estimate for the argon case, and the extreme

linearity of the data for the seven calculated points tend to support the use of equation

(5) in extrapolation.

2.2.3 MODELLING THE PLASMA SHEATH

As this discussion of the plasma sheath draws to a conclusion, it seems

appropriate to note that no small portion of the literature is devoted to modelling the

sheath. In fact, a large portion of this thesis will later be devoted to the development of

a novel model of the plasma sheath. A summary of a few of the many numerical

models for plasmas and plasma/sheath combinations from the literature is given in

Table 3. The entries in this table concentrate on fluid models, as that is the method used

Model	Governing Equations	Major Assumptions
Child [1911] and Langmuir [1913]	• $v = \sqrt{\dfrac{2e\phi}{m}}$ (energy conservation) • $j = nev$ (definition of current density) • $\nabla^2 \phi = \dfrac{en}{\varepsilon_0}$ (Poisson's equation) • $\dfrac{d}{dx}(nv) = 0$ (continuity equation)	• Single charge carrier, collisionless discharge • Monoenergetic carriers
Bohm [1949]	• $\nabla^2 \phi = \dfrac{e}{\varepsilon_0}(n_i - n_e)$ (Poisson's equation) • $n_e = n_s \exp\left(\dfrac{-e(\phi - \phi_0)}{k_B T_e}\right)$ (electron density equation) • $\dfrac{d}{dx}(n_i v_i) = 0$ (ion continuity equation)	• Collisionless plasma sheath • Maxwellian electrons • Constant plasma potential (insignificant fields in the plasma) • Ions arrive at the sheath edge with a specific mean directed energy (monoenergetic ions) • No ionisation in the sheath

Table 3 (Part 1 of 4): Comparison of Selected Numerical Fluid Sheath and Plasma/Sheath Models.

Model	Governing Equations	Major Assumptions
Blank [1968]	$$\left(\nabla - \frac{e\mathcal{E}}{m_e v}\frac{\partial}{\partial v}\right)\cdot\left[\frac{v^3\tau(v)}{3}\left(\nabla - \frac{e\mathcal{E}}{m_e v}\frac{\partial}{\partial v}\right)f_0(r,v)\right]$$ $$+ \frac{m_e}{m_n}\frac{1}{v}\frac{\partial}{\partial v}\left[\frac{v^3}{\tau(v)}\left(f_0 + \frac{k_B T_n}{m_e v}\frac{\partial f_0}{\partial v}\right)\right] + vL\{f_0\} = 0$$ (Reduced electron Boltzmann equation; f_0 is the isotropic part of the electron distribution function, $L\{f_0\}$ is the electron-neutral inelastic collision integral, τ is the mean free time for momentum transfer for electron-neutral recoil collisions) $\nabla\cdot(-D_+\nabla n_i + \mu_+\mathcal{E}n_i)=v_i n_e$ (ion transport equation; v_i is the ionisation frequency per electron, D_+ and μ_+ are the ion diffusion and mobility coefficients) $\nabla\cdot\mathcal{E}=\frac{e}{\varepsilon_0}(n_i - n_e)$ (Poisson's equation) $n_e = 4\pi\int_0^\infty v^2 f_0 dv$ (electron density equation; reduces to $n_e = n_0\exp(-\phi)$ with the accompanying assumptions) $n_i = v_i n_e = \int L\{f_0\}d^3v$ (ion density equation)	• Highly collisional DC plasma • Ion and electron mean free paths small with respect to chamber size • Nearly isotropic electrons • Only significant source of ions is electron-neutral impact • Walls are perfectly absorbing • Ion diffusion and mobility coefficients are constant ($\bar{c} \gg v_{drift}$) • Mean free time between electron recoil collisions is constant • Potential decreases monotonically toward the walls • Electron boundary layer thickness much less than the electron-neutral mean free path
Franklin and Ockendon [1970]	$\nabla\cdot(n_i v_i)=\nabla\cdot(n_e v_e)=Zn_e$ (ion and electron continuity) $\nabla(n_e k_B T_e)+n_e e\nabla\phi=0$ (electron transport equation) $\nabla\cdot(n_i m_i v^2)-n_i e\nabla\phi=0$ (ion transport equation) $\nabla^2\phi=\frac{e}{\varepsilon_0}(n_i - n_e)$ (Poisson's equation)	• Collisionless DC plasma • Cold ions • No ionisation in the sheath • Directed ion flux equals random electron flux at the walls • Maxwellian electrons in equilibrium with the instantaneous field • The Debye distance is much smaller than the scale length of the plasma

Table 3 (Part 2 of 4): Comparison of Selected Numerical Fluid Sheath and Plasma/Sheath Models.

Model	Governing Equations	Major Assumptions
Nitter [1996]	• $n_e(t) = n_s \exp\left(\frac{e\phi(t)}{k_B T_e}\right)$ (electron density equation) • $\frac{d}{dx}(n_i v_i) = 0$ (ion continuity equation) • $m_i v_i \frac{dv_i}{dx} = -e\frac{d\bar{\phi}}{dx} + m_i \sigma n_n v_i^2$ (ion transport equation) • $\frac{d^2\phi(x,t)}{dx^2} = \frac{1}{\varepsilon_0}(en_e - en_i - \rho_d)$ (Poisson's equation; ρ_d is the dust charge density)	• Collisional RF sheath • $\omega_{pi} \ll \omega \ll \omega_{pe}$ • Perfectly absorbing walls; no secondary emission • Quasineutral presheath to the sheath edge • Maxwellian electrons in equilibrium with the instantaneous field • Cold ions with Bohm velocity at the sheath edge • No ionisation in the sheath or presheath • Only significant forces are electrostatic and collisional • Charge exchange collisions dominate • Constant ion collision cross section • Ion acceleration is zero at the sheath edge • Sheath edge has a constant potential with respect to ground
Riemann [1997]	• $n_i - n_e = -\frac{\varepsilon_0}{e}\frac{d^2\phi}{dz^2}$ (Poisson's equation) • $n_e = n_{ch} \exp\left(\frac{e\phi}{k_B T_e}\right)$ (electron density equation; n_{ch} is a characteristic number density) • $\frac{d}{dx}(n_i v_i) = 0$ (ion continuity equation) • $m_i v_i \frac{dv_i}{dz} = -e\frac{d\phi}{dz} - v_c(v_i) m_i v_i$ (ion transport equation; v_c is the charge exchange collision frequency)	• Collision dominated DC plasma sheath • Quasineutral presheath/collisionless sheath (note: the distinction between "sheath" and "presheath" blurs with changes in the ratio of λ_D to λ) • Maxwellian electrons in equilibrium with the field • No ionisation in the sheath or presheath • Charge exchange collisions dominate • Either the collision frequency or the mean free path is constant

Table 3 (Part 3 of 4): Comparison of Selected Numerical Fluid Sheath and Plasma/Sheath Models.

Model	Governing Equations	Major Assumptions
Valentini [1999]	• $\varepsilon_0 \dfrac{\partial^2 \phi(x,t)}{\partial x^2} = e(n_i(x) - n_e(x,t))$ (Poisson's equation) • $\dfrac{d(n_i(x)v_i(x))}{dx} = 0$ (ion continuity equation) • $\frac{1}{2} m_i c_{Bohm}^2 = \frac{1}{2} m_i v_i^2 + e\langle\phi(x)\rangle$ (ion transport equation) • $n_e(x,t)v_e(x,t) = n_s v_{ew} \exp\left[\dfrac{e\phi_{min}}{k_B T_e}\right]$ (electron density equation, $\mathcal{E} \leq 0$; v_{ew} is the electron speed at the wall) • $n_e(x,t) = n_0 \exp\left[\dfrac{e\phi(x,t)}{k_B T_e}\right]$ (electron density equation, $\mathcal{E} > 0$)	• Collisionless RF sheath • No ionisation in the sheath • Sheath edge has a constant potential with respect to ground • $\omega_{pi} \ll \omega \ll \omega_{pe}$ • Maxwellian electrons in equilibrium with the field • Directed ion flux equals random, time-averaged electron flux at the walls • Potential not restricted to monotonic decreases toward the wall, but ions must be monoenergetic between any potential minimum and the wall. • Time of flight of electrons through any portion of the sheath where $\mathcal{E} < 0$ is much less than an RF period
Franklin and Snell [2000]	• $\nabla \cdot (n_i v_i) = \nabla \cdot (n_e v_e) = \nu_i n_e$ (ion and electron continuity) • $k_B T_e \dfrac{dn_e}{dx} - n_e e \dfrac{d\phi}{dx} + m_e n_e v_e v_e + m_e n_e v_i v_e = 0$ (electron transport equation) • $m_i v_i \dfrac{dv_i}{dx} + m_i v_i v_i + e\dfrac{d\phi}{dx} = 0$ (ion transport equation) • $\dfrac{d^2\phi}{dx^2} = \dfrac{e}{\varepsilon_0}(n_e - n_i)$ (Poisson's equation)	• DC plasma (collisionless through highly collisional conditions) • Cold ions • Constant collision frequency • Directed ion flux equals random electron flux at the walls

Table 3 (Part 4 of 4): Comparison of Selected Numerical Fluid Sheath and Plasma/Sheath Models.

in the model developed for this thesis. As can be seen, most of the models use some combination of equations of motion for the ions and electrons, continuity equations, and Poisson's equation to develop a description of the electrical characteristics of the plasma/sheath. The models reviewed here cover the gamut of conditions from collisionless to collision-dominated, for both RF and DC generation techniques. These models will be discussed at greater length later in this thesis.

2.3 CHARGING THEORY

Now that a few of the basic properties of plasmas have been discussed, it becomes time to investigate how a researcher should set out to measure these properties. Plasmas often seem to do their best to defy parameterisation. As soon as a diagnostic probe is inserted to measure a plasma parameter, the plasma rearranges itself to shield itself from the probe. This behaviour means that researchers must deduce the actual plasma parameters from these shielded measurements. In order to understand the probe readings, one must first understand how charged particles move in the neighbourhood of the probe. These theories of carrier motion then lead to expressions for currents, space-charge densities, and potentials, among other things. Perhaps most importantly for the purposes of this thesis, the theories predict the charging of probes. This is important here, as the dust particles that will be inserted into the plasma and sheath are, in essence, isolated probes that become charged to the floating potential.

One of the many important parameters affecting a probe's characteristics is its geometry. Probe theories are usually delineated between three basic probe geometries: planar, cylindrical, and spherical. In this thesis, unless explicitly stated otherwise, all theories discussed will be for spherical probe geometry. This choice of geometry will be the most useful when probe theory is later applied to spherical dust.

Understanding how charged particles arrive at floating probes is essential to quantifying probe properties such as the floating potential and total charge. The angular momentum of the charges relative to the centre of the probe is the parameter that separates the two major theories of probe charging, orbital motion theory and radial motion theory. The more complex theory, that of orbital motion, will be investigated first, followed by a look at the consequences of limiting the allowed values of angular momentum to finally arrive at radial theories.

2.3.1 ORBITAL MOTION THEORY

One of the original theories of how charged particles approach a probe in a plasma was put forth by Mott-Smith and Langmuir [1926] in one of their seminal papers on the subject. Although a great breakthrough toward the goal of understanding the results of probe measurements of current and potential in the plasma, it had major limitations due to several incorrect assumptions about the nature of the plasma. (Their primary fallacy was assuming that the entire probe potential is developed across the sheath, failing to realise small fields can exist in the plasma. As was discussed earlier, Bohm [1949] showed that such fields must exist.) Their theory was extended by Bohm, Burhop, and Massey [1949], later by Bernstein and Rabinowitz [1959], and then by the voluminous report of Laframboise [1966].

2.3.1.1 Orbital Motion Limited Theory

The orbital motion limited theory (OML) is a simplified version of the full orbital motion theory. Its limitations will be described later. The angular momentum, J, of a charged particle with respect to the probe centre may be calculated in the usual way, namely
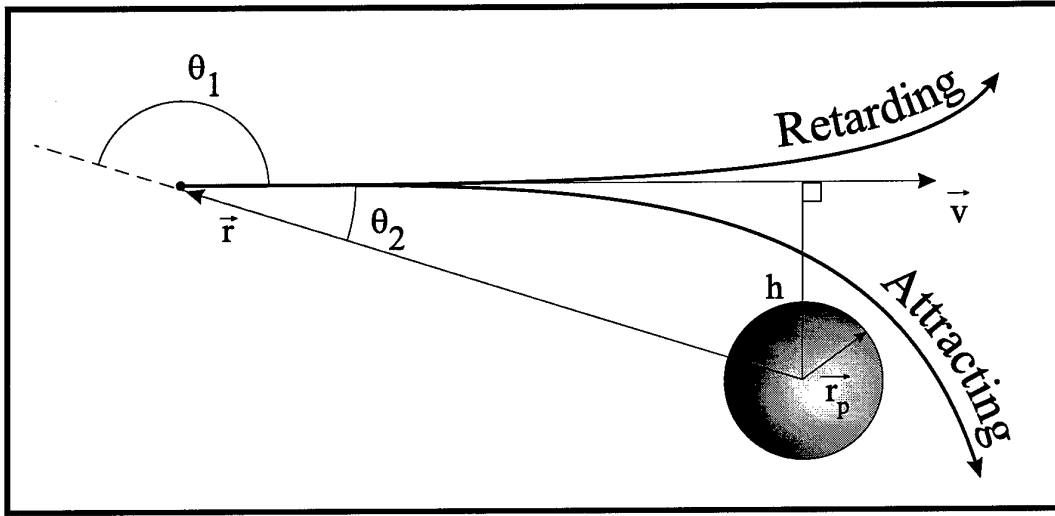
Figure 5: The Impact Parameter. This figure shows the geometry associated with the impact parameter of orbital motion limited (OML) theory. Notional particle trajectories for both retarding and attracting potentials are indicated.

$$(7) \qquad \vec{J} = m\vec{v} \times \vec{r} .$$

where $\vec{r}$ is the position vector of the particle and $\vec{v}$ is its velocity. Consider the general

situation depicted in Figure 5. A particle with an arbitrary angular momentum may

always be characterised by a parameter h, called the impact parameter. This parameter

defines the distance by which the particle on its zero-potential trajectory would miss the

probe centre. Using the notation from the figure, the impact parameter has a magnitude

$h = r_0 \sin \theta_2$, where r_0 is the radius where the potential is very small compared with that

at the probe surface. Considering isolated spherical probes, the charged particles move

in a central field and angular momentum is conserved. Thus, particles that just graze

the surface have angular momentum magnitudes of

$$(8) \qquad m v_p r_p = m v_0 h_p$$

at the probe surface, where v_p and r_p are the particle velocity and radius at the surface

of the probe. Conservation of energy gives the expression

$$(9) \qquad \tfrac{1}{2}mv_0^2 + e\phi_0 \cong \tfrac{1}{2}mv_0^2 = \tfrac{1}{2}mv_p^2 \mp e\phi_p$$

where the negative sign is for electrons and the positive sign is for singly ionised ions.

Combining these two conservation laws yields the following expression for the

impact parameter of a particle that just grazes the probe surface, h_p:

$$(10) \qquad h_p = r_p(1 \pm \phi_p/\phi_0)^{\frac{1}{2}} = r_p(1 \pm e\phi_p/k_B T_{e,i})^{\frac{1}{2}}.$$

This relationship, where the positive sign is for electrons, shows that h_p may be taken

as the effective radius of the probe. Only particles with impact parameters less than this

value will strike the probe. Other particles may be deflected, but they will not

contribute to the particle flux at the probe surface.

Notice that for attracting potentials ($\phi_p < 0$ for ions and $\phi_p > 0$ for electrons),

$h_p > r_p$. The situation for retarding potentials is more complicated, as the radical can

become negative. When the argument of the radical is positive, $h_p < r_p$. The physical

significance of an imaginary solution for h_p is that electrons with these energies will

not overcome the potential barrier to collide with the probe.

For attracting potentials (*e.g.*, negative potentials with positive charges), Allen

[1992] has shown that this analysis leads to an exact equation for current to a spherical

probe given by

$$(11) \qquad I_{e,i} = 4\pi r_p^2 n_0 e (k_B T_{e,i}/2\pi m_{e,i})^{1/2} (1 \pm e\phi_p/k_B T_{e,i})$$

where the positive sign goes with the expression for electrons. A similar analysis

developed for this thesis shows that the spherical probe current for retarding potentials

is exactly

$$(12) \qquad I_{e,i} = 4\pi r_p^2 n_0 e (k_B T_{e,i}/2\pi m_{e,i})^{1/2} \exp(\pm e\phi_p/k_B T_{e,i}).$$

Again, the positive sign is for the electron equation.

The OML theory is of limited application when applied to attractive potentials

because it tacitly assumes that some particles of *all* energies can *graze* the probe

surface, reaching the probe just as they reach zero radial velocity [Allen, 1995]. As will

be shown shortly, a more detailed consideration of the effect of angular momentum will

significantly alter the form of the probe potential seen by the charged particles.

2.3.1.2 Orbital Motion Theory and the Absorption Radius

When a mass moves relative to a fixed point, it possesses an angular

momentum given by equation (7) above. It can be shown that the angular momentum

can be treated as an effective *radial* potential energy [*e.g.* Swift and Schwar, 1970]. As

such, it will add its form to the electrical potential considered in the OML theory. In

OML, the potential was purely attractive or retarding depending on the type of particle

and probe voltage. When the effective potential due to angular momentum is added to

the electrical potential, the radial potential eventually takes on a retarding character
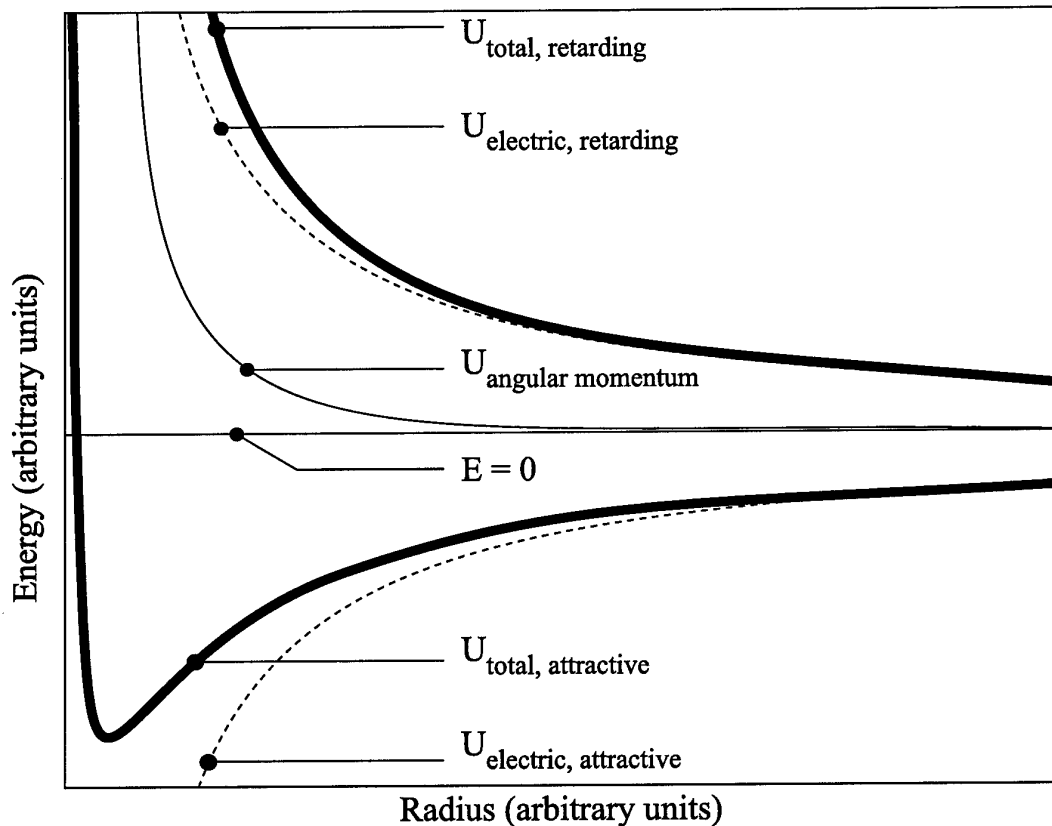
Figure 6: Orbital Motion Potential Energies Showing the Effect of Angular Momentum. This figure shows how the effective potential due to a particle's angular momentum combines with both attracting and retarding potentials to form radial potential energies. The effect of angular momentum is most pronounced for the attracting potentials, where the negative curvature of the electrical potential is overwhelmed at small radii by the effective angular momentum potential, forming a well in the radial potential.

for all values of angular momentum except zero. Figure 6 illustrates this concept for

both attractive and retarding electric potentials. In the orbital motion theory, the probe

radius becomes a much more important factor in determining whether a particle of a

given energy and angular momentum will contribute to the flux at the probe; flux is no

longer just a simple function of probe cross section, as it was in OML theory. Figure 7,

adapted from Bernstein and Rabinowitz [1959], shows a family of curves for the total

radial potential, U(r), due to an attractive electric potential and the effective potential

from the particle's angular momentum. The lowest curve is for zero angular

momentum, *i.e.*, purely radial motion. In that case, all particles will eventually strike

Critical Radius

$J_c^2 < J^2$

$J^2 = J_c^2$

$J_a^2 < J^2 < J_c^2$

$J^2 = J_a^2$

$0 < J^2 < J_a^2$

$J^2 = 0$

$E = 0$

Energy (arbitrary units)

Radius (arbitrary units)
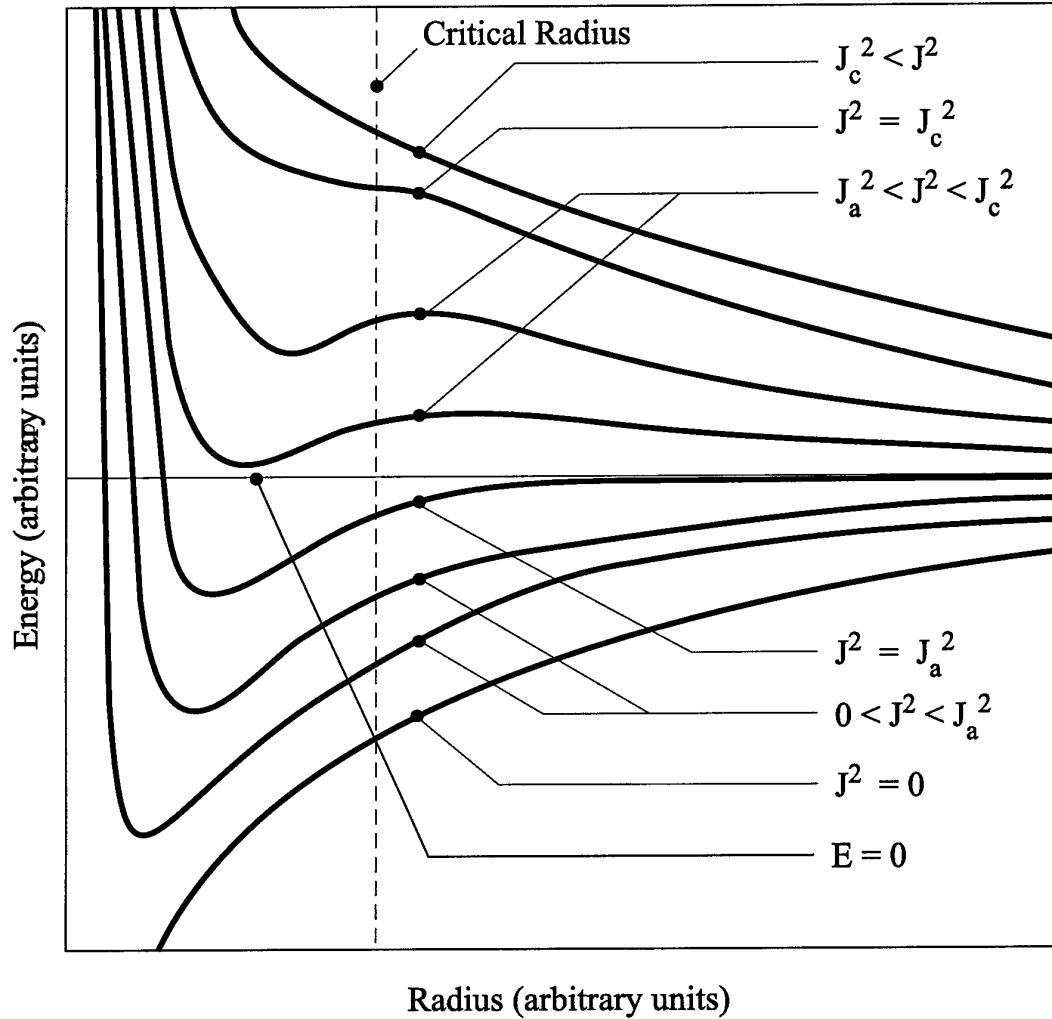
Figure 7: Orbital Motion Potential Energies for a Variety of Angular Momenta. This figure, adapted from Bernstein and Rabinowitz [1959], shows a family of radial potential energy curves for values in every possible range of the particle's angular momentum. Potential energy curves for $J^2 \leq J_a^2$ only have a single local minimum, while curves for angular momenta between J_a^2 and J_c^2 have a local minimum and a local maximum. Curves for angular momenta greater than the critical value, J_c^2, have no local extrema. The critical radius is the point on the critical angular momentum curve where the curvature goes to zero. The $J = 0$ curve relates to the radial motion theory.

the probe, regardless of the particle's initial energy and the probe radius. As soon as the

angular momentum becomes non-zero, however, the shapes of the curves change

dramatically. The effective potential due to angular momentum dominates at small

radii, causing extreme repulsion there. For small values of angular momentum,

the curves exhibit a single minimum at a small radius, followed by an asymptotic

approach from below to the energy level chosen as the zero of potential energy.
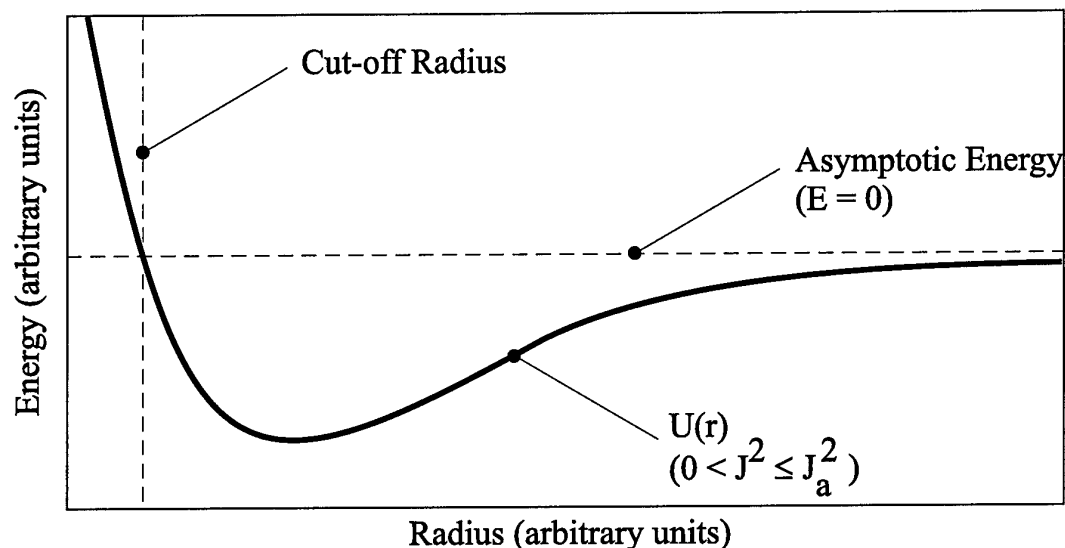
Figure 8: Representative Orbital Motion Potential Energy Curve for Smaller Angular Momenta.
This figure shows the energy well for a low-angular-momentum particle. For probes with radii greater than the indicated cut-off value, all particles with non-negative energies will impact the probe.

Following Bernstein and Rabinowitz, The maximum value of angular momentum for which there is but one local extremum is denoted J_a. Curves for values of angular momenta greater than J_a but below a critical value J_c have two local extrema: a smaller radius minimum and a larger radius maximum. They then approach the $E = 0$ asymptotic limit from the positive side, where E is the total energy of the orbiting particle. Curves for values of J greater or equal to J_c have *no* local extrema; they monotonically decrease toward zero.

How do the shapes of these potential curves affect probe characteristics? Let us look at several cases. Figure 8 shows a schematic of a typical potential energy curve for a specific value of angular momentum such that $0 < J^2 \leq J_a^{\,2}$. For probe radii greater than the indicated cut-off value, *all* particles with this angular momentum and non-negative energy will hit the probe. Collisions could force particles into negative energy, closed orbits; this possibility will be discussed later. For probe radii less than this value, only particles with this specific angular momentum *and* an energy greater
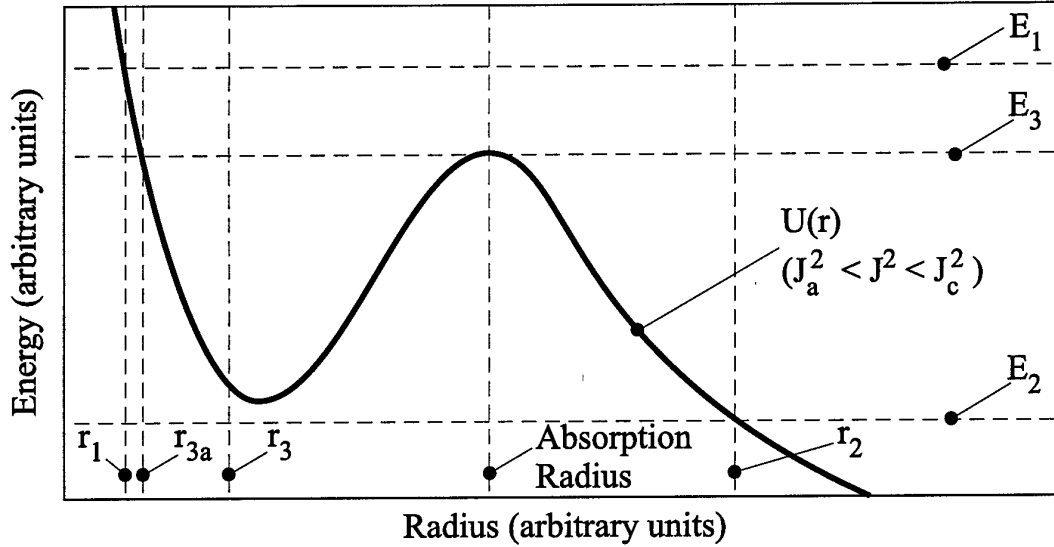
Figure 9: Representative Orbital Motion Potential Energy Curve for Intermediate Angular Momenta. This figure shows the energy well for a medium-angular-momentum particle. For probes with radii r_3 (between r_{3a} and the absorption radius), the absorption radius determines probe charging characteristics, not the probe radius. For these radii, no particles with energies less than E_3 will impact the probe, and all particles with energies greater than this value will reach the probe, albeit with different radial velocities at impact.

than the intersection of the potential curve and the probe radius will contribute to the particle flux at the probe surface.

For particles with angular momenta greater than J_c, there are no extrema. Thus, only particles with energies greater than or equal to the energy at the intersection of the appropriate potential curve and the probe radius will make it to the probe.

Figure 9 shows a schematic of the final subset of specific angular momenta where $J_a^{\,2} < J^2 < J_c^{\,2}$. This area is a bit more complicated than the other ranges of angular momentum. For particles with angular momenta within this range, the most important energy is the energy labelled E_3 in the figure. This energy intersects the potential curve at its local maximum. The radial location of this local maximum is called the *absorption radius*. Let us look at three cases that will describe which particles impact the probe. In case 1, the probe radius, r_1, is very small, smaller than the

small-radius intersection of E_3 with the potential curve. Here, the only effect of the potential energy well is in the timing of the arrival of the particles. Only particles with energies greater than or equal to E_1 will make it to the probe. Case 2 has a probe radius, r_2, greater than the absorption radius. The energy well has no effect at all on these particles and all particles with energies greater than E_2 make it to the probe.

Case 3 is the most interesting situation. Here, the probe radius, r_3, is between the radii corresponding to the intersections of E_3 and the potential curve (between r_{3a} and the absorption radius). For this case, all incoming particles with energies greater than E_3 will make it to the probe. The unique thing about this region, however, is the irrelevance of the actual value of r_3. As long as it remains between r_{3a} and the absorption radius, the number of particles that reach the probe remains constant. For these radii, the *absorption radius* is the determining factor for probe characteristics, *not the probe radius*. All particles that can pass the absorption radius will eventually reach the probe. However, these particles cannot hit the probe *at grazing incidence*. For this range of radii, the particles must have some radial kinetic energy upon probe impact, as is evident from fact that the (constant) particle total energy plot is greater than the potential curve at the probe surface. This is in contradiction to the assumption made earlier for the OML theory that particles of all energies could graze the probe surface.

Expressions for the probe currents and floating potentials derived from this theory are much more complicated than their OML counterparts and require an exact knowledge of the spatial variation of the potential to obtain numerical values. The presence of the potential well for angular momentum values such that $0 < J^2 < J_c^{\,2}$ also complicates current and charge density calculations in another way. Particles initially

having enough energy to make it to the probe surface could suffer energy-losing

collisions prior to reaching the probe. Should enough energy be lost in such a collision,

it is possible for the particle to become trapped in the potential well, orbiting in a

closed, elliptical or circular orbit around the probe. The presence of such trapped

particles has a significant effect on density and current theory. To avoid this problem,

many researchers simply either specify a collisionless sheath, or only consider probes

with radii greater than a critical radius coincident with the inflection point of the

$J^2 = J_c^2$ curve [Bernstein and Rabinowitz, 1959]. (The critical radius is depicted in

Figure 7.)

Note that an absorption radius can still exist for probes with radii greater than

the critical radius. Particles for which $J_a^2 < J^2 < J_c^2$ and for which the radius at which

their specific potential energy curve has a maximum is greater than the probe radius will

have an absorption radius. Figure 10 illustrates this condition. However, the commonly

assumed restriction that the probe radius must be greater than the critical radius ensures

that no closed orbits exist. This fact is due to the lack of a local minimum between the

absorption and probe radii for any value of the angular momentum.

The condition for no absorption radius to exist, then, is a restriction on the

angular momentum of the particle with respect to the probe. As long as the radial

potential curve is monotonic, there will be no absorption radius. This condition

corresponds to the range of angular momentum values $J^2 \geq J_c^2$. If an absorption radius

exists, OML must be invalid due to the grazing incidence assumption. Even if no

absorption radius exists, OML theory is only approximately valid. Annaratone *et al.*
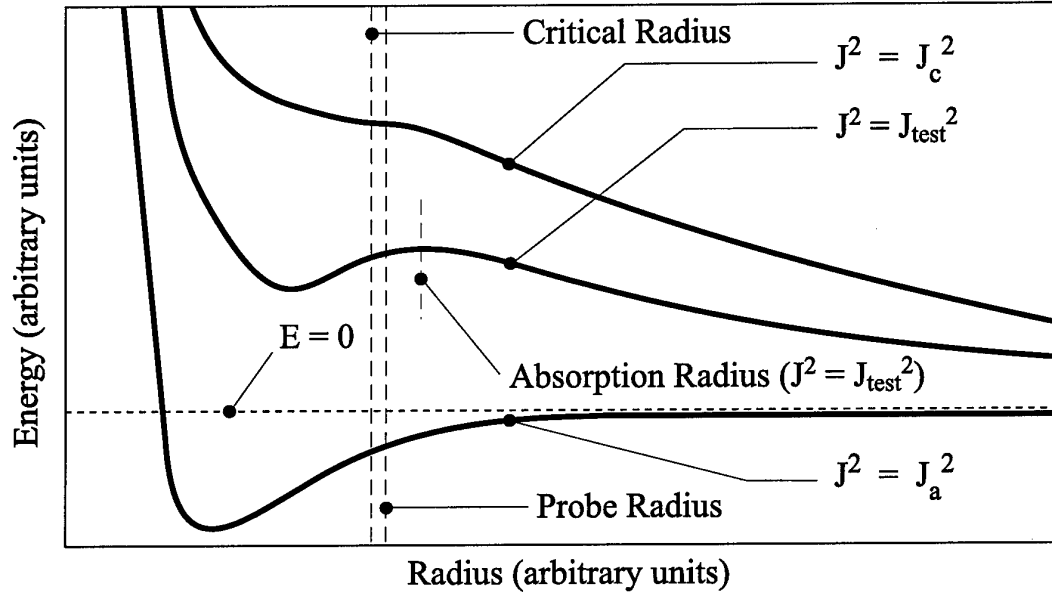
Figure 10: The Existence of Absorption Radii for Probe Radii Greater Than the Critical Radius. This figure demonstrates that for particles with J^2 between J_a^2 and J_c^2, it is possible to have an absorption radius existing outside both the critical radius and the probe radius. However, no closed particle orbits may exist in this situation. As the slope of the potential curve is always positive between the absorption and probe radii, particles suffering energy-losing collisions inside the absorption radius will still impact the probe.

[1992] have estimated that OML theory will fail in a collisional, non-infinite plasma at another angular momentum limit based upon the ratio of the mean free path to the probe radius. They estimate the maximum angular momentum of the particle in a collisional, non-infinite plasma as $J_{max,collisional} \cong (2mk_BT_i)^{1/2}\lambda$ and the angular momentum calculated through collisionless OML theory as $J_{OML} \cong (2mk_BT_i)^{1/2}(1 - e\phi_p/k_BT_i)^{1/2}r_p$. If $J_{OML} > J_{max,collisional}$, then OML will fail. For this thesis, this inequality has been reformulated to state an OML validity criteria based on easily measurable physical quantities:

$$(13) \qquad \frac{\lambda}{r_p} > \left(1 - \frac{e\phi_p}{k_BT_i}\right)^{1/2}.$$

Note that in many practical plasmas, this inequality is false and OML theory is not valid. In short, calculations using OML theory are so much simpler than orbital motion theory that many authors have chosen to use it in their papers without regard to its many limitations. In fact, OML theory will be used later in this thesis as well, but only as a clearly labelled first approximation to the actual physical process being modelled. The general validity of OML theory is also being challenged in the recent literature [Allen *et al.*, 2000]. With the publication of that paper, there exists the strong possibility that a very large number of conclusions from the literature may have to be rethought.

2.3.2 RADIAL MOTION THEORY

Radial motion theory is the limiting case of the orbital motion theories. It is the $h \rightarrow 0$ limit of OML and the $J \rightarrow 0$ limit of orbital motion theory. For the spherical probes being considered here, it can be shown that after the attracted particles have been accelerated to an energy much larger than their thermal energy, their velocity is purely radial [Allen *et al.*, 1957]. This causes them to respond to the $J^2 = 0$ potential curve shown previously in Figure 7.

As a reminder, the exact form of the spatial variation of the potential around the probe that generates the curves shown in the above figures has yet to be stated. For both the OML and orbital motion theories, the existence of the plasma sheath is neglected, or is applied with a discontinuous boundary. In other words, specific plasma and sheath regions are not considered. In contrast to those theories, the Allen-Boyd-Reynolds (ABR) radial motion theory [Allen *et al.*, 1957] includes a pre-sheath
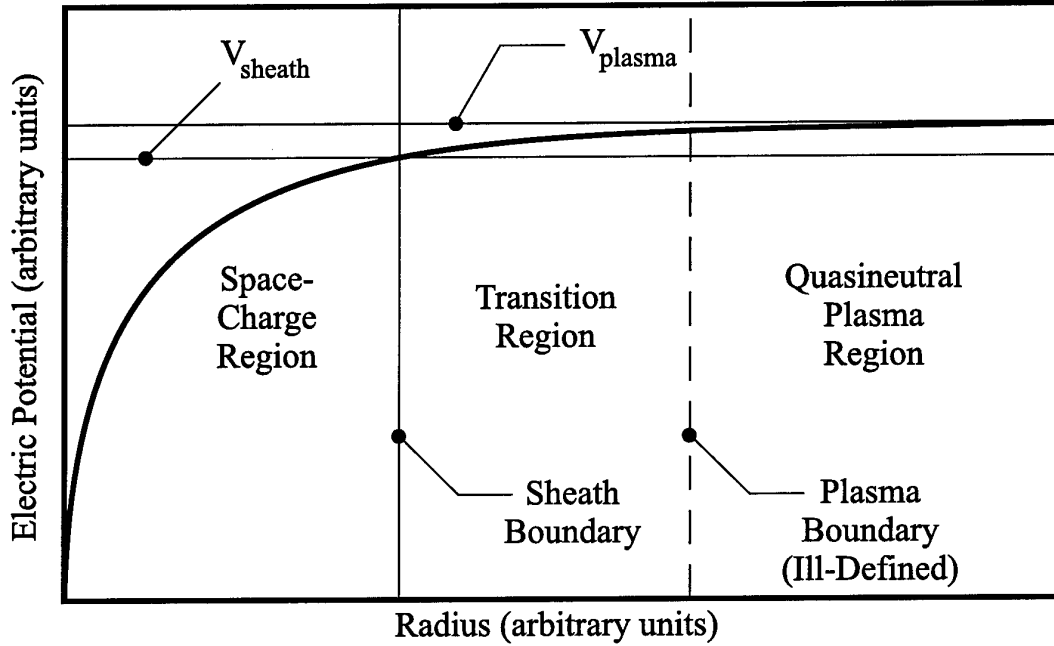
Figure 11: Schematic of the Plasma Sheath. This figure shows the regions present near a boundary of a collisionless plasma. The positive space-charge region, the plasma sheath, ranges from the boundary to the Bohm point, where the ion speed becomes subsonic. The transition region, or presheath, abuts the sheath and ranges out to a nebulous point where the quasineutral approximations of the plasma begin to be valid. For certain collisional sheaths, the sheath boundary is not defined by the Bohm criterion and the transition region may extend to the wall [Franklin and Snell, 2000].

transition region where quasineutrality is satisfied but potentials on the order of the

Bohm [1949] potential,

$$(14) \qquad \phi_{Bohm} \geq k_B T_e \Big/ 2e ,$$

are allowed to exist. The outer, low-field boundary of this transition region is

somewhat nebulous (experimentally, the boundary is often set to the point where the

measurement error is larger than the measured voltage), but its inner location is defined

by this criterion. Between this boundary and the wall, quasineutrality can no longer be

assumed and a space-charge region, the previously discussed plasma sheath, develops.

Figure 11 illustrates these three regions. Again, results in recent papers [Riemann,

1997; Franklin and Snell, 2000] have shown that the inner boundary, between the

Author(s) (Theory)	Absorption Radius?	Ion Energy and Distribution	Sheath Size	Ion Current Expression
Mott-Smith and Langmuir [1926] (OML)	No	Maxwellian $e\phi_0 = k_B T_i$	None	$4\pi r_p^2 n_0 e(2k_B T_i/m_i)^{1/2}\left(1-\dfrac{e\phi_p}{k_B T_i}\right)^{1/2}$
Bohm, Burhop and Massey [1949] (Orbital Motion)	Yes	Positive, finite, monoenergetic $T_i/T_e \neq 0$	$r_s \cong r_p$	$0.57(4\pi r_p^2)n_0 e(k_B T_e/m_i)^{1/2}$ (for $T_i/T_e = 0.01$) $0.54(4\pi r_p^2)n_0 e(k_B T_e/m_i)^{1/2}$ (for $T_i/T_e = 0.5$)
Allen, Boyd, and Reynolds [1957] (ABR/Radial Motion)	Yes	Cold Ions $T_i/T_e \to 0$	$r_s \cong r_p$	$0.61(4\pi r_p^2)n_0 e(k_B T_e/m_i)^{1/2}$
			$r_s > r_p$	No analytic solution. Results presented graphically.
Bernstein and Rabinowitz [1959] (Orbital Motion)	Yes	Cold Ions $T_i/T_e \to 0$	$r_s > r_p$	No analytic solution. Results presented graphically.

Table 4: Comparisons of Theories for Positive Ion Collection by Spherical Probes.

transition region and the plasma sheath, is also ill defined for many collisional plasmas. The latter authors show that when the transition region becomes collisional, the Bohm criterion ceases to describe the sheath edge, and the concept of a definite edge to the sheath ceases to have meaning.

2.3.3 RESULTS FROM THE THEORIES OF MOTION

Table 4, adapted from Annaratone *et al.* [1992] and Allen *et al.* [1957], summarises the theories of motion that have been discussed here and highlights assumptions made in each. As floating probes in plasmas usually are negatively charged, this table only considers the case of positive ions being collected by a negatively charged probe. Notice that analytical solutions for the more usual case of a large sheath do not exist and the results for these theories have to be presented graphically. It is also worth mentioning here that experimental work from the literature tends to support the simple ABR theory rather than the more complicated orbital theories [Annaratone *et al.*, 1992]. Experimental results presented later in this thesis also favour ABR over OML.

2.3.4 CHARGING THEORY IN THE PLASMA SHEATH

Now that expressions for charged particle current have been described, it should be a relatively simple matter to determine the floating potential of an isolated dust particle. In theory, one should simply have to equate ion and electron current expressions and solve for the potential. Unfortunately, the problem is not quite that simple, especially if the dust is located in the plasma sheath instead of the plasma. For the charging theories described above, Maxwellian distributions for the electrons were assumed in all cases, and a variety of distributions from monoenergetic to Maxwellian were assumed for the ion distributions. In the sheath of RF plasmas, electrons have been shown to have distinctly non-Maxwellian electron energy distribution functions (EEDFs), with some theory even showing two distinct temperatures at certain points in the RF cycle [Lichtenberg, 1998]. Probe measurements taken in the OXDUPLAG reactor also show, under certain conditions, the existence of a high-temperature beam of electrons existing among the cooler background electrons. Textbooks on plasmas also detail the non-Maxwellian nature of EEDFs in the plasma and the sheath [*e.g.* Chapman, 1980]. Ions, too, are a far cry from Maxwellian in the sheath. As they become accelerated toward the probe they acquire a streaming velocity and their distribution begins to look more Druyvesteyn [1940] than Maxwellian. These factors and many others significantly complicate the problem of calculating the floating potential.

An extensive literature review turned up only two theories of small-particle charging in the plasma sheath. The first, due to Nitter [1996], assumes that the charge carriers move in a spherically symmetric Coulomb potential centred on the dust particle.

The dust is assumed to be much smaller than the Debye length. Nitter ignores the effects of the sheath field, Debye shielding, and ion wakes by assuming that, inside a Debye sphere surrounding the dust particle, those effects are insignificant when compared to the particle's field. The second theory, that of Chen [1997], uses an independently developed, slightly modified variant of a similar formulation. Unfortunately, both of these theories rely on the discredited OML theory to obtain the ion and electron currents to the particle. A theory of particulate charging in the sheath is currently under development here in Oxford [Kennedy, 2000], but it has yet to be finalised. Thus, it seems that the best that can be done at the present time is to use a central-force-based charging theory that is inappropriate for the conditions in the sheath to approximate the theoretical charge expected on the particles. A comparison of these charging theories for plasmas with experimental data taken in the plasma sheath will be performed in a later chapter of this thesis.

The preceding sections on sheaths and charging theory have been a rather lengthy digression into some well-hashed basic theory. However, the thorough understanding of how charges end up on probes is a fundamental concept for the understanding of the behaviour of dust in a plasma. In the remainder of this chapter, a more complete description of the interaction between dust and plasma sheath will be examined, with the intent of simplifying the theoretical problems posed by dust oscillating in a plasma sheath to a tractable level.

2.4 PLASMA/DUST INTERACTIONS

What remains in this chapter is to tie together plasma sheath theory and charging theory into a cogent description of the behaviour of dust in a plasma. In this section,

dust will be treated as spherical probes at the floating potential. From this treatment, it will be shown that wide varieties of unusual plasma behaviours are possible due to the exceptionally high charges and masses of typical dust particles. As the experiments to be described later were performed on the simpler case of dust in a plasma, the subject of forces on isolated dust will be discussed first. Following that discussion, the more complicated subject of dusty plasmas will be examined, as the results of the dust-in-a-plasma experiments of this thesis will later be compared to several dusty-plasma experiments from the literature.

2.4.1 FORCES ON ISOLATED DUST

Forces acting on isolated dust may be grouped into two broad categories. The first category involves forces that act upon dust regardless of its motion within the sheath. Later, the topic of forces that result from the dust's motion will be addressed.

2.4.1.1 Forces on Stationary Dust

In typical laboratory experiments, there are a number of forces that act on dust particles. Dust is extremely massive in relation to the ions and electrons that make up a plasma. Therefore, the role of the gravitational force is much more relevant to a discussion of dust than of plasmas. In terrestrial dusty plasma experiments, the gravitational attraction actually becomes quite a theoretical nuisance. Gravity generally causes the dust to suspend not in the plasma, where the physics is relatively well understood, but rather in the plasma sheath near the lower electrode. The theory of the plasma sheath is much less developed than plasma theory, especially at higher pressures where collisional effects cannot be neglected. As has been previously discussed, a coherent theory of particle charging in the sheath does not appear to yet exist.

In addition to gravity, the electric field between the electrodes generating the plasma is the source of another very important force acting on dust in the plasma sheath. As the plasma is generally the most positive component in a system, its electric field must point outward toward its container. Near the lower electrode, the field points downward, so the force on the negatively charged dust particles is upward. The electric potential in the sheath is not constant, having a minimum magnitude at the sheath edge and a non-linear, monotonic increase in magnitude as it approaches the electrode. The exact nature of its spatial variation in collisional regimes is still being discussed in the literature. However, it does not take much thought to see that if the opposing gravitational and electric forces are of similar magnitudes there might be an equilibrium point of suspension somewhere in the sheath. Such equilibria will be examined in great detail in later chapters.

Some authors have suggested that the gradient in the Debye length within the sheath could lead to modifications of the basic $F_e = Q_d \, d\phi/dz$ form for the electric force felt by the dust, where F_e is the electric force, Q_d is the dust charge, and z is distance [Daugherty *et al.*, 1993; Hamaguchi and Farouki, 1994]. However, other researchers have discounted this force as insignificant for experimental conditions similar to those used at OXDUPLAG [Nitter, 1996].

As was explained in the preceding section on sheaths, ion flow in the sheath will be of fairly high velocity. Even with their tiny masses and relatively inefficient energy transfer function with respect to the massive dust grains [*e.g.* Chapman, 1980], the sheer number of high-velocity ion-dust collisions may result in a significant force on the dust [Nitter, 1996]. The sheath field continually accelerates ions as they fall toward

the lower electrode. Thus, the ion drag force will not be constant and will depend, among other things, upon the collision distance above the electrode. Again, as the acceleration experienced by the ions is dependent upon the non-linear spatial variation of the poorly understood sheath potential, there will be as many competing models of ion drag as there are sheath models in the current literature.

Another result of the flow of positively charged ions around the negatively charged dust particles is a drag force called Coulomb drag. Not all ions that interact with the dust actually collide with it. Some of the ions pass near enough to be significantly accelerated. The momentum of the slowed ions is transferred to the dust through the Coulomb force. As many more ions are slowed by Coulombic interaction than actually impact the dust, this force is considerably larger than the ion drag due to impact [Bittencourt, 1986].

Should there be a temperature gradient within the sheath, a thermophoretic force will result. This force is primarily transmitted by the neutral gas, as in most laboratory plasmas their numbers greatly exceed those of their ionised counterparts. Energetic particles from the hotter region will transfer more momentum to the dust than collisions with cooler parts of the gas, resulting in a net force toward the cooler region. The magnitude of this force can vary greatly, depending on the temperature gradient during the specific experiment [Waldmann and Schmitt, 1966], and can approach the magnitudes of the electric and gravitational forces under some glow discharge conditions [Jellum et al., 1991].

The relative magnitudes of the forces described above on the dust in the sheath range across several orders of magnitude. Table 5, adapted from Law [1998], compares

Gravitational	Electrical	Polarisation	Ion Drag	Coulomb Drag	Thermophoretic
1 (1)	0.5 to >>1 (1)	0 (0)	0.00 to 0.04 (0.01)	0 to 1 (0.1)	0 to 1 (0.01?)
↓	↑		↓	↓	↑

Table 5: Order of Magnitude Estimates of Forces on Dust in the Plasma Sheath. The range of possible values for each force is listed first, followed in parentheses by the approximate value at the dust suspension height. The direction of each force is also indicated. Forces indicated are in units of the gravitational force.

the relative effects of the various forces acting on dust at rest in the plasma sheath for conditions approximating those described later in the experimental chapters of this thesis. The value for the thermophoretic force depends upon the temperature gradient within the plasma reactor, which has not been accurately determined for the reactor used in the experiments described herein. A value close to zero is considered more likely for plasma conditions similar to the ones in this thesis [Jellum *et al.*, 1991]. The values for the drag forces and the electric force increase as the electrode is approached. It can be seen that for most cases, the only significant forces acting on the dust at the suspension height will be the electrical and gravitational forces.

2.4.1.2 Forces on Moving Dust

Each of the above forces will act on dust particles without regard to the dust speed, assuming the dust speed is much less than the thermal velocity of the ions in the sheath. However, if the dust is moving with respect to the neutral background gas, friction with this gas must be taken into account. Fortunately, for the parameters of most plasmas studied by OXDUPLAG, the mean free path of the neutral gas is very large with respect to the dust radius. This allows us to use kinetic theory to calculate the neutral drag force instead of much more complicated hydrodynamic calculations.

The standard model of neutral drag on small spheres in gases is due to Epstein [1924], developed in response to Millikan's [1923] famous oil drop experiments. The exact drag relationship was found to depend upon the ratio of the dust radius to the

mean free path of the gas molecules, which is very small for the experimental

conditions to be described later. Epstein then derives two physically possible models of

the collision process between gases and spheres for this radius-to-mean-free-path ratio.

The first model, specular reflection, postulates hard-sphere, elastic collisions between

the gas and the sphere. The gas molecules impact the sphere and immediately rebound

according to the laws of specular reflection. The second model, diffuse reflection,

postulates the gas molecules sticking to the sphere, thermally equilibrating, and being

reemitted in random directions according to a thermodynamically permissible cosine

law. The neutral drag forces due to the small-particle specular and diffuse theories are

given by

$$(15) \qquad \vec{F}_{nd} = -(\gamma)\vec{v}_d = -\left(\delta \frac{4\pi}{3} m_n a^2 \bar{c}_n n_n\right)\vec{v}_d$$

where γ is the drag coefficient, the value of δ (the Millikan coefficient) is unity for

specular reflection and $(1+\pi/8)$ for diffuse reflection, a and v_d are the sphere radius

and velocity, and n_n, m_n, and $\bar{c}_n$ are the number density, mass, and average speed of the

neutral gas molecules. Epstein proposed an empirical combination of 90% diffuse and

10% specular drag to match Millikan's data, but later experimental estimates of neutral

drag seem to have eliminated the possibility of specular emission altogether [Talbot *et

al.*, 1980]. Thus, in this thesis the neutral drag will be described using equation (15)

with δ set to $(1+\pi/8)$.

There is one final form of drag that can impede the movement of dust in the

sheath, even in the absence of collisions. This drag is due to "collisionless charge

damping" of the dust as it oscillates in the sheath [Melandsø, 1992; Havnes *et al.*,

1992b; Nitter and Havnes, 1992; Melandsø *et al.*, 1993]. Because the ion and electron

currents are different at each different height in the sheath due to the spatial variation in

carrier densities and velocities, there will be different floating potentials and hence

different equilibrium dust charges for the various heights. As the dust moves through

the sheath, its finite charging time implies that the actual charge on the dust may not be

the equilibrium charge for its current position. The difference between actual and

equilibrium charge can cause a force opposing the dust motion as the actual charge

attempts to approach the equilibrium value. Calculations have shown that this force is

negligible under typical plasma conditions used by OXDUPLAG, as the ratio of the

charging time scale to the oscillation time scale is on the order of 10^{-4} to 10^{-5} [Nitter,

1996].

2.4.2 FORCES ON COLLECTIONS OF DUST

The experiments to be described later in this thesis were performed on dust in a

plasma, implying that there was not enough dust present in the plasma for the

interaction of dust particles to have a significant effect. However, many papers from the

literature that attempt to explain dust behaviour are performed on dusty plasmas,

specifically, when the conditions in the plasma have been purposefully arranged so that

the particles have extremely strong interactions. In order to properly compare the

results from dusty plasma experiments and dust-in-a-plasma experiments, it is necessary

to examine the nature of the interactions between particles in dusty plasmas.

2.4.2.1 The Electrical Interaction Potential

Individually, dust suspended in the plasma sheath will experience the forces

discussed in the preceding section, all of which act in the vertical direction. When large

numbers of dust particles are suspended together, they begin to interact in both the

vertical and horizontal dimensions, behaving almost as a third plasma component with

high charge and high mass. When two dust particles pass near each other, they do not

interact with the usual Coulomb potential. Each particle carries with it a collection of

ions that attempt to shield its potential from the plasma. Thus, a screening potential due

to the positive ions modifies the Coulomb interaction potential. The form of this

potential is usually approximated as a Coulomb potential multiplied by a decreasing

exponential scaled by the appropriate Debye length:

$$(16) \qquad \phi(r) = \frac{Q_d^{\,2}}{4\pi\varepsilon_0 r} \exp\!\left(-\frac{r}{\lambda_D}\right).$$

This form is known as a Debye-Hückel [1923], screened-Coulomb, or Yukawa [1935]

potential in the literature. Konopka *et al.* [2000] have shown that the Debye-Hückel

form is an excellent model for the interaction potential between dust particle pairs in the

plasma sheath.

Although the effect of the Debye-Hückel potential is to decrease the interaction

between dust particles through mutual repulsion, Ikezi [1986] predicted that under

certain conditions, collections of dust could still couple strongly, forming stable

structures in plasmas. It was not until 1994 that these structures, called *plasma crystals*,

were observed [Thomas, *et al.*, 1994; Chu and Lin, 1994]. Figure 12 shows video

frames of typical plasma crystal structures. Intergrain spacing in these images is about
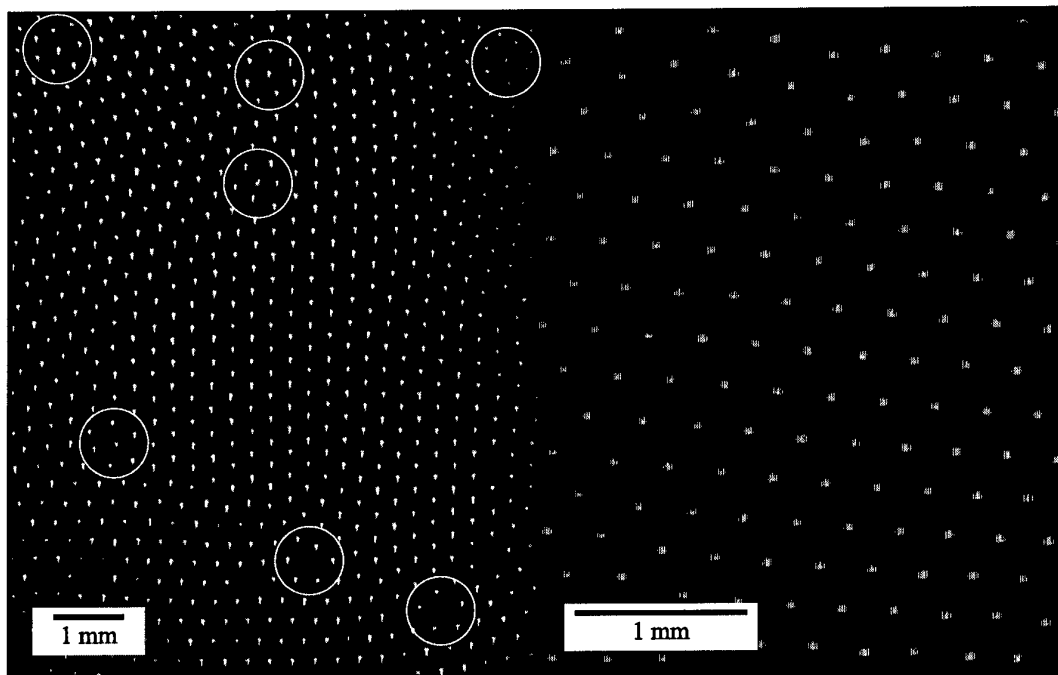
Figure 12: Plasma Crystal Images. This figure shows two images of plasma crystals formed by spherical melamine formaldehyde dust in an argon plasma. The intergrain spacing in these images is about a third of a millimetre. The left image shows the structure formed immediately after plasma parameters have been adjusted to values appropriate for solidification of the crystal. Several of the numerous defects in this crystal are highlighted in this image. The right image, at twice the magnification of the left image, shows the near-perfect hexagonal structure achieved after the crystal was subjected to a small, periodic perturbing force for a few minutes, a technique analogous to the annealing of a metal.

1/3 of a millimetre. These crystals were formed using monodispersive spherical melamine formaldehyde particles. Crystals have also been formed with less symmetric materials such as tungsten dust and carbon toner particles from laser printers [Steel *et al.*, 1997], however, crystals formed of such materials exhibit a great many more defects than do crystals formed of the spherical dust. Electron microscope images of the melamine formaldehyde and carbon toner particles are shown in Figure 13.

As was shown earlier, dust particles having the same mass are confined in the sheath within thin vertical parameters by a number of forces, leaving only the horizontal dimensions free. The forces resulting from the Debye-Hückel potential and the thermal energy of the dust tends to horizontally separate the particles further. The importance of thermal effects on collections of dust is reflected in one of the ways coupled plasma
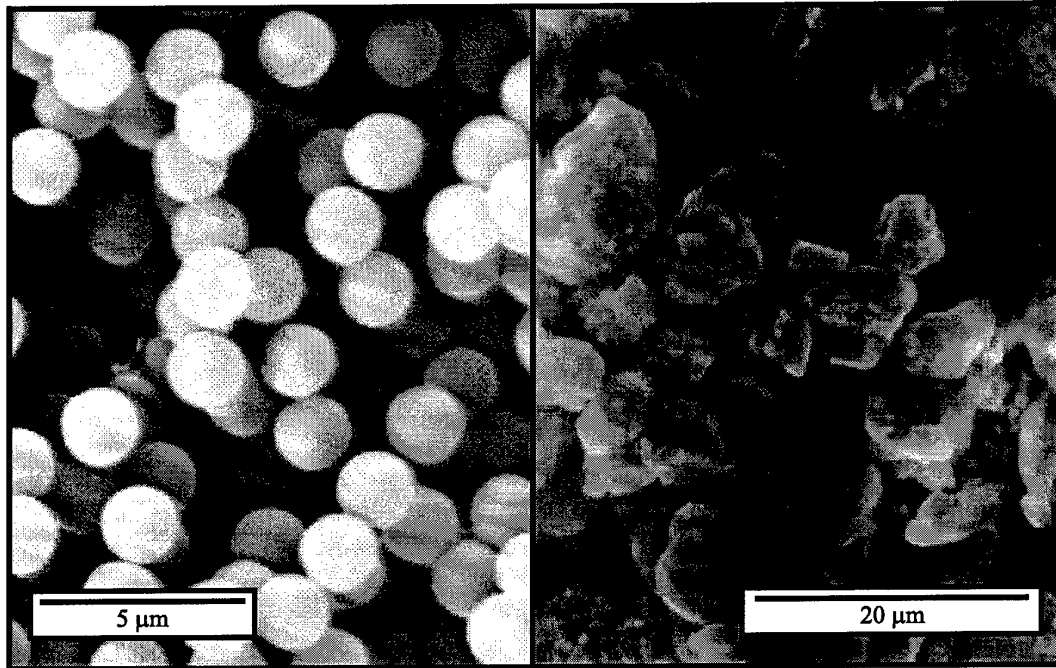
Figure 13: Dust Images. This figure shows images of dust used in OXDUPLAG plasma crystal experiments. The left image shows spherical melamine formaldehyde (MF) particles. The right image (courtesy of D.A. Law) is of carbon particles from a printer toner cartridge. Note the highly irregular shapes and the large size-dispersion of the carbon when compared to the MF particles.

components are characterised. A measure of particulate coupling in plasmas is the dimensionless Coulomb coupling coefficient:

$$(17) \qquad \Gamma = \frac{Q_d^2 / 4\pi\varepsilon_0 r_g}{k_B T_d},$$

where r_g is the average intergrain spacing $\left(n_d^{-1/3}\right)$ and T_d is the dust temperature. This factor is a measure of the strength of the Coulomb potential energy in units of the dust kinetic energy. With strong fields (large charges and small intergrain spacings) and low temperatures, the particles interact very strongly. If the coupling coefficient is greater than one, the plasma is called strongly coupled [Ichimaru, 1982]. A coupling coefficient of greater than about 173 should lead to solidification of the crystal [Slatterly

and Doolen, 1980], although some authors question the use of this exact number for dust as it was derived for one-component plasmas instead of the three-component plasma (electrons, ions, and dust) of the plasma crystal [Morfill and Thomas, 1996]. Typical values for Γ in plasma crystals are on the order of tens of thousands [Thomas, *et al.*, 1994; Homann *et al.*, 1997].

Dust in laboratory plasmas tends to gain energy through collisions with charged particles. However, collisions with the much more numerous room-temperature neutrals tend to cool the dust to near neutral gas temperatures. As the pressure of the neutral gas is lowered, the damping effect of the gas is lessened and the dust temperature increases, decreasing the coupling coefficient. Thus, with relatively small changes in pressure, the coupling coefficient can be significantly modified and a plasma crystal can be melted. [Thomas and Morfill, 1996; Morfill *et al.*, 1997]

2.4.2.2 Attractive Forces between Dust Particles

In order to form a stable plasma crystal, some mechanism must exist to counter the repulsive Debye-Hückel force. So far, this problem has necessitated the use of various artificial horizontal confinement systems to form crystals under most current schemes. However, there exist various natural mechanisms that tend to partially counter the dominant repulsive forces. One of these is the attractive polarisation force that occurs when two Debye-shielded particles approach each other [Hamaguchi and Farouki, 1994]. As the particles come together, their Debye spheres are distorted, effectively providing a gradient to the Debye length. A polarisation force will arise in the direction of the decreasing Debye length, *i.e.*, toward each other.
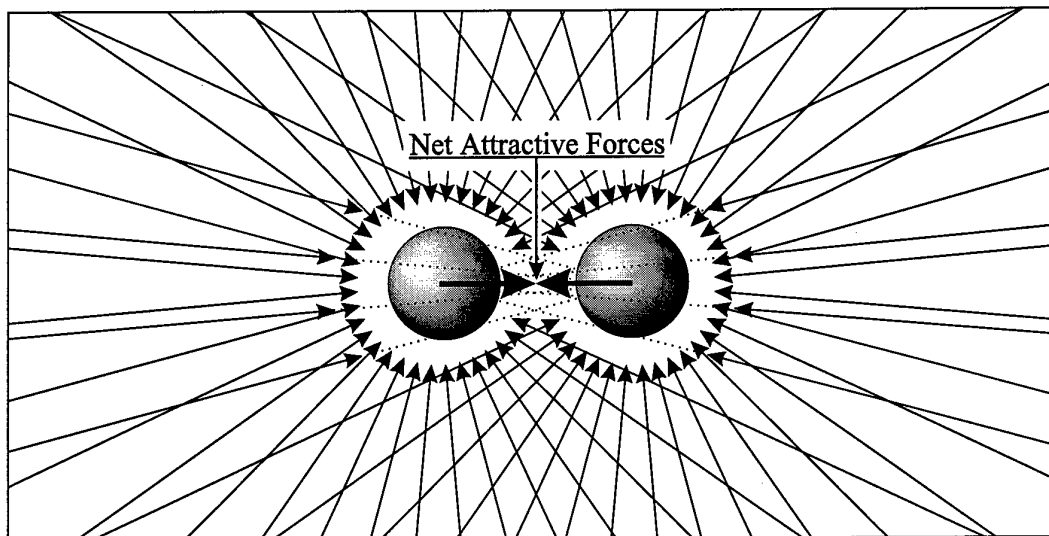
Figure 14: Attractive Forces Due to Collisional Shielding. This figure shows how incoming particles with an isotropic velocity distribution cause a net bombardment force tending to push two dust particles together. In the absence of one of the dust particles, incoming particles would impact the other dust particle from all directions, resulting in no net force. When the second particle is inserted, it intercepts some of the incoming particles that would have hit the first dust particle (as indicated by the dotted trajectories). Symmetry of the system and the assumed isotropy of the incoming particle velocity distribution lead to a net force toward the other particle.

2.4.2.2.1 A NOVEL MODEL FOR THE BOMBARDMENT FORCE IN THE PLASMA SHEATH

Another mechanism for attractive forces between dust particles is the

collisional shielding effect that one particle has on another. Tsytovich [1997] has

investigated this phenomenon, which he calls the bombardment force, in the plasma

environment in detail. As shown schematically in Figure 14, the normal balance of

forces from an isotropic distribution of particles surrounding the dust is disrupted by

interception of some particles by the dust. The force imbalance will always push the

dust particles toward each other. While interesting in a theoretical sense, Tsytovich's

results for charged particles are not applicable to the dust in typical experimental

settings. He assumes isotropic velocity distributions for ions, electrons, and neutral

particles for all of his derivations. In the plasma sheath, these assumptions are true only
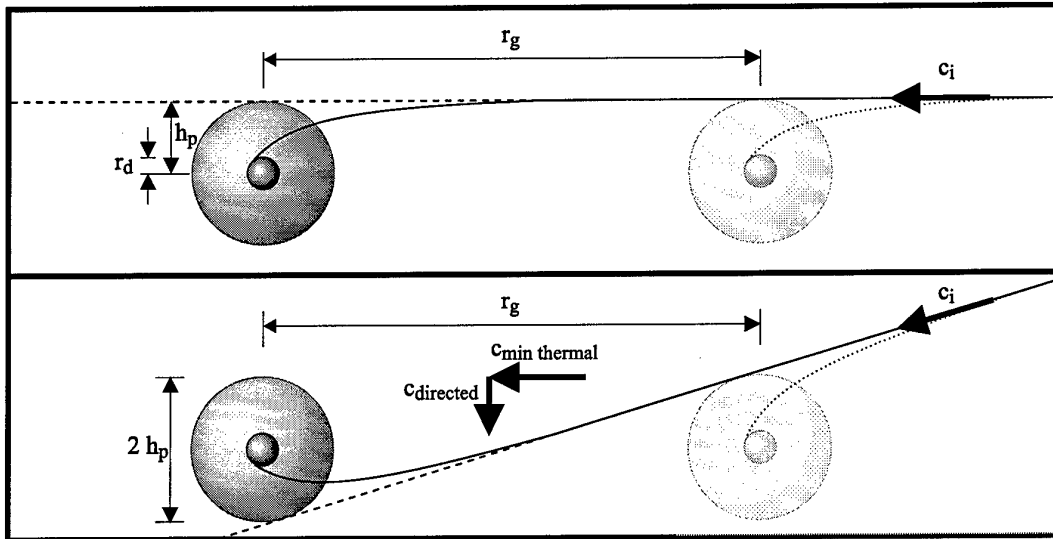
Figure 15: A Simple Model of Ion Bombardment Force in the Plasma and Sheath. The upper frame of this figure shows how ions of any velocity may contribute to the bombardment force in a plasma. If the dust particle on the right were in place, the ion would follow the dotted trajectory, impacting the right dust particle. As shown in the previous figure, the lack of this impact on the left dust particle contributes to the anisotropic bombardment force. The solid line shows the trajectory of the ion in the absence of the right particle. For ions of differing velocity, the grazing impact parameter changes, but in this case some ions of each velocity have the possibility of contributing to the bombardment force.

In the lower frame, the ions possess both thermal and directed velocity components, as is the case in the plasma sheath. In this case, only those ions with thermal velocities greater than $c_{min\ thermal}$ will be able to traverse the intergrain spacing in less time than it takes for the directed velocity to sweep them past the effective diameter of the dust particle. Ions with less than this horizontal velocity will not contribute to the bombardment force.

in the horizontal plane. The presence of the sheath field destroys the vertical isotropy

for the charged particles.

To see how the magnitudes of the attractive forces are affected by the presence

of the sheath, consider the following simple model, developed for this thesis and

illustrated in Figure 15. For this approximation, the OML grazing impact parameter

given in equation (10) will be used for the effective radius of the particle. The use of

the discredited OML theory in this approximation will later be shown to have a

negligible effect on the results. The top frame of the figure shows the situation in a

quasineutral, field-free plasma. An ion enters from the right and follows the trajectory

shown by the dotted line. It impacts on the right dust particle, the momentum change of

this collision contributing to the force felt by that particle. Were the right particle not there, the ion would proceed along the solid trajectory, impacting the left dust particle and depositing its momentum there. The existence of the right dust particle screens this small force from the left particle, contributing to the bombardment force that pushes the two particles together. As there is no preferred direction in the plasma, ions of any velocity may contribute to the bombardment force, as long as their impact parameter is less than the value appropriate for their velocity.

The situation is substantially changed in the plasma sheath. Here, the existence of a strong field imposes a preferred direction on the ions. In this model, monoenergetic velocities in the vertical direction are assumed, while the velocity in the horizontal plane is assumed to be thermal from a two-dimensional Maxwellian distribution. As can be seen from the figure, ions enter from the right at an angle to the horizontal determined by the ratio of their thermal velocity to the directed velocity. For an ion to contribute to the bombardment force, the ratio of its thermal velocity to the directed velocity must be greater than the ratio of the intergrain spacing, r_g, to the effective diameter of the dust particle, $2h_p$. Thus, there is a minimum horizontal ion velocity for which the bombardment screening effect will occur.

To determine this minimum velocity, it is necessary to calculate the impact parameter, directed velocity, and thermal velocity. For this analysis, it is desirable to write equation (10), the impact parameter equation, into a form involving dust charge instead of dust potential. To do this, the vacuum capacitance equation

$$(18) \qquad Q_d = 4\pi\varepsilon_0 a\phi_d ,$$

is used, valid in the small a/λ_D limit. This relationship has previously been shown to be

valid for the case of small, isolated spheres surrounded by screening charges, as is the

case in the sheath [Whipple *et al.*, 1985]. In the general case, the directed ion velocity

in the sheath at the dust suspension height will be given by $c_z = Mc_{Bohm}$ where c_{Bohm} is

given by the equality in equation (3) and M is the Mach number, which is greater than

unity for ions in the sheath. The horizontal ion velocity is found from the definition of

(monoenergetic) kinetic energy, $k_B T_i = \frac{1}{2} m_i c_i^2$.

Using the vacuum capacitance equation and the horizontal dust velocity

equation in the grazing impact parameter equation, then equating the ratios of ion

velocities and distances in the horizontal and vertical directions

$$(19) \qquad \frac{r_g}{2h_p} = \frac{c_{\text{min thermal}}}{c_{\text{directed}}}$$

and solving for the ion velocity, one obtains a relationship for the minimum ion speed,

which will contribute to the bombardment force,

$$(20) \qquad c_{i,\min} = \sqrt{\frac{1}{2m_i}\left(\frac{r_g^2 M^2 k_B T_e}{2a^2} - \frac{eQ_d}{\pi\varepsilon_0 a}\right)},$$

For the purpose of this model, the following parameters are chosen: $r_g = 0.25$

mm, $M = 1$, $k_B T_e = 2eV$, $Q_d = 20{,}000$ e, $m_i = 39.9 \cdot (1.67 \cdot 10^{-27})$ kg (for argon), $a = 5$ μm.

In actuality, typical plasma crystal parameters differ slightly from the ones chosen

above ($r_g \cong 0.33$ mm, $M \cong 2$, $k_B T_e \cong 4eV$, $Q_d \cong 10{,}000$ e), but the former parameters will

allow a conservative estimate of the minimum ion speed in an attempt to compensate for the approximations used in the model. Using the former parameters, it is found that only ions with horizontal velocities greater than 55,000 m/sec will contribute to the bombardment force. This speed is approximately 125 times the thermal speed of ions with the typical experimental value of $k_B T_i = 0.04$ eV. (It was previously stated that the OML impact parameter approximation would prove to be insignificant to the final results. At this minimum ion speed, the impact parameter is virtually the same as the dust radius, differing by only 0.06%. This result implies that, essentially, only direct impact collisions are meaningful and the use of the OML approximation is insignificant.) For a pressure of 13.33 Pa (0.1 Torr), a conservative ionisation fraction of 10^{-6}, and using the two-dimensional Maxwellian for the ion speed distribution, the number density of ions involved in the bombardment force is 0.4 per cubic metre. This number density is quite obviously insignificant, even though it was based on parameters that would overestimate the actual number density.

The effects of Coulomb drag [e.g. Bittencourt, 1986] on the attractive forces has not been considered in the above model. However, that effect can be expected to suffer a similar reduction in magnitude from its value in a plasma due to the fact that very few ions possess velocities great enough to traverse significant horizontal portions of the Debye spheres of the dust particles before being whisked away by the sheath field. Tsytovich estimates that Coulomb drag forces should be on the order of $\sqrt{T_e/T_i}$ greater than the bombardment force (on the order of 10 for typical plasma crystal conditions), which is still rendered insignificant when the directed ion velocity in the sheath is considered.

The effect of neutral particles on the attractive forces should be only slightly changed by the presence of the sheath. This is due to the slight increase in the vertical component of the neutral gas momentum due to collisions with directional ions. At the low ionisation ratios typical of most plasma crystal experiments (n_i/n_n on the order of 10^{-5} to 10^{-8}), this effect is negligible. Tsytovich discusses only the effect of thermal neutrals being absorbed and reemitted with a temperature that has been modified by the dust temperature as a mechanism for a neutral-related attractive force. It is possible for a neutral particle bombardment force to exist, similar to the ion bombardment force discussed above. However, for the conditions of most dusty plasma experiments, the neutral-neutral mean free paths are small when compared to the intergrain spacing, so the bombardment effect due to neutral particles may be safely ignored.

Tsytovich claims that the attractive bombardment and Coulomb drag forces will dominate the repulsive electrostatic force between dust particles at moderate intergrain spacings. It must be noted that at the present time, experimental evidence tends to discount the effects of attractive forces on dust suspended in the sheath. As a consequence of showing that the interaction potential between dust-particle pairs in the horizontal dimension could be well modelled by the Debye-Hückel potential, Konopka *et al.* [2000] have determined that such attractive forces, should they exist, must be smaller than can be measured by their reasonably sensitive technique. These experimental results tend to support the strong reductions in attractive forces due to the anisotropy of the plasma sheath developed in this section.
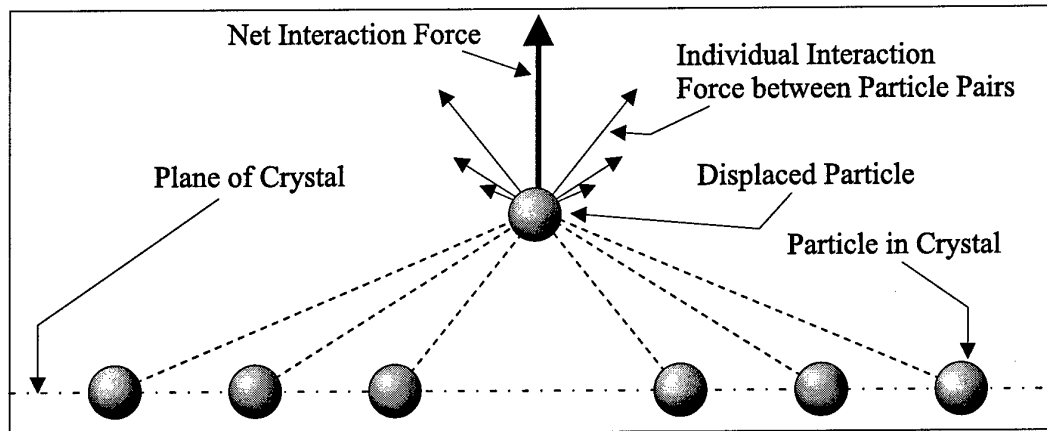
Figure 16: Effect of Interaction Forces on a Particle Displaced from the Crystal Plane. This figure displays the net vertical interaction force due to a repulsive interaction force between particles, such as the Debye-Hückel force. For attractive forces, such as the bombardment or polarisation forces, the net force would be vertically down.

2.4.2.3 Interaction Forces on Particles Displaced from the Plane of a Plasma Crystal

Exactly what effects the interaction forces will have on dust particles displaced slightly from the horizontal plane of a plasma crystal, the situation in a number of experiments in the literature [Melzer *et al.*, 1994; Trottenberg *et al.*, 1995; Kortshagen *et al.*, 1996; Homann *et al.*, 1999; Nunomura *et al.*, 1999], is not well understood. Figure 16 schematically shows the effect of such interaction forces on such a dust particle. As can be seen, as soon as the particle is displaced from the plane of the crystal, the interaction forces acquire a vertical component.

Just how significant the vertical component of the force on the displaced particle may be is unknown at this time, depending upon further research into the mechanisms behind the forces. As most of the intergrain forces are proportional to an inverse power of the distance between the displaced particle and the particles in the lattice, it is reasonable to say that the effects of these forces will be greatest when the displaced particle is near the plane of the lattice. However, the bombardment force will become more significant as the particle's displacement increases due to the increase in

vertical distance from $2h_p$ to $(2h_p + z_d)$ in equation (19), where z_d is the displacement distance. Although each of the experiments cited above uses a potential energy formulation for analysis of the vertical motion of such a displaced dust particle, none of the authors take any of the interaction potentials into account, nor discuss their neglect. The only reasonable way to neglect them is to ensure that at no time in the experiment are two dust particles allowed to come into close proximity (by definition, the situation in dust-in-a-plasma experiments). Also by definition, that method of neglecting intergrain forces is incompatible with analysis of dusty plasmas in general and plasma crystals in specific.

This chapter has been a brief survey of theories supporting the extremely complicated subject of dust interactions within a plasma sheath. In the following chapters many of the concepts developed and discussed above will be applied to additional theoretical, numerical, and experimental work performed for this thesis.

Note: A substantial portion of this chapter has been published in Plasma Sources: Science and Technology 9(2) (2000) 87-96. Appendix B contains a copy of that paper.

3. DUST OSCILLATION THEORY

The understanding of dust in the plasma sheath is of great importance to researchers in a variety of disciplines. The study of dust levitating in terrestrial sheaths, especially in so-called plasma crystals, has been underway since 1994, when groups in Garching, Germany [Thomas *et al.*, 1994] and Chungli, Taiwan [Chu *et al.*, 1994] first experimentally produced the crystals. One of the properties of such dust that is not well understood, either experimentally or theoretically, is its charge.

The analysis of the trajectories of dust particles oscillating in a plasma sheath has been used as a method for determining the charge on the dust by a number of researchers during the past few years. Groups in Germany first used a time varying potential [Melzer *et al.*, 1994; Trottenberg *et al.*, 1995; Kortshagen *et al.*, 1996] induced across the sheath and, more recently, a laser [Homann *et al.*, 1999] to cause resonant oscillation of dust in a plasma crystal. Harmonic resonance equations were then used to determine the dust charge. Nunomura *et al.* [1999] used an observed natural instability in the dust position to calculate the dust charge. However, many of these experiments rely upon assumptions about the nature of the plasma sheath potential or the charging of dust in such a potential, significantly perturb the sheath during the experiment, discount the effects of significant forces in the system, or involve some combination of the

above. The specific effects of these assumptions and techniques will be discussed later in this paper. Another group [Konopka et al. 1997; Morfill et al., 1999, Konopka et al., 2000] has also used horizontal collisions of dust particle pairs to determine the interaction potential of the collision, and from that potential, the charge on the dust. Their self-consistent method does not require any external assumptions concerning plasma parameters or charging mechanisms. In this chapter, a novel [Tomme et al., 1998] use of the dust oscillation technique is presented that highlights (and stays within) the limits of the assumptions noted above while maintaining stable experimental conditions and accounting for every significant force.

Small particles present in plasmas tend to acquire a negative charge due to the higher mobility of electrons in the plasma. In terrestrial plasmas, negatively charged particles of sufficient size fall toward lower regions of the plasma until they reach the plasma sheath. In the sheath, the electric field from the negatively self-biased electrode begins to repel the particles, or dust. Under certain conditions, this repulsion is sufficient to cause the dust to suspend above the lower electrode. At this point, the particles encounter a balance between upward and downward forces, or in other words, they encounter a minimum in the potential well formed by the sum of these forces.

As a dust particle falls from the plasma into the sheath and enters the potential well, its trajectory oscillates about an equilibrium height, the damping of the oscillations being related to chamber pressure and dust mass. An initial analysis of several trajectories indicated that the oscillations might be approximately damped-harmonic.

In order to explain this motion, a brief review of applicable damped harmonic motion theory will first be presented. Next, a theory that uses dust trajectory parameters

to estimate the charge on a dust particle at its equilibrium height will be developed. The two succeeding chapters will then discuss a simple model of a collisional radio frequency plasma sheath needed for the charge estimation theory. Finally, experimental results of the trajectory analysis for a number of dust particles with different masses at different pressures will be presented.

3.1 Harmonic Dust Oscillation Theory

As previously stated, isolated dust in a plasma sheath oscillates in a potential well formed by the opposing electrostatic and gravitational forces. While those forces are not the only ones acting on the dust (ion drag being the most significant of the other forces), they have been shown to be several orders of magnitude larger than other dust-velocity-independent forces in the upper sheath region where the experimental data were taken for most of the studied particle sizes [Northrop et al., 1990; Barnes et al., 1992; Kilgore et al., 1993]. For the smaller particles (< 2.5 μm radius), the ion drag begins to approach the magnitude of the gravitational force. However, it will be shown that the change on the calculated dust charge due to consideration of this force for these smaller particles will be below the level of the error of the technique presented here. For this reason, dust-velocity-independent forces other than gravity and electrostatic repulsion will be ignored.

The initial hypothesis was to test whether the oscillations were harmonic, and if so, over what amplitude range. To test this theory, the data was fit to the well-known equation of motion for the damped harmonic oscillator, e.g. [Baerline, 1983],

$$(21) \qquad m\ddot{z} + \gamma\dot{z} + \kappa(z - z_{eq}) = 0,$$

where κ is the restoring constant, z is the particle height above the electrode (the subscript "eq" denotes the equilibrium height), and $\dot{z}$ and $\ddot{z}$ are the first and second time derivatives of the height.

For an undamped oscillator with a restoring force F(z) = -κz the potential well has the form U(z) = ½κz², showing that the curvature of the potential is just κ/2. By adding the damping term, the shape of the well does not change; energy is merely allowed to leave the system. It can be shown that for the damped simple harmonic oscillator,

$$(22) \qquad \kappa = m[(2\tau)^{-2} + \omega^2],$$

where the damping time constant, τ, is defined by

$$(23) \qquad \tau = m/\gamma.$$

Equation (22) demonstrates that the curvature of the potential well may be found by measuring the damping time constant and the oscillation frequency.

3.2 DUST DRAG THEORY

Measurements of the oscillation parameters described above not only yield data on the potential well, but also can be directly compared with standard drag theory. The standard theory of the motion of small spherical particles in a gas was developed in the early 20th century by Epstein [1924]. That theory is described in detail in the preceding

chapter. Since the drag coefficient in equation (21) is defined by $F_{nd} = \gamma v_d$, it can be

seen that the quantity in parenthesis in the Epstein drag law, equation (15), must be the

drag coefficient, which is seen to be linear in the neutral gas density as

$$(24) \qquad \gamma = \left(\left(1 + \frac{\pi}{8} \right) \frac{4\pi}{3} m_n a^2 \bar{c}_n \right) n_n .$$

As we have experimental control over the neutral density through the chamber pressure,

equation (24) provides a method to test our measured damping time constant data

against the Epstein drag law. Other researchers [Homann et al., 1999] have previously

shown that the Epstein drag law holds in the plasma sheath. Should the data confirm

that the dust particles in experiments detailed later in this study follow the Epstein law,

it will provide an additional, independent check on the plausibility of the measured

values.

3.3 DUST CHARGE THEORY

The charge on dust particles suspended in the plasma is not well known. Recent

experimental and theoretical estimates place its value on the order of roughly 10^3 to 10^4

electron charge units for micron-sized particles in plasmas with pressures on the order

of 10 Pa and electron densities on the order of 10^{16} per cubic metre [Melzer et al., 1994;

Kortshagen et al., 1996; Nairn et al., 1998; Homann et al., 1999]. The value of about

4000 electron-charges on a 4.7 μm radius particle from [Trottenberg, 1995] is the only

published value directly comparable with results presented in this thesis (melamine

formaldehyde dust suspended in an argon plasma sheath), although that value was
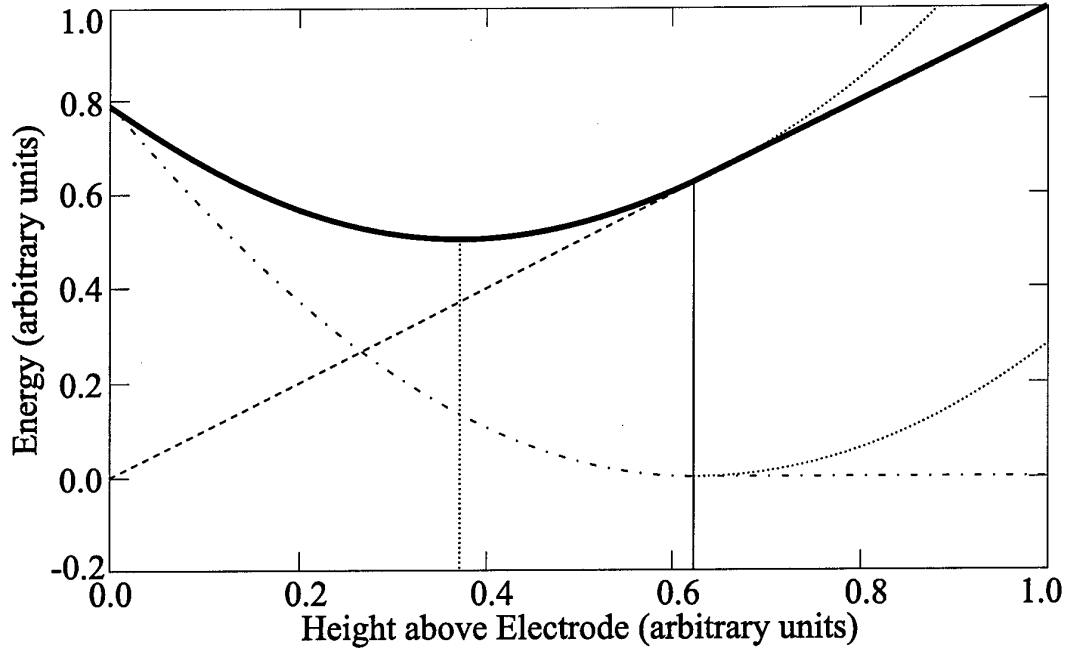
Figure 17: The Theoretical Potential Well. This schematic shows how a harmonic total potential results from the addition of the linear gravitational potential and a harmonic electric potential energy curve. The location of the sheath edge is shown by the vertical solid line and the dust equilibrium height is indicated by the vertical dotted line. In this model, the electric potential (dash-dot curve) is essentially zero to the right of the sheath edge. This causes the total potential (solid curve) to be parabolic in the sheath and linear in the plasma. The gravitational potential is shown as a dashed line. The dotted extensions to the total and electric potential energy curves show their full parabolic forms.

quoted for dust in a plasma crystal suspended in a perturbed sheath. As will be shown here, analysis of the damped oscillation of a dust particle can provide another method for estimating this value.

The total potential in which the dust moves in the sheath is formed by the sum of the electrical and gravitational potential energies,

$$(25) \qquad U_{tot} = U_e + U_g,$$

as shown in Figure 17. The gravitational potential energy is simply $U_g = mgz$, where g is the gravitational acceleration. The determination of κ, as discussed above, fixes the

curvature of the total potential energy for small-amplitude oscillations, and the position

of its minimum is fixed by the measurement of the equilibrium height, z_{eq}.

Determination of the electric potential energy is not as straightforward. The

assumption of a parabolic total potential and the linear gravitational potential implies

that the electric potential must be parabolic as well. Transforming the line-plus-

parabola form of the electric potential energy,

$$(26) \qquad U_e(z) = \left(\frac{\kappa}{2}(z - z_{eq})^2 + U_{eq} \right) - mgz ,$$

into the standard form ($y = K(z - z_0)^2 + y_0$)

$$(27) \qquad U_e(z) = \frac{\kappa}{2} \left[z - \left(z_{eq} + \frac{mg}{\kappa} \right) \right]^2 + \left(U_{eq} - \frac{(mg)^2}{2\kappa} - mgz_{eq} \right) ,$$

allows identification of the distance from the electrode at which the extremum occurs.

This distance,

$$(28) \qquad z_0 = z_{eq} + \frac{mg}{\kappa} ,$$

is a rough gauge of the sheath thickness predicted by this harmonic theory, assuming

now that the electric potential is globally harmonic throughout the sheath. As the

curvature of this parabola, $\kappa/2$, is the curvature of the *electric potential energy*, no direct

conclusions can be drawn about the magnitude of the curvature of the *electric potential*

without knowing the charge on the dust; all that has been assumed is that both the potential and the potential energy are harmonic.

At this point, these harmonic assumptions and conclusions may seem quite tenuous. Other researchers [Melzer *et al.*, 1994; Kortshagen *et al.*, 1996; Homann *et al.*, 1999] have used similar assumptions *a priori*; they will be similarly used here and their use will be justified later by showing that the data and the results from models available in the literature independently support the parabolic assumptions. In fact, it will be shown that the data and models support the parabolic assumptions *globally* in the sheath.

The electric potential energy of a dust particle is just

$$(29) \qquad U_e(z) = Q_d \phi(z).$$

It can now be shown that physically, κ represents $-Q_d(d^2\phi/dz^2)$ or, equivalently, $Q_d(d\mathcal{E}/dz)$, where $\mathcal{E}$ is the electric field.

By assuming a parabolic sheath potential and a constant dust charge throughout the oscillation, the charge on the dust at its equilibrium height may be obtained as

$$(30) \qquad Q_d = \frac{(m_d g)^2}{2\kappa\left(\phi(z_{eq}) - \phi_0\right)},$$

where ϕ_0 is the extreme value of the (harmonic) electric potential. In this equation, m_d and κ are experimentally determined parameters. The potential difference in that equation, however, is not experimentally determinable by current probe methods. To

fix its value, one needs to rely on a model of the sheath. In the next chapter, just such a

model will be developed.

4. A NUMERICAL MODEL OF THE RF PLASMA SHEATH

The task of modelling the sheath of a plasma is not a new one. Many researchers have attempted to develop an improved understanding of the electrical properties of plasmas since Schottky's [1924] and Langmuir's [Langmuir, 1923; Langmuir and Mott-Smith, 1924; Langmuir, 1929; Tonks and Langmuir, 1929] early analytical attempts. With the advent of computer technology, the development of numerical models has come to the fore.

In the recent literature, there are primarily two distinct, widely used techniques by which plasmas have been numerically modelled [Hamaguchi, 1999]. The first technique is the kinetic model, where a major goal is to understand the time-evolution of the velocity distribution functions of the plasma components. Many researchers [e.g. Vender and Boswell, 1990; Farouki et al., 1991; Procassini and Birdsall, 1991; Nanbu and Kitatani, 1995; Nagayama et al., 1996] use particle-in-cell (PIC) simulations to obtain these distributions. In these simulations, the positions in a grid of cells of a large number of charged and neutral particles are noted. Their projected positions following a small time interval are calculated based on the net forces on each particle due to every other particle using the standard Newtonian equations of motion. Particle

collisions are usually treated stochastically. The process is iterated until an equilibrium develops, determining the steady-state parameters.

The PIC method has the advantage that *a priori* assumptions about the distribution of the particle densities are unnecessary, but it is computationally cumbersome, as the calculations must be performed for a very large number of interrelated particles of different masses for the results to be reasonable. The PIC method also allows distributions of particle energies to be used. This simulation technique requires extremely fast processing and large amounts of memory to achieve reasonable results due to the vast number of particles that must be tracked on a small grid. Results improve greatly with reductions in grid size and time step and increases in particle numbers. The trade-off is that small improvements in the quality and accuracy of the results usually require huge increases in computational power or time.

The other common modelling method is called the fluid model. In this type of model, the quantities of interest are not individual particles but instead the bulk motion of aggregates of the constituent particles. The primary strength of this method lies in its relative computational simplicity. By foregoing the ability to track the motion of individual particles, equations of motion based on average particle parameters may be used. The motion of a single particle of each type under consideration becomes the model for the motion of all like-particles.

For primarily one-dimensional problems where the angular effects of scattering may be ignored, this method can provide quick solutions to complex problems. The plasma sheath far from any edges is approximately such a one-dimensional problem. The directed ion velocity is typically much greater than most random thermal ion

velocities so that the effects of the physical distribution of ion speeds may be safely ignored. Strong sheath fields tend to accelerate particles that suffer collisions back to trajectories normal to the electrode, preserving the quasi-one-dimensionality of the problem and obviating the need for the inclusion of random scattering effects. Due to its inherent advantage in simplicity, this thesis will concentrate on the fluid model. A summary of a few of the many numerical fluid models for plasmas and plasma/sheath combinations from the literature has previously been given in Table 3 (p. 21).

Most of the models from the literature either do not match the exact experimental conditions of the plasmas in experiments which will be described in later chapters, are so detailed that an attempt to recreate them from their journal descriptions would have taken many months, or use dubious assumptions in their derivation. For these reasons it was decided that development of an improved, relatively simple sheath model was warranted. This proposed model was developed to provide numerical results against which the dust charge theory developed previously in this thesis, equation (30), could be tested. It will also allow calculation of results germane to the specific experimental parameters described in following chapters. However, as will be seen, the model was never actually used for its intended purpose. Instead, results from the model spurred the development of an even simpler method for approximating the potential function in the plasma sheath. It was this simple method that was actually used to derive the experimental results.

4.1 THE PHYSICAL BASIS FOR THE MODEL

The fluid modelling approach used in here consists of iteratively solving Poisson's equation and the ion equation of motion until a convergent solution is

obtained. Assumptions in the model are that the RF driving frequency is low enough to allow free movement of the Maxwellian electrons but high enough to cause the monoenergetic ions to respond only to the average field ($\omega_{pi} \ll \omega_{rf} \ll \omega_{pe}$). The modelled system was assumed so asymmetric that all of the RF potential variation was developed across the sheath of the driven electrode [Coburn and Kay, 1972]. The area of the driven electrode is assumed large enough that one-dimensional calculations may be used near its centre. The effects of ionisation in the sheath may be neglected [Börnig, 1992]. Sheath ionisation and secondary electron generation at the electrode are not taken into account in these calculations. These techniques and assumptions are similar to those used by Skorik and Allen [1993] for the collisionless case and by Nitter [1996] for the collisional plasma sheath.

Several improvements to existing RF sheath models were incorporated into the model presented here. First, the ion collision cross section is allowed to vary with ion energy, instead of specifying a constant cross section. This improvement allows for the approximate halving of the charge exchange cross section for argon ions whose energies increase from thermal to wall impact energies [Phelps, 1994]. Another improvement allows for a smooth transition of the potential function and ion speed profile across the sheath edge. The zero-ionisation assumption commonly used as a simplifying technique in sheath models [e.g. Nitter, 1996; Riemann, 1997] is clearly wrong past the sheath edge toward the plasma. That assumption is mitigated in the present model by matching the calculated sheath solution to the plasma form in a manner that is much less arbitrary than, say, previously used assumptions for ion accelerations at the sheath edge [Nitter, 1996]. In this model, the calculated potentials are matched to the slab-geometry analogue of the cylindrical plasma form found by Blank [1968] in order to get a smooth

ion-velocity profile across that boundary. It must be stressed that, although the potential curves are extended into the transition region and the plasma, this model is designed to be valid in the sheath only, where the effects of the ionisation assumptions and solution matching should have limited impact. The reasons for the extension of the calculations into the transition region will be discussed later. Although not as sophisticated as a true matched asymptotic solution [Van Dyke, 1964], this simpler technique was only employed here to obtain more physically reasonable (*i.e.*, not strictly correct but at least more reasonable than previous attempts) boundary conditions on ion accelerations and electric fields at the sheath edge; we are not concerned here with the nature of the potential outside of the sheath.

Following an approach that has become somewhat common in the literature, the two equations that explicitly govern this model are Poisson's equation and the ion equation of motion. Implicit in the formulation are the zero-ionisation ion continuity equation and the Boltzmann relation for the electron energy distribution. The ion equation of motion contains only two force terms: the electrical force due to the average field, and a drag force. The drag model employed assumes that, on average, an ion loses all its momentum to a neutral atom during a charge exchange collision. This type of collision predominates at the energies expected in the sheath [McDaniel, 1964]. The collisional force given by this model may be stated as

$$(31) \qquad F_c = m_i f_c v_i \, ,$$

where the collision frequency, f_c, is given by

$$(32) \qquad f_c = n_n \mathrm{v}_i \sigma(\mathrm{v}_i),$$

Hence, the collisional force is

$$(33) \qquad F_c = m_i \mathrm{n_n} \sigma(\mathrm{v}_i) \mathrm{v}_i^2.$$

A statistical analysis is not attempted here. However, it has been shown that for the case of a uniform field, such an analysis yields a collisional force differing from the above equation by only a factor of $\pi/2$ [Smirnov, 1981].

The energy-dependent cross section model for charge exchange collisions in argon used in this model was [Phelps, 1994]

$$(34) \qquad \sigma(\mathrm{v}_i) = \left(5.356 \cdot 10^{-18} \mathrm{v}_i^{-0.2}\right)\left(1 + \frac{7.204 \cdot 10^4}{\mathrm{v}_i^2}\right)^{0.6},$$

where the cross section σ is in square metres and the ion velocity is in metres/second. Thus, the governing equations are

$$(35) \qquad \frac{d^2 \phi(z,t)}{dz^2} = -\frac{e}{\varepsilon_0}(n_i - n_e) \text{ and}$$

$$(36) \qquad \mathrm{v}_i \frac{d\mathrm{v}_i}{dz} = -e \frac{d\overline{\phi}(z)}{dz} + m_i n_n \sigma(\mathrm{v}_i) \mathrm{v}_i^2.$$

where t is time. Use of the time-averaged potential in equation (36) is due to the massive ion assumption discussed previously.

In normalised form, Poisson's equation and the ion equation of motion become, respectively,

$$(37) \qquad \frac{d^2\eta(\xi,t)}{d\xi^2} = \exp(\eta(\xi,t)) + (u_i(\xi))^{-1} \text{ and}$$

$$(38) \qquad u_i \frac{du_i}{d\xi} = -\frac{d\overline{\eta}(\xi)}{d\xi} + \alpha(u_i)u_i^2,$$

where the following normalisations apply:

$$(39) \qquad \eta = \frac{e\phi}{k_B T_e},$$

$$(40) \qquad \xi = \frac{z}{\lambda_D},$$

$$(41) \qquad u_i = \frac{v_i}{|c_{Bohm}|}, \text{ and}$$

$$(42) \qquad \alpha(u_i) = \frac{\lambda_{D,s}}{\lambda_i(u_i)}.$$

In these equations, η is the normalised electric potential (with $\overline{\eta}$ being its time-averaged value), ξ is the normalised distance above the electrode, $\lambda_{D,s}$ is the electron

Debye length measured at the sheath edge, u_i is the normalised ion speed, c_{Bohm} is the Bohm speed from equation (3) and α is the plasma collisionality (a normalised drag parameter). The two terms on the right hand side of equation (37) are the normalised electron and ion densities, respectively. The term on the left hand side of equation (38) is the normalised convective derivative, while the two terms on the right hand side are the normalised electric and collisional forces. Additionally, the following relationships apply:

$$(43) \qquad \lambda_{D,s} = \sqrt{\varepsilon_0 k_B T_e \big/ n_s e^2} \;,$$

$$(44) \qquad v_B = -\sqrt{k_B T_e \big/ m_i} \;, \text{ and}$$

$$(45) \qquad \lambda_i(v_i) = 1 \big/ n_n \sigma(v_i) \;,$$

where n_s is the electron number density at the sheath edge. The positive z direction is defined to be away from the electrode.

4.2 BOUNDARY CONDITIONS

The governing differential equations and assumptions for the plasma sheath model have now been detailed. It only remains to specify the boundary conditions on the equations to complete the description of the model. Equation (37) is a second-order equation, and hence requires two boundary conditions to be uniquely satisfied. The

boundary conditions used in this model will be the electric potential at the electrode and the electric field at the sheath edge. Equation (38) is first order, and the boundary condition used to uniquely specify its solution will be the ion speed at the sheath edge. Strictly speaking, for a large subset of collisional plasmas there is no well-defined sheath edge [Franklin and Snell, 2000]; the discrepancy between this physical reality and the model boundary conditions will be discussed later.

The first boundary condition applied to Poisson's equation was that the potential on the electrode ($\xi = 0$) was sinusoidal about the RF self-bias potential [Boschi and Magistrelli, 1963]. The resulting self-bias, η_{sb}, has the form

$$(46) \qquad \eta_{sb} = \eta_{fp} - \ln[I_0(\eta_{rf})],$$

where η_{fp}, the normalised floating potential, is given by

$$(47) \qquad \eta_{fp} = \frac{1}{2}\left[\ln\left(\frac{2\pi m_e}{m_i}\right)\right].$$

Here, η_{sb} and η_{rf} are the normalised self-bias potential and applied RF amplitude, respectively, m_e is the electron mass, and $I_0(x)$ is the modified zero-order Bessel function.

The use of the above form for the RF self-bias assumed the existence of a Bohm [1949] sheath, in which the ions attain supersonic velocities exactly at the sheath edge. This condition is strictly only valid when the presheath is collisionless [Franklin and Snell, 2000]. As the experimental parameters used in later chapters will be shown

to be in the vicinity of the region where the presheath becomes collisional, it would

seem prudent to investigate the effect of different sheath-edge ion speeds on the RF self-

bias.

It has been proposed [Godyak, 1982; Godyak and Sternberg, 1990; Sternberg

and Godyak, 1994] that in collisional situations, the normalised ion speed at the sheath

edge is not unity, as is the case in the Bohm sheath, but is reduced by some factor that

depends on the collisionality of the plasma. The ion speed at the sheath edge according

to this theory, v_G, is given by the equation

$$(48) \qquad v_G = v_B \left(1 + \alpha(v_G)\right)^{-1/2},$$

where $\alpha(v_G)$ is the collisionality of the plasma at the sheath edge. Since $\alpha(v_G) \geq 0$, $v_G \leq$

v_B always.

Godyak's theory has been shown to be false [Riemann, 1997; Franklin and

Snell, 2000], as it is based upon a fundamental misunderstanding of the nature of the

sheath edge under collisional conditions. However, the speed he proposes gives a rough

gauge of how collisions could affect ion speeds if a distinct sheath edge were to exist

under those conditions. To see how this reduction in sheath-edge ion speed affects the

RF self-bias, the new speed may be inserted into the ion current equation $j_i = -e n_s v_G$,

where j_i is the ion current density. Using the fact that the time-averaged ion and

electron currents to the electrodes must exactly cancel for a capacitively-coupled system

that includes a blocking capacitor, the expression for the random electron current due to

Maxwellian electrons in the presence of a retarding potential, and the above expression

for the ion current, the modified floating potential may be obtained as
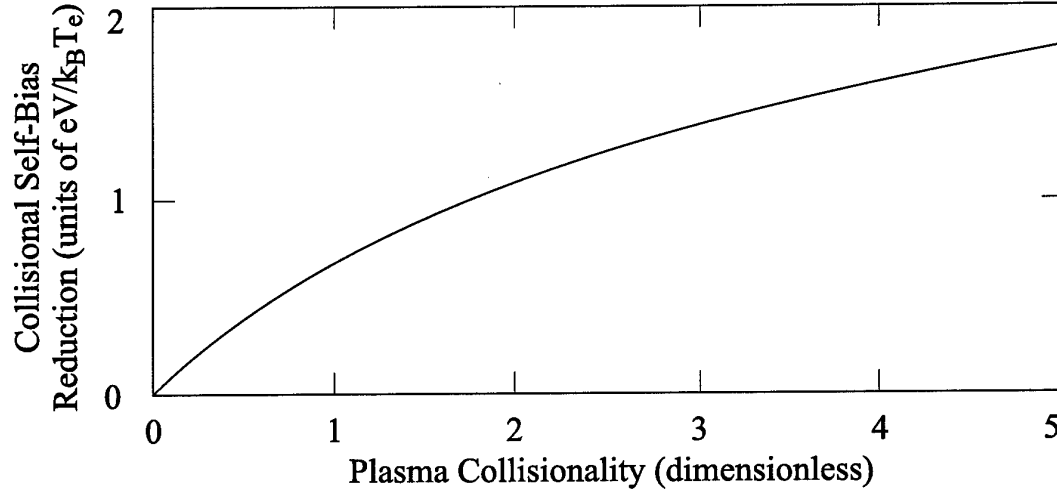
Figure 18: The Reduction of the Self-Bias Due to Collisions. This figure shows a plot of the self-bias reduction, $\ln[1+\alpha(v_G)]/2$, as a function of the plasma collisionality, $\alpha(v_G)$. For the experimental conditions described later, the collisionalities are on the order of unity, implying that the reduction factor is also of order unity.

$$(49) \qquad \eta_{fp} = \frac{1}{2}\left(\ln\left(\frac{2\pi m_e}{m_i} \right) - \ln\left(1 + \alpha(v_G) \right) \right).$$

This expression is reduced from the collisionless case [equation (47)] by the factor

$\ln(1+\alpha(v_G))/2$. A plot of the reduction factor as a function of α is shown in Figure 18.

For the experimental parameters explored later in this thesis, α is on the order of unity,

and the change in the normalised self-bias potential is thus also on the order of unity, a

negligible difference when compared with the magnitude of the self-bias, which is on

the order of 100. Thus, we may be relatively confident that the use of the self-bias

equation predicated upon the existence of a Bohm sheath, equation (47), will introduce

no significant errors into the collisional model.

As has been previously stated, the second boundary condition on Poisson's

equation is the field (slope of the potential) at the sheath edge. In the model presented

here, cold ions are assumed so that the diffusion term in the ion transport equation is

much less than the mobility term. The ions are then assumed to reach terminal velocity

between collisions such that the collisional force equals the electric force at any point in

the plasma [Franklin and Snell, 1997]. This may be expressed as $m_i v_i v_i = e\mathcal{E}$, where v_i

is the ion-neutral collision frequency, given by

$$(50) \qquad v_i = \frac{v_i}{\lambda}.$$

Thus, the electric field at any point in the plasma is

$$(51) \qquad \mathcal{E} = \frac{m_i v_i^2}{e\lambda}.$$

In this model, the ions are assumed to reach the Bohm speed at the sheath edge

[Riemann, 1991]. Thus, using equation (3) for the Bohm speed, the electric field at the

sheath edge in the modelled plasma is

$$(52) \qquad \mathcal{E}_s = \frac{kT_e}{e\lambda_i}.$$

(This field is also the limiting value of the sheath-edge field for marginally-collisional

plasmas proposed by Riemann [1997], $E_s = kT_e/e\lambda_D^{2/5}\lambda^{3/5}$, in the limit $\alpha \rightarrow 1$.)

Franklin and Snell [2000] show that there exists no expression that exactly

describes the location of the sheath edge under many collisional conditions. Riemann

himself also realized that his definition was only an approximation. Regardless, this

boundary condition shall be used here as the best-available approximation for this

relatively simple numerical model. In fact, for the purposes of this model, the sheath
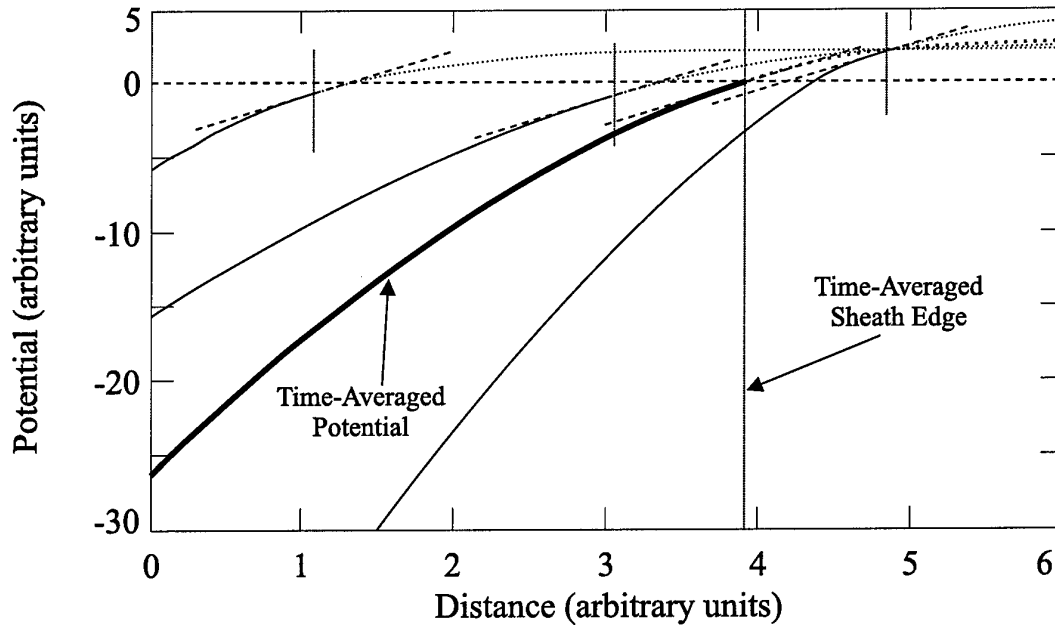
Figure 19: Schematic Potential Curves Illustrating the Need for Integration Past the Sheath Edge.
This figure shows a plot of notional potential curves for three instantaneous times in the RF cycle (light curves) and a time-averaged curve (heavy curve). In each case, the sheath edge (vertical dotted lines) is defined by the same, specific electric field (dashed lines). The portion of each potential curve outside the sheath is shown as a dotted extension to the solid sheath potential. To obtain the time-averaged curve, the potentials at each spatial location must be averaged for all times in the cycle. For each instantaneous curve, a portion of the curve that is outside the sheath contributes to the time-averaged curve.

edge will be *defined* as the point where the time-averaged value of the electric field matches the value given by equation (52). It is also at that spatial location that the normalised ion speed will be set to unity, the boundary condition for equation (38).

For a DC model, the above discussion would be sufficient to begin integration of the model. However, an additional consideration arises when dealing with the RF case. It is necessary to extend the solution of the potential function into the presheath region for the RF case. As stated previously, the sheath equations do not apply in this region due to the assumption of zero ionisation. The reason the solutions need to be extended past the sheath edge is due to the time-averaged term in the ion speed equation. Figure 19 shows several notional instantaneous potential curves and a notional time-averaged curve. Notice that the instantaneous location of the sheath edge

fluctuates with the applied RF voltage, as is to be expected. The dotted portion of each of the instantaneous curves is thus outside the sheath, lying in the presheath and plasma regions not truly described by the sheath equations. However, inclusion of the dotted portions is necessary to obtain the time-averaged curve. It now remains to specify a method for extending the sheath curves into the plasma region in order to allow calculation of the time-averaged potential curve.

Blank [1968] has shown that for highly collisional plasmas the plasma solution takes on the form $\eta(r) = \ln[J_0(z_{01}r)]$ in cylindrical geometry, where $J_0(x)$ is the zeroth-order Bessel function which has its first zero at $x = 2.404825...$, and r is the normalised distance from the axis, which takes a value of unity at the wall. This form is also the traditional Schottky [1924] solution. In slab geometry, this solution becomes

$$(53) \qquad \eta(z) = \ln\left[\cos\left(\frac{\pi}{2}z\right)\right],$$

where z is the normalised distance from the plasma midpoint, again taking a value of unity at the wall. To extend the numerically integrated potential curves obtained from equations (37) and (38) past the sheath edge, each curve will thus be smoothly matched to the plasma solution from equation (53). In this manner, the physical reality of the ionisation that occurs outside the plasma sheath is roughly taken into account.

The use of the Blank model for plasma solution matching is not inconsistent with the present model, even though it assumes that $v = \mu\mathcal{E}$, while it has been shown above that in the present model, $v \propto \sqrt{\mathcal{E}}$ [see equation (51)]. This seeming inconsistency is resolved when one realises that the velocity used in the collision

frequency derivation should actually be $v = \sqrt{\bar{c}^2 + v_{drift}^2}$, where v_{drift} is the directed

velocity. In the small field limit, *i.e.*, in the plasma, $\bar{c} \gg v_{drift}$ and $v \approx \bar{c}$. Substituting

this result into equation (50), the field becomes $\mathcal{E} = (m_i \bar{c}/e\lambda)v_{drift}$, consistent with the

Blank mobility assumption. When the field increases in the sheath, the drift velocity

dominates the thermal velocity and equation (51) is recovered. Hornbeck [1951] shows

experimental evidence of just such a transition between mobility regimes.

4.3 NUMERICAL INTEGRATION TECHNIQUE

The numerical solution of the coupled differential equations (37) and (38) was

begun by dividing the problem into a matrix of time steps and space steps. For the

results presented later in this chapter, time steps were typically on the order of a

hundredth of an RF period and space steps were on the order of a hundredth of a Debye

length. A set of initial potential functions was then assumed, one for each time step in

the model. A number of monotonic functions ranging from linear to parabolic to

hyperbolic that met the previously stated boundary conditions for Poisson's equation

were tested. (The final iterated solution was found to be highly insensitive to the form

of these initial guesses, and the hyperbolic initial guess set was actually used for the

results presented in this chapter.) These initial functions were time-averaged, and the

resulting function was inserted into equation (38). The location of the sheath edge was

calculated from equation (52), and the ion speed was set to unity at that location.

During the initial iteration, the (collisionless) condition $\alpha(u_i) = 0$ was imposed, as an ion

velocity profile had not yet been generated. Equation (38) was then numerically

integrated, solving for $u_i(z)$; the resulting function was then substituted into equation (37).

The numerical integration of equation (37) involved mixed boundary conditions, the potential at a definite spatial location and the field at another, undefined location, and hence required a shooting technique [Press et al., 1992]. The location of the sheath edge was left undefined at this stage during each iteration, as it was desired that the integration of equation (37) be the determining factor for its location. The starting values used were the known value of the potential at the electrode and an assumed slope (electric field). If, during the integration, the potential ever became a large positive number or the slope of the potential ever became negative, the integration was terminated and a new trial slope was used. The goal was to extend the numerical solution as far from the electrode as possible without violating the monotonic assumption or having the solution diverge upward. In this way, the actual field at the electrode was systematically determined.

Unfortunately, the solution of equation (37) is extremely sensitive to the value of the slope of the potential at the electrode. During code development, trials were run where the final digit of a ten-decimal-place number representing the slope was varied by unity. During this sort of trial, the numerical solution was observed to abruptly change its divergence from positive to negative infinity. Due to this sensitivity, it was decided to set an arbitrary cut-off precision beyond which the slope guesses would not be increased. For the results presented later in this chapter, this precision level was chosen to be a change in the normalised slope of less than 0.5^{22} (about 10^{-7}), where the typical slope at the wall was of order unity. Once this cut-off was reached, the slope was varied
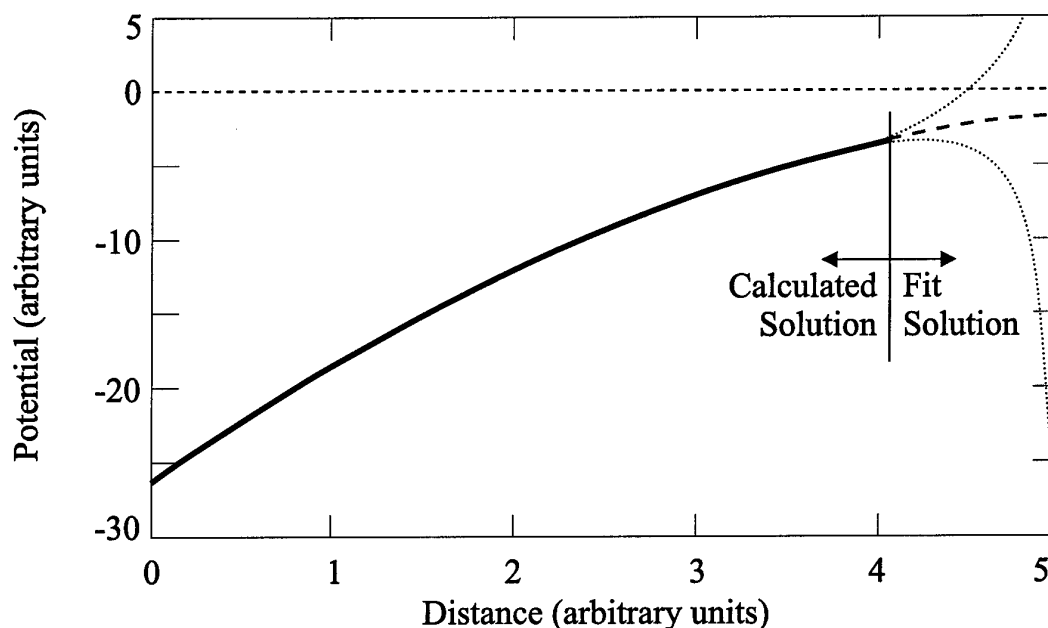
Figure 20: Illustration of the Solution Method for the Potential. This figure shows the results of two integrations of equation (37) [dotted curves, extended under the heavy solid curve] where the slope at the electrode was varied by an extremely tiny amount. For the steeper initial slope, the integration diverged positively, while the converse was true for a shallower initial slope. Once this divergence occurred at the arbitrarily set precision limit, the actual potential curve (heavy solid curve) was defined to be the portion of the numerically integrated curve where the two curves differed by less than an arbitrary factor. The calculated solution was then fit to the plasma solution from equation (53), as indicated by the dashed curve.

at the precision limit until it either went positive or had a negative slope. The slope was

then raised/lowered until the other limiting condition occurred (the potential became

very positive or the slope became negative). The two solutions thus obtained were

compared and were truncated when the difference between them reached a significant

level, arbitrarily chosen for this model to be a difference of $5 \cdot 10^{-4}$, where a typical

potential in the region of the truncation was of order unity. Figure 20 illustrates this

technique. Using a standard cubic spline routine, the calculated curve was then fit to the

Blank plasma solution [equation (53)].

The potential was thus determined for each time step and the process was then

repeated. For iterations other than the first, $\alpha(u_i)$ was calculated for each spatial step

from the numerical results from the previous integration of equation (38) and used in its

subsequent integration. The iterations were repeated until a selected convergence criterion was met, namely that no individual point on any of the potential curves at any time or on the ion speed curve differed from its value at the previous iteration by some small amount. It was found that a convergence of better than 0.05 eV/$k_B T_e$ for the potential (where the maximum potential magnitude was on the order of 30 eV/$k_B T_e$) and better than 0.001 v_i/v_B for the ion speed (where the wall speed was approximately 2) could be obtained in as few as five iterations. Figure 21 shows the convergence of the coupled differential equations for one set of parameters through a number of iterations.
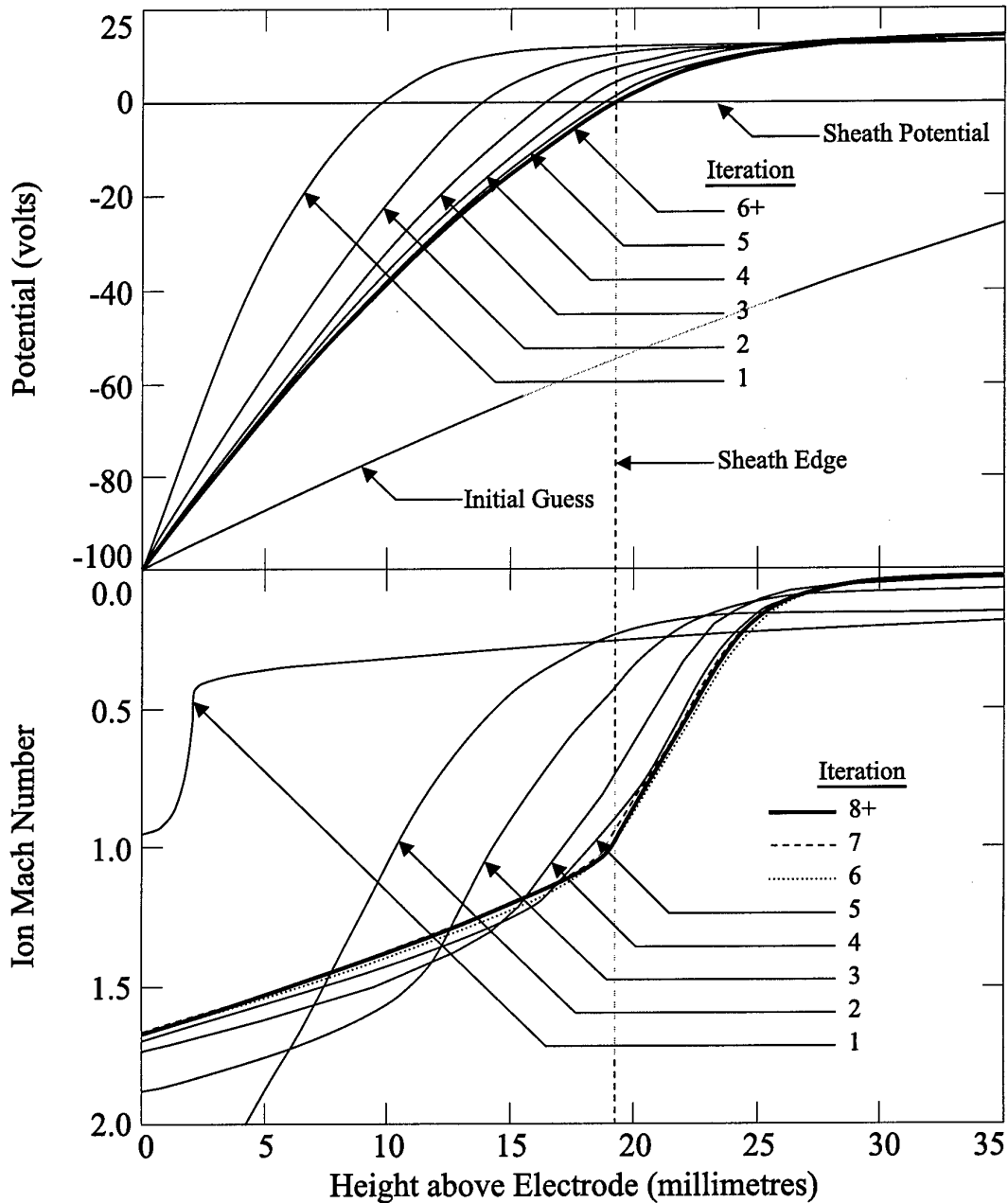
Figure 21: Convergence of the Iterated Numerical Results. This figure shows numerical results for the time-averaged potential as a function of height above the electrode following the first few iterations of the modelling process. The top frame shows the convergence of the potential function, beginning with the postulated initial guess. Within six iterations, changes to the potential function become insignificant at this scale. The bottom frame shows the similarly rapid convergence of the modelled ion speed. In that frame, the 6th and 7th iterated solutions are shown by dotted and dashed curves, respectively. The converged solution (the solution reached after 30 iterations) is shown by the bold curve in both frames. The vertical dashed line shows the sheath edge, based upon the slope of the converged solution.

4.4 NUMERICAL RESULTS

Now that the model has been thoroughly explained, it is time to examine some results. First, the results of the model for the parameters used in experiments to be described later in this thesis will be presented. Then, a study in parametric variation will be attempted to demonstrate that this model behaves as one would expect when given a change in plasma conditions.

4.4.1 NUMERICAL RESULTS FOR THE EXPERIMENTAL PARAMETERS

Once the potential functions and the ion speed profile had been calculated, derivatives could then be taken and the electric fields, charge densities, and carrier densities obtained. Plots of these functions are shown in Figure 22 to Figure **26**. Parameters used for these plots and in the experiments to be described in later chapters of this thesis are as follows: $k_B T_e = 3.7eV$; $k_B T_n = 0.025eV$; $P = 13.3Pa$; $n_e = 3.3 \times 10^{16} m^{-3}$;

$n_n = 3.3 \times 10^{23} m^{-3}$; $\phi_{rf} = 96.4V$; $f_{rf} = 13.56MHz$.

The inclusion of an energy-dependent collision cross section shrinks the sheath slightly when compared to Nitter's [1996] work; for his parameters, the sheath width from this model is approximately 16 λ_D, while his is about 22 λ_D. When his constant collision cross section ($\sigma = 3 \cdot 10^{-19} m^2$) and his plasma parameters are used, virtually identical results are obtained. Inserting the appropriate collisionless parameters also results in good agreement with the work of Skorik and Allen [1993]. The agreements with these disparate theories tend to bolster the case that our simple model does a very
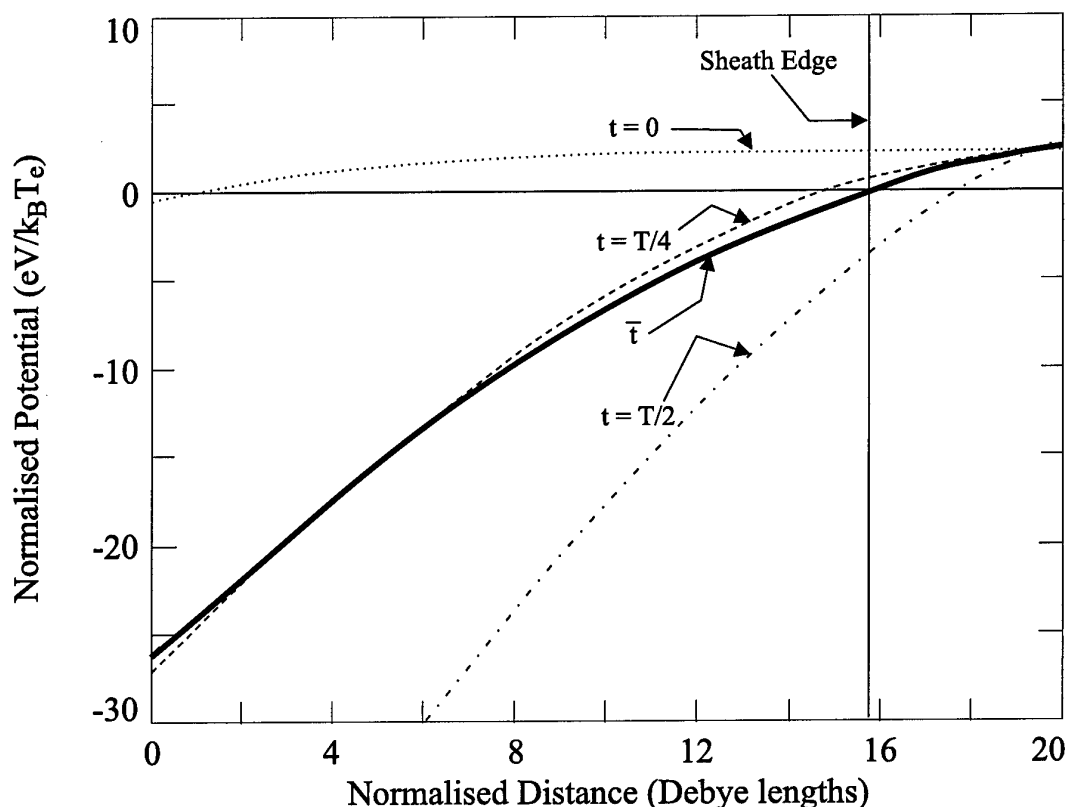
Figure 22: Variation of the Electric Potential in the Plasma Sheath. This figure shows numerical results for the potential as a function of height above the electrode. The dotted, dashed, and dashed-dotted curves represent the potential at t = 0, T/4, and T/2, respectively. The heavy solid curve is the time-averaged potential to which the ions respond. The vertical solid line shows the location of the sheath edge; the spatial fluctuation of the sheath edge through the RF cycle is approximately shown by the locations where the instantaneous potential curves pass through zero. Notice that the near-collapse of the sheath is quite short-lived. In this case, the instantaneous sheath edge stays within 2 Debye lengths of the average value for more than 80% of the RF period.

reasonable, if not exact, job of approximating the potential variation in the RF plasma sheath.

It is interesting to note that for a large fraction of the sheath, the average electric field is almost linear, indicating that the average potential is very nearly parabolic. This trend occurs despite the fact that the fields at individual times in the RF cycle are definitely not linear. Such linear/parabolic tendencies bolsters arguments made previously concerning harmonic dust oscillations. The topic of the parabolic sheath potential will be discussed at length in the following chapter.
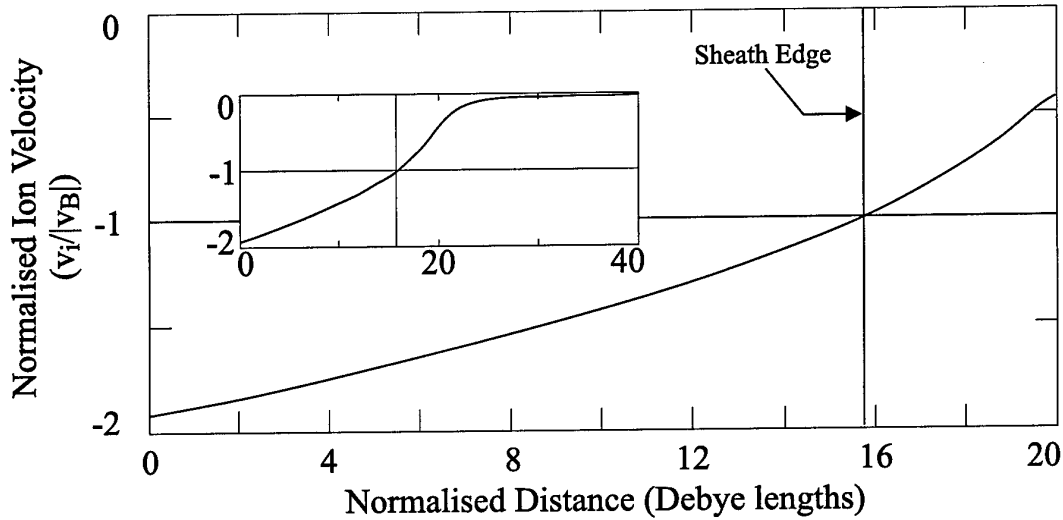
Figure 23: Variation of the Ion Velocity in the Plasma Sheath. This figure shows numerical results for the ion velocity as a function of height above the electrode. The vertical solid line shows the location of the sheath edge, while the horizontal solid line indicates the Bohm velocity. The inset shows the same data for a larger distance range, illustrating the behaviour of the ion speed further from the plasma sheath.
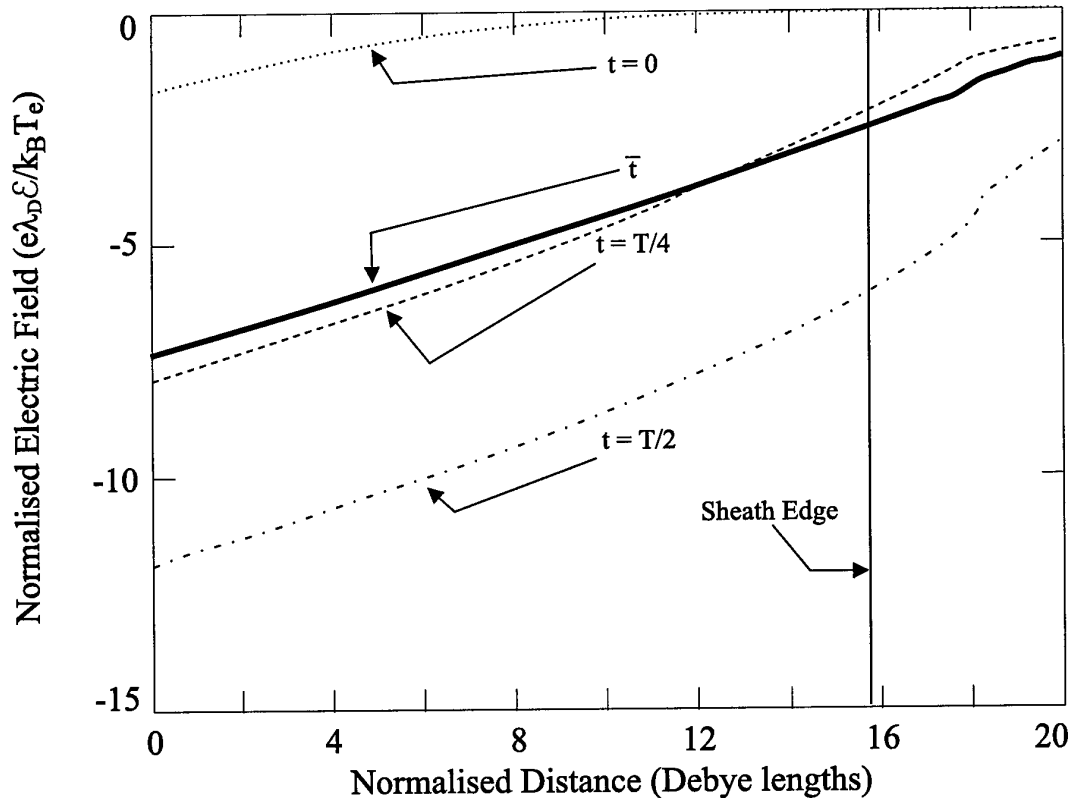
Figure 24: Variation of the Electric Field in the Plasma Sheath. This figure shows numerical results for the electric field as a function of height above the electrode. The dotted, dashed, and dash-dot curves represent the field at $t = 0$, $T/4$, and $T/2$, respectively. The heavy solid curve is the time-averaged field. The vertical line is the sheath edge. Notice the near-linearity of the time-averaged field over a large portion of the sheath and the non-linearity of the field at the discrete times. The implications are that while the potential at any specific time is not necessarily parabolic, the average potential is almost globally parabolic in the sheath.
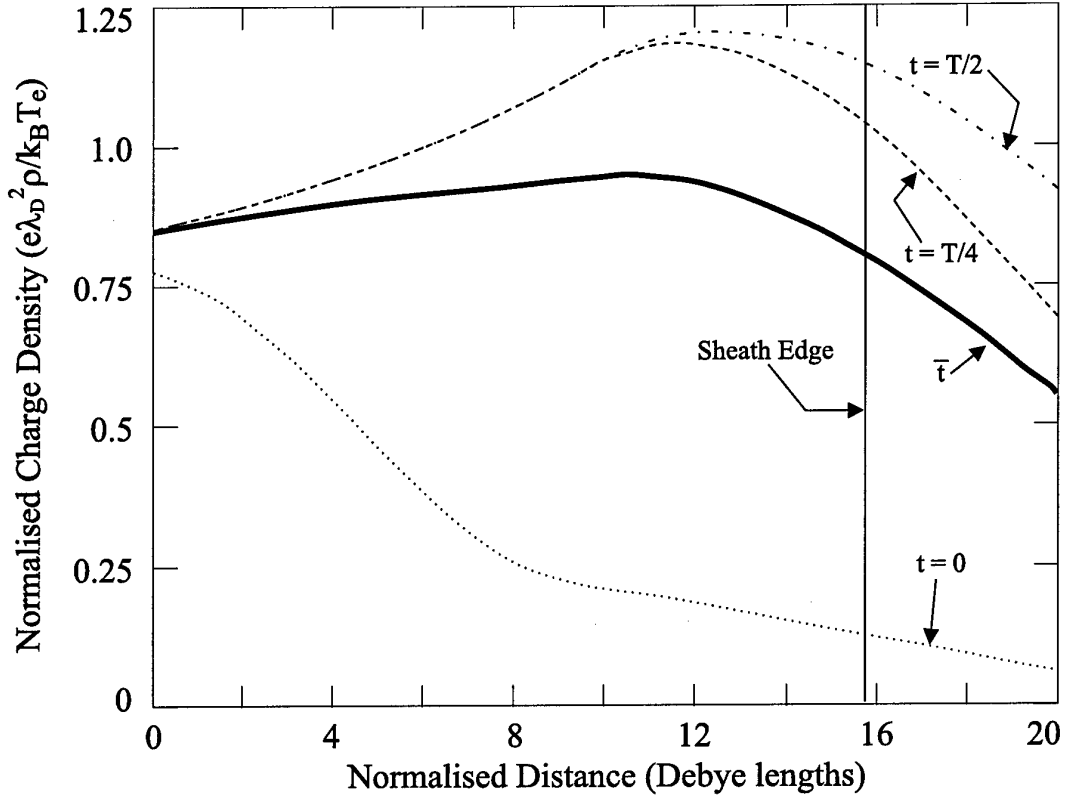
Figure 25: Variation of the Charge Density in the Plasma Sheath. This figure shows numerical results for the charge density as a function of height above the electrode. The dotted, dashed, and dashed-dotted curves represent the densities at t = 0, T/4, and T/2, respectively. The heavy solid curve is the time-averaged charge density. The vertical solid line shows the location of the sheath edge.

4.4.2 NUMERICAL RESULTS FOR PARAMETRIC VARIATIONS

Now that the results from the model for the specific experimental parameters used later have been thoroughly discussed, it remains to record results of the model for a variety of plasma parameters. Figure 27 to Figure **31** show how the potential functions and carrier densities change in response to changes in the electron temperature, electron density, pressure, RF amplitude, and ion mass. The parameters were varied around a set that commonly are used for plasma crystal and dust oscillation experiments. These parameters are as follows: $k_B T_e = 3eV$; $k_B T_i = 0.04eV$; $k_B T_n = 0.025eV$; $n_e = 1 \cdot 10^{14} m^{-3}$; $P = 10Pa$; $f_{rf} = 13.56MHz$; $\phi_{rf} = 100V$; gas: argon.
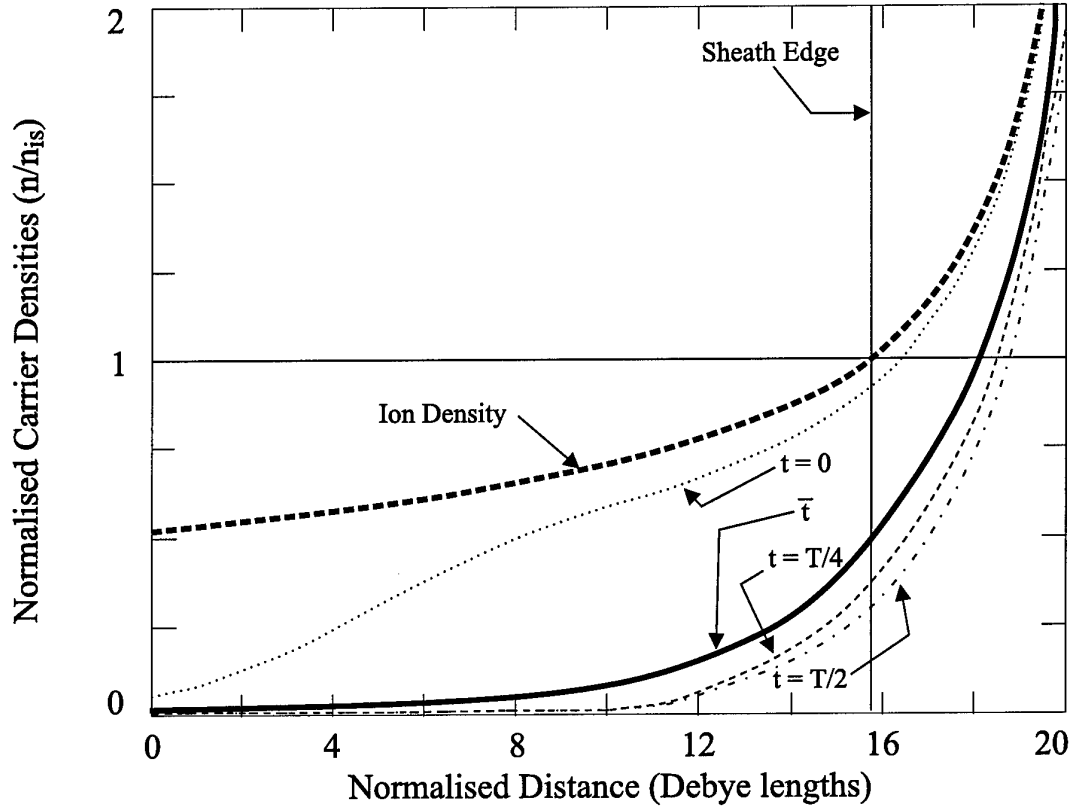
Figure 26: Variation of the Carrier Densities in the Plasma Sheath. This figure shows numerical results for the carrier densities as a function of height above the electrode. The thin dotted, dashed, and dash-dot curves represent the electron densities at t = 0, T/4, and T/2, respectively. The heavy solid curve is the time-averaged electron density and the heavy dashed line is the ion density, which is time-invariant. The vertical line is the sheath edge.

As can be seen from these figures, the model responds qualitatively as would be expected from an actual plasma. As some of the assumptions used in the development of this model are generally unobtainable in our system (most notably, the assumption that the driven electrode is of much smaller area than the grounded electrode), meaningful quantitative comparisons with experimental values were not possible. However, as will be shown in the next chapter, the real result of this model was to direct the course of study toward generalisations of a number of existing models. Due to the success in generalising these models, the potentials predicted by the model developed in this chapter were never used in the experimental work described later in this thesis.
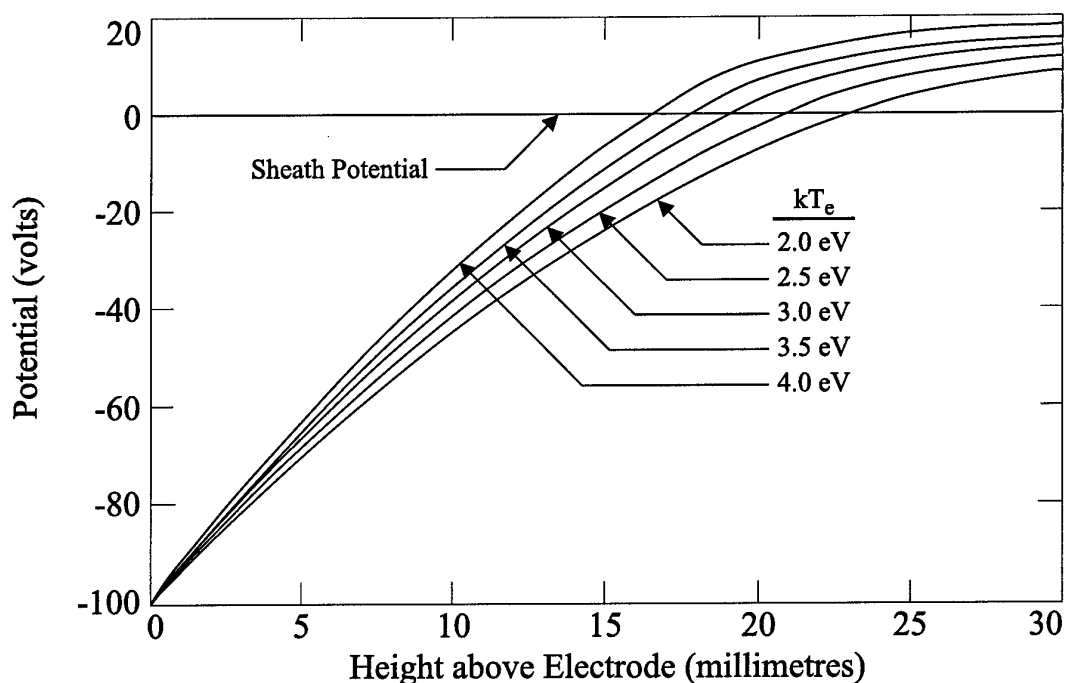
Figure 27: Variation of the Potential in the Sheath with Changes in the Electron Temperature. This figure shows numerical results for the time-averaged potential as a function of height above the electrode for several values of the electron temperature. As the electrons become more energetic, more of them can penetrate nearer to the electrode. This physical reality is reflected in the numerical curves by the decrease in the sheath width as the electron temperature increases. Parameters used to generate this plot are as follows: $k_B T_n = 0.025 eV$; $n_e = 1 \cdot 10^{14} m^{-3}$; $P = 10Pa$; $f_{rf} = 13.56MHz$; $\phi_{rf} = 100V$; gas: argon.
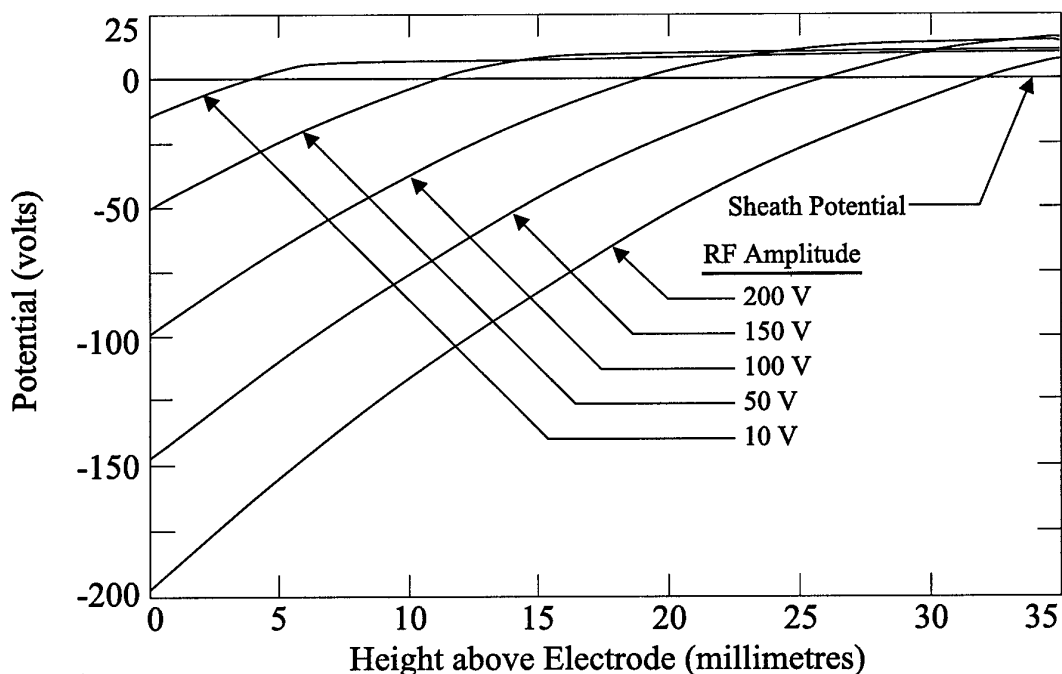
Figure 28: Variation of the Potential in the Sheath with Changes in the RF Amplitude. This figure shows numerical results for the time-averaged potential as a function of height above the electrode for several values of the RF Amplitude. As the electrode becomes more negative, fewer electrons can penetrate near the electrode, as is reflected in the numerical curves by the increase in the sheath width as the driving amplitude increases. Parameters used to generate this plot are as follows: $k_B T_e = 3eV$; $k_B T_n = 0.025eV$; $n_e = 1 \cdot 10^{14} m^{-3}$; $P = 10Pa$; $f_{rf} = 13.56MHz$; gas: argon.
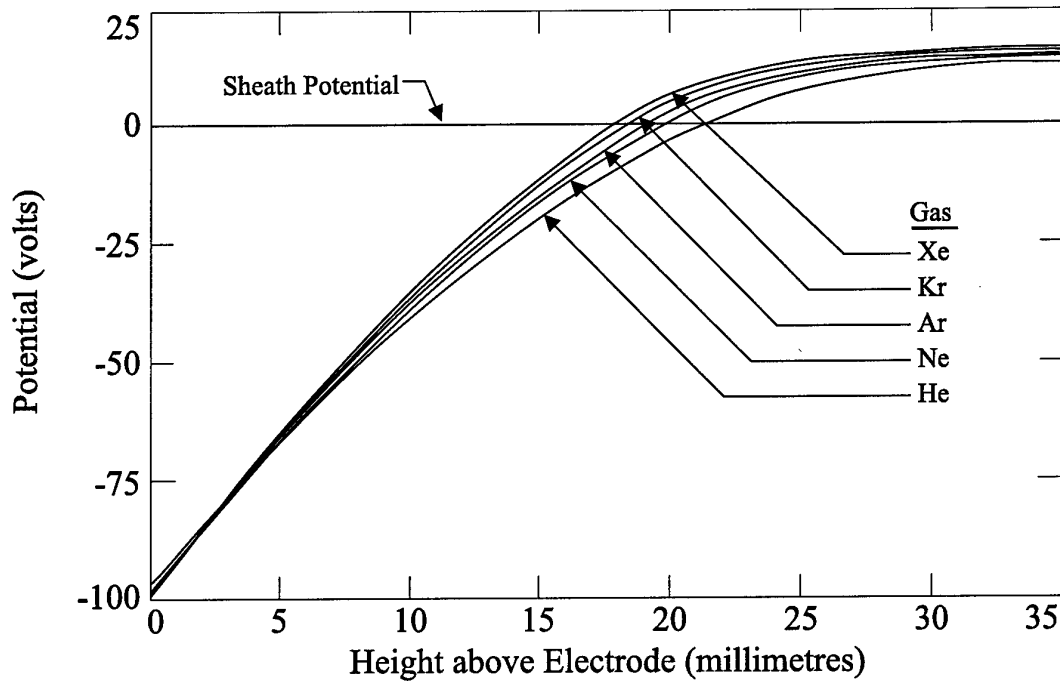
Figure 29: Variation of the Potential in the Sheath with Changes in the Constituent Gas. This figure shows numerical results for the time-averaged potential as a function of height above the electrode for the noble gases. As the gas becomes less massive, less field is required to accelerate the ions to the Bohm speed, as is reflected in the numerical curves by the increase in the sheath width as the mass decreases. Parameters used to generate this plot are as follows: $k_BT_e = 3eV$; $k_BT_n = 0.025eV$; $n_e = 1 \cdot 10^{14}m^{-3}$; $P = 10Pa$; $f_{rf} = 13.56MHz$; $\phi_{rf} = 100V$.
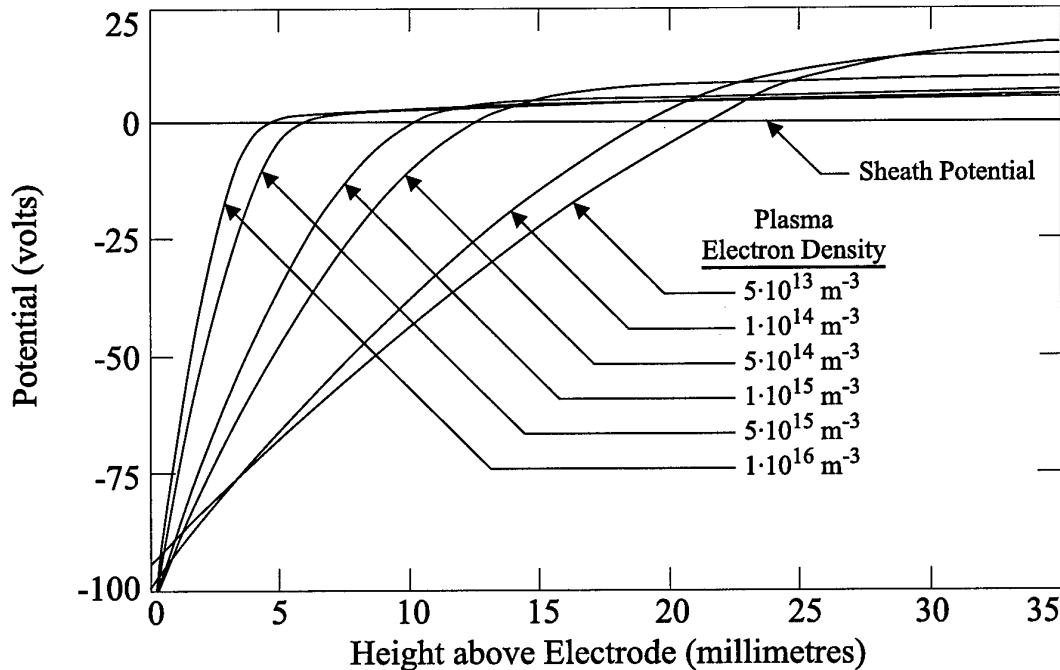
Figure 30: Variation of the Potential in the Sheath with Changes in the Electron Density. This figure shows numerical results for the time-averaged potential as a function of height above the electrode for several values of the electron density in the quasineutral plasma. As the density increases, the characteristic screening length decreases, allowing electrons to penetrate nearer to the electrode before being influenced by the sheath field. This physical case is reflected in the numerical curves by the decrease in the sheath width as the density increases. Parameters used to generate this plot are as follows: $k_BT_e = 3eV$; $k_BT_n = 0.025eV$; $P = 10Pa$; $f_{rf} = 13.56MHz$; $\phi_{rf} = 100V$; gas: argon.
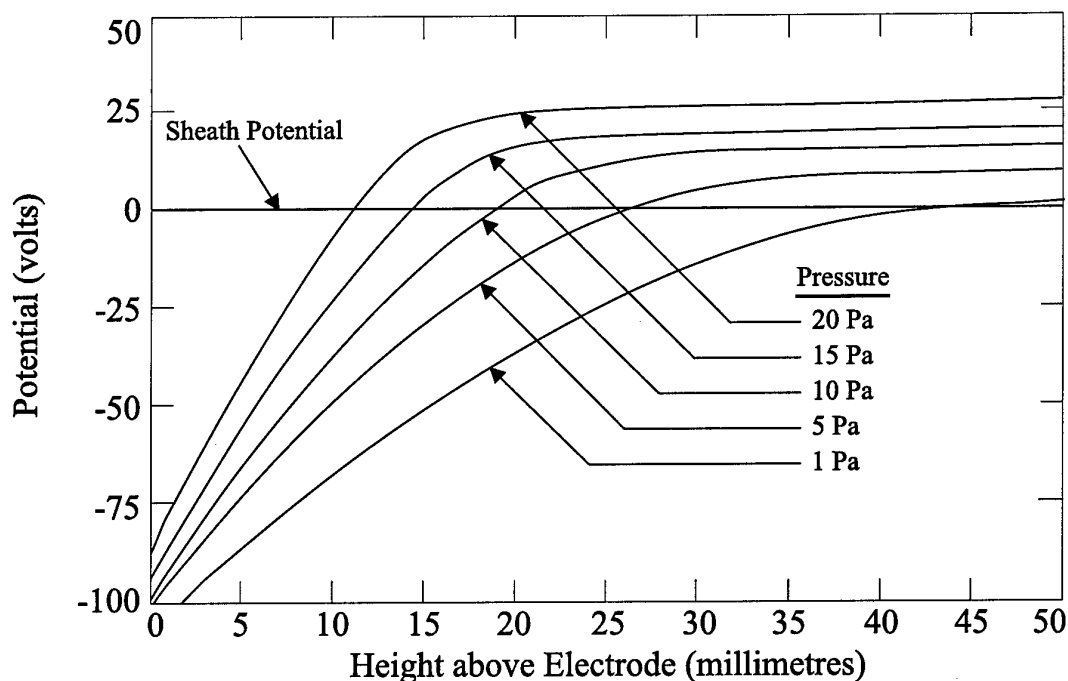
Figure 31: Variation of the Potential in the Sheath with Changes in Pressure. This figure shows numerical results for the time-averaged potential as a function of height above the electrode for several values of the chamber pressure. As the pressure increases, collisional effects become more pronounced and it takes a greater field to accelerate the ions to the Bohm speed. This physical effect is reflected in the numerical curves by the decrease in the sheath width as the pressure increases. Parameters used to generate this plot are as follows: $k_BT_e = 3eV$; $k_BT_n = 0.025eV$; $n_e = 1 \cdot 10^{14}m^{-3}$; $f_{rf} = 13.56MHz$; $\phi_{rf} = 100V$; gas: argon.

This chapter has detailed the development and implementation of a relatively

simple model of the RF plasma sheath. The model was never intended to be state-of-

the-art, but rather was designed as an in-house tool to assist in the examination of dust

oscillations observed in the plasma sheath. As such, it contains a number of

approximations and assumptions that may or may not be physically realistic. However,

it appears to be at least as accurate as several recent, published RF models while

containing several improvements over those models and incorporating applicable

lessons learned from DC numerical modellers. The results from this model appear to be

physically realistic, as changing parameters in the model result in changes to the sheath

that are qualitatively similar to those observed experimentally. Perhaps the most

interesting result from the development of this model is that the form of the potential in

the plasma sheath may indeed be approximated by much simpler techniques. That

approximation technique is the subject of the next chapter.

Note: Most of this chapter has been submitted to Physical Review Letters. Appendix C contains a copy of that paper.

5. THE PARABOLIC PLASMA SHEATH POTENTIAL

As has been previously stated, the fluid model described in the preceding chapter is by no means the only plasma sheath model in existence. In this chapter, results of models described in Table 3 (p. 21) will be reproduced for the purposes of comparison with each other. Each model, though based on disparate boundary conditions and valid for different ranges of plasma parameters, will be shown to have several important features in common. This commonality of the numerical solutions will be exploited to draw some general conclusions about the nature of the plasma sheath, primarily that for a wide range of plasma parameters, a simple parabola closely approximates the electric potential in the sheath.

The models to be examined in detail in this thesis are those of Bohm [1949], Blank [1968], Franklin and Ockendon [1970], Nitter [1996], Riemann [1997], Valentini [1999], and Franklin and Snell [2000]. Although not dealing specifically with plasmas, the Child-Langmuir model [Child, 1911; Langmuir, 1913] will also be investigated due to its relevance in the single-carrier, space-charge-limited conditions that approximately exist near the electrode of DC plasmas. Of these models, only those of Nitter and

Model	Spatial Extent	Generation Technique	Collisionality
Child [1911] and Langmuir [1913]	N/A	DC	Collisionless
Bohm [1949]	Sheath	DC	Collisionless
Blank [1968]	Sheath and Plasma	DC	Highly Collisional
Franklin and Ockendon [1970]	Sheath and Plasma	DC	Collisionless
Nitter [1996]	Sheath	RF	Moderately Collisional
Riemann [1997]	Sheath and Plasma	DC	Moderately Collisional
Valentini [1999]	Sheath	RF	Collisionless
Franklin and Snell [2000]	Sheath and Plasma	DC	Collisionless to Highly Collisional
Tomme	Sheath	RF	Collisionless to Moderately Collisional

Table 6: Summary of Analysed Numerical Models. This table shows the broad range of collisionalities and plasma generation techniques covered by the analysis of this chapter. A more detailed summary of the governing equations and assumptions behind each model may be found in Table 3 (p. 21).

Valentini directly address the RF sheath; the others deal with DC plasmas. The RF model developed in the previous chapter will also be discussed. Table 6 summarises the important differences between each of these models. There exist many other fluid models [*e.g.* Börnig, 1992; Daugherty *et al.*, 1992; Skorik and Allen, 1993; Sternberg and Godyak, 1994; Benilov, 1997; Gierling and Riemann, 1998], differing in boundary conditions or other subtleties; the ones from the literature that are detailed in this thesis are, by many measures, the premier representatives of the bulk.

5.1 STATIC MODELS

5.1.1 THE MODEL OF BLANK

The first model to be considered will be that of Blank [1968]. Blank's method involved simultaneously solving electron and ion transport and density equations along with Poisson's equation, assuming a constant ion mobility. In his paper, he shows that a matched asymptotic solution exists for the highly collisional plasma and sheath. It is well known that plasmas are bounded by thin space-charge regions known as sheaths. The scale of the plasma is on the order of its smallest dimension (L), and the scale of the sheath is on the order of the Debye length (λ_D), which ordinarily is much smaller than the plasma scale. By an asymptotic solution, it is meant that the plasma solution, where

the electric field becomes infinite near the plasma boundary, and the sheath solution, where the field becomes zero at the sheath edge, may be matched without singularity through the use of an intermediate scaling [Van Dyke, 1975]. For the case of Blank, this intermediate scaling was found to be $\lambda_D^{2/3}L^{1/3}$. Far from the wall, the plasma solution has the potential following the form $\phi(x)\sim\ln(\cos(x/L))$, where x is measured from the centre of the plasma. (In actuality, Blank's cylindrical solution showed the potential function to be $\phi(r)\sim\ln(J_0(z_{01}r))$, where $J_0(x)$ is the zeroth order Bessel function and z_{01} is the location of its first zero. The cosine form presented above was derived for this thesis to assist in the use of the Blank model for the planar experimental conditions discussed later.) The sheath solution has a much more complicated numerical form. By matching the sheath and plasma solutions and applying appropriate boundary conditions, Blank showed that the plasma/sheath solution could be found from a single differential equation in the transition region. A numerical integration of his equations carried out for this thesis resulted in the plot shown in Figure 32. As a comparison, the reader is referred to Blank's Figure 6.

An interesting feature of Blank's solution was noticed as a result of experimental work that will be detailed in the next chapter. That work was based on an assumption that the electric potential in the sheath was globally parabolic. In fact, that parabolic assumption (or the equivalent assumption of a linear electric field in the sheath) has been used by numerous other researchers [*e.g.* Melzer, 1994; Trottenberg, 1995; Kortshagen, 1996; Homann, 1999; Nunomura, 1999] without proof.
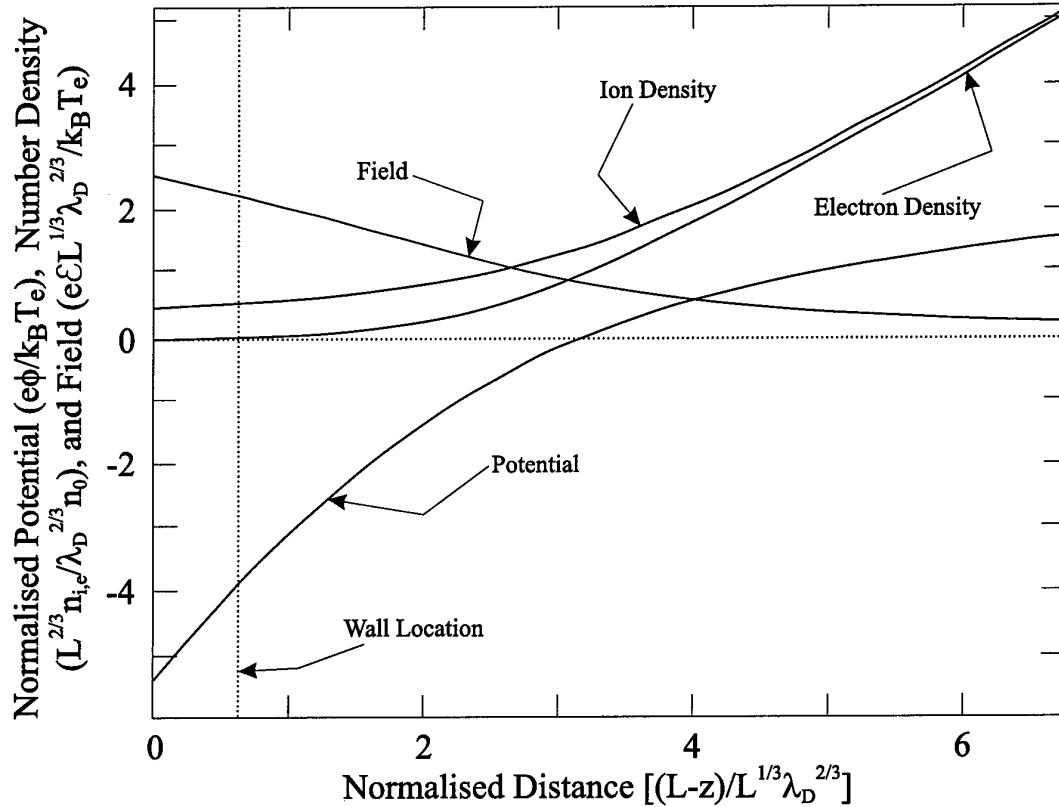
Figure 32: Reproduction of the Model of Blank [1968]. This figure shows a numerical duplication, developed for this thesis, of the model of Blank. The wall location from the boundary conditions for helium is also shown. In contrast to a similar figure in Blank, all four curves are plotted at the same vertical scale.

Figure 33 shows a view of just the electric potential from Blank's model, superimposed on a best-fit parabola. The match is striking for a large portion of the plot immediately adjacent to the wall. (For this model, Blank does not explicitly state where his sheath edge lies; later discussion will show that in this collision-dominated case, there exists no definitive sheath edge.) The frame below the potential plot shows the deviation of the parabolic fit from the numerical solution. In the region prior to the rapid divergence of the two curves, the difference between the parabolic solution and the model is no more than 0.2%. Following an exhaustive literature search, the close correspondence between the numerical model and the parabolic approximation presented here appears to be the first concrete numerical support for the widely used *a*
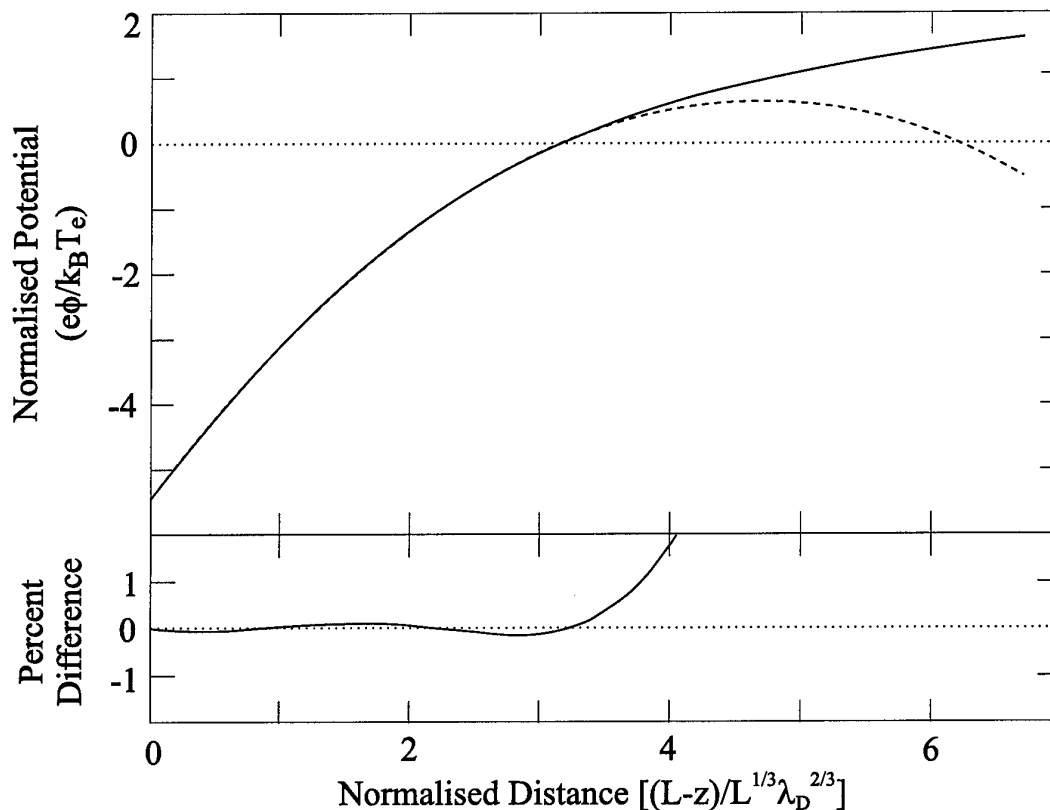
Figure 33: Parabolic Approximation to the Model of Blank [1968]. This figure shows plots of the numerically derived normalised potential (upper plot, solid curve) and the best-fit parabolic approximation (upper plot, dashed curve). The percent difference between the curves is shown in the lower plot. For this particular parabola, the approximation does not differ by more than 0.2% of the maximum potential from the numerical curve across the entire sheath.

priori parabolic potential assumptions. Blank himself certainly did not describe the

parabolic nature of his solution near the wall.

5.1.2 THE MODEL OF FRANKLIN AND OCKENDON

Shortly after Blank's collision-dominated model was published, Franklin and

Ockendon [1970] released a similar model for collisionless plasmas. Utilising the

matched asymptotic technique, they were able to simultaneously solve the electron and

ion continuity and transport equations and Poisson's equation to reveal a single

differential equation for the potential in the plasma/sheath transition region. A major

difference from Blank's model was that the scaling of their matched intermediate region
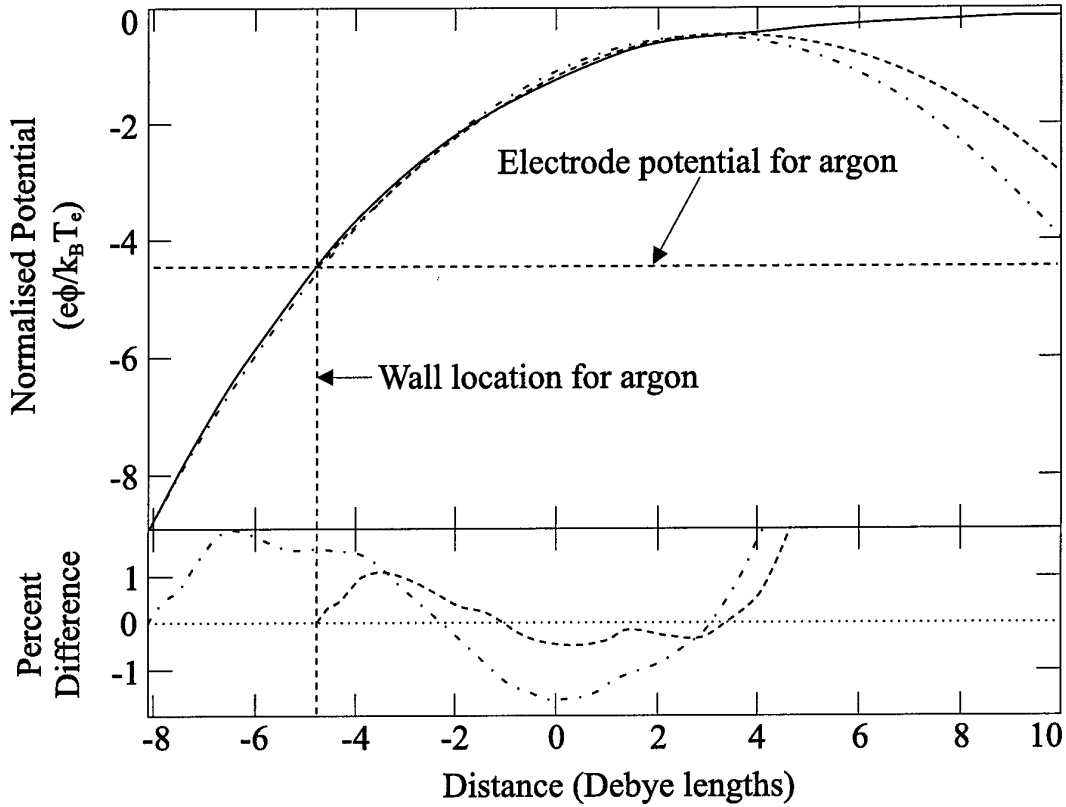
Figure 34: Parabolic Approximation to the Model of Franklin and Ockendon [1970]. This figure shows plots of the numerically derived normalised potential (upper plot, solid curve) and the best-fit parabolic approximation (upper plot, dashed curve) for argon. The percent difference between the two curves is shown in the lower plot. For this particular parabola, the approximation does not differ by more than 1% of the maximum potential from the numerical curve over a span of more than eight Debye lengths. A parabolic fit to the entire numerical curve is also shown (upper plot, dash-dotted curve), and this fit is also shown to be quite parabolic. In order to facilitate direct comparison of potential diagrams throughout this thesis, mirror images of the abscissa and ordinates of the numerical plot from the original paper are shown in this plot.

was instead $\lambda_D^{4/5} L^{1/5}$.

Figure 34 shows the Franklin/Ockendon solution in the region near the wall

(adapted from their Figure 4), along with fit parabolas. As was the model of Blank,

their model is translationally invariant, and the wall location is defined as the point

where the ion and electron fluxes equate. Again, the match between the parabolic

approximations and the numerical results is striking. The parabolic approximation has

now been shown to be reasonable for the highly disparate cases of collisionless and
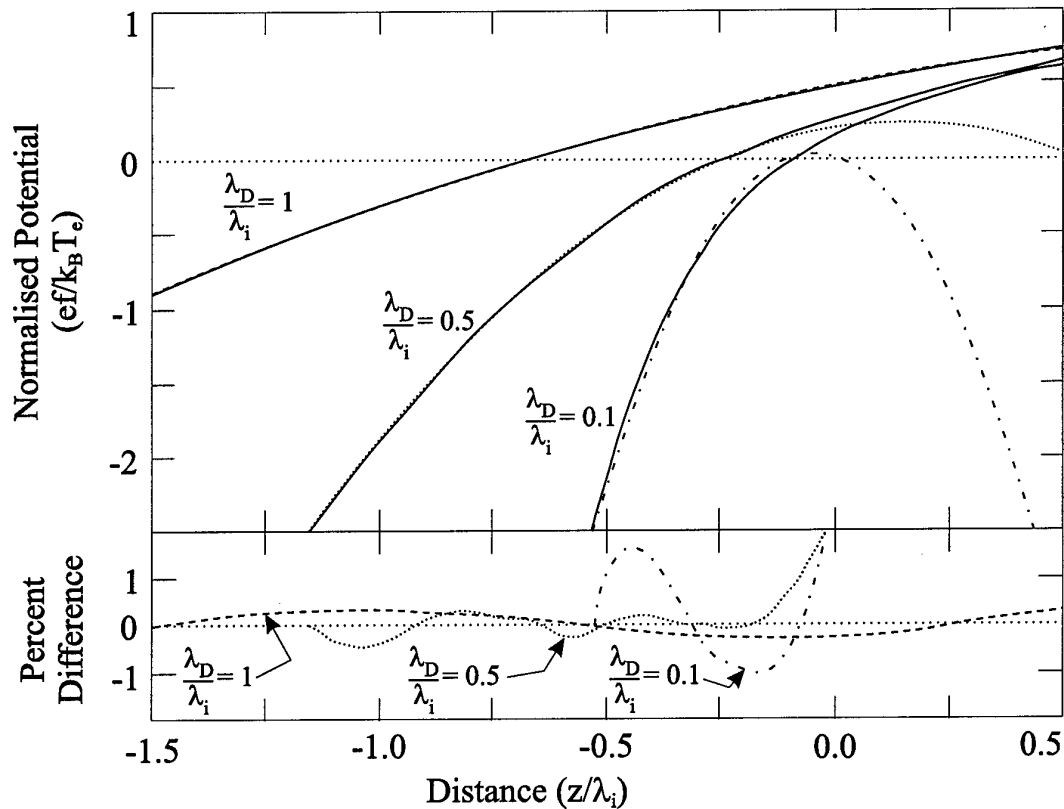
Figure 35: Parabolic Approximation to the Model of Riemann [1997]. This figure shows plots of the numerically derived normalised potentials (upper plot, solid curves) and the best-fit parabolic approximations (upper plot, broken curves) for three different values of the collisionality parameter, assuming a constant mean free path. The percent differences between the curve pairs are shown in the lower plot. For these particular parabolas, the approximations do not differ by more than 2% of the maximum potential from the numerical curves across the entire sheath (the sheath edge is at zero potential in this model). In order to facilitate direct comparison of potential diagrams throughout this thesis, mirror images of the abscissa and ordinates of the numerical plot from the original paper are shown in this plot.

collision-dominated plasmas for models solving two separate sets of equations and

boundary conditions.

5.1.3 THE MODEL OF RIEMANN

The next model to be examined is that of Riemann [1997]. Riemann examines

the regime where the plasma starts to become collisional, but not so collisional to be

considered collision-dominated. In other words, this model examines a large portion of

the parameter space between the previous two models. His governing equations are

similar to the two previous models, simultaneously solving the electron and ion

transport equations, the ion density equation, and Poisson's equation. Interestingly,

Riemann ignores ionisation both in the sheath and in the pre-sheath, a region where a

significant electron population would seem to make ionisation a relevant factor.

Riemann's model similarly uses asymptotic solution matching and determines the

matching scale to be $\lambda_D^{4/5}\lambda_i^{1/5}$, where λ_i is the ion-neutral mean free path. Results for

this model for several cases of his collisionality parameter λ_D/λ_i are shown in Figure 35

(see his Figure 8 for comparison), along with parabolic fits for each case. As would be

expected when the bounding collisional and collisionless cases were well modelled by

parabolas, these intermediate cases also fit the parabolic approximation.

5.1.4 THE MODEL OF FRANKLIN AND SNELL

One of the most recent and most complete DC plasma/sheath model to be

proposed is that of Franklin and Snell [2000]. It uses a method very similar to that of

Franklin and Ockendon [1970], adding terms in the transport equations to account for

collisions. The addition of these terms allows the model to accurately represent plasma

conditions from collisionless to collision-dominated. The scaling of the sheath is shown

to range from Blank's $\lambda_D^{2/3}L^{1/3}$ to Franklin and Ockendon's $\lambda_D^{4/5}L^{1/5}$ for collision-

dominated to collisionless plasmas, respectively. For intermediate collisionalities, the

scaling is shown to transition smoothly between those limits. Appropriately generalized

Franklin and Ockendon and Blank models are also shown to be limiting cases of the

Franklin and Snell model. The Riemann model is also shown to follow from this more

generalized treatment.

Professors Franklin and Snell kindly agreed to furnish this researcher with

simulations of DC plasmas from their model for several sets of specific plasma

parameters. These parameters were chosen to closely approximate those used in experiments that will be fully described in later chapters. The parameters used in the Franklin and Snell model are α_i, the ratio of the ionisation rate to the ion plasma frequency, and δ_i, the ratio of the ion collision frequency to the ionisation rate. It can be shown that for a given plasma dimension, an increase in α_i is related to an increase in the Debye length, while an increase in δ_i is related to an increase in the collisionality of the plasma.

Analysis of the parameters for the plasmas used in the next chapter indicated that the conditions were those of transitional (between collision-dominated and collisionless) plasmas joined to collisional sheaths. Plots of carrier densities, electric fields, and electric potentials from these simulations are shown in Figure 36 and Figure 37. For comparison with an RF model for similar parameters, the reader is referred to Figure 22 through Figure 26 in the previous chapter; the conditions in those figures are most closely approximated by the cases in the present figure where $\alpha_i \leq 0.004$ and $\delta_i \leq 40$. The most obvious difference between the models is the sheath width, which is considerably enhanced in the RF case due to the increased self-bias on the driven electrode in the RF case [Braithwaite, 1985]. The enhancement of the sheath width tends to cause the sheath to take on even more of a collisional nature due to the increased distance the ions must traverse prior to absorption by the wall.

Returning to the question of the parabolic sheath potential, it is no surprise that near the wall, the potential of Franklin and Snell is quite parabolic. The potential functions and their parabolic fits are shown in Figure 38. These curves represent
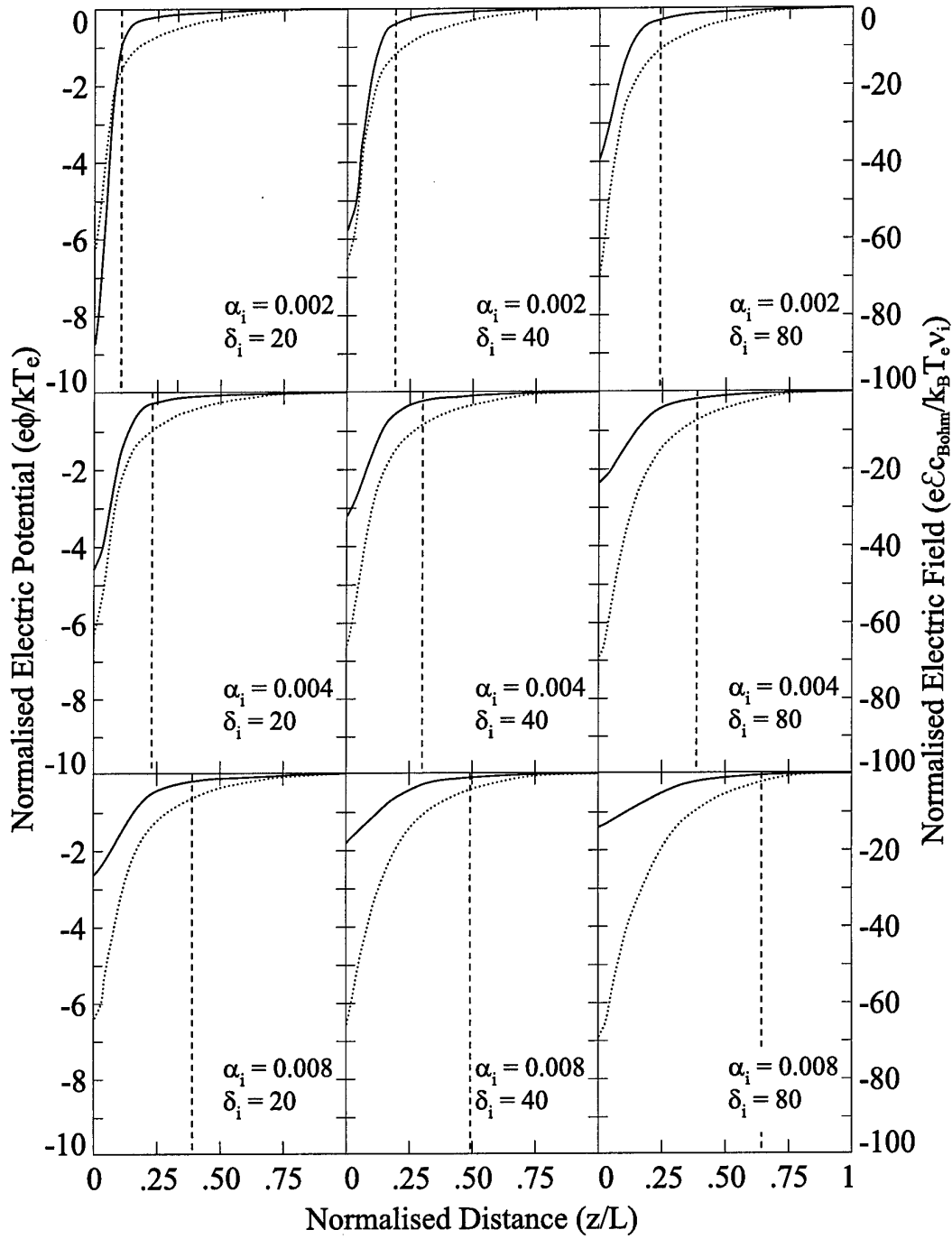
Figure 36: Electric Fields and Potentials from the Model of Franklin and Snell [2000]. This figure plots electric fields (solid curves) and electric potentials (dotted curves) for nine sets of parameters supplied by the model authors. The parameters shown are intended to bracket the experimental conditions to be described in subsequent chapters and may be used to compare DC results to similar RF results. The indicated sheath edges (vertical, dashed lines) are based on the point where the electron and ion densities differ by 1% [Franklin, 1999].
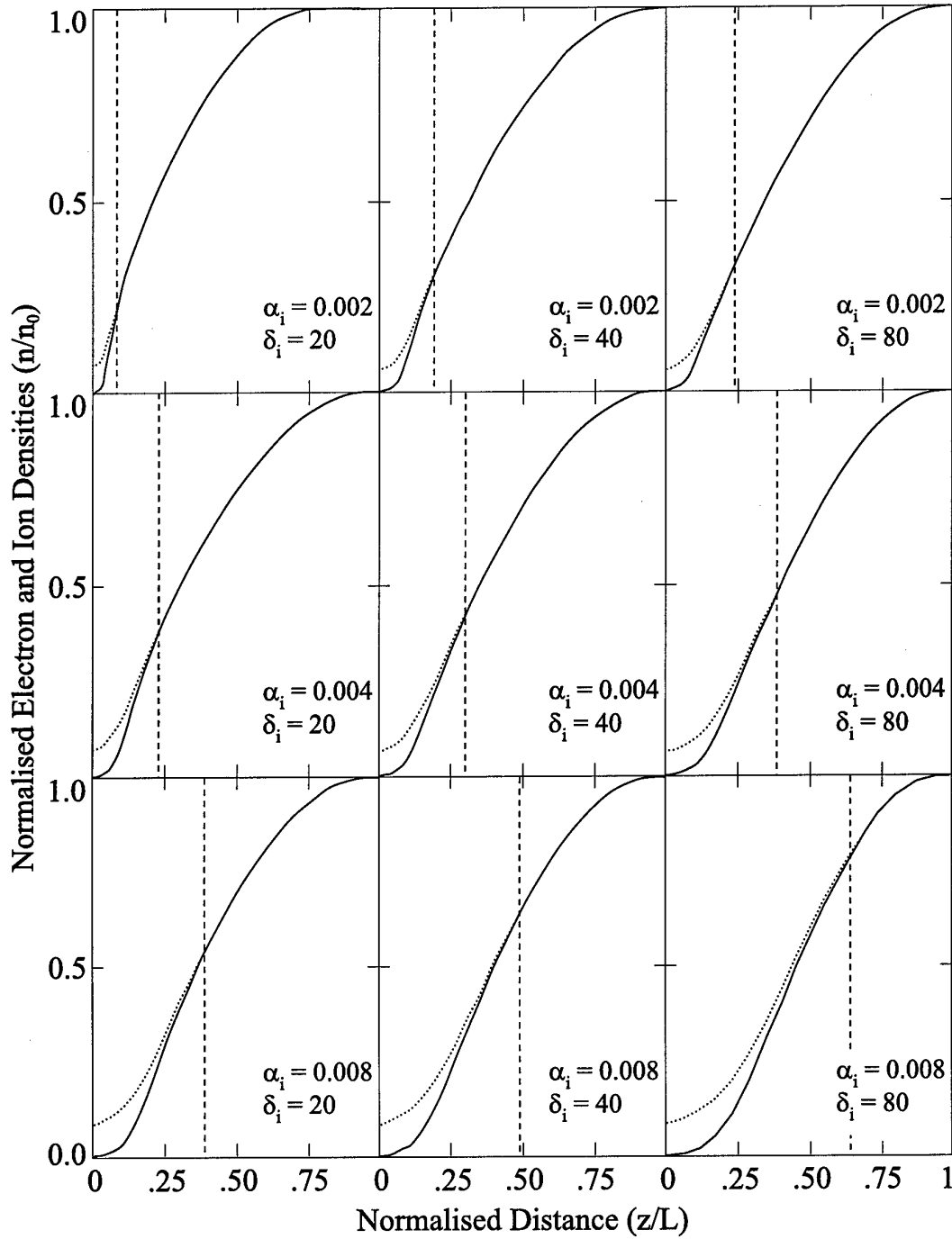
Figure 37: Electron and Ion Densities from the Model of Franklin and Snell [2000]. This figure plots electron densities (solid curves) and ion densities (dotted curves) for the nine sets of parameters supplied by the model authors. The parameters shown are intended to bracket the experimental conditions to be described in subsequent chapters and may be used to compare DC results to similar RF results. The indicated sheath edges (vertical dashed lines) are based on the point where the electron and ion densities differ by 1% [Franklin, 1999].
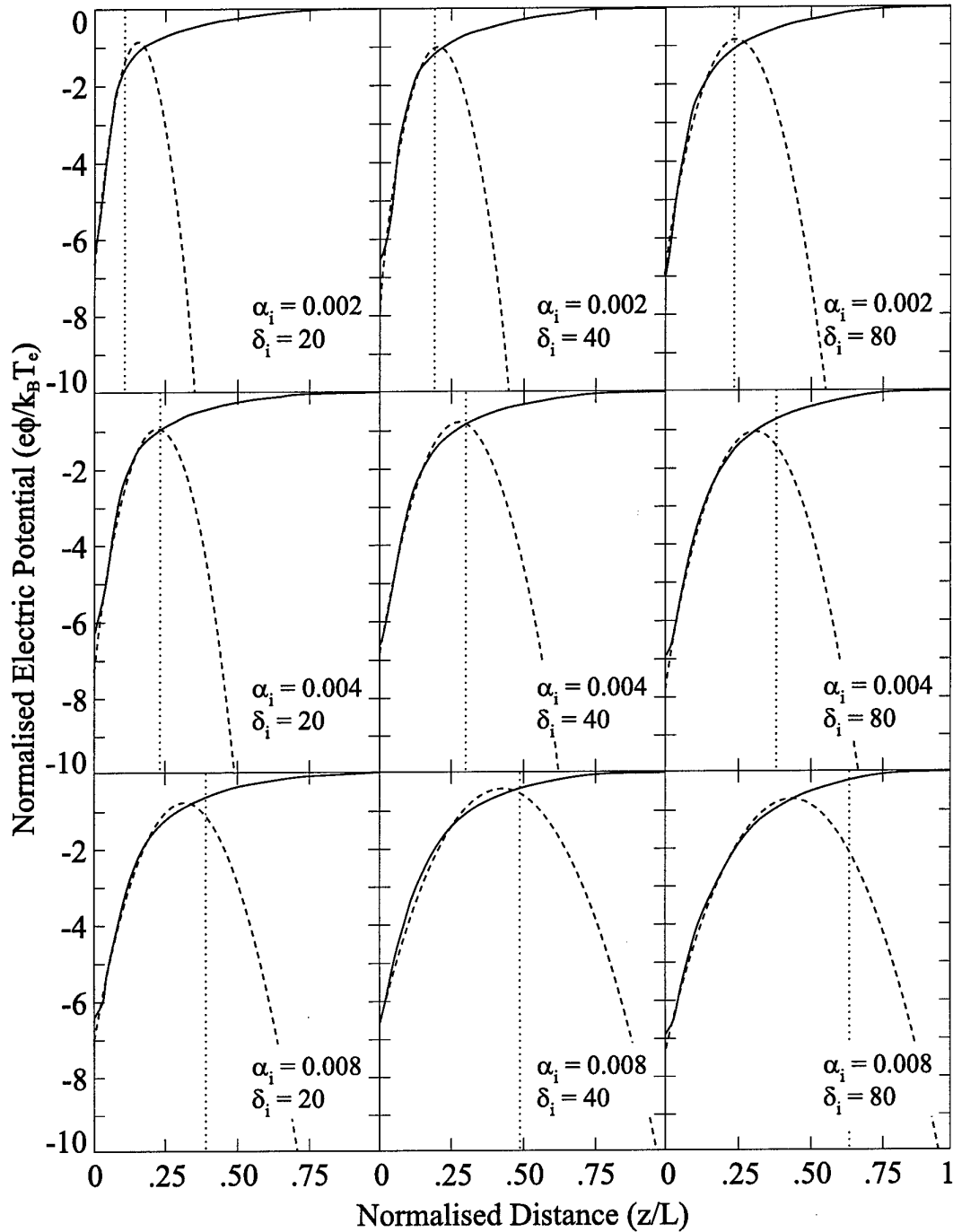
Figure 38: Parabolic Approximation to the Model of Franklin and Snell [2000]. This figure shows plots of the electric potential for the nine sets of parameters supplied by the authors (solid curves) and their best-fit parabolic approximations (dashed curves). For most of these parameters, the approximations do not differ by more than 3% of the maximum potential from the numerical curve across the entire sheath. The indicated sheath edges (vertical, dotted lines) are based on the point where the electron and ion densities differ by 1% [Franklin, 1999].

transitional cases between the models of Franklin and Ockendon and of Blank, *i.e.*, between collisionless and collision-dominated. As both those limiting cases have been shown to have parabolic sheath potentials, it follows that intermediate cases could easily follow the same pattern, as they are here shown to do.

Although the potentials from this model are the least parabolic of any of the models analysed for this thesis, the differences between the parabolic approximations and the numerical results are less than 5%, and so are probably not experimentally significant. There are a number of reasons why this particular model might not fit the parabolic approximation as well as do the others. The first reason is the relative sparseness of data points available. For most of the nine parameter sets analysed, there were on the order of ten data points in the sheath regions available for curve fitting, compared with several hundred points from the other models. Close examination of each of the plots will also show a slight decrease in the slope of the potential just prior to the wall, which is contrary to a parabola, in which the slope constantly increases. The decrease in slope corresponds to a decrease in the field, an effect that not only is not reflected in the accompanying plots of the field, but also would appear to have no obvious physical basis. Thus, this decrease appears to be an artifice of the modelling technique, most likely a problem with the termination of the numerical integration, and only appears to affect the final data point in each set. At any rate, the fact that the slope of the potential changes in an inconsistent manner definitely has an effect on the curve fitting results. Finally, the definition of the sheath from this model is significantly different from most others. That is not to say that this sheath definition is incorrect, just different. Here, the sheath is defined to be the point where the electron and ion densities differ by 1% [Franklin, 1999]. This definition extends the sheath significantly

further from the wall than the definitions used in many of the other examined models.

If the sheath were defined in a different manner, such that the sheath was less extensive,

the parabola would fit more closely across a larger portion of the sheath. A final

consideration is that the sheath from this model just may not be as parabolic as other

results.

5.1.5 THE MODEL OF CHILD AND LANGMUIR

For two final examples of just how pervasive the parabolic potential is under

static, plasma-like conditions, we will take a brief look at some early theory from the

literature. In the early 1900s, Child [1911] and Langmuir [1913] independently

developed a theory explaining diode currents observed from thermionic emitters in high

vacuum conditions. The so-called Child-Langmuir theory predicts a relationship

between the potential and the distance from the emitter to be $\phi \propto x^{4/3}$. The Child-

Langmuir theory assumes collisionless conditions for a single type of charge carrier, so

the concept of a sheath is not strictly valid. However, for purposes of illustration, the

example shown here will consider the Child-Langmuir case where ions are emitted with

the Bohm speed. If the resulting potential is normalised by $\eta = e\phi/kT_e$ and the distance

is normalised by $\xi = z/\lambda_{Ds}$, where $\lambda_{DS} = \left(\varepsilon_0 kT_e / n_s e^2\right)^{1/2}$, and n_s is the electron density

at the "sheath" edge, the normalised Child-Langmuir law may be expressed as

$$(54) \qquad \eta = \left(\frac{81}{32}\right)^{1/3} \xi^{4/3}.$$

A plot of the normalised Child-Langmuir law is shown in Figure 39. In order to

present this figure in a similar manner to the remainder of the potential plots in this
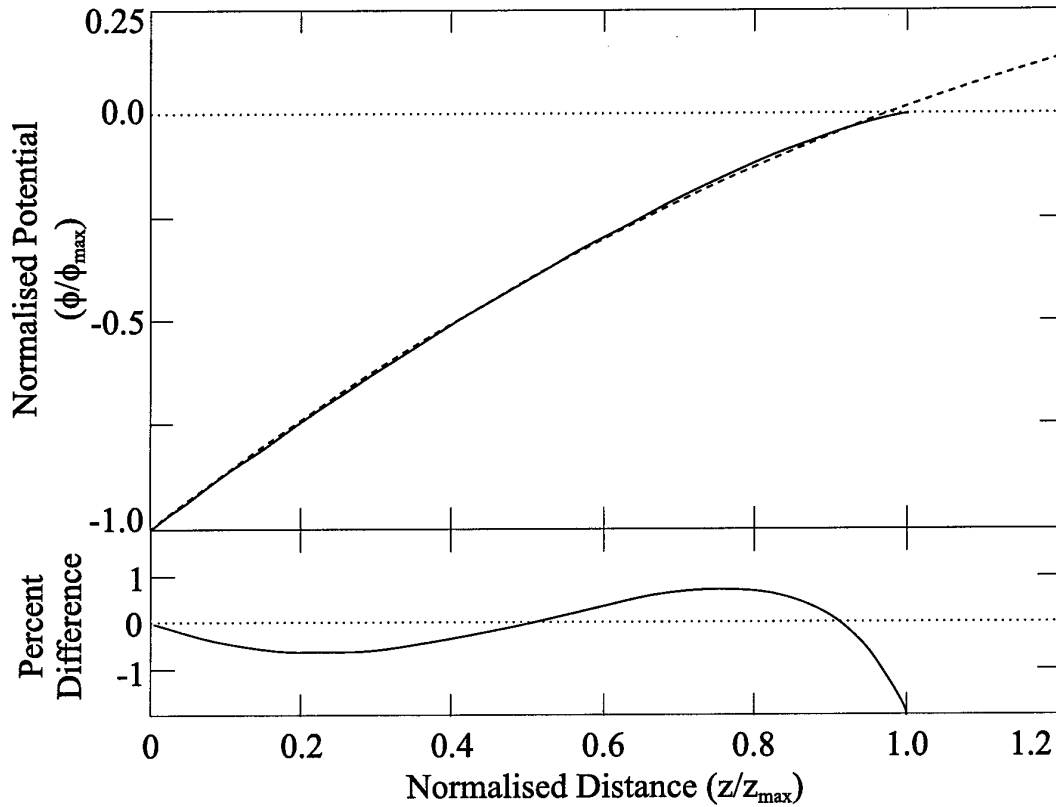
Figure 39: Parabolic Approximation to the Model of Child [1911] and Langmuir [1913]. This figure shows plots of the Child-Langmuir potential where the voltage is proportional to $x^{4/3}$ (upper plot, solid curve) and the best-fit parabolic approximation (upper plot, dashed curve) for the normalisations stated in the text. The difference between the curves is shown in the lower plot. Regardless of the distance scale chosen the approximation does not differ by more than 1% of the maximum calculated potential across the vast majority of the sheath.

chapter, the actual equation plotted is $\eta = -(81/32)^{1/3}(\xi - \xi_{max})^{4/3}$. The axes have also

been renormalized such that the distance and potential are in terms of $Z = \xi/\xi_{max}$ and

$\Phi = \eta/\eta(0)$, respectively. The parabolic approximation that best fits this particular

curve is $\Phi = -0.367(Z - 1.894)^2 + 0.316$. In fact, this particular parabola is the best fit

for *any* choice of ξ_{max}, as the fit is scale invariant. Thus, the curves shown in the figure,

including the percent difference curve, remain exactly as shown regardless of the choice

of distance scale. It is obvious from the figure that this approximation is quite good for

the vast majority of the sheath, with a slight divergence only very near the emitter.
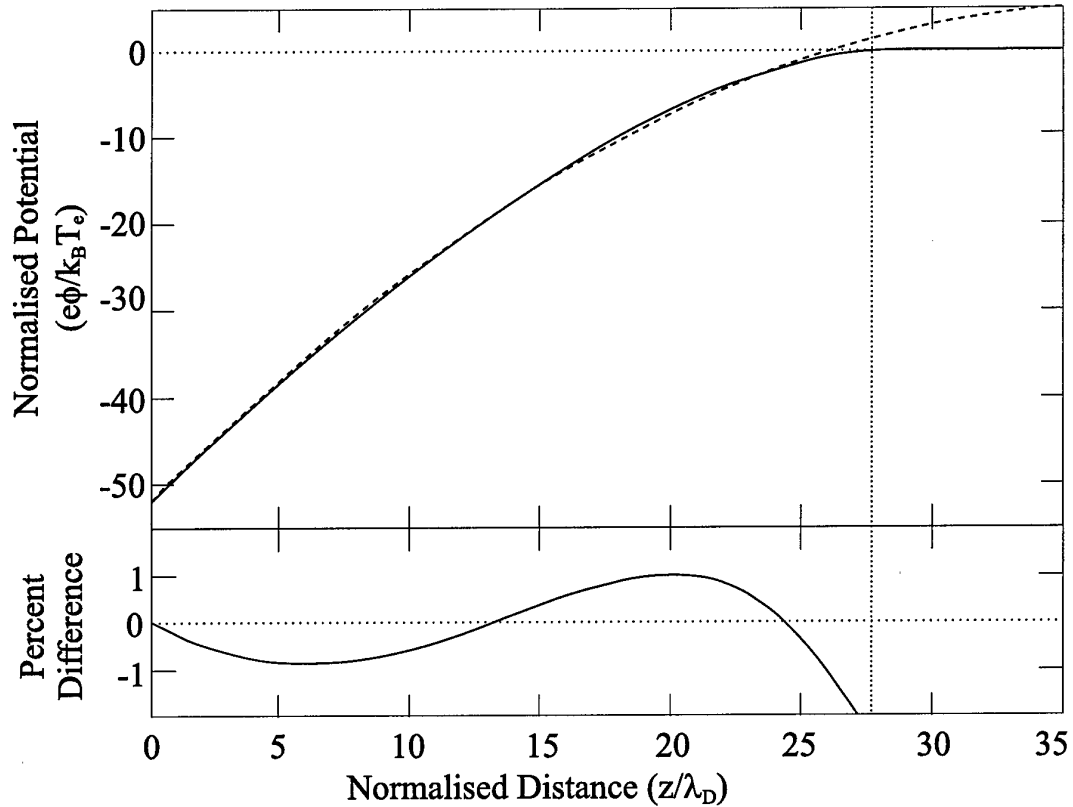
Figure 40: Parabolic Approximation to the Model of Bohm [1949]. This figure shows plots of the Bohm potential (upper plot, solid curve) and the best-fit parabolic approximation (upper plot, dashed curve) for the conditions stated in the text. The difference between the curves is shown in the lower plot. For these particular conditions, the approximation does not differ by more than 1% of the maximum potential from the numerical curve across a vast majority of the sheath.

5.1.6 THE MODEL OF BOHM

The historically important model of Bohm [1949] also shows the same parabolic

trend. This model was developed to explain the minimum kinetic energy required for

ions to form a stable sheath, a condition that later became known as the Bohm criterion.

Bohm chose to ignore the plasma and concentrate on the sheath, only specifying that

some sort of field must exist in the plasma to account for ions arriving at the sheath

edge with a directed energy. However, he assumed that these fields were small enough

even on the plasma side of the sheath edge that they could be neglected. Figure 40

shows a numerical integration of the Bohm sheath equation (a normalised version of

Bohm's equation 7) for the marginal case of the sheath edge potential, $\phi_0 = kT_e/2e$. As

has been the case with each of the preceding models, the parabolic approximation to the

Bohm model is strikingly accurate across almost the entire sheath.

5.2 TIME-DEPENDENT MODELS

To this point, the models examined have all been for static, DC plasmas. It has

now been demonstrated that such plasmas have potentials near their walls that are well

approximated by simple parabolic forms over the entire spectrum of collisionality.

However, as many relevant experiments in the literature are carried out in RF plasmas,

it is of interest to see if the parabolic approximation applies there as well.

5.2.1 THE MODEL OF NITTER

The first RF model to be examined here is that of Nitter [1996]. Nitter's model

was developed to assist in a theoretical understanding of the oscillation of dust in the

plasma sheath, conditions much like those detailed in a later chapter of this thesis. He

solved Poisson's equation, the ion continuity equation, and the electron and ion

transport equations in the sheath. His model is valid for massive ions and dust particles,

particles so large that their inertia prevents them from responding to instantaneous

fluctuations in the electric field caused by the applied RF. The electrons, on the other

hand, are assumed to be completely responsive to the RF field. In other words, the

applied frequency must be greater than the ion plasma frequency but below the electron

plasma frequency. As a result, the ions and dust only respond to the time-averaged field

due to the RF self-bias on the electrodes.

The restriction on the allowed applied frequency means that the ions are never in equilibrium with the instantaneous field, and thus the potential cannot be solved analytically with a single differential equation, as was the case in the DC models. In this case, two differential equations are necessary: one for the ion velocity profile and one for the potential profile. Nitter uses an iterative approach where an initial time-averaged potential is assumed and used to determine the ion velocity profile in the sheath. Once the ion velocity profile is known, it fixes the ion density profile, which, with the time-dependent electron density profile, can be used in Poisson's equation to find the potential profile at any time during the RF cycle. The potential profile is calculated for a large number of times during the RF cycle, and the results are time-averaged. The new time-averaged results are then put back into the differential equation for the ion velocity, and the process is repeated until the solution converges. A scaling similar to that of the DC models is not obtained, as no attempt to model the plasma itself has been made.

Results from Nitter's model are shown in Figure 41 (for comparison, see his Figure 2). Here, only the time-averaged potential profile and its parabolic approximation are plotted. Again, the fit is good across virtually the entire sheath, diverging near the sheath edge. This divergence is primarily due to his boundary condition that sets the ion acceleration to zero at the sheath edge; in reality the ions continue to accelerate across the sheath edge. It will be shown later that the improved boundary conditions presented in the previous chapter allow the good parabolic fit to extend well past the sheath edge.
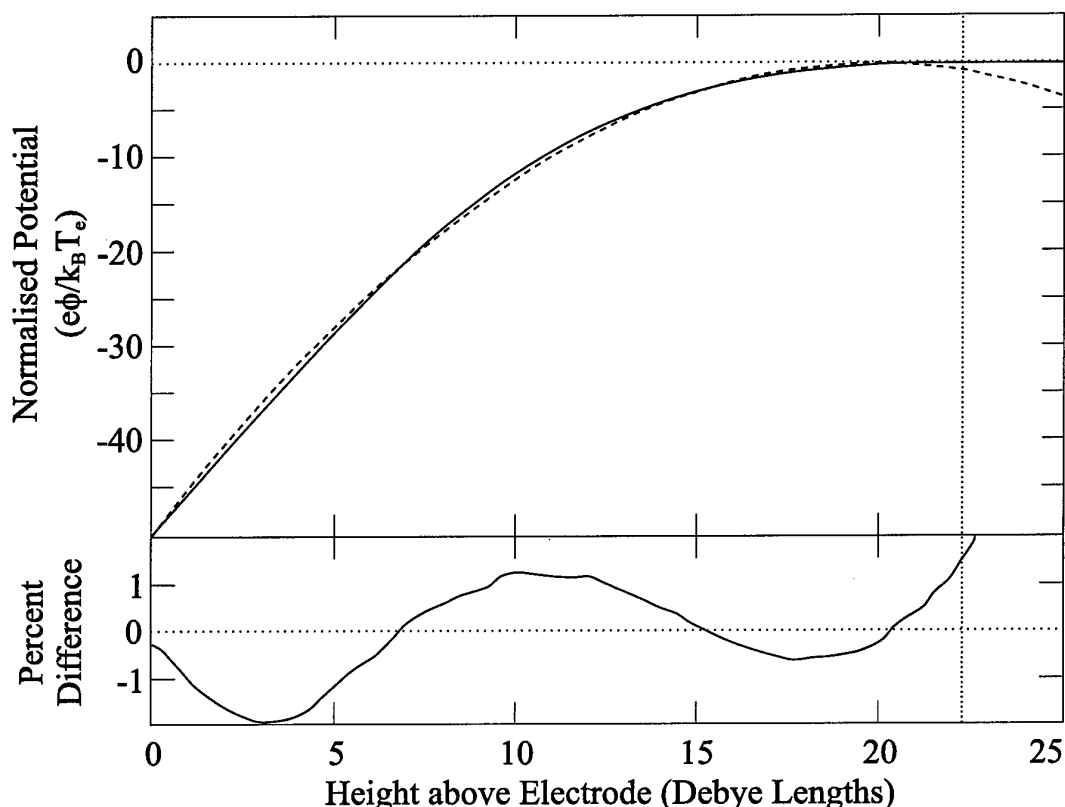
Figure 41: Parabolic Approximation to the Model of Nitter [1996]. This figure shows plots of the numerically derived normalised potential (upper plot, solid curve) and the best-fit parabolic approximation (upper plot, dashed curve). The percent difference between the two curves is shown in the lower plot. For this particular parabola, the approximation does not differ by more than 2% of the maximum potential from the numerical curve across the entire sheath. The approximation would be better with better numerical boundary conditions, as discussed in the text.

5.2.2 THE MODEL OF VALENTINI

A very recent RF sheath model has been proposed by Valentini [1999]. One major difference between this model and the model of Nitter is in its relaxation of the assumption that the sheath potential must monotonically decrease from the plasma to the wall. This model is also collisionless, whereas the Nitter model was for a constant collision cross section. Valentini solves Poisson's equation, the ion continuity and transport equations, and the electron transport equation under constraints similar to those of Nitter, obtaining instantaneous results for the potential profile. These results may then be time-averaged to obtain the profile to which the ions (and more massive
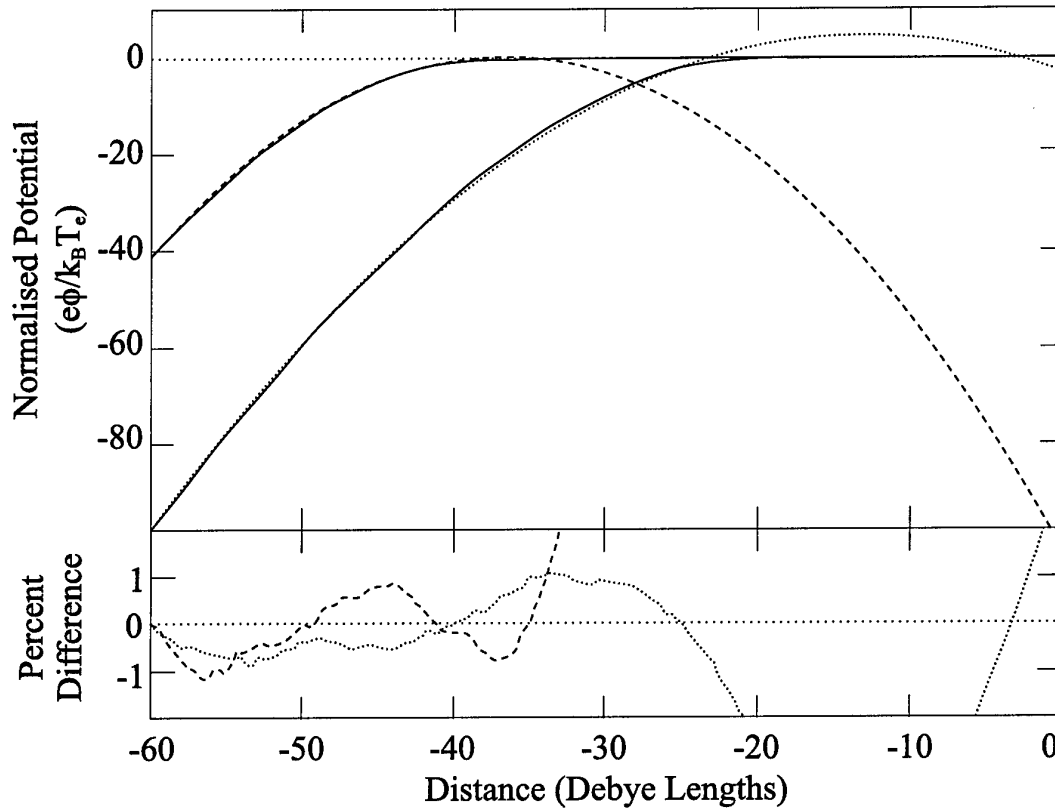
Figure 42: Parabolic Approximation to the Model of Valentini [1999]. This figure shows plots of the numerically derived normalised potentials (upper plot, solid curves) and the best-fit parabolic approximations (upper plot, broken curves) for two different applied RF voltages. The differences between the curve pairs are shown in the lower plot. For these particular parabolas, the approximations do not differ by more than 1% of the maximum potential from the numerical curves across the entire sheath. In order to facilitate direct comparison of potential diagrams throughout this thesis, mirror images of the abscissa and ordinates of the numerical plot from the original paper are shown in this plot.

charged particles such as dust) will respond. Figure 42 shows the results of Valentini

(see his Figure 1 for comparison) for two values of the driving RF amplitude. In each

case, parabolas closely approximate the potential.

5.2.3 THE MODEL OF TOMME

As a final example of the parabolic nature of the time-averaged potential in the

sheath, we re-examine the model developed in the previous chapter of this thesis. The

potential functions for various times in the RF cycle, as well as the time-averaged

potential function, are shown in Figure 43. It is interesting to note that at no individual
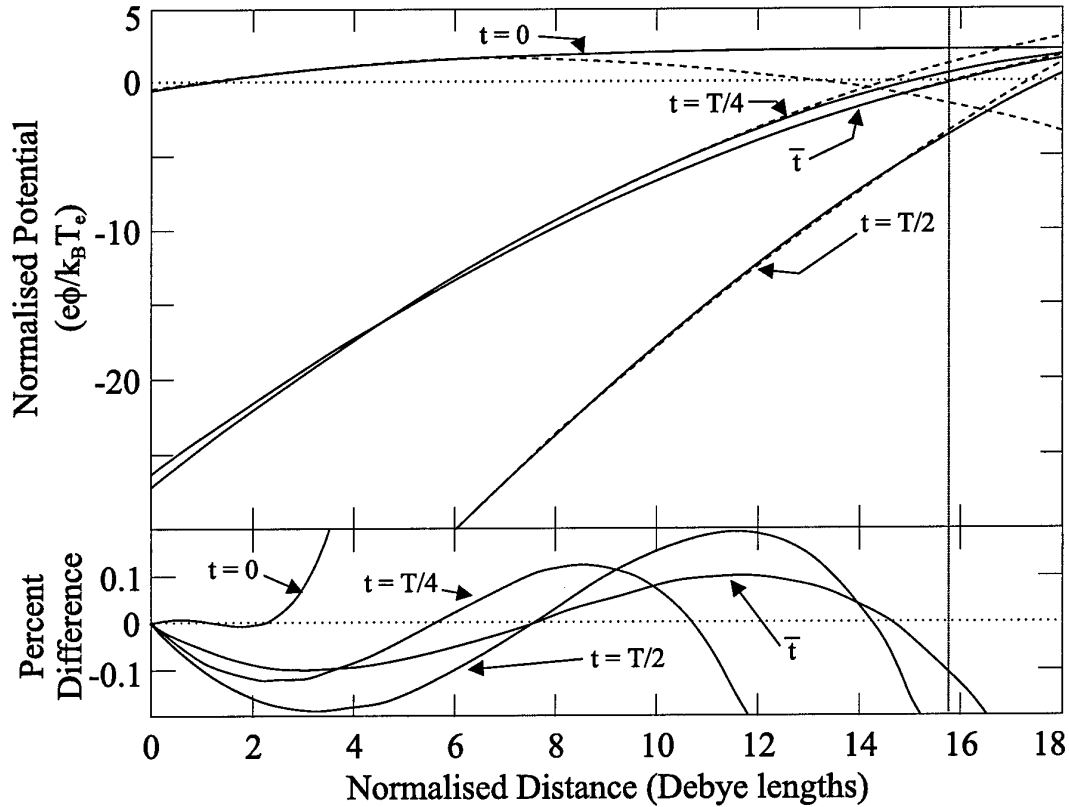
Figure 43: Parabolic Approximation to the Model of Tomme. This figure shows a plot of potentials from the model developed for this thesis (upper plot, solid curves) and the best-fit parabolic approximations (upper plot, dashed curves). The differences between the curves are shown in the lower plot. As can be readily seen, a parabola much better fits the time-averaged plot across the whole of the sheath than do the instantaneous plots. For these particular conditions, the approximation to the time-averaged plot does not differ by more than 0.1% of the maximum potential from the numerical curve across the entire sheath.

time is the potential strictly parabolic. However, the time averaging of these non-parabolic curves yields a strikingly parabolic form. This claim is more readily apparent in Figure 44, a plot of the spatial variation of the electric field. In this figure, it is easy to see that only the time-averaged field is linear over almost the entire sheath; at other times the curvature of the sheath field is distinctly positive or negative, and any linear regions are of much smaller spatial extent. Also note that the parabolic fit now extends well past the sheath edge, in distinct contrast to the model of Nitter, where the fit diverged rapidly as the sheath edge was approached. The improved parabolic fit is a
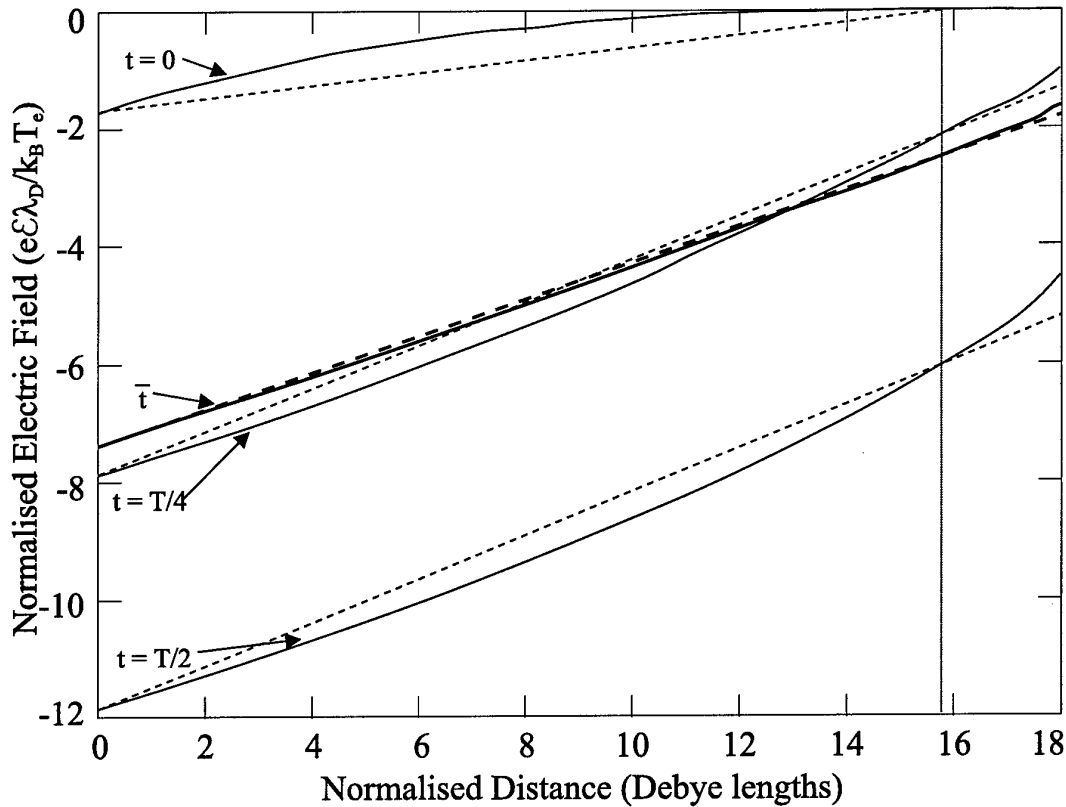
Figure 44: Linear Approximation to the Model of Tomme. This figure shows a plot of electric fields from the model developed for this thesis (solid curves) and linear approximations across the sheath (dashed curves). It is easy to see that the field is almost completely linear for the time averaged case, while the instantaneous cases each have curvatures ranging from distinctly negative for t=0 to distinctly positive for t=T/2. The linear form of the time-averaged electric field corresponds to a highly parabolic form for the time-averaged potential.

result of imposing the more physically realistic boundary conditions developed in the

previous chapter.

The conclusion to be drawn from this chapter is that for a wide variety of

plasmas, both DC and RF, from collision-dominated to collisionless, the potential

profile near the wall may be closely approximated by a parabola. The approximations,

usually valid to within a few percent across the entire sheath, are good enough that

discrepancies between the parabolas and the numerical results are experimentally

insignificant. The recognition of this common, simplified form of the potential,

common to a large number of existing models, has apparently gone unnoticed in the

literature until this thesis. Thus, in many fields related to work in the plasma sheath,

experimentalists may now rely on their own simplified sheath models without the need

to consult their local numerical modeller for advice. Simple experimental

measurements of a few boundary conditions are sufficient to fix the form of the sheath

potential with suitable accuracy. Some of the experimental work presented in the

following chapters will rely on just such a parabolic approximation.

Now that theory behind harmonic dust oscillations, dust drag, and dust charge

have been discussed and the parabolic results from the model of the collisional RF

sheath developed for this thesis have been shown to be general, it is time to turn to a

description of experiments and experimental results.

Note: A substantial portion of this chapter has been published in Plasma Sources: Science and Technology 9(2) (2000) 87-96. Appendix B contains a copy of that paper.

6. DUST OSCILLATION EXPERIMENTS

The chief experimental thrust of this thesis is the observation and characterisation of the oscillations of dust particles as they are introduced into a plasma chamber. The initial impetus for this research was a request from the United Kingdom Atomic Energy Authority (UKAEA) to our group to study methods of dust removal from the Joint European Torus (JET) tokamak. Our group was tasked to study not only methods of moving suspended dust, a subject in which we already possessed considerable expertise, but with actually getting the dust suspended as well. The JET reactor produces several kilograms of toxic, radioactive dust each year [Piet *et al.*, 1997]. This dust accumulates primarily on the diverter plates at the bottom of the reactor, settling out between periods of active plasmas in the reactor. Our task was to see if the dust could be re-suspended in a weak plasma and then moved to a collection area for disposal.

By mounting a small solenoid plunger directly below the bottom electrode of our plasma reactor, we demonstrated the feasibility of re-levitation of dust through a purely mechanical "thumping" of the electrode. During this demonstration, it was noted that at some pressures the dust appeared to oscillate before settling down at an
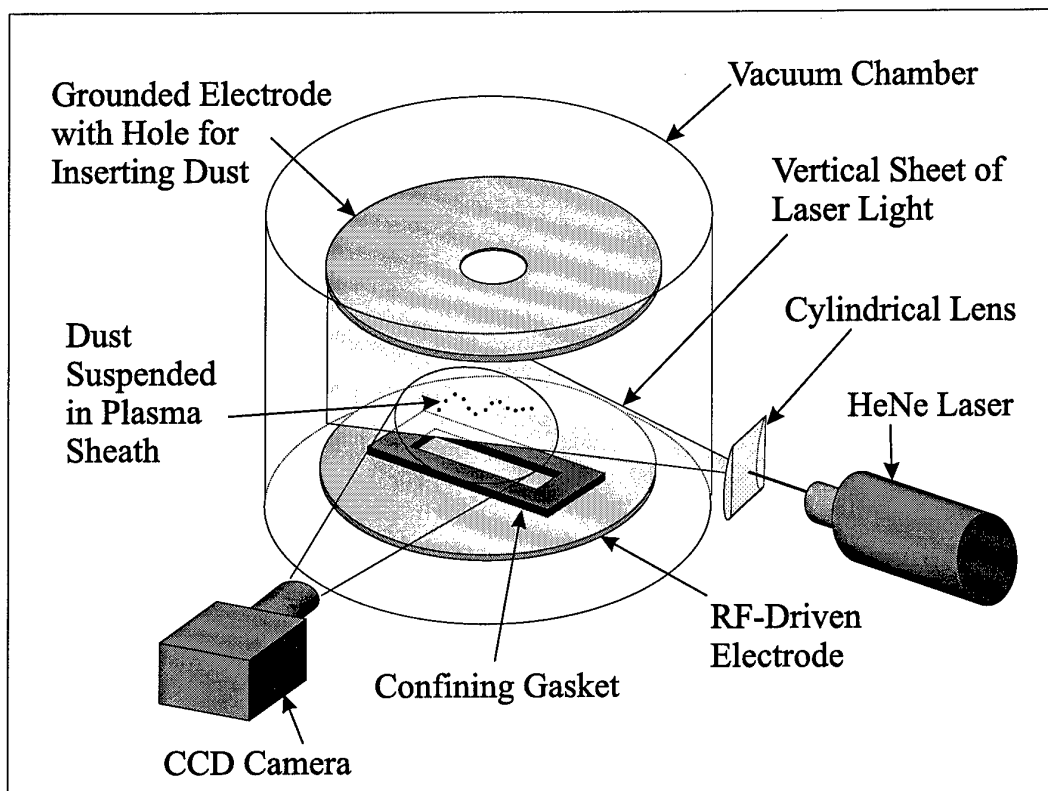
Figure 45: Experimental Set-up. The set-up is described in detail in the text.

equilibrium height. It was quickly theorised that the dust must be moving in some sort

of potential well formed by the sum of gravitational and electrostatic potentials, among

others. The nature of this potential well soon became a major topic of interest within

this research group.

6.1 EXPERIMENTAL APPARATUS AND PROCEDURE

The experimental set-up is shown in Figure 45. It is similar to that used by

most other contemporary dust oscillation researchers. The vacuum chamber had

internal diameter and height of 28 cm and 13 cm, respectively. Glass windows in the

top and around the sides of the chamber allowed visual observation of internal

conditions.

Within the chamber were two 18 cm diameter circular electrodes. The upper electrode was grounded while a matched 13.56 MHz RF voltage was applied to the lower electrode. The spacing between the electrodes was adjustable, and it was set at 4.0 cm for these experiments. The upper electrode had a central 3 cm hole cut in it to allow for dust insertion and observation. It must be noted that for the plasma parameters used in these experiments, this electrode configuration resulted in a rather asymmetric situation. The plasma was not only strongly influenced by the potentials on the electrodes, but by the grounded chamber as well, which made the effective size of the driven electrode much smaller than the grounded surfaces. This asymmetry resulted in most of the RF potential appearing across the driven sheath [Salem and Loiseau, 1996].

The presence of the hole in the upper electrode also resulted in an abnormality in the electron distribution below it. Langmuir probe measurements indicated that below the hole there existed a high-temperature beam of electrons (about 10eV) in addition to the 2-4eV distributions present in the remainder of the chamber. The presence of this beam could possibly cause dust charges measured with the technique to be described later to be slightly high, but it is estimated that this effect will be no more than about 10%, well within the range of the remainder of the experimental error. Subsequent experiments could use a mesh electrode to avoid this problem.

A low-power (30 mW) HeNe laser illuminated the dust in the chamber. For this experiment, the laser was spread into a vertical fan through a combination of cylindrical and spherical lenses. A small copper gasket was placed on the lower electrode to form a small potential well that localised the dust in the central region of

the chamber. The dimensions of this gasket were varied with the needs of the experiment. For this particular experiment, a rectangular gasket having dimensions 2.5 x 10.0 x 0.2 cm, with a 0.5 x 8.0 cm slit removed from its centre was used. The high aspect ratio of the slit confined the dust to the region illuminated with the laser, but allowed the dust to spread out along the laser beam, minimising the effects of forces between particles. The laser fan was approximately 1 mm thick across the width of the gasket. A high-speed (up to 12,000 fps), image-intensifying charge-coupled device (CCD) camera on loan from the Engineering and Physical Sciences Research Council (EPSRC) was employed to record the dust trajectories. The camera was fitted with a macro lens and a bandpass filter to eliminate background light from the plasma emission.

Dust was inserted into the plasma through a glass dust-dropper positioned above the hole in the upper electrode (the dropper is not shown in Figure 45). The dust-dropper had a small vessel at its end in which the dust was placed. The vessel was open on the top and had a small hole covered with extremely fine mesh at the bottom. The dropper extended through a Wilson-seal in the wall of the vacuum chamber and was tapped gently, causing dust to fall into the chamber. The dust used here was spherical melamine formaldehyde (ρ = 1514 kg/m^3), a dielectric polymer, of a variety of individual sizes ranging between approximately 1 and 7 microns in radius. The spheres were supposedly quite monodispersive, having a quoted radius variation of less than about 0.1%. However, it was suspected that the manufacturer, MicroParticles GmbH. of Berlin, Germany, exercised less quality control on their product than one would have preferred. The reasons for these suspicions will be discussed later in this chapter.

To perform the experiment, the dropper was loaded with a specific radius dust, inserted into the chamber, and the chamber was evacuated to high vacuum. The chamber was then flushed with argon gas, and the evacuation was repeated. Argon was then allowed to enter the chamber until the desired operating pressure was attained. A plasma was produced by applying a 13.56 MHz RF signal to the lower electrode. Sufficient time was allowed to elapse so that the temperature of the electrodes could stabilise, and then very small numbers of dust particles (< 10) were dropped through the hole in the upper electrode into the plasma.

Dust trajectories were monitored via the CCD display and recorded digitally directly to a computer. Plasma parameters were also recorded during the dust oscillations. Following a successful data collection, the chamber was immediately opened and an image was taken of a precision ruler placed on the lower electrode in the plane of the dust oscillation. This step was important for two reasons. First, the chamber did not allow viewing of the dust oscillations at right angles to the plane of oscillation, which introduced a perspective error into the images (level lines did not appear exactly level in the images). Second, as the position of the camera and the location of the confining gasket may have changed between data sets, it was important to establish a pixel-to-millimetre scaling factor for each individual trajectory data set.

In other words, the spatial relationship between the camera and the dust is critical to calibrating the exact height of the dust above the electrode. Any physical movement of the camera or the focus of the lens causes a change in the mapping of pixel locations to physical space. To compensate for deliberate and accidental camera movements during data collection (the experiments occurred over a number of days), a

set of calibration frames were imaged for each data set collected. When it was determined that a "good" data set had indeed been captured, the system was immediately depressurised, care being taken not to touch the camera at all. (A good data set was one in which the trajectory of a single dust particle could be followed for a number of oscillations where it did not interact with other dust particles.) The chamber cover (attached to the upper electrode) was then removed, the ruler was placed on the lower electrode in the field of view of the camera, and a few frames were captured. Analysis of the ruler frame was then used to calibrate the spatial scale for that data set. The location of the tick marks on the ruler and their values were noted, corresponding to actual heights above the electrode. The spacing in pixels of these tick marks was then determined, and from that, the pixel-to-millimetre scaling was fixed. From the millimetre values on the ruler scale, the height shift between the bottom of the CCD frame and the actual location of the lower electrode could also be determined.

Once the trajectory and ruler scaling data had been collected and analysed, the series of dust images were analysed on the computer. The digital movies were converted to a series of bitmaps, one bitmap per video frame. The scaling and shift data derived from the ruler image were applied first. Next, a frame late in the data set in which the dust had settled to its equilibrium height was analysed. Custom software developed in-house by D.A. Law was used to determine the position and position error of dust particles in the digital images. The cursor was manually positioned over the bright image of an individual particle and the software then fit a Gaussian surface to the grey-scale image brightness. The position error from the video frames was estimated by the method of Crocker and Greer [1996] to be less than 10 μm. Figure 46 shows an example of a data frame and a fit from a localised particle image. By locating the
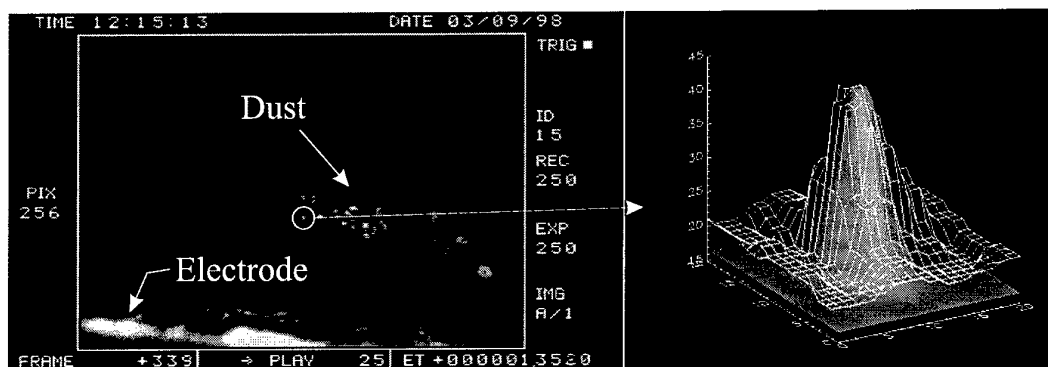
Figure 46: Determination of Dust Position and Position Error. The left frame shows a typical image frame (containing much more dust than was present in the experiments presented here). The horizontal electrode is visible at the bottom of the frame, illustrating the perspective problem discussed in the text. The right frame shows the fit when the indicated dust particle was selected with the mouse. The 256-bit grey-scale is plotted vs. two-dimensional position. The Gaussian fit to the data is also shown.

positions of several dust particles suspended at their equilibrium height and calculating

a best-fit line through them, the perspective error could be corrected. Thus, analysis of

a single data frame and the ruler frame was used to correct for the scale and perspective

variations in the data.

During the experiments, the dust oscillated above the confining gasket. As the

central region of the confining gasket was quite small, the effect of its perturbation on

the sheath had to be taken into account. To do this, the equilibrium height of each of

the dust particles was measured while suspended above the small gasket, and then

measured again while suspended above a large, washer-shaped gasket (inside diameter:

10 cm). The size of the second gasket was chosen to be large enough that its

perturbation of the sheath in the region where the dust was suspended would be

insignificant. The height at which the dust suspended above the large gasket was taken

to be the actual equilibrium height. The difference in equilibrium heights between the

experiments involving the different gaskets was then subtracted from the equilibrium

height from the oscillation data frames. This height, corrected for the perturbation of

the small dimension gasket, was used in the calculations.

Each data set consisted of the images of a small number (<10) of dust particles undergoing simultaneous oscillation. Dust trajectories were analysed by identifying a particle that underwent a number of oscillations with only minor interaction with its neighbours. Once that particle was identified, its position was manually tracked over a number of frames (~100) using the position-locating technique previously described. The position and position error data was then corrected for scale, perspective, and gasket perturbation, and a plot of height-above-electrode vs. time was generated.

The trajectories were quite distinctive. At higher pressures (~10 Pa), the dust almost immediately settled at an equilibrium height. When the pressure was lowered (~5 Pa), however, the dust took much longer to stop moving, its trajectory appearing to oscillate a number of times around the equilibrium height. The trajectories were quite dependent upon mass as well, being less damped for particles that were more massive.

6.2 COMPARISON WITH EXPERIMENTS FROM THE LITERATURE

This experimental technique differs from previously cited dust oscillation techniques in several respects. Those methods typically use some induced or natural driving force to cause resonant oscillation. This technique is much simpler, although its accuracy for very low-mass particles diminishes due to the very high damping rate for these conditions.

The self-bias of the driven electrode was not varied, nor were any variable-bias external probes placed near the dust, as was done in some experiments [Melzer *et al.*, 1994; Trottenberg *et al.*, 1995; Kortshagen *et al.*, 1996; Law *et al.*, 1999]. This allowed us to base the results on a stable sheath with a potential profile that is essentially time-

independent on the scale of relevant dust charging times. There was no need to account

for the non-zero electrode currents that would have naturally flowed during induced,

slow oscillations of the self-bias. Thus, this method does not involve any external sheath

perturbations, the effects of which would tend to greatly complicate any charge analysis.

The benefit of resonant analysis used in other techniques [Melzer *et al.*, 1994;

Trottenberg *et al.*, 1995; Kortshagen *et al.*, 1996; Homann *et al.*, 1999; Law *et al.*, 1999;

Nunomura *et al.*, 1999] would seem to be quite apparent, especially for low-mass

particles and/or high pressures where the damping is so high that very few oscillations

may be observed by the undriven method. This would seem to be especially true for

relatively non-intrusive methods that utilise lasers to excite the resonance without

disturbing the sheath. However, with all of these resonant methods, there exists the

possibility of inadvertently overdriving the resonant oscillations to the point where

charge fluctuations on the dust particle become significant enough to spoil the harmonic

nature of the potential well.

The issue of charge fluctuation and its effect on the trajectories of dust in

plasmas and sheaths has been discussed in the literature, and was also previously

touched upon in the literature review chapter of this thesis. Havnes *et al.* [1992a] first

examined the fluctuations of the charge on the particles composing planetary dust rings.

They showed that the finite charging time of the particle would have a *damping* effect

on spatial oscillations of these particles. This theory was later expanded and

strengthened [Melandsø, 1992; Nitter and Havnes, 1992; Melandsø *et al.*, 1993].

Interestingly, Nunomura *et al.* [1999] propose this same mechanism as the *amplifying*

factor for spontaneous dust oscillations they observe in DC plasmas. The apparent

conflict between these two theories has not, as yet, been resolved. However, for the purposes of this thesis, one only needs to know the relative magnitude of the charge fluctuation in order to evaluate its effect on the theoretical potential well.

Nitter *et al.* [1994] show that the charge fluctuation may be ignored in the cases of small amplitude oscillations or long charging times. Just how small or long these quantities may be while remaining insignificant is left nebulous. Goree [1994] and Nitter [1996] show that for dust under similar conditions to that used in this experiment, the charging time is on the order of a few microseconds. Oscillations observed during this experiment had frequencies on the order of tens of Hertz, meaning that it did not meet the "long charging time" criterion mentioned above. Nunomura *et al.* [1999] calculate that the charge fluctuation on their spontaneous dust oscillations is on the order of a few percent. Whether this figure may be considered to be due to "small amplitude oscillations" is not discussed.

Charge fluctuation has been ignored in this treatment. This is because the experimental oscillations observed in this laboratory were determined to be of "small amplitude." This fact will be demonstrated by the results of these experiments, which will show the oscillations to be extremely well modelled by harmonic equations, implying that the charge fluctuations are either very small or average out during the oscillation. However, as the oscillation amplitude increases past a critical point, the harmonic nature of the potential breaks down rapidly, invalidating techniques that rely on harmonic equations to get charge from the now-anharmonic resonance frequency. This critical amplitude has been found to be typically about 10-20% of the sheath width, based on results presented later in this thesis. At the sampling rates used in some of the

cited experiments [Melzer *et al.*, 1994; Trottenberg *et al.*, 1995; Kortshagen *et al.*, 1996; Homann *et al.*, 1999], it would seem to be difficult to determine whether the oscillations were indeed harmonic or merely periodic. This shortcoming precludes determination of the significance of charge fluctuation in those trials.

Great efforts were made in this experiment to eliminate extraneous forces acting on the oscillating dust. Several of the cited techniques [Melzer *et al.*, 1994; Trottenberg *et al.*, 1995; Kortshagen *et al.*, 1996; Homann *et al.*, 1999; Nunomura *et al.*, 1999] involve the resonant excitation of dust in a crystal lattice, and then use harmonic equations to find the charge on the excited dust. That analysis fails to take into account the strong interaction potentials between the large numbers of dust particles in the lattice, leading to questionable results due to the non-harmonic form of the physical potential. The effects of the interaction forces have been previously examined in the literature review chapter of this thesis. The analysis presented here involves very small numbers of particles inserted into the sheath, and only particles that are observed to be relatively free of interaction with other particles are used for the charge analysis.

The technique in this experiment measures oscillations that occur in the vertical plane. Techniques that utilise horizontal oscillations [Konopka *et al.*, 1997; Morfill *et al.*, 1999; Konopka *et al.*, 2000] generally only determine the shape of the confining potential well of the gasket and the interaction potential between dust particles. While these techniques can derive a value for the dust charge, they give little information on the vertical potential profile through significant fractions of the sheath.

Some previous techniques have also relied upon estimates of the charged particle densities from such sources as extrapolations of sine-shaped ion density profiles

into the sheath [Melzer et al., 1994; Homann et al., 1999], assumptions that the sheath

is a perfect rectifier [Kortshagen et al., 1996], or Child [1911]-Langmuir [1913] ion

profiles [Nunomura et al., 1999]. The technique of this thesis instead relies on the

previously discussed assumption of a harmonic sheath potential profile.

6.3 EXPERIMENTAL RESULTS

The solution to the equation of motion [equation (21)] is

$$(55) \qquad z(t) = \exp\left(-\frac{t}{2\tau}\right)\left[z(0)\cos(\omega t) + \frac{\dot{z}(0) + z(0)/2\tau}{\omega}\sin(\omega t)\right] + z_{eq},$$

where t is time and ω is the observed oscillation frequency. Thus, the curve fitting

routine used the five parameters $z(0)$, $\dot{z}(0)$, z_{eq}, ω, and $(2\tau)^{-1}$ to fit damped harmonic

theory [equation (55)] to the data. Table 7 lists the plasma parameters and relevant

curve-fitting parameters for all the data sets. Six typical plots of the experimental data

and the associated curve fits from damped harmonic theory are shown in Figure 47.

The plots show combinations of three different radii dust particles taken at two different

pressures. The decrease in the equilibrium height with an increase in pressure and/or

mass is apparent, as is the decrease in the damping rate as the pressure is decreased

and/or the mass is increased. The difference in oscillation frequency between the small

and large particles is also visually apparent.

In many of the trajectories, the average error between the data points and the

theoretical fit over a large portion of the plot is less than the width of a pixel (1 pixel $\cong$

30 μm) from a data image frame. It must also be emphasised that the theoretical

Dust Radius a (μm)	Chamber Pressure P (Pa)	Equilibrium Height z_{eq} (mm)	Oscillation Frequency ω (rad/sec)	Decay Constant $(2\tau)^{-1}$ (sec^{-1})	Dust Mass $4\pi r^3\rho/3$ (10^{-13} kg)	Restoring Constant equation (22) (10^{-9} kg/sec^2)	Nominal Sheath Edge equation (28) (mm)	Dust Charge equation (30) (1000e)
1.01 ± 0.02	6.67 ± 0.13	8.97 ± 0.01	125 ± 2	27.5 ± 0.9	0.065 ± 0.004	0.11 ± 0.01	9.6 ± 0.1	0.2± 0.1
1.52 ± 0.04	6.67 ± 0.13	9.17 ± 0.01	153 ± 2	8.5 ± 0.9	0.22 ± 0.02	0.52 ± 0.04	9.6 ± 0.1	0.8 ± 0.5
2.2 ± 0.1	6.67 ± 0.13	9.34 ± 0.01	192 ± 2	9.9 ± 0.9	0.67 ± 0.09	2.5 ± 0.3	9.6 ± 0.1	3.3 ± 2.1
3.46 ± 0.04	6.67 ± 0.13	8.93 ± 0.01	160 ± 2	5.1 ± 0.9	2.62 ± 0.09	6.7 ± 0.3	9.3 ± 0.1	4.8 ± 3.1
4.86 ± 0.03	6.67 ± 0.13	7.60 ± 0.01	85.7 ± 2	5.0 ± 0.9	7.2 ± 0.1	5.4 ± 0.3	8.9 ± 0.1	6.9 ± 4.1
6.85 ± 0.1	6.67 ± 0.13	6.95 ± 0.01	67.5 ± 2	3.5 ± 0.9	20.3 ± 0.9	9.3 ± 0.7	9.1 ± 0.2	18.6 ± 6.4
6.95 ± 0.1	6.67 ± 0.13	7.61 ± 0.01	69.0 ± 2	2.9 ± 0.9	21.2 ± 0.9	10.1 ± 0.7	9.7 ± 0.2	31.7 ± 9.9
1.01 ± 0.02	13.33 ± 0.13	8.68 ± 0.01	140 ± 2	51 ± 0.9	0.065 ± 0.004	0.14 ± 0.01	9.1 ± 0.1	0.3 ± 0.2
1.52 ± 0.04	13.33 ± 0.13	8.29 ± 0.01	138 ± 2	19 ± 0.9	0.22 ± 0.02	0.43 ± 0.04	8.8 ± 0.1	0.4 ± 0.2
2.2 ± 0.1	13.33 ± 0.13	8.65 ± 0.01	130 ± 2	24 ± 0.9	0.67 ± 0.09	1.2 ± 0.2	9.2 ± 0.1	3.7 ± 2.3
3.46 ± 0.04	13.33 ± 0.13	7.83 ± 0.01	74 ± 2	11 ± 0.9	2.62 ± 0.09	1.5 ± 0.1	9.6 ± 0.1	7.5 ± 3.3
4.86 ± 0.03	13.33 ± 0.13	7.84 ± 0.01	95 ± 2	11 ± 0.9	7.2 ± 0.1	6.6 ± 0.3	8.9 ± 0.1	12.9 ± 5.6
6.85 ± 0.1	13.33 ± 0.13	6.95 ± 0.01	59 ± 2	5.2 ± 0.9	20.3 ± 0.9	7.1 ± 0.6	9.7 ± 0.3	34.6 ± 9.6
6.95 ± 0.1	13.33 ± 0.13	6.58 ± 0.01	56 ± 2	5.4 ± 0.9	21.2 ± 0.9	6.7 ± .06	9.7 ± 0.3	29.6 ± 9.3

Table 7: Experimental Conditions and Curve Fitting Parameters. Data in the first two columns are the controlled experimental conditions. Data in the central three columns are the resulting curve-fitting parameters (errors for oscillation frequencies and decay constants are estimated). Data in the last four columns are derived from data in the other columns using the indicated equations. For all cases the electrode spacing was 40.0 mm, the RF amplitude was 96.4 V, the RF frequency was 13.56 MHz, the dust density was 1510 kg m^{-3}, and the working gas was argon. For the high-pressure case, $k_B T_e$ and n_0 were 3.9eV and 2.4×10^{15} m^{-3}, respectively, while at low pressure they were 3.7eV and 1.7×10^{15} m^{-3}. Plasma parameters were determined by Langmuir probe measurements at the centre of the plasma. The visually-determined sheath widths were 9.4 ± 0.25 mm and 8.5 ± 0.25 mm for 6.67 Pa and 13.33 Pa, respectively.

fit to the data is very good for oscillations that approach 20% of the sheath thickness. This amplitude range is much better than one would normally expect for a small-amplitude match between an arbitrary, non-parabolic potential well and a harmonic approximation. The close fits between theory and experiment over these large amplitude ranges tend to support the hypothesis that the electric potential is indeed very nearly harmonic throughout the sheath.

As is evident from the increasingly good theoretical fit in each of the plots, the theoretical equation was fit from right to left (backwards in time). This choice of initial fitting point was selected because during small amplitude oscillations the constant charge and parabolic potential approximations would be the most applicable and the fit would be expected to be better. It is quite apparent from the figure that as oscillation amplitude increases past a certain point, the quality of the fit drops markedly. This is due in some part to the fact that the trajectories of the higher amplitude oscillations are
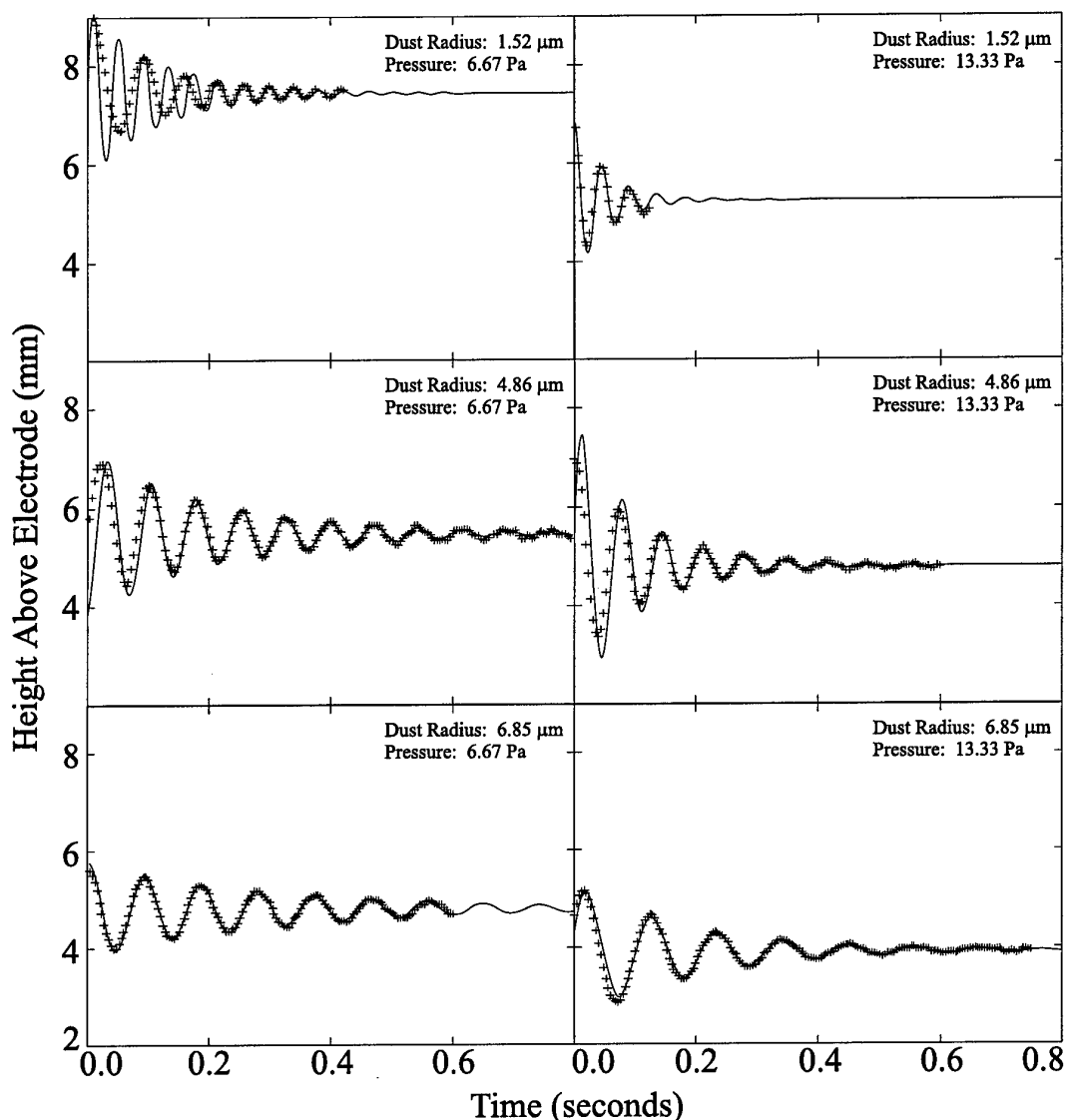
Figure 47: Dust Oscillation Data and Harmonic Theory. These six plots show dust trajectories obtained as described in the text. The scales and origins are the same for all six plots to facilitate direct comparison. The solid lines are damped harmonic theoretical curves from equation (55) using the parameters shown in Table 7. Error bars, on the order of 10 μm, are too small to be shown at this scale. Each column of plots is for the same pressure, while each row of plots is for the same mass dust particle. The other experimental parameters are discussed in the text.

not exclusively in the plasma sheath. While the dust continues to oscillate between the plasma/presheath and sheath regions, the potential well it sees is not even approximately harmonic. As soon as the dust oscillations become damped enough to confine it exclusively to the sheath, the theoretical fit becomes much better. Another reason for the discrepancy between theory and experiment is the assumption of constant charge on

Chamber Pressure P (Pa)	Decay Constant $(2\tau)^{-1}$ (sec^{-1})	Drag Coefficient γ [equation (24)] (10^{-12} kg/sec^2)	
		3.46 µm dust radius	7.45 µm dust radius
66.67 ± 0.13	45.6 ± 0.9	24.0 ± 7.65	239 ± 41.7
33.33 ± 0.13	32.8 ± 0.9	17.2 ± 4.57	172 ± 29.9
13.33 ± 0.13	11.5 ± 0.9	6.04 ± 2.07	60.3 ± 19.0
10.00 ± 0.013	9.19 ± 0.9	4.83 ± 2.01	48.2 ± 19.0
6.67 ± 0.013	10.8 ± 0.9	5.67 ± 2.05	56.6 ± 19.0
3.33 ± 0.13	5.31 ± 0.9	2.79 ± 1.93	27.8 ± 18.9

Table 8: Data for Determination of the Drag Coefficient. Data in the first column are the controlled experimental conditions. Data in the second column are the measured decay constants (errors for the decay constants are estimated). Data in the last two columns are the derived drag coefficients using two different radii for the dust particles: the radius specified by the manufacturer and the radius observed using an electron microscope. Other experimental conditions are as described in the caption for Table 7.

the dust particle. As previously discussed, the charging time of a dust particle has been shown to be on the order of 10^{-6} sec [Goree, 1994; Nitter, 1996; Trottenberg *et al.*, 1997], much faster than the oscillation time scale of 10^{-2} sec, so the dust charge may vary with position during an oscillation. The larger the oscillation, the worse the constant-charge assumption becomes, adding to the fit/data mismatch. Less massive dust particles, oscillating nearer the sheath edge, would seem to be affected more by both of these problems. They oscillate nearer the sheath edge where the harmonic potential assumption breaks down. They also have smaller charges, making even small charge changes during oscillations significant. These effects are apparent in Figure 47, where the amplitude at which theory and experiment break down is much smaller for less massive particles.

As preliminary measures of agreement between theory and experiment, the experimental results were compared with standard drag laws and the predicted sheath width from the harmonic theory. To determine the drag law on small spheres in a plasma sheath, the fitting parameter $(2\tau)^{-1}$ along with equation (23) was used to calculate the drag constant, γ. Initial analysis of experimental results gave results that did not agree well with standard drag theory. For most of the experiments presented in
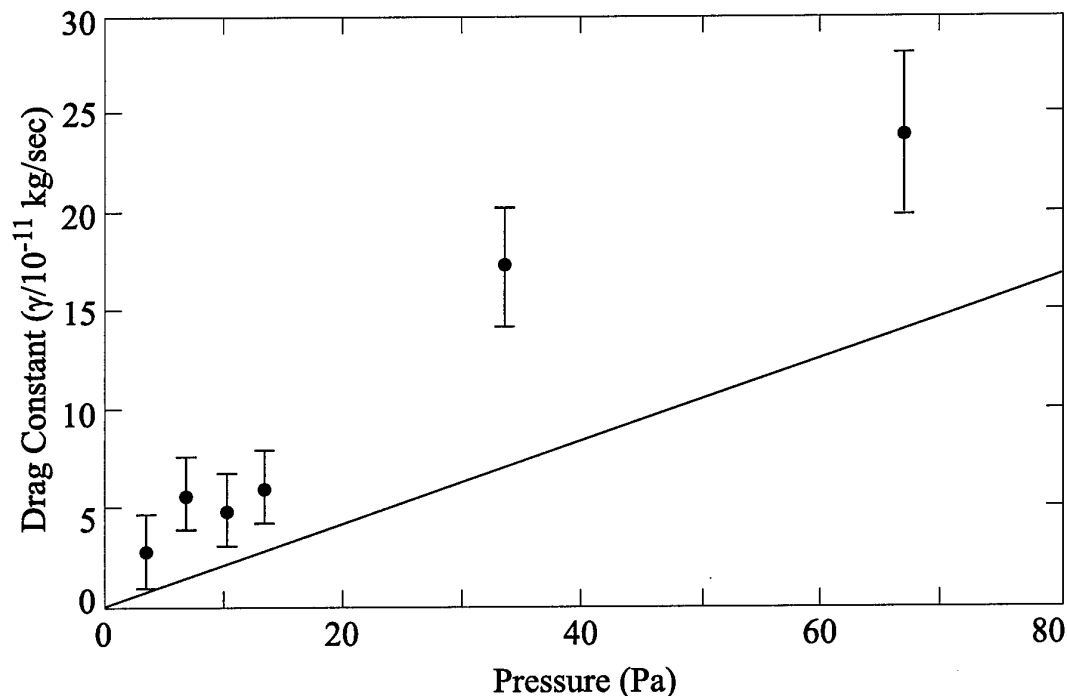
Figure 48: Drag Constant vs. Pressure (Incorrect). This plot shows the drag constant obtained from data in Table 8, using the incorrect dust radius of 7.45 mm supplied by the manufacturer. The solid line is the diffuse Epstein drag law obtained from equation (24). The drag constant data is roughly linear, but with a slope approximately twice that of the theoretical curve.

this chapter, one of two pressures was set and the mass of the dust was varied,

producing the data in Table 7. However, for this initial drag analysis, oscillations of

dust particles of a particular mass were examined at a variety of plasma pressures. Data

for these experiments are given in Table 8. Figure 48 shows the initial results for the

drag analysis along with an Epstein [1924] drag curve. It can be seen that the drag

constant data is fairly linear in pressure, as would be expected from theory (which is

linear in number density), but the slope of the line differs from theory by a factor of

approximately 2.5. Discussion of these results with other researchers [Konopka and

Morfill, 1998] revealed that they were finding similar results, a surprising circumstance,

considering that Epstein theory has been the standard for over 75 years.

After quite a bit of puzzling on this question, it was decided that the mass of

the dust must not be correct. To test this hypothesis, samples of each dust size were
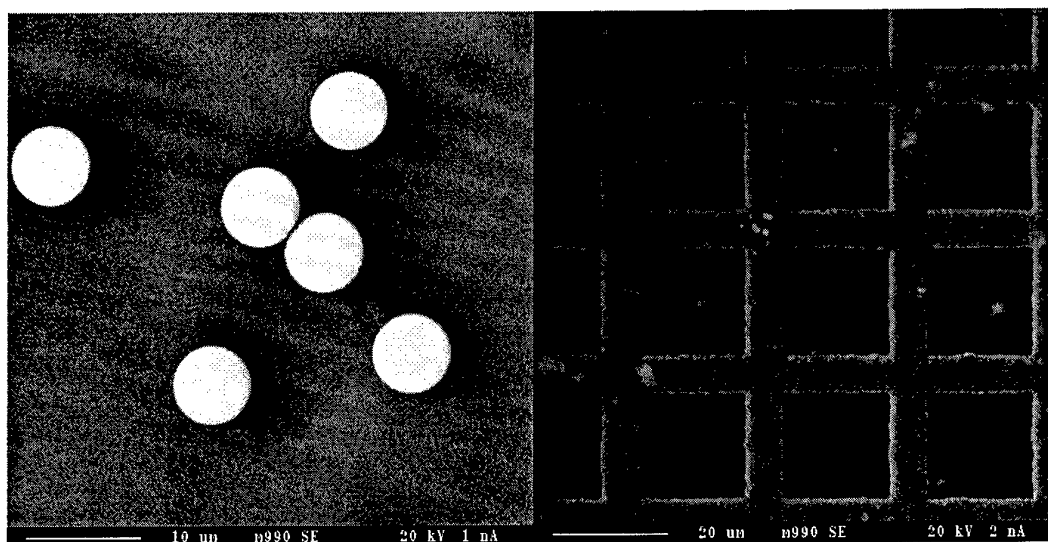
Figure 49: Scanning Electron Microscope Images of the Dust. The left pane of this figure shows a scanning electron microscope image of several dust particles from the vial labelled by the manufacturer as containing 14.9 mm diameter dust. Based on the calibration line in the lower left portion of the frame, it is immediately apparent that the dust is nowhere near that diameter (later analysis of this image and others determined the actual diameter to be 6.92 ± 0.08 mm). The right frame shows an image of the calibration grid used to check the electron microscope. The grid is nominally 20 mm square, which was confirmed by digital analysis of the image to better than 1%.

Dust Diameters as Quoted by the Manufacturer (μm)	Dust Diameters Determined by Electron Microscope Analysis (μm)	Percent Error
1.003 ± 0.053	1.05± 0.03	4.5%
2.03 ± 0.04	2.02 ± 0.03	0.5%
3.25 ± 0.11	3.03 ± 0.08	7.3%
4.74 ± 0.07	4.40 ± 0.10	7.7%
14.90 ± 0.23	6.92 ± 0.08	120%
10.33 ± 0.11	9.72 ± 0.06	6.3%
14.62 ± 0.27	13.7 ± 0.20	6.7%
7.464 ± 0.111	13.9 ± 0.10	46%

Table 9: Quoted and Measured Dust Diameters. This table demonstrates the relatively large discrepancies (compared to the manufacturer's quoted dispersions) between the quoted and observed dust diameters.

prepared and examined under an electron microscope. Comparing the images from these observations to an image of a standard test grid showed that the dust radii quoted by the manufacturer were inaccurate, and in several circumstances, were in error by very large amounts. An example of the test grid image and an image of some of the dust is shown in Figure 49. As can be seen in the figure, the deviations of the dust radii were quite small, but the quoted radii themselves were inaccurate. Table 9 lists the quoted and observed radii and deviations. Once the observed radii were used in the
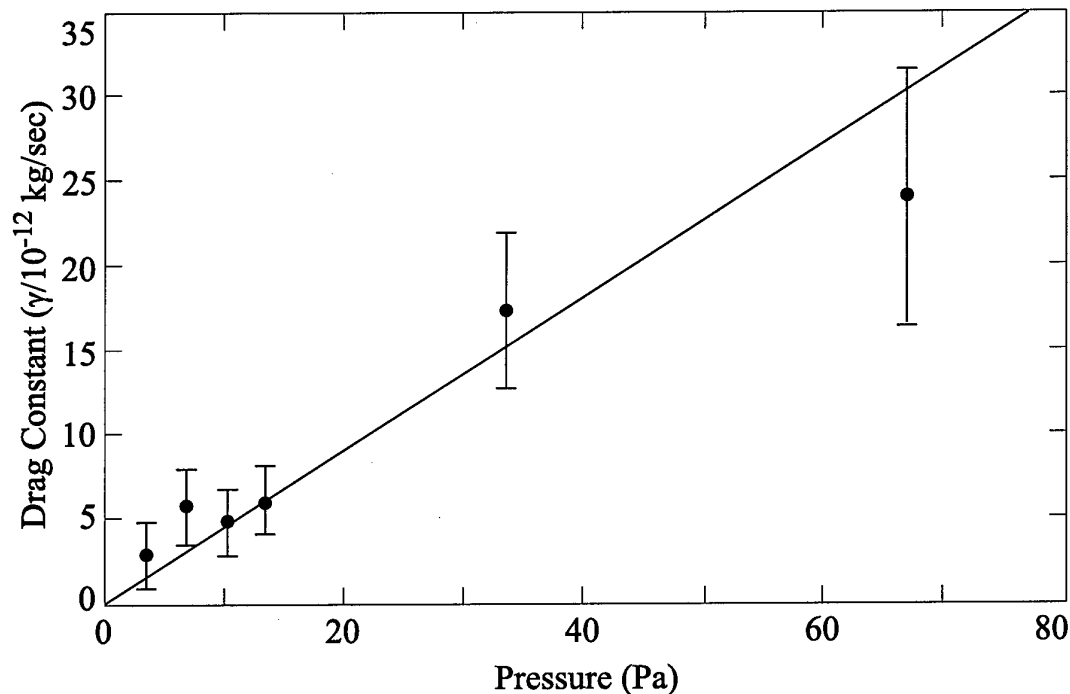
Figure 50: Drag Constant vs. Pressure (Correct). This plot shows the drag constant obtained from data in Table 9, using the dust radius of 3.46 mm obtained from analysis of electron microscope images of the dust. The solid line is the diffuse Epstein drag law obtained from equation (24). The drag constant data is well fit by theory, especially when compared with the plot that used the manufacturer's erroneous radius shown in Figure 48.

calculations, the observed drag agreed with standard theory to within 20%. The experimental results using the corrected dust radii are shown in **Error! Reference source not found.** and Figure 51, along with Epstein drag plots for the same conditions. These results would seem to reconfirm that Epstein diffuse drag is indeed the correct law in the plasma sheath.

As another measure of agreement between theory and experiment, the location of the minimum in the electrical potential energy was calculated from the experimentally determined restoring constants [using κ and equation(28)]. With a negative dust charge, this value would be where the maximum electrical potential would occur, or nominally, where the sheath edge should occur if the potential were globally harmonic. From this calculation (the results of which are presented in Table 7),
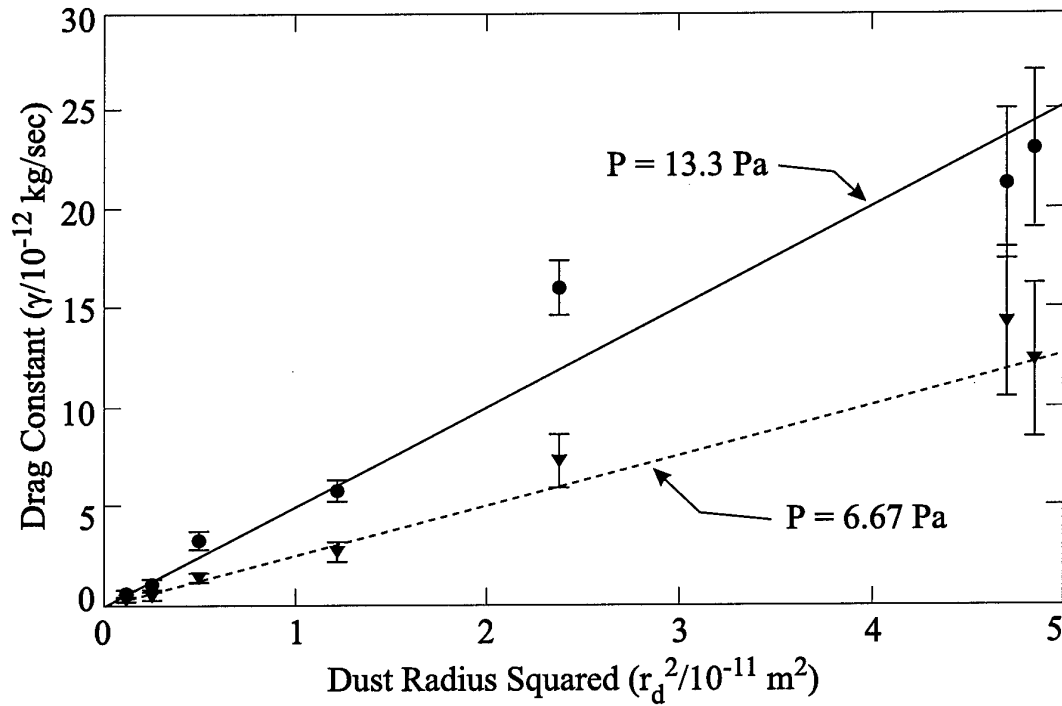
Figure 51: Drag Constant vs. Dust Radius. This plot shows the drag constant obtained from data in Table 7. The solid and dotted lines are the diffuse Epstein drag law obtained from equation (24) for 13.3 Pa and 6.67 Pa, respectively. Circles show data for 13.3 Pa while triangles show data for 6.67 Pa.

theoretical sheath widths of 9.5 ± 0.3 mm (6.67 Pa) and 9.2 ± 0.3 mm (13.33) Pa were obtained, agreeing quite well with the observed widths of 9.4 ± 0.25 and 8.5 ± 0.25 mm, respectively. Again, this agreement tends to support the assumption of a parabolic electric potential within the sheath.

Equation (30) showed that determining the charge on a dust particle at its equilibrium position required knowledge of not only its mass and the restoring constant, but also of the potential difference between two definite points in the sheath. The chapter on numerical sheath models also showed that for a wide variety of plasma parameters, the sheath could be considered to have a parabolic electric field to a high degree of accuracy. Thus, it was decided to model the sheath in this experiment with a simple parabola.

The first step in developing the potential function was to determine the

potential drop across the driven sheath. To determine this drop, a two-sheath model

was assumed

$$(56) \qquad \phi_d = \phi_g + \phi_{sb},$$

where ϕ_d and ϕ_g are the driven and grounded DC sheath potential differences and ϕ_{sb} is

the measured DC self-bias between the grounded and driven electrodes. This model

also requires that the sum of the AC sheath potentials, $\phi_{d,ac}$ and $\phi_{g,ac}$ equals the applied

AC voltage, or

$$(57) \qquad \phi_{ac} = \phi_{d,ac} + \phi_{g,ac}.$$

Calculation of the self-bias voltage developed across an RF-enhanced sheath was

carried out using the standard method [Boschi and Magistrelli, 1963; Braithwaite *et al.*,

1985], for the case of zero DC current flow, providing the link between the AC and DC

sheaths. (Use of this method for calculating the self-bias voltage under collisional

conditions has previously been discussed in the chapter of this thesis on the

development of the numerical sheath model.) Equations (56) and (57) were then

iteratively solved for the DC sheath potential. In this experiment, the applied RF

amplitude was 96.4 V and the self-biases were 56.9 ± 1.5 V (6.67 Pa) and 49.3 ± 1.9 V

(13.33 Pa). Thus, the DC potentials across the driven electrode sheath were 86.3 ± 0.8

V (6.67 Pa) and 83.0 ± 1.0 V (13.33 Pa).

The validity of this voltage division is supported by considering the resulting

ratios of the effective areas of the grounded to driven electrodes. Salem and Loiseau

[1996] have demonstrated experiments that substantiate the much-used power law

relating these ratios,

$$(58) \qquad \frac{\phi_{driven}}{\phi_{grounded}} = \left(\frac{A_{grounded}}{A_{driven}} \right)^n$$

where ϕ and A are the voltage drop across and area of the indicated sheaths,

respectively. Those authors show that, for the pressure regime used in the present

experiment, the exponent in equation (58) should be 2, in accordance with the

theoretical model of Maniv [1988]. Substituting the appropriate voltage values from the

two-sheath model into this equation results in area ratios of 1.7 (6.67 Pa) and 1.5 (13.33

Pa), ratios that are quite reasonable for this experimental set-up.

The boundary conditions for the parabolic sheath model then became: $\phi(0)=$-

86.3 V, $z_{sh}=9.4$ mm, $\phi(z_{sh})=0$ (6.67 Pa); $\phi(0)=-83.0$ V, $z_{sh}=8.5$ mm, $\phi(z_{sh})=0$ (13.33 Pa).

Values for $\mathcal{E}_s$ come from equation (51). The potential functions derived from parabolic

fit to the above boundary conditions were

$$(59) \qquad \phi(z) = -0.906(z - 9.77)^2 + 0.124 \quad (6.67 \text{ Pa}) \text{ and}$$

$$(60) \qquad \phi(z) = -0.985(z - 9.21)^2 + 0.499 \quad (13.33 \text{ Pa}),$$
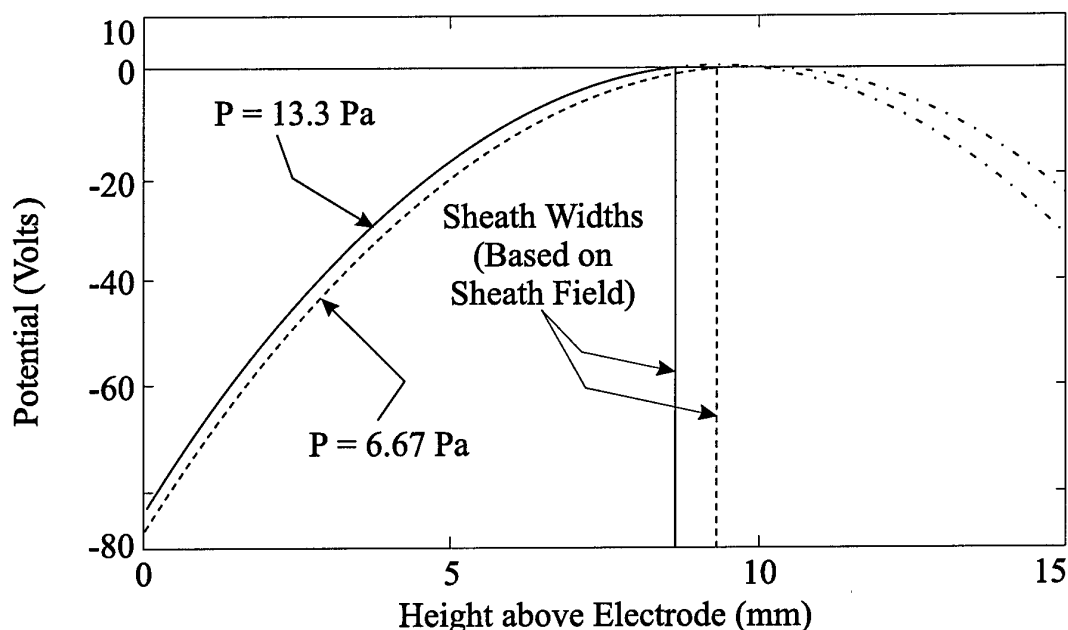
Figure 52: Parabolic Sheaths Used for Charge Determination. This figure shows the parabolas given in equations (59) and (60) that will subsequently be used to determine the charge on the dust particles. The solid and dashed curves show the sheath potentials for 13.3 Pa and 6.67 Pa, respectively. The indicated sheath edges were determined using equation (51). The dash-dotted extensions to these potentials show the harmonic solutions past the sheath edges.

with z in millimetres and $\phi(z)$ in volts. These parabolic sheath potential approximations are plotted in Figure 52. It must be emphasised that the potential functions presented here stem from what are considered to be the most reasonable choices of the boundary conditions from current literature. Should better parabolic boundary conditions be determined at a later date, they may be used with the data in this thesis to provide improved results.

Once the potential functions had been determined, it was a relatively simple procedure to calculate the dust charge. The values for the dust charges for the experimental conditions are given in Table 7, and are in reasonably good order of magnitude agreement with those of a number of previous researchers [Melzer et al., 1994; Trottenberg et al., 1995; Kortshagen et al., 1996; Homann et al., 1999; Law et al., 1999], considering differences in experimental parameters.

The effect of changing the dust radius on the equilibrium charge is fairly complex, as the increased radius not only provides a larger surface area for charged particle impact, but causes the dust to suspend at a lower level in the sheath where the charged particle densities could be markedly changed. To visualise this convoluted effect, equation (30) may be rewritten as a function of dust radius. Assuming a globally harmonic sheath potential, using the Epstein drag law [equation (24)], substituting $(4\pi/3)a^3\rho$ for the dust mass, and employing equations (22), (23), and (30), the following equation for the charge as a function of dust radius is obtained:

$$(61) \qquad Q_d(a) = \frac{2g^2\alpha_d{}^3 a^5}{K\left(z_{eq}(a)-z_0\right)^2\left[\left(2\alpha_d\omega(a)a\right)^2+\beta^2\right]},$$

where

$$(62) \qquad \alpha_d = \frac{4}{3}\pi\rho \quad \text{and}$$

$$(63) \qquad \beta = \left(1+\frac{\pi}{8}\right)\frac{4}{3}\pi m_n \bar{c}_n n_n.$$

Here, a is the sphere radius, n_n, m_n, and $\bar{u}_n$ are the number density, mass, and average speed of the neutral gas molecules, z_0 is the location of the maximum of the harmonic sheath electric potential, ρ is the mass density of the dust, and K is the curvature of the modelled potential. Note that the constants α_d and β concern physical properties related to the dust particle and the suspending gas, respectively. The functional relationships

$\omega(a)$ and $z_{eq}(a)$ must be determined from *experimental* results while the values for K and

z_0 come from the *modelled* sheath potential.

From the data listed in Table 7, ω tended to be roughly quadratic in a,

described approximately by the functions

$$(64) \qquad \omega = 1.05 \cdot 10^{12} a^2 - 2.90 \cdot 10^7 a + 2.21 \cdot 10^2 \quad (P = 6.67 \text{ Pa})$$

and

$$(65) \qquad \omega = 1.31 \cdot 10^{12} a^2 - 2.49 \cdot 10^7 a + 1.68 \cdot 10^2 \quad (P = 13.33 \text{ Pa})$$

The linear relationship between z_{eq} and a was roughly described by

$$(66) \qquad z_{eq} = -3.55 \cdot 10^2 a + 9.73 \cdot 10^{-3} \quad (P = 6.67 \text{ Pa}) \text{ and}$$

$$(67) \qquad z_{eq} = -3.15 \cdot 10^2 a + 9.04 \cdot 10^{-3} \quad (P = 13.33 \text{ Pa})$$

In the above relationships, both z_{eq} and a are in metres, while ω is in rad/sec.

Figure 53 shows the variation of dust charge vs. dust radius, along with the

theoretical curve based on the use of equations (59), (60), and (64) to (67) in equation

(61). The theoretical curve could be improved by using more complicated functional

relationships for $\omega(a)$ and $z_{eq}(a)$. The simple linear and quadratic relationships used

here were chosen to illustrate how a reasonably close fit could be made with very

simple functional assumptions. The limited dependency of the charge of the smaller
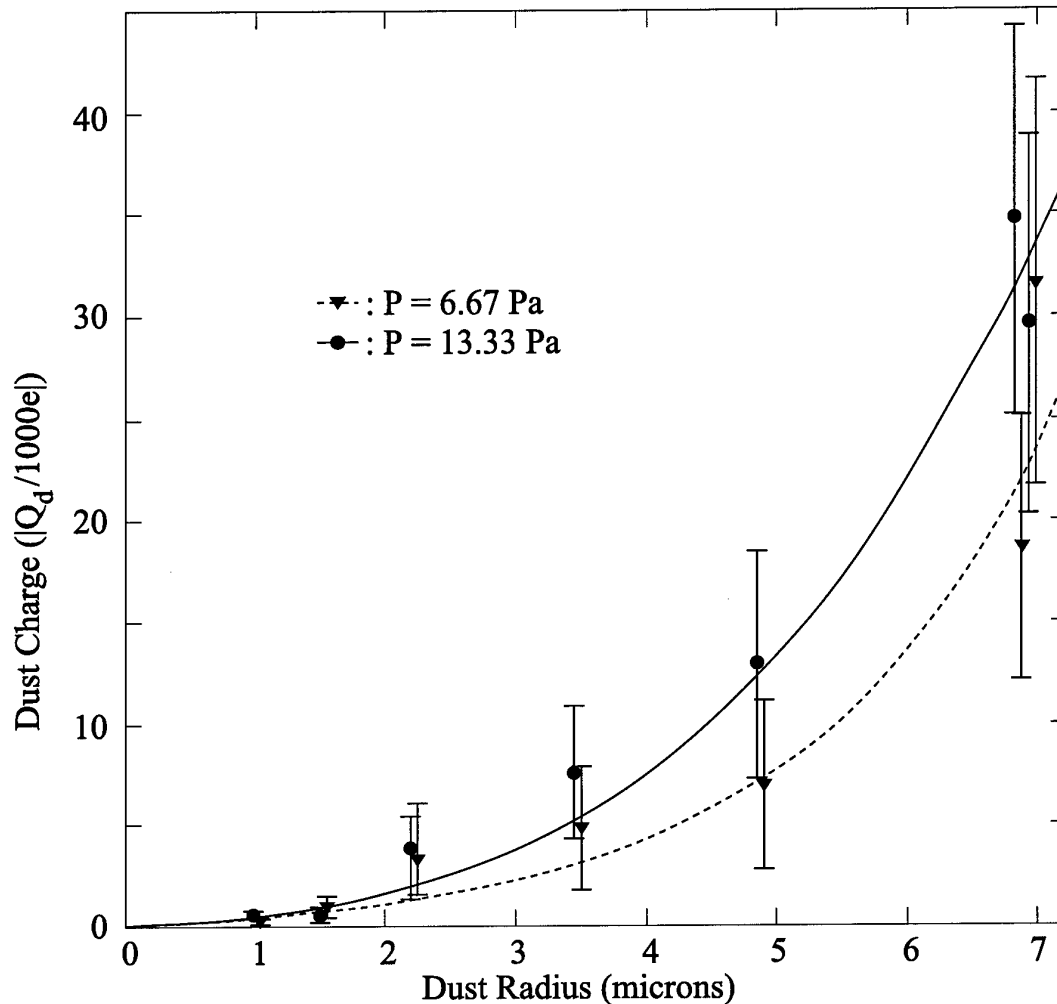
Figure 53: Variation of the Dust Charge as a Function of Dust Radius. This figure shows plots of normalised dust charge for two different pressures: circles and the solid line represent the data and fit for P = 13.33 Pa while triangles and the dotted line show data and fit for P = 6.67 Pa. The circles are offset slightly to the left and the triangles to the right for clarity. The actual horizontal position is halfway between the pairs of error bars. The fits were obtained from equation (61), using the appropriate functions [equations (59), (60), and (64) to (67)] as noted in the text. This plot is for melamine formaldehyde suspended in an argon plasma.

particles on pressure, evident from the figure, has also been noted by other researchers

[Trottenberg *et al.*, 1995].

    To demonstrate that the ion drag force on the smaller dust particles may safely

be ignored, it is assumed that the worst case would be if the ion drag force were equal to

the gravitational force on a 2.0 µm radius dust particle. (In reality, for this large a

particle, the ion drag at the equilibrium height is estimated to be about 20% of the

magnitude of the gravitational force [Nitter, 1996].) A first approximation is to assume

that this additional force causes the particle to suspend at the same height of a particle

whose mass is twice as large, or whose radius is about 2.5 μm. In this region of Figure

53, the charge curve is very flat for both pressures shown. The change of charge due to

this change in radius, from equation (61), is just a noise-level 500 electron-charges for

the worst-case pressure (13.33 Pa).

It must be emphasised that the assumptions that went into generating Figure 53

are dependent upon the mass-density of the dust and the atomic mass of the suspending

gas, so this plot applies to melamine formaldehyde particles suspended in an argon

plasma. The theory [equation (61)], however, is quite general, and may be adapted to

any combination of dust and plasma gas.

As a final demonstration of the self-consistency of this model, recall the force

balance equation assumed in the preceding chapter on dust oscillation theory. In the

development of the harmonic potential energy function, it was assumed that the

electrical and gravitational forces balanced at the dust equilibrium height, or

$$(68) \qquad Q_d \mathcal{E}(z_{eq}(a)) = m_d(a)g \,.$$

Knowing the potential functions [equations (59) and (60)], the relationship between

equilibrium height and dust radius [equations(66) and (67)], and the dust mass, the

charge required to suspend a dust particle of a given radius may then be calculated.

Plots of this function against the calculated dust charges are shown in Figure 54. These

plots show regions where the charge is between 0.5 and 1.5 times that required for
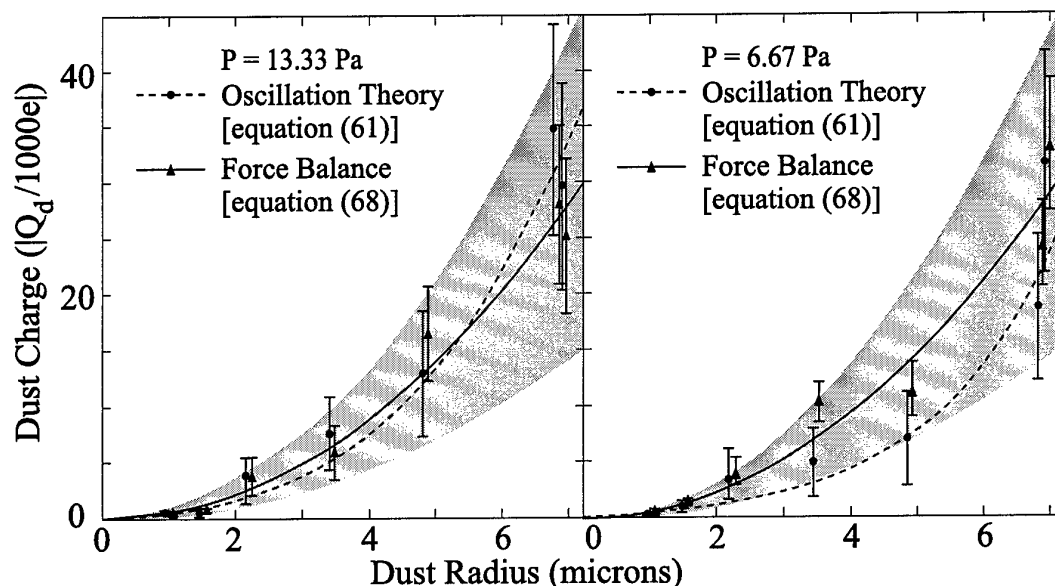
Figure 54: Comparison of the Experimental and Calculated Charges with the Required Balancing Charge. This figure shows plots of normalised dust charge for 13.33 Pa and 6.67 Pa. The dashed lines and circles represent the charges from the dust oscillation theory [equation (61)], previously presented in Figure 53. The solid line and triangles are plots of the charges from equation (68), the charge required to balance the electrical and gravitational forces acting on the dust as discussed in the text. The grey shaded area represents the portion of the plot that is less than 1.5 times and greater than 0.5 times the solid, charge-balancing curve. All of the data points are within this range. The data points have been offset from each other for clarity; the actual horizontal positions are halfway between the corresponding vertical error bars. This plot is for melamine formaldehyde suspended in an argon plasma.

suspension and balance. The experimentally determined charges all lie within this 50% error range, a quite reasonable result considering the assumptions, approximations, and simplifications used in the derivations.

6.4 DISCUSSION

A comparison of these experimental charges with those obtained from purely theoretical work was attempted, but a self-consistent theory of particulate charging in the *plasma sheath* does not appear to exist. (At least two sheath-charging models [Nitter, 1996; Chen, 1997] have been developed. However, they both rely on the orbital motion limited (OML) charging theory [*e.g.* Allen, 1992], which does not seem to be a good approximation in the non-central field environment surrounding dust particles in the plasma sheath.) Several theories concerning dust charging in a *plasma* environment

exist, and the correlation of these experimental results with some of those theories was investigated.

Nairn et al. [1998] have published a charging theory that numerically calculates floating potentials for spherical particles in a plasma based on the Allen-Boyd-Reynolds (ABR) radial motion theory [Allen et al., 1957] of the ions toward the particle. The charge on the particles may then be calculated using the vacuum capacitance equation, equation (18). In Nairn's calculations, the floating potential approaches a non-zero constant as the ratio a/λ_D becomes small. Improved numerical techniques [Kennedy, 1999] have shown that the floating potential should actually approach zero as that ratio approaches zero. Nairn et al. [1998] also have calculated the floating potentials that arise due to the widely quoted OML theory. Results based on this theory are presented here as well, although the general validity of OML is being seriously questioned [Allen et al., 2000]. It is also noted that the charges calculated in much of the previous work [Melzer et al., 1994; Trottenberg et al., 1995; Kortshagen et al., 1996; Homann et al., 1999; Nunomura et al., 1999] rely on the OML charging theory.

The theoretical charges on dust particles having the same local a/λ_D ratios as the experimental data were calculated. The ratios of the experimental charges to the theoretical ones from the radial motion and OML theories are shown in Figure 55. It is obvious from this figure that the experimental charges do not agree with the questionable OML charging theory. Somewhat better agreement with charging calculations based on the ABR (radial motion) theory is found. It should be remembered, however, that the ABR theory was originally developed for a probe in a
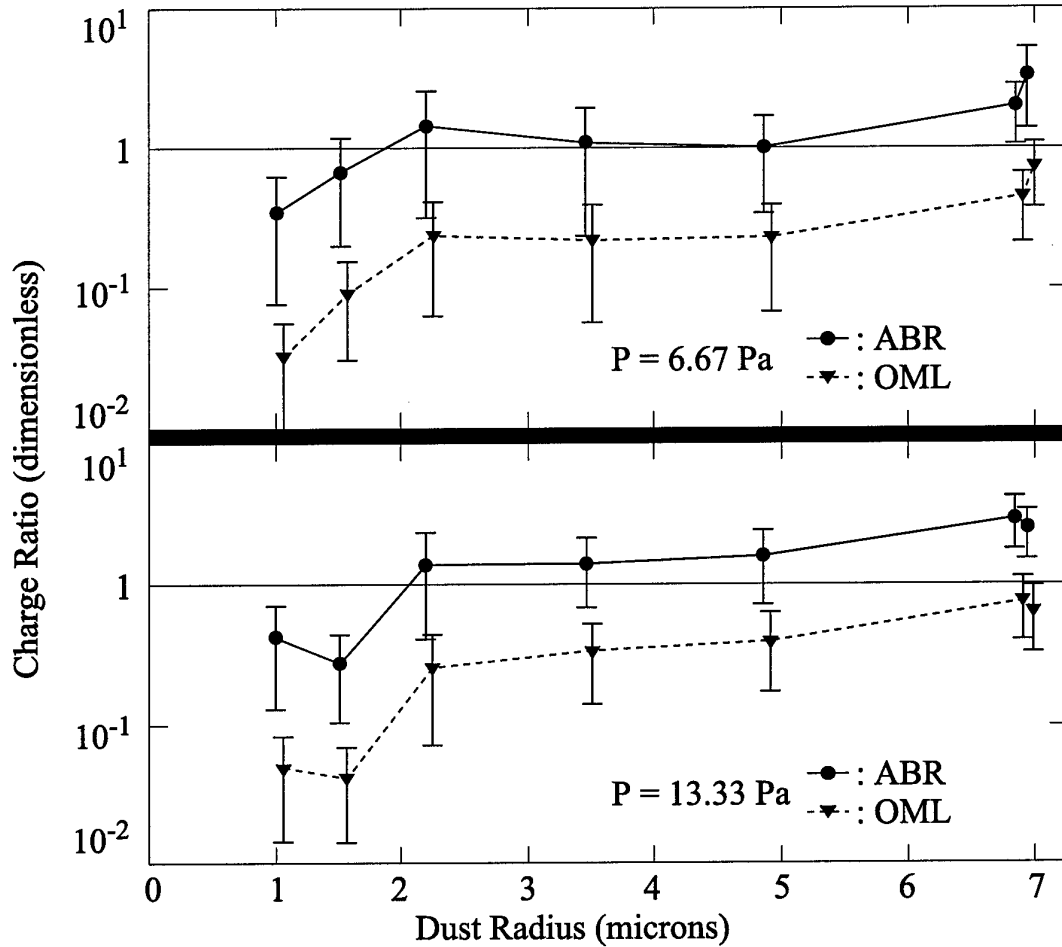
Figure 55: Comparison of Dust Charges from Various Theories. This plot shows the ratio of the experimentally determined charge to the theoretical charge on spherical particles obtained from the radial (solid line and circles) and orbital motion limited (OML) (dotted line and triangles) theories. The upper and lower frames show the results for P = 6.67 Pa and P = 13.33 Pa, respectively. The circles are offset slightly to the left and the triangles to the right for clarity. The actual horizontal position is halfway between the pairs of error bars. The discrepancies between these measurements and the theories are discussed in the text.

quasineutral plasma, not in the space-charge sheath region. These results are presented

primarily as a motivation for the development of an applicable charging theory in the

sheath.

It is also noted that the charges presented in this thesis most likely are slight

underestimates. When the numerical potential from the harmonic model is used in

equation (30), it is tacitly assumed that only the charge on the dust is the charge

responsible for the oscillation characteristics. In reality, the dust floats at a potential

somewhat lower than the local potential [Nitter, 1996]. Dust particles attract a sheath of screening ions that moves with a dust particle throughout its oscillations (individual ions do not remain with the dust, but collectively, the total screen does). The charge of this moving screen will affect the oscillation parameters, and hence the calculated charge. Another way of looking at this effect is to note that as ions are deflected by the negative potential of the dust particle, they form a region of higher ion concentration below the particle. Calculations of this effect in a plasma (not the sheath) were carried out by Stangeby and Allen [1971]. The electrostatic attraction between this positive ion wake region and the negatively charged dust particle (and repulsion between the wake and the shielding ions) could cause variations in the equilibrium height, inducing charge calculation errors. Quantitative estimates of this effect require the development of a theory of charging in the sheath.

6.5 SUMMARY

A number of assumptions have been made to produce the results in this chapter. For the theory, it was assumed that the total potential was globally harmonic, and that the charge on the dust particle remained constant during the oscillation. These assumptions implied that the electric potential must also have been harmonic.

At first, the harmonic assumptions may have seemed a bit tenuous, especially for larger amplitude oscillations. However, it has been shown that the experimental results strongly support the assumption that the potential in the plasma sheath is generally parabolic. The harmonic oscillation theory alone leads to results that agree quite well with established drag laws. It also predicts sheath widths to accuracies on the order of those derived from many techniques of considerably greater sophistication.

The parabolic model of the sheath potential, while extremely simple, agrees well with

numerical models of much higher complexity. Those models also predict parabolic

time-averaged sheath potentials, again supporting the original harmonic assumption.

The large amplitude ranges over which the dust oscillation trajectories are fit by the

damped harmonic oscillator theory also tend to support the existence of a harmonic

sheath potential. When the harmonic oscillation theory is combined with the simplified

sheath model, one is able to deduce the charge on dust particles suspended in the sheath.

Charges calculated in this way are quite consistent with the initial force-balance

postulation of the harmonic theory.

7. FUTURE WORK

In the preceding chapters, it has been shown that the charge on dust particles suspended in the plasma sheath can be determined by two reasonably straightforward, novel methods. The first method relies on accurate measurement and characterisation of the trajectories of dust as it is introduced into the plasma sheath. The second method relies on knowledge of the equilibrium suspension height of the dust particles. Both methods share the common requirement for an *a priori* knowledge of the electrical potential function in the plasma sheath in order to make the charge calculation.

It has also been shown that a parabola may closely approximate the potential function in the sheath. This claim was supported not only by results from a numerical analysis technique developed for this thesis, but by the analysis of a convincing variety of models from the literature and by the experimental data from the previous chapter.

These two major results from this thesis are closely linked. The charge determination from the experimental chapter relies heavily on the parabolic results of the previous chapters. Better determination of the sheath potential function will decrease the error in the experimentally determined charges. Conversely, better knowledge of the charge on suspended dust will help to verify sheath models through

the simple force-balancing technique. Knowledge of the charge could also assist with the validation of forthcoming models of probe charging in the plasma sheath.

One issue not addressed in this thesis, and critical to the specification of the parabolic potential function and the dust charge, is the location of the sheath edge. In this thesis, the sheath edge was defined theoretically as the point where the condition of equation (52) was met, *i.e.*, where the electric field reached a specific value. Experimentally, the sheath edge was defined to be the visually determined physical location of the dark space. It has not been shown that these two definitions agree. The dark-space boundary is commonly used as the sheath edge, but whether it actually occurs at the point where the field reaches the value postulated in this thesis, or some other point entirely, is a question that begs investigation.

The determination of this question will not be an easy task, as it is obvious that the dark space boundary must occur in a region where the plasma is transitioning from quasineutrality to space-charge, and hence in a region where existing probe theories are lacking in detail. It may be that the boundary may be found from theoretical investigations related to electron number densities, EEDFs, and excitation cross-sections. It may also be that it may be determined via an as-yet-undiscovered experimental technique, deconvolved from the response curve of the detector used to locate the boundary. Regardless, the determination of the parameter set at which the dark space occurs will assist greatly in removing error from the charge values determined by the methods of this thesis.

Another avenue of future research involves comparing experimental dust trajectories to those of simulations involving modelled sheath potentials. A numerical integration of the trajectory of dust into the sheath does not seem initially to be that

difficult a task. However, as more and more fidelity is sought, considerations of less and less significant influences will have to be made. For example, a small-amplitude oscillation may be simulated with just a knowledge of the local potential profile from a numerical model, which could come from the parabolic model developed herein. Larger amplitude oscillations that begin to approach the sheath edge would have to begin to take into account not only the increasingly anharmonic oscillation potential profile, but the effects of charge fluctuation on the dust particle. Trajectories that approach the electrode may have to include terms that account for the increased effect of ion drag in that region. As each of these additional perturbations is taken into account, less and less certain results will be obtained, as the effects of the perturbations are either not well understood, are convoluted, or both. Regardless, a numerical trajectory simulation that accurately reflects experimental results would go far toward demonstrating an in-depth knowledge of the myriad processes that affect the motion of the dust grains.

Attacking the same problem from a different direction, experimental trajectories could drive the development of techniques to better describe the potential profile in the sheath. As has been shown in this thesis, small- to medium-amplitude oscillations in the heart of the plasma sheath are very well modelled with a purely harmonic theory. Although the value of the resonant oscillation experiments from the literature have been seriously questioned here, other resonant techniques could possibly be devised to take advantage of the much longer trajectories resulting from such long-term oscillations. The dust could be driven to oscillate at increasingly large amplitudes, and the changes in trajectories noted. For small amplitudes, the frequency spectrum of the trajectory should be overwhelmingly single-valued. As the amplitude increased slightly,

additional harmonics would begin to appear one by one. The spatial locations of the trajectories and the appearance of the harmonics could be compared. As the trajectory harmonics depend upon the potential profile, its deviation from its basic parabolic form could be inferred from this data. In order to perform such an analysis, one would have to use a very high-speed camera to capture subtle changes in trajectory, as well as to develop a method of driving the dust particle without disturbing the sheath. One suggested method would be to use a small gasket to confine a single dust particle horizontally and then to drive it from above with a laser.

Damped oscillations could assist in an investigation that could shed new light on the charge on dust in a crystal. As opposed to the resonant oscillation experiments from the literature detailed in the previous chapter, damped oscillations could provide a way to avoid the pitfalls of a perturbed sheath. An oscillation of an entire plasma crystal could be induced via a low-frequency sinusoidal voltage applied to the driven electrode, as in Melzer *et al.* [1994], Trottenberg *et al.* [1995], and Kortshagen *et al.* [1996]. However, instead of making measurements involving the perturbed sheath, the driving voltage is terminated prior to data collection. As the sheath response to the changing voltage is extremely quick, it would almost immediately settle to its equilibrium solution. The crystal would then undergo damped oscillations in the undisturbed sheath. Analysis of this motion in the manner of the previous chapter could then yield values for the charge on the particles in the crystal. A problem to be overcome with this method would be to show convincingly that the large number of dust particles in the system does not significantly affect the parabolic nature of the undisturbed sheath, allowing the harmonic charge theory to be used.

A final proposed path for further study involves making one of the last substantial improvements to the plasma/sheath model. As the model developed in this thesis only considers the plasma sheath, it has probably been pushed as far as it can go. To make any significant improvement, one needs to consider not only the sheath, but the transition region and the plasma as well. The model of Franklin and Snell [2000] has been shown to give reasonable results from the wall to the centre of the plasma. The collisionality parameters in that model have been varied, and the results smoothly blend into those from previously published models for collisionless and highly collisional cases. Using an iterative solution method similar to that in this thesis, this DC model could be extended to encompass the RF plasma generation techniques so frequently employed in practical situations today. The formulation of such a model would be difficult, however, as the wall potential, which is a known boundary condition for most RF models, is instead a result from the Franklin and Snell model. However, it may be possible to use the DC result for the potential and ion speed profile from that model as the seed for an RF improvement.

In summary, the study of dust in plasmas and the study of the plasma sheath is nowhere near being a closed subject. There are a myriad of potential improvements to the theoretical and experimental investigations of both of these fields. Only a few of them have been touched on here. About these subjects, only one thing is known with certainty: much remains for future discovery.

APPENDIX A: PUBLICATIONS

The works listed below were published during the course of this program:

Law, D.A., W.H. Steel, E.B. Tomme, B.M. Annaratone, and J.E. Allen. "Plasma Crystal in a Weak Magnetic Field." *Proceedings of the 14th European Conference on the Atomic and Molecular Physics of Ionised Gases* (Malahyde, Ireland), in *Europhysics Conference Abstracts*, edited by D. Riley, C.M.O. Mahoney, and W.G. Graham, Volume **22H** (1998) 78-79.

Law, D.A., E.B. Tomme, W.H. Steel, B.M. Annaratone, and J.E. Allen. "Particle Charge Measurements in Dusty Plasmas." *Proceedings of the 26th Institute of Physics (Plasma Physics) Conference* (Pitlochry, Scotland) (1999) 37.

♣Law, D.A., E.B. Tomme, W.H. Steel, B.M. Annaratone, and J.E. Allen. "Dust as a Sheath Diagnostic." *Proceedings of the 24th International Conference on Phenomena in Ionized Gases* (Warsaw, Poland) (1999) 4-109.

Steel, W.H., D.A. Law, E.B. Tomme, B.M. Annaratone, and J.E. Allen. "Effect of Infra Red Radiation and Laser Light on a Plasma Crystal." *Proceedings of the 25th Institute of Physics (Plasma Physics) Conference* (Oxford, England) (1998) T9.

Steel, W.H., D.A. Law, E.B. Tomme, B.M. Annaratone, and J.E. Allen. "Effect of Laser Light on a Plasma Crystal." *Proceedings of the 14th European Conference on the Atomic and Molecular Physics of Ionised Gases* (Malahyde, Ireland), in *Europhysics Conference Abstracts*, edited by D. Riley, C.M.O. Mahoney, and W.G. Graham, Volume **22H** (1998) 114-5.

♥Steel, W.H., D.A. Law, E.B. Tomme, B.M. Annaratone, and J.E. Allen. "Plasma Crystal Interaction with a Laser." *Proceedings of the 26th Institute of Physics (Plasma Physics) Conference* (Pitlochry, Scotland) (1999) 73.

♣ Presentation judged "Best of Conference" out of over 500 entries.
♥ Presentation judged "Best of Conference" out of over 50 entries.

Tomme, E.B, D.A. Law, W.H. Steel, B.M. Annaratone, and J.E. Allen. "Levitation of Dust from an Electrode in a Plasma." *Proceedings of the 25th Institute of Physics (Plasma Physics) Conference* (Oxford, England) (1998) W9.

Tomme, E.B, D.A. Law, W.H. Steel, B.M. Annaratone, and J.E. Allen. "Dust Oscillations in a Plasma Sheath." *Proceedings of the 14th European Conference on the Atomic and Molecular Physics of Ionised Gases* (Malahyde, Ireland), in *Europhysics Conference Abstracts*, edited by D. Riley, C.M.O. Mahoney, and W.G. Graham, Volume **22H** (1998) 334-5.

Tomme, E.B, D.A. Law, W.H. Steel, B.M. Annaratone, and J.E. Allen. "Dust as a Plasma Sheath Diagnostic." *Proceedings of the 26th Institute of Physics (Plasma Physics) Conference* (Pitlochry, Scotland) (1999) 61.

✦Tomme, E.B, B.M. Annaratone, and J.E. Allen. "Damped Dust Oscillations as a Plasma Sheath Diagnostic." *Plasma Sources: Science and Technology* **9**(2) (2000) 87-96.

Tomme, E.B., D.A. Law, B.M. Annaratone, and J.E. Allen. "The Parabolic Plasma Sheath and Its Application to Dust Levitation Experiments." *Proceedings of the 27th Institute of Physics (Plasma Physics) Conference* (Brighton, England) (2000) 18.

♥Tomme, E.B, D.A. Law, B.M. Annaratone, and J.E. Allen. "Parabolic Plasma Sheath Potentials and Their Implications for the Charge on Levitated Dust Particles." Submitted to *Physical Review Letters*, March 2000.

✦ The manuscript of this article is reproduced in Appendix B.
♥ The manuscript of this letter is reproduced in Appendix C.

APPENDIX B: PLASMA SOURCES PAPER

The following ten pages contain the manuscript of an article published in

Plasma Sources: Science and Technology **9**(2) (2000) 87-96.

Damped dust oscillations as a plasma sheath diagnostic

E B Tomme†, B M Annaratone and J E Allen

Department of Engineering Science, University of Oxford, Parks Road, Oxford OX1 3PJ, UK

E-mail: ed.tomme@usafa.af.mil, beatrice.annaratone@eng.ox.ac.uk and john.allen@eng.ox.ac.uk

Abstract. Dust can be suspended in a plasma sheath under certain conditions. An analysis of the dust trajectory as it approaches its equilibrium suspension height can provide a description of the spatial variation of the potential in the sheath. We describe an experiment in which we track such trajectories and calculate their oscillation frequencies, equilibrium heights and damping constants. These three measured parameters are then interpreted in such a manner as to reveal the neutral drag force on the dust and the curvature of the sheath electric potential in which the dust moves. We then calculate the charge on the dust particles suspended in the plasma sheath. We also show that, to a high degree of accuracy, the sheath potential predicted by several numerical models in the literature as well as by our experimental results is parabolic, i.e. the sheath field is quite linear.

1. Introduction

The understanding of dust in a plasma sheath is of great importance to researchers in a variety of disciplines. The study of dust levitating in terrestrial sheaths, especially in so-called plasma crystals, has been underway since 1994, when Chu *et al* [1] and Thomas *et al* [2] experimentally produced such crystals. One of the properties of such dust that is not well understood, either experimentally or theoretically, is its charge.

The analysis of the trajectories of dust particles oscillating in a plasma sheath has been used as a method for determining the charge on the dust by a number of researchers during the past few years. Groups in Germany first used a time varying potential [3–5] induced across the sheath and, more recently, a laser [6] to cause resonant oscillation of dust in a plasma crystal. Harmonic resonance equations were then used to determine the dust charge. Nunomura *et al* [7] used an observed natural instability in the dust position to calculate the dust charge. However, many of these experiments rely upon assumptions about the nature of the plasma sheath potential or the charging of dust in such a potential, significantly perturb the sheath during the experiment, discount the effects of significant forces in the system, or involve some combination of the above. The specific effects of these assumptions and techniques will be discussed later in this paper. Konopka *et al* [8] and Morfill *et al* [9] have also used horizontal collisions of dust particle pairs to determine the interaction potential of the collision, and from that potential, the charge on the dust. Their self-consistent method does not require

† Permanent address: Department of Physics, United States Air Force Academy, Colorado 80840, USA.

any external assumptions concerning plasma parameters or charging mechanisms, but their reported error is larger than the other techniques. In this paper, we present a novel [10] use of the dust oscillation technique that highlights (and stays within) the limits of the assumptions noted above while maintaining stable experimental conditions and accounting for every significant force.

Small particles present in plasmas tend to acquire a negative charge due to the higher mobility of electrons in the plasma. In terrestrial plasmas, negatively charged particles of sufficient size fall toward lower regions of the plasma until they reach the plasma sheath. In the sheath, the electric field from the negatively self-biased electrode begins to repel the particles, or dust. Under certain conditions, this repulsion is sufficient to cause the dust to suspend above the lower electrode. At this point, the particles encounter a balance between upward and downward forces, or in other words, they encounter a minimum in the potential well formed by the sum of these forces.

As a dust particle falls from the plasma into the sheath and enters the potential well, its trajectory oscillates about an equilibrium height, the damping of the oscillations being related to the chamber pressure and the dust mass. An initial analysis of several trajectories indicated that the oscillations might be approximately damped harmonic.

In order to explain this motion, we will first present a review of applicable damped harmonic motion theory. Next, we will develop a theory that uses dust trajectory parameters to estimate the charge on a dust particle at its equilibrium height. We will then discuss a simple model of a collisional radio frequency (RF) plasma sheath needed for our charge estimation theory. Finally, we will present experimental

E B Tomme *et al*

results of our trajectory analysis for a number of dust particles with different masses at different pressures.

2. Harmonic dust oscillation theory

As previously stated, dust in a plasma sheath oscillates in a potential well formed by the opposing electrostatic and gravitational forces. While those forces are not the only forces acting on the dust (ion drag being the most significant of the other forces), they have been shown to be several orders of magnitude larger than other dust-velocity-independent forces in the upper sheath region where our experimental data were taken for most of the studied particle sizes [11–13]. For the smaller particles (<2.5 μm radius), the ion drag begins to approach the magnitude of the gravitational force. However, we will show that the change on the calculated dust charge due to consideration of this force for these smaller particles will be less than the error of our technique. For this reason, we will ignore dust-velocity-independent forces other than gravity and electrostatic repulsion.

Our initial hypothesis was to test whether the oscillations were harmonic, and if so, over what amplitude range. To test this theory, we fit our data to the well known equation of motion for the damped harmonic oscillator, for example [14],

$$m\ddot{z} + \gamma\dot{z} + \kappa(z - z_{eq}) = 0 \qquad (1)$$

where m is the particle mass, γ is the drag constant, κ is the restoring constant, z is the particle height above the electrode (the subscript 'eq' denotes the equilibrium height), and $\dot{z}$ and $\ddot{z}$ are the first and second time derivatives of the height.

For an undamped oscillator with a restoring force $F(z) = -\kappa z$ the potential well has the form $U(z) = \frac{1}{2}\kappa z^2$, showing that the curvature of the potential is just $\kappa/2$. By adding the damping term, we do not change the shape of the well; we merely allow energy to leave the system. It can be shown that for the damped simple harmonic oscillator,

$$\kappa = m[(2\tau)^{-2} + \omega^2] \qquad (2)$$

where the damping time constant, τ, is defined by

$$\tau = \frac{m}{\gamma}. \qquad (3)$$

Equation (2) demonstrates that the curvature of the potential well may be found by measuring the damping time constant and the oscillation frequency.

Measurements of the oscillation parameters described above not only yield data on the potential well, but also can be directly compared with the standard drag theory of Epstein [15]. Other researchers [6] have previously shown that this drag law holds in the plasma sheath. Should the data confirm that our dust particles follow the Epstein law, it will provide an additional, independent check on the plausibility of our measured values.

3. Dust charge theory

The charge on dust particles suspended in the plasma is not well known. Recent experimental and theoretical estimates
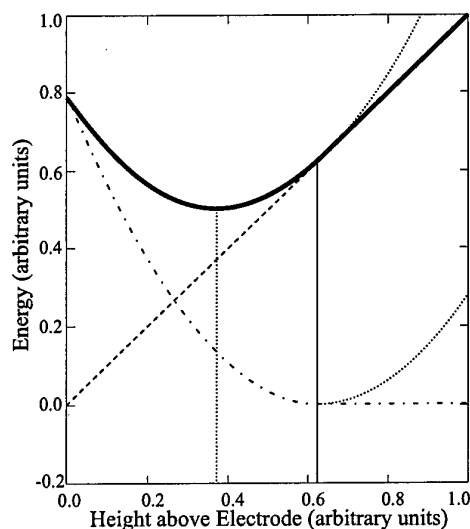
Figure 1. The theoretical potential well. This schematic diagram shows how a harmonic total potential results from the addition of the linear gravitational potential and a harmonic electric potential energy curve. The location of the sheath edge is shown by the vertical full line and the dust equilibrium height is indicated by the vertical dotted line. In this model, the electric potential (dash-dot curve) is essentially zero to the right of the sheath edge. This causes the total potential (full curve) to be parabolic in the sheath and linear in the plasma. The gravitational potential is shown as a dashed line. The dotted extensions to the total and electric potential energy curves show their full parabolic forms. Note that in this figure, the electric potential energy is zero at the minimum point of the parabola, while later in this paper we define zero electric potential at the sheath edge.

place its value on the order of roughly 10^3–10^4 electron charge units for micrometre-sized particles in plasmas with pressures on the order of 10 Pa and electron densities on the order of 10^{16} m^{-3} [3,5,6,16]. The value of about 4000 electron charges on a 4.7 μm radius particle from [4] is the only published value directly comparable with results presented in this paper (melamine formaldehyde dust suspended in an argon plasma sheath), although that value was quoted for dust in a plasma crystal suspended in a perturbed sheath. As we will show here, analysis of the damped oscillation of a dust particle can provide another method to estimate this value.

The total potential in which the dust moves in the sheath is formed by the sum of the electrical and gravitational potential energies,

$$U_{tot} = U_e + U_g \qquad (4)$$

as shown in figure 1. The gravitational potential energy is simply $U_g = mgz$, where g is the gravitational acceleration. The determination of κ, as discussed above, fixes the curvature of the total potential energy for small-amplitude oscillations, and the position of its minimum is fixed by the measurement of the equilibrium height, z_{eq}.

Determination of the electric potential energy is not as straightforward. Our assumption of a parabolic total potential and the linear gravitational potential implies that the electric

88

potential must also be parabolic. Transforming the line-plus-parabola form of the electric potential energy

$$U_e(z) = \left(\frac{\kappa}{2}(z - z_{eq})^2 + U_{eq}\right) - mgz \qquad (5)$$

into the standard form $(y = K(z - z_0)^2 + y_0)$

$$U_e(z) = \frac{\kappa}{2}\left[z - \left(z_{eq} + \frac{mg}{\kappa}\right)\right]^2 + \left(U_{eq} - \frac{(mg)^2}{2\kappa} - mgz_{eq}\right) \qquad (6)$$

allows us to identify the distance from the electrode at which the extremum occurs. This distance

$$z_0 = z_{eq} + \frac{mg}{\kappa} \qquad (7)$$

is a rough gauge of the sheath thickness predicted by this harmonic theory, assuming now that the electric potential is globally harmonic throughout the sheath. As the curvature of this parabola, $\kappa/2$, is the curvature of the *electric potential energy*, we cannot draw any direct conclusions about the magnitude of the curvature of the *electric potential* without knowing the charge on the dust; all we have assumed is that both the potential and the potential energy are harmonic.

At this point, these harmonic assumptions and conclusions may seem quite tenuous. Other researchers [3, 5, 6] have used similar assumptions *a priori*; we will use them here and later justify their use by showing that our data and the results from models available in the literature independently support the parabolic assumptions. In fact, we will show that the data and models support the parabolic assumptions *globally* in the sheath.

The electric potential energy of a dust particle is just

$$U_e(z) = Q_d V(z) \qquad (8)$$

where Q_d is the charge on the dust and $V(z)$ is the electric potential. It can readily be shown that physically, κ represents $-Q_d(\mathrm{d}^2 V/\mathrm{d}z^2)$ or, equivalently, $Q_d(\mathrm{d}E/\mathrm{d}z)$, where E is the electric field.

By assuming a parabolic sheath total potential energy and a constant dust charge throughout the oscillation, we obtain the charge on the dust at its equilibrium height

$$Q_d = \frac{(mg)^2}{2\kappa\left(V(z_{eq}) - V_0\right)} \qquad (9)$$

where V_0 is the extreme value of the (harmonic) electric potential. In equation (9), m and κ are experimentally determined parameters. The potential difference in that equation, however, is not experimentally determinable by current probe methods. To fix its value, we need to rely on a model of the sheath.

4. A simple parabolic sheath model

We are currently in the process of developing an improved numerical model of the RF plasma sheath that is valid for wide ranges of the collisionality parameter (the ratio of the Debye length to the ion mean free path at the sheath edge). This model will also incorporate velocity-dependent ion collision

cross sections. We expect to publish this model in the near future. During the course of the development of this model, we have conducted detailed analyses of a number of other models from the literature [17–20]. We determined that one thing all the models have in common is that a simple parabola is an extremely good approximation for the form of the time-averaged electric potential over the entire spatial extent of the sheath.

To construct such a parabolic approximation, one merely needs to know the RF self-bias potential at the electrode and the potential and field at the sheath edge. For the plasma parameters involved in our experiment, we needed to use a collisional model that was valid for the collisionality parameter, α, greater than unity, where $\alpha = \lambda_D/\lambda$, λ_D is the electron Debye length and λ is the ion mean free path. In this model, we assume cold ions so that the diffusion term in the ion transport equation is much less than the mobility term. The ions are then assumed to reach terminal velocity between collisions such that the collisional force equals the electric force at any point in the plasma [20]. This may be expressed as $M\nu_i v_i = eE$, where M is the ion mass, ν_i is the ion–neutral collision frequency, e is the elementary charge and v_i is the ion velocity. As $\nu_i = v_i/\lambda$, the electric field at any point in the plasma is $E = Mv_i^2/e\lambda$. The ions reach the Bohm speed at the sheath edge [21], where $v_B = (kT_e/M)^{1/2}$ and kT_e is the electron temperature in energy units. Thus, the electric field at the sheath edge in the modelled plasma is just

$$E_s = kT_e/e\lambda. \qquad (10)$$

(This field is also the limiting value of the sheath-edge field for marginally-collisional plasmas proposed by Riemann [22], $E_s = kT_e/e\lambda_D^{2/5}\lambda^{3/5}$, in the limit $\alpha \to 1$.)

Using this field at the sheath edge, our parabolic approximation differs from several accepted models [17, 19, 20], as well as from our own developmental model, by no more than 1% across the entire sheath for parameters similar to our experimental conditions. We thus consider the harmonic nature of the potential in the sheath to be a general result. The parabolic approximation and the Blank model [17] for a set of specific plasma parameters are shown in figure 2 to illustrate the quality of the approximation.

5. Experimental procedure

The well-like nature of the total sheath potential became quite apparent while we were performing experiments that involved observation of dust dropped through the plasma. The experimental set-up is shown in figure 3. It is similar to that used by most other dust oscillation researchers. The 23 cm diameter vacuum chamber is 13 cm high and, for this experiment, the electrodes had diameters of 18 cm and were set 4 cm apart. The upper electrode was grounded and the lower driven by a matched 13.56 MHz RF voltage source. It must be noted that for the plasma parameters used in these experiments, this electrode configuration resulted in an asymmetric situation. The plasma was not only strongly influenced by the potentials on the electrodes, but by the grounded chamber as well, which made the effective size of the driven electrode smaller. This asymmetry resulted in a

E B Tomme *et al*
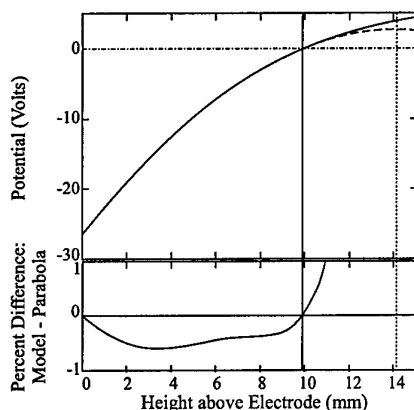
Figure 2. Parabolic fit to the average potential. The upper frame shows a typical numerical potential from the model of Blank [17] (full curve) and the parabola fit to the boundary conditions described in the text (dashed curve). The horizontal dash-dotted line shows the sheath potential (while Blank does not explicitly identify this potential as the sheath potential, our analysis shows that it occurs approximately at the point where the field equals that given by equation (10)). The vertical full line is the sheath edge derived from the numerical data and the vertical dotted line is the harmonic theory sheath edge derived in equation (7). The numerical and harmonic potential curves are indistinguishable at this scale until just above the numerical sheath edge, where the divergence becomes more pronounced. The lower frame shows the difference between the numerical data and the parabolic fit, demonstrating the close approximation harmonic theory makes to the numerical results.
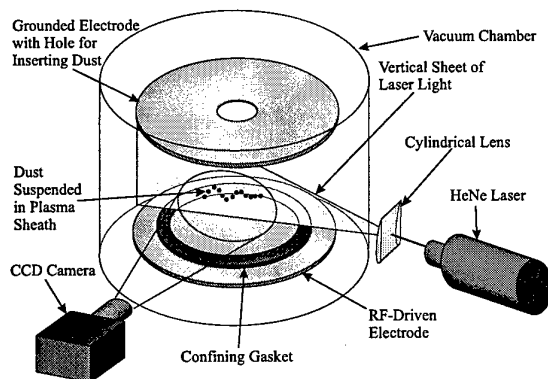
Figure 3. Experimental set-up. The set-up is described in detail in the text.

large fraction of the RF potential appearing across the driven sheath [23].

The dust used in our experiments was spherical melamine formaldehyde ($\rho = 1510$ kg m^{-3}), an insulating polymer, of a variety of individual sizes ranging between approximately 0.5 and 7 μm in radius. The spheres were quite monodispersive, having a quoted radius variation of less than about 0.1%. Prior to each trial, a specific size dust was loaded into a glass container suspended above the upper electrode (not shown in the figure). Very small numbers of dust particles (<10) were dropped through the hole in the upper electrode into the plasma. As it entered the plasma, the dust was illuminated by a HeNe laser beam that had been

spread to a thin, vertical sheet. A small, rectangular copper gasket ($2.5 \times 10 \times 0.2$ cm, with a 0.5×8 cm slit removed from its centre) was placed on the lower electrode to form a small potential well that localized the dust in the central region of the chamber. The high aspect ratio of the slit confined the dust to the region illuminated with the laser, but allowed the dust to spread out along the laser beam, minimizing the effects of forces between particles. A high-speed (up to 12 000 fps), image-intensifying CCD camera was employed to record the dust trajectories. Dust trajectories were monitored via the CCD display and recorded digitally directly to a computer.

Dust trajectories were analysed by identifying a particle that underwent a number of oscillations with only minor interaction with its neighbours. Once a particle was identified, its position was manually tracked over a number of frames (~100). The position and position error data was then corrected for scale, perspective, and gasket perturbation, and a plot of the height-above-electrode against time was then generated.

Our experimental technique differs from previously cited dust oscillation techniques [3–9] in several respects. Those methods typically use some induced or natural driving force to cause resonant oscillation. Our technique is much simpler, although its accuracy for very low-mass particles diminishes due to the very high damping rate for these conditions.

We did not vary the self-bias of the driven electrode nor did we place any variable-bias external probes near the dust. This allowed us to base our results on a stable sheath with a potential profile that is essentially time-independent on the scale of the relevant dust charging times. We also did not have to account for the non-zero electrode currents that would have naturally flowed during induced, slow oscillations of the self-bias. Thus, our method does not involve any external sheath perturbations, the effects of which would tend to greatly complicate any charge analysis.

The benefit of the resonant analysis used in other techniques would seem to be quite apparent, especially for low-mass particles and/or high pressures where the damping is so high that very few oscillations may be observed by our undriven method. This would seem to be especially true for relatively non-intrusive methods that utilize lasers to excite the resonance without disturbing the sheath. However, with all of these resonant methods, there exists the possibility of inadvertently overdriving the resonant oscillations to the point where charge fluctuations on the dust particle become significant enough to spoil the harmonic nature of the potential well. (For a discussion of this charge fluctuation, see e.g. [7, 19, 24, 25].) For small-amplitude oscillations, our results will show the oscillations to be extremely well modelled by harmonic equations, implying that the charge fluctuations are either very small or average out during the oscillation. However, as the oscillation amplitude increases past a critical point, the harmonic nature of the potential breaks down rapidly, invalidating techniques that rely on harmonic equations to obtain charge from the now-anharmonic resonance frequency. We have found this critical amplitude to be typically about 10–20% of the sheath width, based on results presented later in this paper. At the sampling rates used in several of the cited experiments, it would appear to be difficult to determine whether the oscillations were indeed harmonic or merely periodic.

90

Damped dust oscillations
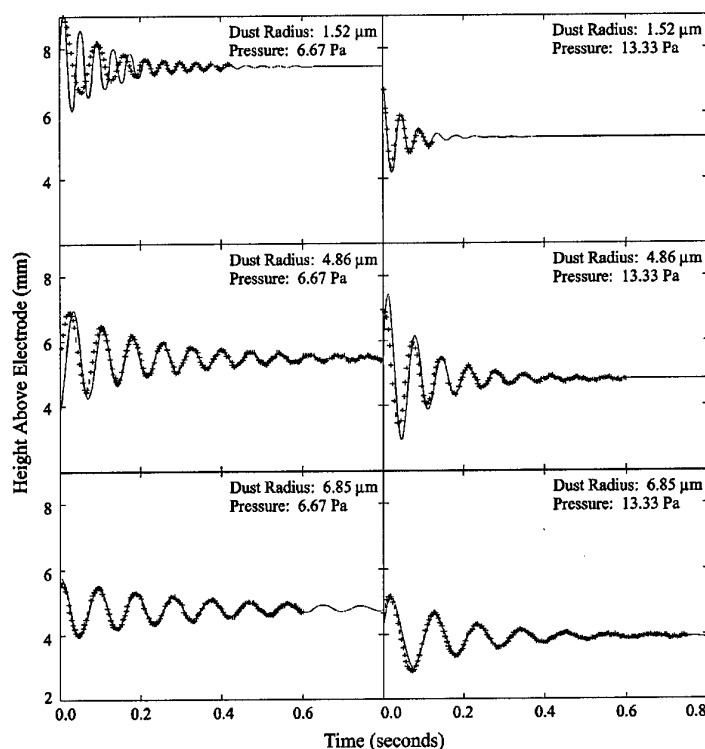
Figure 4. Dust oscillation data and harmonic theory. These six plots show dust trajectories obtained as described in the text. The scales and origins are the same for all six plots to facilitate direct comparison. The full lines are damped harmonic theoretical curves from equation (11) using the parameters shown in table 1. Typical position errors are on the order of 10 μm; these error bars are not visible at this scale. Each column of plots is for the same pressure, while each row of plots is for the same mass dust particle. The other experimental parameters are discussed in the text.

We also go to great lengths to eliminate extraneous forces acting on the oscillating dust. Several of the cited techniques involve the resonant excitation of dust in a crystal lattice, and then use harmonic equations to find the charge on the excited dust. This analysis fails to take into account the strong interaction potentials between the large numbers of dust particles in the lattice, leading to questionable results. Our analysis involves very small numbers of particles inserted into the sheath, and only particles that are observed to be relatively free of interaction with other particles are used for our charge analysis.

We also measured oscillations that occur in the vertical plane. Techniques that utilize horizontal oscillations generally only determine the shape of the confining potential well of the gasket and the interaction potential between dust particles. While these techniques can derive a value for the dust charge, they give little information on the vertical potential profile through significant fractions of the sheath.

Some previous techniques have also relied upon estimates of the charged particle densities from such sources as extrapolations of sine-shaped ion density profiles into the sheath, assumptions that the sheath is a perfect rectifier, or Child–Langmuir ion profiles. Our method instead uses the previously discussed assumption of a harmonic sheath potential.

6. Experimental results

The solution to the equation of motion (equation (1)) is

$$z(t) = \exp\left(-\frac{t}{2\tau}\right)\left[z(0)\cos(\omega t)\right.$$
$$\left. +\frac{\dot{z}(0) + (z(0)/2\tau)}{\omega}\sin(\omega t)\right] + z_{eq} \tag{11}$$

where t is the time and ω is the observed oscillation frequency. Thus, our curve-fitting routine used the five parameters $z(0)$, $\dot{z}(0)$, z_{eq}, ω, and $(2\tau)^{-1}$ to fit the damped harmonic theory (equation (11)) to our data. Table 1 lists the plasma and relevant curve-fitting parameters for all the data sets. Six typical plots of our experimental data and the associated curve fits from the damped harmonic theory are shown in figure 4. The plots show combinations of three different radii dust particles taken at two different pressures. The decrease in the equilibrium height with an increase in pressure and/or mass is apparent, as is the decrease in the damping rate as the pressure is decreased and/or the mass is increased. The difference in oscillation frequency between the small and large particles is also visually apparent.

In many of the trajectories, the average error between the data points and the theoretical fit over a large portion of the plot is less than the width of a pixel (1 pixel $\cong$ 30 μm) from a data image frame. We also emphasise that the theoretical fit to the data is very good for oscillations that approach

91

E B Tomme *et al*

Table 1. Experimental conditions and curve-fitting parameters. The data in the first two columns are the controlled experimental conditions. The data in the central three columns are the resulting curve-fitting parameters (errors for oscillation frequencies and decay constants are estimated). The data in the last four columns are derived from data in the other columns using the equations indicated. For all cases the electrode spacing was 40.0 mm, the RF amplitude was 96.4 V, the RF frequency was 13.56 MHz, the dust density was 1510 kg m^{-3}, and the working gas was argon. For the high-pressure case, kT_e and n_0 were 3.9 eV and 2.4×10^{15} m^{-3}, respectively, while at low pressure they were 3.7 eV and 1.7×10^{15} m^{-3}. The plasma parameters were determined by Langmuir probe measurements at the centre of the plasma. The visually-determined sheath widths were 9.4 ± 0.25 mm and 8.5 ± 0.25 mm for 6.67 Pa and 13.33 Pa, respectively.

Dust radius A (μm)	Chamber pressure P (Pa)	Equilibrium height z_{eq} (mm)	Oscillation frequency ω (rad s^{-1})	Decay constant $(2\tau)^{-1}$ (s^{-1})	Dust mass $4\pi r^3 \rho/3$ (10^{-13} kg)	Restoring constant, equation (2) (10^{-9} kg s^{-2})	Nominal sheath edge, equation (7) (mm)	Dust charge, equation (9) (1000e)
1.01 ± 0.02	6.67 ± 0.13	8.97 ± 0.01	125 ± 2	27.5 ± 0.9	0.065 ± 0.004	0.11 ± 0.01	9.6 ± 0.1	0.2 ± 0.1
1.52 ± 0.04	6.67 ± 0.13	9.17 ± 0.01	153 ± 2	8.5 ± 0.9	0.22 ± 0.02	0.52 ± 0.04	9.6 ± 0.1	0.8 ± 0.5
2.2 ± 0.1	6.67 ± 0.13	9.34 ± 0.01	192 ± 2	9.9 ± 0.9	0.67 ± 0.09	2.5 ± 0.3	9.6 ± 0.1	3.3 ± 2.1
3.46 ± 0.04	6.67 ± 0.13	8.93 ± 0.01	160 ± 2	5.1 ± 0.9	2.62 ± 0.09	6.7 ± 0.3	9.3 ± 0.1	4.8 ± 3.1
4.86 ± 0.03	6.67 ± 0.13	7.60 ± 0.01	85.7 ± 2	5.0 ± 0.9	7.2 ± 0.1	5.4 ± 0.3	8.9 ± 0.1	6.9 ± 4.1
6.85 ± 0.1	6.67 ± 0.13	6.95 ± 0.01	67.5 ± 2	3.5 ± 0.9	20.3 ± 0.9	9.3 ± 0.7	9.1 ± 0.2	18.6 ± 6.4
6.95 ± 0.1	6.67 ± 0.13	7.61 ± 0.01	69.0 ± 2	2.9 ± 0.9	21.2 ± 0.9	10.1 ± 0.7	9.7 ± 0.2	31.7 ± 9.9
1.01 ± 0.02	13.33 ± 0.13	8.68 ± 0.01	140 ± 2	51 ± 0.9	0.065 ± 0.004	0.14 ± 0.01	9.1 ± 0.1	0.3 ± 0.2
1.52 ± 0.04	13.33 ± 0.13	8.29 ± 0.01	138 ± 2	19 ± 0.9	0.22 ± 0.02	0.43 ± 0.04	8.8 ± 0.1	0.4 ± 0.2
2.2 ± 0.1	13.33 ± 0.13	8.65 ± 0.01	130 ± 2	24 ± 0.9	0.67 ± 0.09	1.2 ± 0.2	9.2 ± 0.1	3.7 ± 2.3
3.46 ± 0.04	13.33 ± 0.13	7.83 ± 0.01	74 ± 2	11 ± 0.9	2.62 ± 0.09	1.5 ± 0.1	9.6 ± 0.1	7.5 ± 3.3
4.86 ± 0.03	13.33 ± 0.13	7.84 ± 0.01	95 ± 2	11 ± 0.9	7.2 ± 0.1	6.6 ± 0.3	8.9 ± 0.1	12.9 ± 5.6
6.85 ± 0.1	13.33 ± 0.13	6.95 ± 0.01	59 ± 2	5.2 ± 0.9	20.3 ± 0.9	7.1 ± 0.6	9.7 ± 0.3	34.6 ± 9.6
6.95 ± 0.1	13.33 ± 0.13	6.58 ± 0.01	56 ± 2	5.4 ± 0.9	21.2 ± 0.9	$6.7 \pm .06$	9.7 ± 0.3	29.6 ± 9.3

20% of the sheath thickness. This amplitude range is much better than one would normally expect for a small-amplitude match between an arbitrary, non-parabolic potential well and a harmonic approximation. The close fits between theory and experiment over these large amplitude ranges tend to support our hypothesis that the electric potential is indeed very nearly harmonic throughout the sheath.

It is quite apparent that as the oscillation amplitude increases past a certain point, the quality of the fit drops markedly. This is due, in some part, to the fact that the trajectories of the higher-amplitude oscillations are not exclusively in the plasma sheath. While the dust continues to oscillate between the plasma and plasma sheath regions, the potential well it sees is not even approximately harmonic. As soon as the dust oscillations become damped enough to confine it exclusively to the sheath, the theoretical fit becomes much better. Another reason for the discrepancy between theory and experiment is our assumption of constant charge on the dust particle. The charging time of a dust particle has been shown to be on the order of 10^{-6} s [4, 19], much faster than our oscillation time scale of 10^{-2} s, so the dust charge might vary with position during an oscillation. The larger the oscillation, the worse our constant-charge assumption becomes, adding to the fit/data mismatch. Less massive dust particles, oscillating nearer the sheath edge, would seem to be affected more by both of these problems. They oscillate nearer the sheath edge where the harmonic potential assumption breaks down. They also have smaller charges, making even small charge changes during oscillations significant. These effects are apparent in figure 4, where the amplitude at which theory and experiment break down is much smaller for less massive particles.

As preliminary measures of agreement between theory and experiment, we compared our parameters with standard drag laws and the predicted sheath width from our harmonic theory. To determine the drag law on small spheres in a plasma sheath, we used our fitting parameter $(2\tau)^{-1}$ along with equation (3) to calculate the drag constant, γ. Our experimental results showed close (within 20%) agreement with the Epstein theory [15]. We next calculated the location of the minimum in the electrical potential energy from our experimentally determined restoring constants, κ, and equation (7). With a negative dust charge, this value would be where the maximum electrical potential would occur, or nominally, where the sheath edge should occur if the potential were globally harmonic. From this calculation (the results of which are presented in table 1), we obtained theoretical sheath widths of 9.5 ± 0.3 mm (6.67 Pa) and 9.2 ± 0.3 mm (13.33 Pa), agreeing quite well with our observed widths of 9.4 ± 0.25 and 8.5 ± 0.25 mm, respectively. Again, this agreement tends to support our assumption of a parabolic electric potential within the sheath

Equation (9) showed that determining the charge on a dust particle at its equilibrium position required a knowledge of not only its mass and the restoring constant, but also of the potential difference between two definite points in the sheath. Thus, we must develop a parabolic sheath potential function.

The first step in developing the potential function is to determine the potential drop across the driven sheath. To determine this drop, we assumed a two-sheath model $\phi_d = \phi_g + \phi_{sb}$, where ϕ_d and ϕ_g are the driven and grounded dc sheath potential differences and ϕ_{sb} is the measured dc self-bias between the grounded and driven electrodes. This model also requires that the sum of the ac sheath potentials, $\phi_{d,ac}$ and $\phi_{g,ac}$ equals the applied ac voltage, or $\phi_{d,ac} + \phi_{g,ac} = \phi_{ac}$. Calculation of the self-bias voltage developed across an RF-enhanced sheath was carried out using the standard method [26], for the case of zero dc current flow. We then iteratively solved for the dc sheath potential using these two equations.
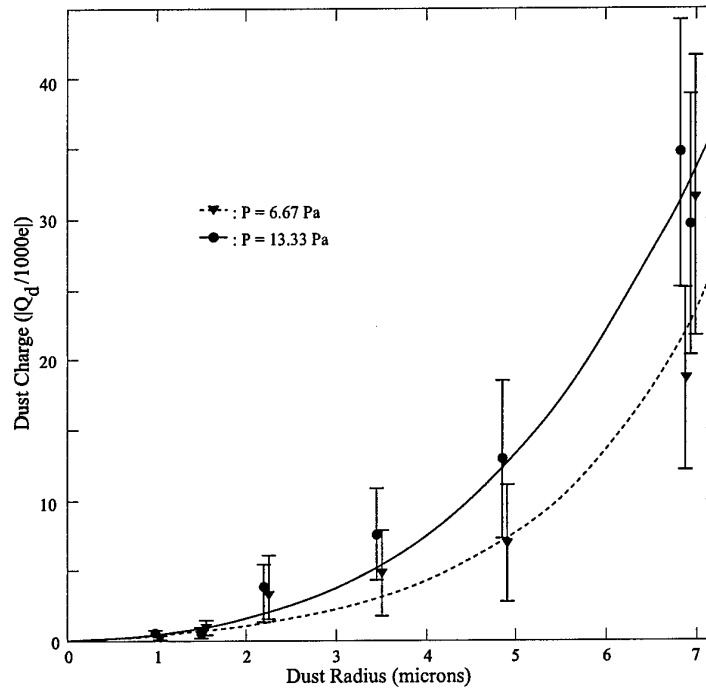
Figure 5. Variation of the dust charge as a function of dust radius. This figure shows plots of normalized dust charge for two different pressures: circles and the full curve represent the data and fit for $P = 13.33$ Pa while triangles and the broken curve show data and fit for $P = 6.67$ Pa. The circles are offset slightly to the left and the triangles to the right for clarity. The actual horizontal position is halfway between the pairs of error bars. The fits were obtained from equation (12), with the appropriate functions as noted in the text. This plot is for melamine formaldehyde suspended in an argon plasma.

In our experiment, the applied RF amplitude was 96.4 V and the self-biases were 56.9 ± 1.5 V (6.67 Pa) and 49.3 ± 1.9 V (13.33 Pa). Thus, the dc potentials across the driven electrode sheath were 86.3 ± 0.8 V (6.67 Pa) and 83.0 ± 1.0 V (13.33 Pa). The validity of this voltage division is supported by considering the resulting ratios of the effective areas of the grounded to driven electrodes [23, 27] of 1.7 (6.67 Pa) and 1.5 (13.33 Pa), ratios which are quite reasonable for our experimental set-up.

The boundary conditions for our parabolic sheath model then became: $\phi(0) = -86.3$ V, $z_{sh} = 9.4$ mm and $\phi(z_{sh}) = 0$ (6.67 Pa); and $\phi(0) = -83.0$ V, $z_{sh} = 8.5$ mm and $\phi(z_{sh}) = 0$ (13.33 Pa). The values for E_s come from equation (10). The potential functions derived from a parabolic fit to the above boundary conditions were $\phi(z) = -0.906(z - 9.77)^2 + 0.124$ (6.67 Pa) and $\phi(z) = -0.985(z - 9.21)^2 + 0.499$ (13.33 Pa), with z in millimetres and $\phi(z)$ in volts. We must emphasise that the potential functions presented here stem from what we consider to be the most reasonable choices of the boundary conditions from current literature. Should better parabolic boundary conditions be determined at a later date, they may be used with our data to provide improved results.

Once the potential functions had been determined, it was a relatively simple procedure to calculate the dust charge. These values for the dust charge are given in table 1, and are in reasonably good order of magnitude agreement with those of a number of previous researchers [3–6, 28], considering the differences in the experimental parameters.

The effect of changing the dust radius on the equilibrium charge is fairly complicated, as the increased radius not only provides a larger surface area, but also causes the dust to suspend lower in the sheath. To visualize this effect, we can rewrite equation (9) as a function of dust radius. Assuming a globally harmonic sheath potential, using the Epstein drag law ($\gamma = (1 + \pi/8)(4\pi/3)m_n \bar{u}_n n_n a^2$), substituting $(4\pi/3)a^3 \rho$ for the dust mass, and employing equations (2), (3) and (9), we obtain the following equation for the charge as a function of dust radius:

$$Q_d(a) = \frac{2g^2 \alpha^3 a^5}{K(z_{eq}(a) - z_0)^2 [(2\alpha\omega(a)a)^2 + \beta^2]} \quad (12)$$

where

$$\alpha = \tfrac{4}{3}\pi\rho \quad (13)$$

and

$$\beta = \left(1 + \frac{\pi}{8}\right)\frac{4}{3}\pi m_n \bar{u}_n n_n \quad (14)$$

where, a is the sphere radius, n_n, m_n and $\bar{u}_n$ are the number density, mass and average speed of the neutral gas molecules, z_0 is the location of the maximum of the harmonic sheath electric potential, ρ is the mass density of the dust and K is the curvature of the modelled potential. Note that the constants α and β concern physical properties related to the dust particle and the suspending gas, respectively. The functional relationships $\omega(a)$ and $z_{eq}(a)$ must be determined from *experimental* results while the values for K and z_0 come from the *modelled* sheath potential.

93

E B Tomme *et al*
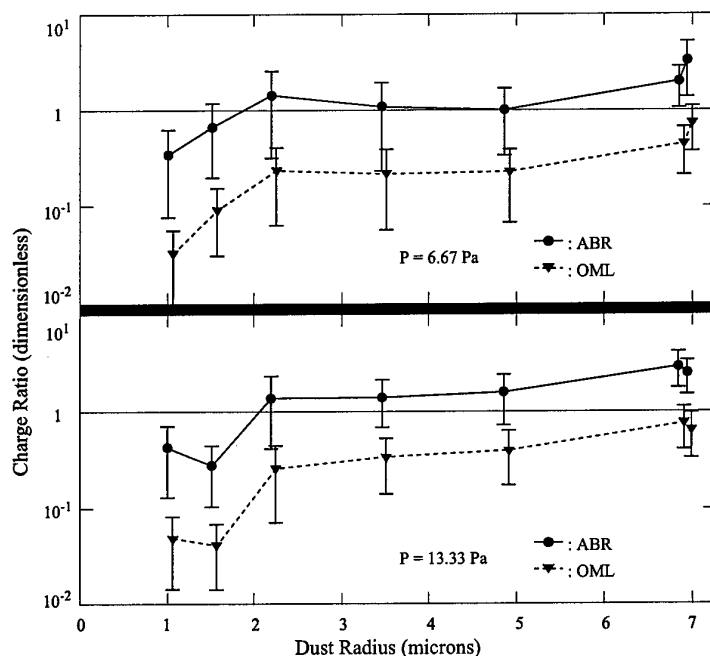
Figure 6. Comparison of dust charges from various theories. This plot shows the ratio of our experimental charge to the theoretical charge on spherical particles obtained from the radial (full lines and circles) and orbital motion limited (broken lines and triangles) theories. The upper and lower frames show the results for $P = 6.67$ Pa and $P = 13.33$ Pa, respectively. The circles are offset slightly to the left and the triangles to the right for clarity. The actual horizontal position is halfway between the pairs of error bars. The discrepancies between our measurements and the available theories are discussed in the text.

From the data listed in table 1, ω tended to be roughly quadratic in a, described approximately by the functions

$$\omega = 1.05 \times 10^{12}a^2 - 2.90 \times 10^7 a$$
$$+2.21 \times 10^2 \qquad P = 6.67 \text{ Pa}$$

and

$$\omega = 1.31 \times 10^{12}a^2 \ (\text{s}^{-1} \ \text{m}^{-2}) - 2.49 \times 10^7 a \ (\text{s}^{-1} \ \text{m}^{-1})$$
$$+1.68 \times 10^2 \ (\text{s}^{-1}) \qquad P = 6.67 \text{ Pa}.$$

The linear relationship between z_{eq} and a was roughly described by $z_{eq} = -3.55 \times 10^2 a + 9.73 \times 10^{-3}$ ($P = 6.67$ Pa) and $z_{eq} = -3.15 \times 10^2 a + 9.04 \times 10^{-3}$ ($P = 13.33$ Pa). In the above relationships, both z_{eq} and a are in metres and ω is in rad/s. Figure 5 shows the variation of dust charge against dust radius, along with the theoretical curve based on the above functions used in equation (12). The theoretical curve could be improved by using more complicated functional relationships for $\omega(a)$ and $z_{eq}(a)$. We chose to use the simple linear and quadratic relationships here to illustrate how a reasonably close fit could be made with very simple functional assumptions. The limited dependency of the charge of smaller particles on pressure has also been noted by other researchers [4].

To demonstrate that we can safely ignore the ion drag force on the smaller dust particles, let us assume that the worst case would be if the ion drag force were equal to the gravitational force on a 2.0 μm radius dust particle. (In reality, for this large a particle, the ion drag at the equilibrium height is about 20% of the magnitude of the gravitational force [19].) Our first approximation is to assume that this

additional force causes the particle to suspend at the same height as a particle whose mass is twice as large, or whose radius is 2.5 μm. In this region of figure 5, the charge curve is very flat for both of the pressures shown. The change of the charge due to this change in radius, from equation (12), is just a noise-level 500 electron charges for the worst-case pressure (13.33 Pa).

We must emphasise that the assumptions that went into generating figure 5 are dependent upon the mass–density of the dust and the atomic mass of the suspending gas; this plot applies to melamine formaldehyde particles suspended in an argon plasma. The theory (equation (12)), however, may be adapted to any combination of dust and plasma gas.

7. Discussion

We attempted to compare our experimental charges with those obtained from purely theoretical work, but a self-consistent theory of particulate charging in the *plasma sheath* does not appear to exist. (At least two sheath-charging models [19, 29] have been developed. However, they both rely on the orbital motion limited (OML) charging theory, e.g. [30], which does not seem to be a good approximation in the non-central field environment surrounding dust particles in the plasma sheath.) Several theories concerning dust charging in a *plasma* environment exist, and we investigated the correlation of our results with some of those theories.

Nairn *et al* [16] published a charging theory that numerically calculates floating potentials for spherical particles in a plasma based on the Allen, Boyd and Reynolds

94

Damped dust oscillations

(ABR) radial motion theory [31] of the ions toward the particle. The charge on the particle may then be calculated using the vacuum capacitance equation

$$Q_d = 4\pi\varepsilon_0 a V_f \qquad (15)$$

where ε_0 is the permittivity of free space and V_f is the floating potential, valid in the small a/λ_D limit. (Equation (15) has been shown to be valid for our case of small, isolated spheres surrounded by screening charges, as is the case in the sheath [32].) In this theory, the floating potential approaches a non-zero constant as the ratio a/λ_D becomes small. Improved numerical techniques [33] have shown that the floating potential should actually approach zero as that ratio approaches zero. Nairn has also calculated the floating potentials that arise due to the widely quoted OML theory. We present results based on this theory as well, although the general validity of OML is being seriously questioned [34]. We also note that the charges calculated in much of the previous work [3–5, 7] rely on the OML charging theory.

We have calculated the theoretical charges on dust particles having the same a/λ_D ratios as our experimental data. The ratios of our experimental charges to the theoretical charges from the radial motion and OML theories are shown in figure 6. It is obvious from figure 6 that our experimental charges do not agree with the questionable OML charging theory. We find somewhat better agreement with charging calculations based on the ABR (radial motion) theory. It should be remembered, however, that the ABR theory was originally developed for a probe in a quasineutral plasma, not in the space-charge sheath region. We present these results primarily as a motivation for the development of an applicable charging theory in the sheath.

We also note that the charges presented in this paper most likely are slight underestimates. When we use the potential from our model in equation (9), we tacitly assumed that only the charge on the dust is the charge responsible for the oscillation characteristics. In reality, the dust floats at a potential somewhat lower than the local potential [19]. Dust particles attract a sheath of screening ions that moves with the dust throughout its oscillations (individual ions do not remain with the dust, but collectively, the total screen does). The charge of this moving screen will affect the oscillation parameters, and hence the calculated charge. Another way of looking at this effect is to note that as ions are deflected by the negative potential of the dust particle, they form a region of higher ion concentration below the particle. Calculations of this effect in a plasma (not the sheath) were carried out by Stangeby and Allen [35]. The electrostatic attraction between this positive ion wake region and the negatively charged dust particle (and repulsion between the wake and the shielding ions) could cause variations in the equilibrium height, inducing charge calculation errors. Quantitative estimates of this effect require the development of a theory of charging in the sheath.

8. Summary

We have made a number of assumptions to produce the results in this work. For our theory, we assume that the total

potential energy is globally harmonic and that the charge on the dust particle remains constant during the oscillation. These assumptions imply that the electric potential must also be harmonic.

We have shown that our experimental results strongly support the assumption that the potential in the plasma sheath is generally parabolic. Our harmonic oscillation theory alone leads to results that agree quite well with the established drag laws. Our parabolic model of the sheath potential, while extremely simple, agrees well with numerical models of much higher complexity. Those models also predict parabolic time-averaged sheath potentials, again supporting our original harmonic assumption. The large amplitude ranges over which the dust oscillation trajectories fit the damped harmonic oscillator theory also tend to support the existence of a harmonic sheath potential. When we combine the harmonic oscillation theory with our simplified sheath model, we are able to deduce the charge on dust particles suspended in the sheath.

Acknowledgments

References

[1] Chu J H, Du J B and Lin I 1994 *J. Phys. D: Appl. Phys.* **27** 296

[2] Thomas H, Morfill G E, Demmel V, Goree J, Feuerbacher B and Mohlmann D 1994 *Phys. Rev. Lett.* **73** 652

[3] Melzer A, Trottenberg T and Piel A 1994 *Phys. Lett.* A **191** 301

[4] Trottenberg T, Melzer A and Piel A 1995 *Plasma Sources Sci. Technol.* **4** 450

[5] Kortshagen U and Mümken G 1996 *Phys. Lett.* A **217** 126

[6] Homann A, Melzer A and Piel A 1999 *Phys. Rev.* E **59** R3835

[7] Nunomura S, Misawa T, Ohno N and Takamura S 1999 *Phys. Rev. Lett.* **83** 1970

[8] Konopka U, Ratke L and Thomas H M 1997 *Phys. Rev. Lett.* **79** 1269

[9] Morfill G E, Thomas H M, Konopka U and Zuzic M 1999 *Phys. Plasmas* **6** 1769

[10] Tomme E B, Law D A, Steel W H, Annaratone B M and Allen J E 1998 *Proc. 14th European Conf. Atomic and Molecular Physics Ionised Gases (ESCAMPIG) (Malahide, Ireland)* Europhysics Conference Abstracts vol 22H, p 334

[11] Northrop T G and Birmingham T J 1990 *Planet. Space Sci.* **38** 319

[12] Barnes M S, Keller J H, Forster J C, O'Neill J A and Coultas D K 1992 *Phys. Rev. Lett.* **68** 313

[13] Kilgore M D, Daugherty J E, Proteous R K and Graves D B 1993 *J. Appl. Phys.* **73** 1617

[14] Baerline R 1983 *Newtonian Dynamics* (London: McGraw-Hill) pp 45–70

[15] Epstein P S 1924 *Phys. Rev.* **23** 710

95

E B Tomme *et al*

[16] Nairn C, Annaratone B M and Allen J E 1998 *Plasma Sources Sci. Technol.* **7** 478

[17] Blank J L 1968 *Phys. Fluids* **11** 1686

[18] Skorik M and Allen J E 1993 *Proc. 21st Int. Conf. Phenomena in Ionized Gases (Bochum, Germany)* p 113

[19] Nitter T 1996 *Plasma Sources Sci. Technol.* **5** 93

[20] Franklin R N and Snell J 1997 *J. Phys. D: Appl. Phys.* **30** L45

[21] Riemann K-U 1991 *J. Phys. D: Appl. Phys.* **24** 493

[22] Riemann K-U 1997 *Phys. Plasmas* **4** 4158

[23] Salem M M and Loiseau J F 1996 *J. Phys. D: Appl. Phys.* **29** 1181

[24] Nitter T, Aslaksen T K, Melandsø F and Havnes O 1994 *IEEE Trans. Plasma Sci.* **22** 159

[25] Melandsø F 1992 *Phys. Scr.* **45** 515

[26] Boschi A and Magistrelli F 1963 *Nuovo Cimento* **29** 487

[27] Maniv S 1988 *J. Appl. Phys.* **63** 1022

[28] Law D A, Tomme E B, Steel W H, Annaratone B M and Allen J E 1999 *Proc. 24th Int. Conf. Phenomena in Ionized Gases (Warsaw, Poland)* **4** 109

[29] Chen X 1997 *IEEE Trans. Plasma Sci.* **25** 1117

[30] Allen J E 1992 *Phys. Scr.* **45** 497

[31] Allen J E, Boyd R L F and Reynolds P 1957 *Proc. Phys. Soc.* B **70** 297

[32] Whipple E C, Northrop T G and Mendis D A 1985 *J. Geophys. Res.* **90** 7405

[33] Kennedy R 1999 *Proc. 24th Int. Conf. Phenomena in Ionized Gases (Warsaw, Poland)* **3** 97

[34] Allen J E, Annaratone B M and de Angelis U 2000 *J. Plasma Phys.* **63** 299

[35] Stangeby P C and Allen J E 1971 *J. Plasma Phys* **6** 19

APPENDIX C: PHYSICAL REVIEW LETTER

The following four pages contain the manuscript of an article submitted to Physical Review Letters in April 2000.

Parabolic plasma sheath potentials and their implications for the charge on levitated dust particles

E. B. Tomme*, D. A. Law, B. M. Annaratone, and J. E. Allen

Department of Engineering Science, University of Oxford, Parks Road, Oxford OX1 3PJ, United Kingdom

(Submitted 17 April 2000)

Analysis of a number of numerical plasma sheath models as well as data from several previously reported experiments are shown to indicate that the sheath potential function may be very closely approximated with a parabola. We also demonstrate that once this potential function is suitably determined the charge on dust particles levitated in the plasma sheath may be calculated directly from their equilibrium heights.

52.25.Zb, 52.25.Vy, 52.40.Hf

Plasmas are commonly contaminated by dust. For example, ionospheric dust complicates interpretation of over-the-horizon radar returns [1] while dust from volcanic emissions and other sources form rings around several planets in the solar system [2]. While exact yield numbers are closely held industrial secrets, it is known that dust contamination in semiconductor processing plasmas causes a large portion of the product to be discarded as waste [3]. Dust purposely grown in plasmas can also be used in a variety of positive ways. For example, the deposition of dust during the manufacture of nanostructured silicon can accelerate the crystallisation process [4], lower the number of crystal defects [5] and lead to the production of more efficient solar cells [6]. The charge on dust suspended in these plasmas is a critical but not well-understood parameter for eliminating or efficiently using the dust.

The subject of the plasma sheath is also of wide interest. As the ions required for etching of semiconductors receive their energy from the fields within the sheath, knowledge of the spatial variation of these fields is essential for the intelligent design of manufacturing processes. Other disciplines requiring a detailed understanding of the plasma sheath range from basic astronomical research [7] to applications mitigating the effects of the charging of artificial satellites [8].

The purpose of this letter is twofold. First, we discuss a very simple, highly accurate approximation to the potential function in the plasma sheath. This approximation is well supported by existing numerical and experimental results. It can be determined by simple experimental measurements, instead of requiring the time-consuming modification of a complex numerical model from the literature to fit experimental conditions. We then discuss a simple method for determining the magnitude of the charge on dust suspended in the plasma sheath based on our novel generalisation concerning the nature of the sheath potential function.

In terrestrial plasmas, dust typically settles not in the plasma itself, but in the plasma sheath, where a balance of forces exists between, primarily, gravity and electrostatic repulsion [9]. Calculation of the charge residing on dust particles suspended in the plasma sheath has been the subject of much recent research. Several experimental techniques have been used in attempts to understand this phenomenon better. The most prevalent technique uses resonant oscillations of the dust, driven by various methods, and employs various assumptions about the electrical nature of the sheath to calculate the charge [10–15]. However, many of these techniques either significantly disturb the sheath, fail to account for significant intergrain forces, or both. Another technique involves observing collisions between dust particles, deriving the interaction potential, and thence the charge [16,17]. Analysis of the speed of sound in plasma crystals, dust that settles into stable, lattice-like structures under specific plasma parameters, e.g. [18], has also led to another charge calculation proposal [19].

Much of the experimental work is motivated by the lack of a coherent theory of dust charging in the plasma sheath. At least two sheath-charging theories exist in the literature [9,20], but both rely on the discredited [21] orbital motion limited (OML) charging theory, e.g. [22]. Development of such a sheath charging theory is highly desirable, as it would help to put this body of experimental work on stronger footing.

The majority of the cited experimental work relies on an *a priori* assumption that the electric field in the sheath varies linearly, or the electric potential varies parabolically, with the height above the electrode. The next few paragraphs will demonstrate that experimental evidence and numerical simulations available in the literature strongly support this assumption.

Numerical support for the parabolic sheath potential has existed, unrecognised, in the literature for some time. Detailed analysis of several models have shown that, to an accuracy of better than 5% (often better than 1%) across the entire sheath, the potentials calculated by a number of accepted plasma/sheath and sheath models [9,23–29] may be modelled by simple parabolas. A novel model, similar to [9] and [29], was developed for this analysis. The chief improvements incorporated into this model were to the boundary conditions, where the log-cosine form of the plasma potential from [26] was matched to the numerical solution to allow a smooth ion velocity profile, and to the collisionality assumptions, where the new model allows for velocity-dependent variations in the ion-neutral collision cross section. Further description of this model is beyond the scope of this paper, and is planned for a future article. Suffice it to say that its results were in agreement with the parabolic generalisations noted above.

The models cited above represent a cross section of plasma
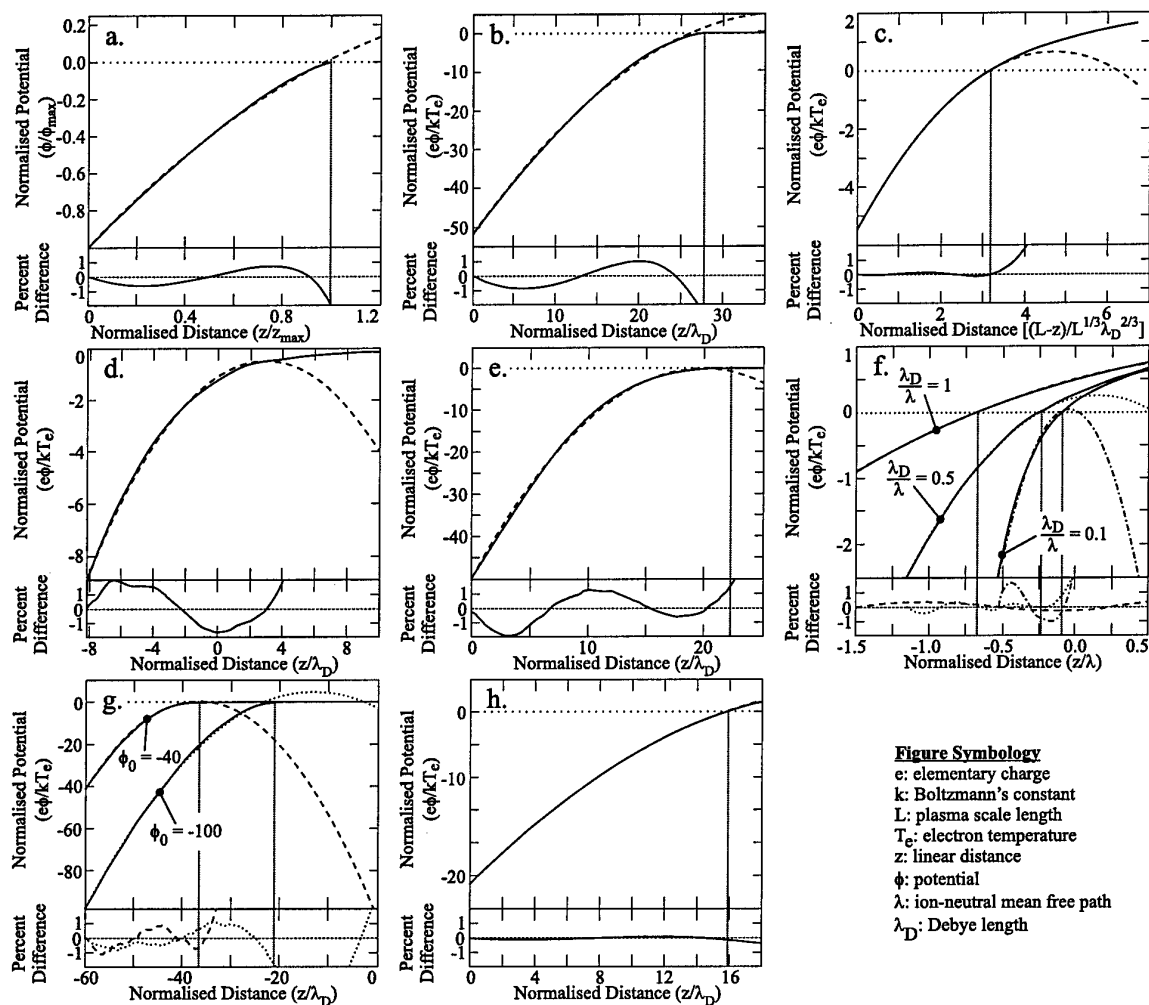
Figure 1: Parabolic Approximations to Sheath Models from the Literature. The upper portion of each frame shows the numerically derived sheath potentials from the indicated models (full curves) and their parabolic approximations (dotted/dashed/dash-dotted curves). The lower portion shows the percent difference between the parabolic approximation and the numerical results. Where applicable, the sheath edge is indicated by a vertical dotted line. The models analysed (and the applicable collisionality and generating voltage type) are as follows: a. Child-Langmuir [23,24] (collisionless DC); b. Bohm [25] (collisionless DC); c. Blank [26] (fully collisional DC); d. Franklin and Ockendon [27] (collisionless DC); e. Nitter [9] (collisional RF); f. Riemann [28] (transitional DC); g. Valentini [29] (collisionless RF); h. A model produced for the present analysis (transitional RF). The time-averaged potential is shown for the RF models. Specific parameterisations and sheath-edge definitions are discussed in the cited references.

parameters, from collisionless to transitional to fully collisional, and encompass both DC and RF plasma generation techniques; the parabolic nature of the sheath potential appears to be a general result for this wide variety of plasma parameters in electropositive gases. Figure 1 shows the sheath potentials calculated for these models, their corresponding parabolic fits, and the small deviations of the fits from the numerical calculation. Although the definitions of the sheath edge vary from model to model, in general, the parabolic fits are extremely

good (to better than 2%) across a very substantial fraction of the sheath.

Convincing experimental evidence for a parabolic sheath electric potential also exists. Analysis of the trajectories of isolated, micron-sized dust particles injected into the plasma sheath showed them to be extremely well modelled by a damped harmonic oscillator for amplitudes approaching 20% of the sheath width. Figure 2 shows a typical dust particle trajectory, along with the fit to damped harmonic theory.

2

Figure 2: Typical Dust Oscillation Data [30]. The solid line is the damped harmonic theoretical curve fit to the data. Typical position measurement errors are on the order of 10 μm; these error bars are not visible at this scale.

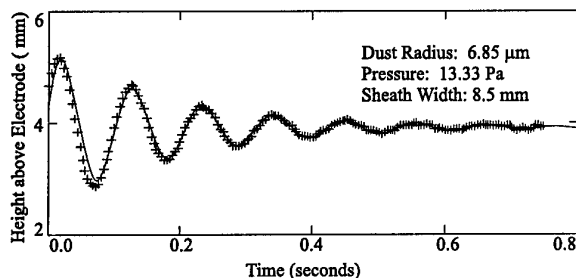Additional data and analysis has been presented elsewhere [30]. The theoretical fit breaks down for larger amplitude oscillations, most probably due to the increasing significance of charge fluctuation on the dust particle as it is exposed to different local potentials during its oscillations; however, the fits are extremely good over much larger amplitudes than would be expected from the standard small-amplitude approximation.

These data show that the dust must oscillate in a parabolic potential energy well. The only significant forces are gravity and electrostatic repulsion [30], so the electrical potential energy is the difference between the total potential and the gravitational potential. As the total potential energy has been shown to be parabolic and the gravitational potential energy is linear, the electrical potential energy - and hence, the electric potential - must be parabolic as well. Thus, the experimental and numerical evidence both strongly support the assumption that the sheath electric potential is a parabolic function of height above the electrode.

Now that the general parabolic nature of the sheath potential has been demonstrated, it remains to determine the boundary conditions for the parabola in order to get specific sheath potential functions. The boundary conditions we feel to be convenient were the spatial location of the sheath edge, the potential difference between the sheath edge, and electrode as well as the electric field at the sheath edge. The sheath edge location may be determined either visually or via probe measurements, the sheath-edge-to-electrode potential difference may be determined by probe measurements, and the sheath edge electric field may be calculated from one of several proposed in the literature, e.g. [28]. These boundary conditions together with the assumed parabolic nature of the sheath serve to specify the sheath potential function.

The second purpose of this letter is to show that, once the parabolic nature of the electric potential has been suitably determined, there exists a relatively simple way of calculating the charge on dust suspended in the sheath. To do this one simply measures the mass of the dust and the height at which it suspends and then employs the force-balance equation (gravitational force equals electrostatic force) at the dust equilibrium suspension height.

$$Q_d(r_d) = \frac{m_d(r_d) \cdot g}{E(z_{eq}(r_d))}. \tag{1}$$

Here, Q_d is the equilibrium dust charge, r_d is the dust radius, $E(z)$ is the electric field, z_{eq} is the equilibrium suspension height, m_d is the dust mass, and g is the acceleration due to gravity. As the electric field is just the negative derivative of the sheath potential, the value of the dust charge may readily be obtained.

The experimental results of [30], which show the dust charge as a function of dust radius determined by analysis of damped oscillations, may be compared with the force-balance method discussed above. These experiments were performed at two pressures, 6.67 Pa ($kT_e = 3.7$ eV and $n_0 = 1.7 \cdot 10^{15}$ m^{-3}, $z_{sh} = 9.4$ mm) and 13.33 Pa ($kT_e = 3.9$ eV and $n_0 = 2.4 \cdot 10^{15}$ m^{-3}, $z_{sh} = 8.5$ mm). Here, kT_e and n_0 are the electron temperature and electron density at the centre of the discharge determined by Langmuir probe measurements and z_{sh} is the visually-determined sheath width. In all cases, the dust was monodispersive melamine formaldehyde ($\rho = 1514$ kg/m^3) suspended in an argon plasma, the electrode spacing was 40.0 mm, the RF frequency was 13.5 MHz, and the RF Amplitude was 96.4 V. The derivation of the parabolic sheath functions from these experimental conditions is presented in detail in the cited reference. It must be noted that the boundary conditions for the electric field at the sheath edge, E_s, used in [30] were merely the ones found to be the most convincing at the time that paper was written (i.e., $E_s = kT_e/e\lambda$, where e is the elementary charge, and λ is the ion mean free path); should better boundary conditions become available, they may be used with existing equilibrium height data to calculate improved values for the dust charge.

Experimental charges and the charge curve from [30] are shown in Figure 3. Also shown is a plot of the dust charge calculated from equation (1). The solid trend line was calculated using the same equation and a fit to the experimental equilibrium heights as a function of the dust radius. It is important to note that the charge results are not entirely independent of theory; E comes from the parabolic sheath model justified above. As can be seen in this figure, simple measurement of the equilibrium heights of the dust particles can provide charge values in good agreement with previous measurements and theories. We also note that the force-balance charge curves from equation (1) are remarkably similar for the two different pressures, supporting the limited dependency of the dust charge on pressure noted by other researchers [11]. The charges predicted by these curves also agree well with those from other methods [10–19], considering differences in experimental parameters.

In summary, experimental and numerical evidence both strongly support the existence of a parabolic electric potential profile in the plasma sheath. Boundary conditions specifying the exact sheath potential function are readily available from experimental measurements and theory from the litera-
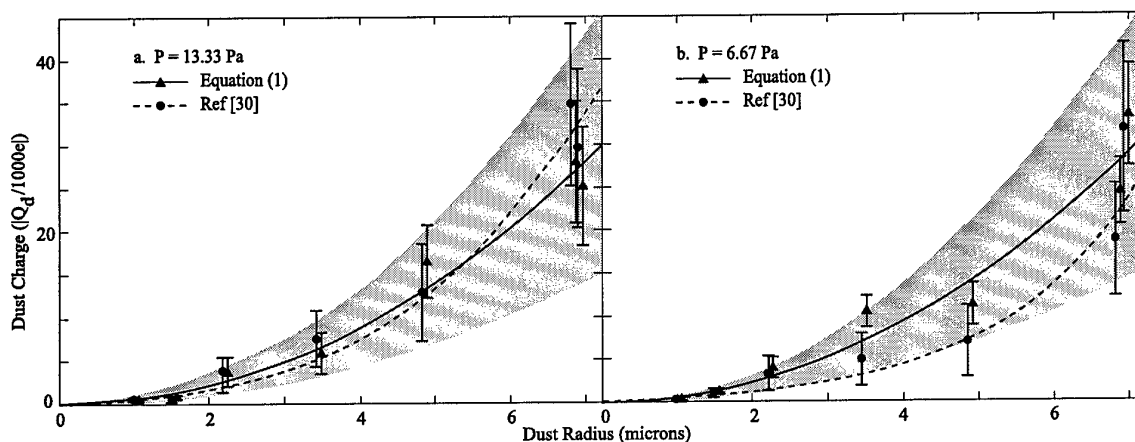
3

Figure 3: Variation of the Dust Charge as a Function of Dust Radius. This figure shows plots of normalised dust charge for (a) 13.33 Pa and (b) 6.67 Pa. The dashed lines with circles represent the charge curve from the theory in [30]. The solid line with triangles is a plot of the charge from equation (1), as discussed in the text. Shading indicates the region between 1.5 and 0.5 times the fit line from equation (1). The mean values for the ratios of the charges obtained from these two methods are 1.1 and 1.5 for 13.33 Pa and 6.67 Pa, respectively, indicating their good agreement. The data points have been offset from each other for clarity; the actual horizontal positions are halfway between the corresponding vertical error bars. These plots are for melamine formaldehyde suspended in an argon plasma.

ture. Once the potential function is known, the dust charge may be calculated from knowledge of the dust mass and equilibrium suspension height.

*   Permanent address: Department of Physics, United States Air Force Academy, Colorado, 80840

[1]   C. La Hoz, Physica Scripta **45**, 529 (1992).

[2]   C. K. Goertz, Rev. Geophys. **27**, 271 (1989).

[3]   G.S. Selwyn, in *International Integrated Reliability Workshop Final Report* (Lake Tahoe, California, USA, 1996), p. 122.

[4]   E. Bertran et al., J. Materials Res. **13**, 2476 (1998).

[5]   E. Stoffels et al., Electron Tech. **31**, 255 (1998).

[6]   G. W. Kroesen et al., Eindhoven (Netherlands) Technical University Report No. BE 7328 (1998).

[7]   H. Kimura and I. Mann, Astrophys. J. **499**, 454 (1998).

[8]   K. Torkar et al., Ann. Geophysicae **16**, 1086 (1998).

[9]   T. Nitter, Plasma Sources Sci. Technol. **5**, 93 (1996).

[10] A. Melzer, T. Trottenberg, and A. Piel, Phys. Lett. A **191**, 301 (1994).

[11] T. Trottenberg, A. Melzer, and A. Piel, Plasma Sources Sci. Technol. **4**, 450 (1995).

[12] U. Kortshagen and G. Mümken, Phys. Lett. A **217**, 126 (1996).

[13] A. Homann, A. Melzer, and A. Piel, Phys. Rev. E **59**, R3835 (1999).

[14] D. A. Law et al., in *Proceedings of the 24th International Conference on Phenomena in Ionized Gases* (Warsaw, Poland, 1999), Vol. 4, p. 109.

[15] S. Nunomura, T. Misawa, N. Ohno, and S. Takamura, Phys. Rev. Lett. **83**, 1970 (1999).

[16] U. Konopka, L. Ratke, and H. M. Thomas, Phys. Rev. Lett. **79**, 1269 (1997).

[17] U. Konopka, G.E. Morfill, and L. Ratke, Phys. Rev. Lett. **84**, 891 (2000).

[18] G. E. Morfill, H. M. Thomas, U. Konopka, and M. Zuzic, Phys. Plasmas **6**, 1769 (1999).

[19] D. Samsonov, J. Goree, Z. W. Ma, and A. Bhattacharjee, Phys. Rev. Lett. **83**, 3649 (1999).

[20] X. Chen, IEEE Trans. Plasma Sci. **25**, 1117 (1997).

[21] J. E. Allen, B. M. Annaratone, and U. de Angelis, J. Plasma Phys. **63**, 299 (2000).

[22] J. E. Allen, Physica Scripta **45**, 497 (1992).

[23] C. D. Child, Phys. Rev. **32**, 492 (1911).

[24] I. Langmuir, Phys. Rev. **2**, 450 (1913).

[25] D. Bohm, in *The Characteristics of Electrical Discharges in Magnetic Fields*, edited by A. Guthrie and R.K. Wakerling (McGraw-Hill, New York, 1949), Chap. 3.

[26] J. L. Blank, Phys. Fluids **11**, 1686 (1968).

[27] R. N. Franklin and J. R. Ockendon, J. Plasma Phys. **4**, 371 (1970).

[28] K. U. Riemann, Phys. Plasmas **4**, 4158 (1997).

[29] H. B. Valentini, J. Appl. Phys. **86**, 6665 (1999).

[30] E. B. Tomme, B. M. Annaratone, and J. E. Allen, Plasma Sources Sci. Technol. **9**, 87 (2000).

BIBLIOGRAPHY

Abramowitz, M. and I.A. Stegun. *Handbook of Mathematical Functions.* New York: Dover, 1972.

Allen, J.E., R.L.F. Boyd, and P. Reynolds. "The Collection of Positive Ions by a Probe Immersed in a Plasma." *Proceedings of the Physical Society, B.* **70** (1957), 297-304.

Allen, J.E. "Probe Theory: The Orbital Motion Approach." *Physica Scripta* **45** (1992) 497-503.

Allen, J.E. and M.A. Skorik. "The Bohm Criterion in the Presence of Radio-Frequency Fields." *Journal of Plasma Physics* **50** (1993) 243-49.

Allen, J.E. "Probe Theory and Applications: Modern Aspects." *Plasma Sources Science and Technology* **4** (1995) 234-41.

Allen, J.E., B.M. Annaratone, and U. deAngelis. "On the Orbital Motion Limited Theory for a Small Body at Floating Potential in Maxwellian Plasmas." *Journal of Plasma Physics* **63** (2000) 299-310.

Annaratone, B.M., M.W. Allen, and J.E. Allen. "Ion Currents to Cylindrical Langmuir Probes in RF Plasmas." *Journal of Physics D: Applied Physics* **25** (1992) 417-24.

Baerline, R. *Newtonian Dynamics.* London: McGraw-Hill, 1983.

Barnes, M.S., J.H. Keller, J.C. Forster, J.A. O'Neill, and D.K. Coultas. "Transport of Dust Particles in Glow-Discharge Plasmas." *Physical Review Letters* **68** (1992) 313-16.

Benilov, M.S. "Theory of a Collision-Dominated Space-Charge Sheath on an Emitting Cathode." *Journal of Physics D: Applied Physics* **30** (1997) 1115-19.

Bernstein, I.B. and I. Rabinowitz. "Theory of Electrostatic Probes in a Low-Density Plasma." *Physics of Fluids* **2** (1959) 112-21.

Bertran, E., S.N. Sharma, G. Viera, J. Costa, P. St'ahel, and P. Roca i Cabarrocas. "Effect of the Nanoparticles on the Structure and Crystallization of Amorphous Silicon Thin Films Produced by RF Glow Discharge." *Journal of Materials Research* **13**(9) (1998) 2476-79.

Bittencourt, J.A. *Fundamentals of Plasma Physics*. Oxford: Pergamon Press, 1986.

Blank, J.L. "Collision-Dominated Positive Column of a Weakly Ionized Gas." *Physics of Fluids* **11** (8) (1968) 1686-98.

Bohm, D. "Minimum Ion Kinetic Energy for a Stable Sheath." Chapter 3 in *The Characteristics of Electrical Discharges in Magnetic Fields*. A. Guthrie and R.K. Wakerling, eds. New York: McGraw-Hill, 1949.

Bohm, D., E.H.H. Burhop, and H.S.W. Massey. "The Use of Probes for Plasma Exploration in Strong Magnetic Fields." Chapter 2 in *The Characteristics of Electrical Discharges in Magnetic Fields*. A. Guthrie and R.K. Wakerling, eds. New York: McGraw-Hill, 1949.

Börnig, K. "Modeling a Collisional, Capacitive Sheath for Surface Modification Applications in Radio-Frequency Discharges." *Applied Physics Letters* **60** (13) (1992) 1553-55.

Boschi, A., and F. Magistrelli. "Effect of a R.F. Signal on the Characteristic of a Langmuir Probe." *Nuovo Cimento* **29** (1963) 487-499.

Braithwaite, N. St. J., A. J. Crosby, and J. E. Allen. "Space Charge Sheaths Adjacent to RF Plasmas." *Proceedings of the 8th International Conference on Gas Discharges and Their Applications (Oxford, England)* (1985) 482.

Chapman, B. *Glow Discharge Processes: Sputtering and Plasma Etching*. New York: John Wiley and Sons, 1980.

Chen, F.F. *Introduction to Plasma Physics and Controlled Fusion, Volume 1: Plasma Physics*. 2nd ed. New York: Plenum Press, 1984.

Chen, X. "Dust Charge in the Sheath of Collisional Low-Pressure Capacitive RF Discharges." *IEEE Transactions on Plasma Science* **25** (5) (1997), 1117-1123.

Child, C.D. "Discharge from Hot CaO." *Physical Review* **32** (1911) 492-511.

Chu, J.H. and I. Lin. "Direct Observation of Coulomb Crystals and Liquids in Strongly Coupled RF Dusty Plasmas." *Physics Review Letters* **72** (1994) 4009-12.

Coburn, J.W. and E. Kay. "Positive-Ion Bombardment of Substrates in RF Diode Glow Discharge Sputtering." Journal of Applied Physics 43(12) (1972) 4965-71.

Cohen, I.M. "Asymptotic Theory of Spherical Electrostatic Probes in a Slightly Ionized, Collision-Dominated Gas." *Physics of Fluids* **6** (10) (1963) 1492-99.

Coleman, J.H., Plasma Physics Corporation, Private Communication (1998).

Crocker, J.C., and D.G. Greer. "Methods of Digital Video Microscopy for Colloidal Studies." *Journal of Colloidal Interface Science* **179** (1996) 298-310.

Daugherty, J.E, R.K. Porteous, M.D. Kilgore, and D.B. Graves. "Sheath Structure around Particles in Low-Pressure Discharges." *Journal of Applied Physics* **72**(9) (1992) 3934-42.

Daugherty, J.E., R.K. Porteous, and D.B. Graves. "Electrostatic Forces on Small Particles in Low-Pressure Discharges." *Journal of Applied Physics* **73** (1993) 1617-20.

deAngelis, U. "The Physics of Dusty Plasmas." *Physica Scripta* **45** (1992) 465-74.

Debye, P. and E. Hückel. "Zur Theorie der Elektrolyte." *Physikalische Zeitschrift* **24** (1923) 185-206.

Druyvesteyn, M.J. and F.M. Penning. "The mechanism of Electrical Discharges in Gases of Low Pressure." *Reviews of Modern Physics* **12**(2) (1940) 87-174.

Epstein, P.S. "On the Resistance Experienced by Spheres in Their Motion through Gases." *Physical Review* **23** (1924) 710-33.

Farouki, R.T., S. Hamaguchi, and M. Dalvie. "Monte Carlo Simulations of Space-Charge-Limited Ion Transport through Collisional Plasma Sheaths." *Physical Review A* **44**(4) (1991) 2664-81.

Franklin, R.N. and J.R. Ockendon. "Asymptotic Matching of Plasma and Sheath in an Active Low Pressure Discharge." *Journal of Plasma Physics* **4**(2) (1970) 371-85.

Franklin, R.N. and J. Snell. "Joining a Collisional Sheath to an Active Plasma." *Journal of Physics D: Applied Physics* **30** (1997) L45-L47.

Franklin, R.N. Private Communication (1999).

Franklin, R.N. and J. Snell. "The Transition from Collisionless to Collisional Active Plasma and the Relevance of the Bohm Criterion to Sheath Formation." Accepted by *Physics of Plasmas* (2000).

Garscadden, A. "Particles in Plasmas." *Proceedings of the 20th International Conference on Phenomena in Ionized Gases, Pisa, Italy* (1991) 147-54.

Gierling, J. and K.-U Riemann. "Comparison of a Consistent Theory of Radio Frequency Sheaths with Step Models." *Journal of Applied Physics* **83**(7) (1998) 3521-28.

Godyak, V.A. "Modified Bohm Criterion for a Collisional Plasma." *Physics Letters* **89A** (1982) 80-81.

Godyak, V.A. and N. Sternberg. "Smooth Plasma-Sheath Transition in a Hydrodynamic Model." *IEEE Transactions on Plasma Science* **18**(1) (1990) 159-68.

Goertz, C.K. "Dusty Plasmas in the Solar System." *Reviews of Geophysics* **27** (1989) 271-92.

Goree, J. "Charging of Dust Particles in a Plasma." *Plasma Sources: Science and Technology* **3** (1994) 400-06.

Hamaguchi, S. "Modeling and Simulation Methods for Plasma Processing." *IBM Journal of Research and Development* **43**(1/2) (1999) 199-215.

Hamaguchi, S. and R.T. Farouki. "Polarization Force on a Charged Particulate in a Nonuniform Plasma." *Physical Review E* **49** (1994) 4430-41.

Havnes, O., F. Melandsø, C. La Hoz, and T.K. Aslaksen. "Charged Dust in the Earth's Mesopause; Effects on Radar Backscatter." *Physica Scripta* **45** (1992a) 535-44.

Havnes, O., T. Aslaksen, F. Melandsø, and T. Nitter. "Collisionless Braking of Dust Particles in the Electrostatic Field of Planetary Dust Rings." *Physica Scripta* **45** (1992b) 491-96.

Homann, A., A. Melzer, S. Peters, and A. Piel. "Determination of the Dust Screening Length by Laser-Excited Lattice Waves." *Physical Review E* **56** (1997) 7138-41.

Homann, A., A. Melzer, and A. Piel. "Measuring the Charge on Single Particles by Laser-Excited Resonances in Plasma Crystals." *Physical Review E* **59**(4) (1999) R3835-38.

Hornbeck, J.A. "The Drift Velocities of Molecular and Atomic Ions in Helium, Neon, and Argon." *Physical Review* **84**(4) (1951) 615-20.

Huang, F.Y., H.H. Hwang, and M.J. Kuschner. "A Model for Transport and Agglomeration of Particles in Reactive Ion Etching Plasma Reactors." *Journal of Vacuum Science and Technology A: Vacuum, Surfaces, and Films* **14** (1996) 562-66.

Ichimaru, S. "Strongly Coupled Plasmas: High-Density Classical Plasmas and Degenerate Electron Liquids." *Reviews of Modern Physics* **54** (1982) 1017-59.

Ikezi, H. "Coulomb Solid of Small Particles in Plasmas." *Physics of Fluids* **29** (1986) 1764-66.

Jellum, G.M., J.E. Daugherty, and D.B. Graves. "Particle Thermophoresis in Low Pressure Glow Discharges." *Journal of Applied Physics* **69** (1991) 6923-34.

Kennedy, R. "On the Floating Potential of Spherical Probes and Dust Grains."
    *Proceedings of the 24th International Conference on Phenomena in Ionized
    Gases* (Warsaw, Poland) (1999) III-97.

Kennedy, R. Private Communication (2000).

Kersten, H., G.M.W. Kroesen, and R. Hippler. "On the Energy Influx to the Substrate
    During Sputter Deposition of Thin Aluminium Films." *Thin Solid Films*
    332(1-2) (1998a) 282-289.

Kersten, H., P. Schmetz, and G.M.W. Kroesen. "Surface Modification of Powder
    Particles by Plasma Deposition of Thin Metallic Films." *Surface and Coatings
    Technology* **109**(1-3) (1988b) 507-12.

Kilgore, M.D., J.E. Daugherty, R.K. Porteous, and D.B. Graves. "Ion Drag on an
    Isolated Particulate in a Low Pressure Discharge." *Journal of Applied Physics*
    73 (1993) 7195-202.

Konopka, U., L. Ratke, and H.M. Thomas. "Central Collisions of Charged Dust
    Particles in a Plasma." *Physical Review Letters* **79**(7) (1997) 1269-72.

Konopka, U. and G.E. Morfill, Max-Planck-Institut für extraterrestrische Physik,
    Garching, Germany, Private Communication (1998).

Konopka, U., G.E. Morfill, and L. Ratke. "Measurement of the Interaction Potential of
    Microspheres in the Sheath of a RF Discharge." *Physical Review Letters* **84**(5)
    (2000) 891-94.

Kortshagen, U. and G. Mümken. "The Electrical Charging of Micron-Sized Dust
    Particles in a Capacitively Coupled RF Plasma." *Physics Letters, A* **217** (1996)
    126-32.

Kroesen, G.W. *et al.* "Synthesis Report: Micropowder Processing Using Low-Pressure
    Plasma Technology." *Eindhoven (Netherlands) Technical University Report
    No. BE 7328* (1998).

La Hoz, C. "Radar Scattering from Dusty Plasmas." *Physica Scripta* **45** (1992) 529-34.

Laframboise, J.G. " Theory of Spherical and Cylindrical Langmuir Probes in a
    Collisionless Maxwellian Plasma at Rest." *U.T.I.A.S. Report No. 100,* 1966.

Langmuir, I. "The Effect of Space Charge and Residual Gases on Thermionic Currents
    in High Vacuum." *Physical Review* **2**(6) (1913) 450-486.

Langmuir, I. "The Effect of Space Charge and Initial Velocities on the Potential
    Distribution and Thermionic Current between Parallel Plane Electrodes."
    Physical Review **21** (1923) 419-35.

Langmuir, I. and H. Mott-Smith. "Studies of Electrical Discharges in Gases at Low
    Pressures." *General Electric Review* **27**(12) (1924) 810-20.

Langmuir, I. "The Interaction of Electron and Positive Ion Space Charges in Cathode Sheaths." *Physical Review* **33** (1929) 954-89.

Law, D.A. *Dusty Plasmas and Plasma Crystals.* D.Phil. Thesis, University of Oxford (1998).

Law, D.A., E.B. Tomme, W.H. Steel, B.M. Annaratone, and J.E. Allen. "Dust as a Sheath Diagnostic." *Proceedings of the 24th International Conference on Phenomena in Ionized Gases* (Warsaw, Poland) (1999) 4-109.

Lichtenberg, A. "Kinetic Theory in a Stochastically-Heated Capacitative RF Discharge at Low Pressure." *Notes from a lecture presented at Culham Laboratories, Abingdon, England,* 1998.

Maddox, J. "Plasma Dust as Model Crystals." *Nature* **370** (1994) 411.

Maniv, S. "Modeling for RF Discharge Characteristics." *Journal of Applied Physics* **63**(4) (1988) 1022-31.

McDaniel, E.W. *Collision Phenomena in Ionized Gases.* London: John Wiley & Sons, 1964.

McDonnel, J.A.M., ed. *Cosmic Dust.* New York: Wiley Interscience, 1978.

Melandsø, F. "Collisionless Damping of Oscillations in Electrically Supported Dust Rings." *Physica Scripta* **45** (1992) 515-20.

Melandsø, F., T. Aslaksen, and O. Havnes. "A New Damping Effect for the Dust-Acoustic Wave." *Planetary and Space Science* **41** (1993) 321-25.

Melzer, A., T. Trottenberg, and A. Piel. "Experimental Determination of the Charge on Dust Particles Forming Coulomb Lattices." *Physics Letters, A* **191** (1994) 301-08.

Millikan, R.A. "The General Law of Fall of a Small Spherical Body through a Gas, and Its Bearing upon the Nature of Molecular Reflection from Surfaces." *Physical Review* **22** (1923) 1-23.

Morfill, G.E., E. Grün, and T.B. Johnson. "Dust in Jupiter's Magnetosphere: Physical Processes." *Planetary and Space Science* **28** (1980) 1087-1100.

Morfill, G.E. and H. Thomas. "Plasma Crystal." *Journal of Vacuum Science and Technology A: Vacuum, Surfaces, and Films* **14** (1996) 490-95.

Morfill, G.E., H.M. Thomas, and M. Zuzic. "Plasma Crystals: A Review." In *Advances in Dusty Plasmas: Proceedings of the International Conference on Physics of Dusty Plasmas.* P.K. Shukla, D.A. Mendis, and T. Desai, eds. World Scientific: Singapore, 1997.

Morfill, G.E., H.M. Thomas, U. Konopka, and M. Zuzic. "The Plasma Condensation: Liquid and Crystalline Plasmas." *Physics of Plasmas* **6**(5) (1999) 1769-80.

Mott-Smith, H. and I. Langmuir. "The Theory of Collectors in Gaseous Discharges." *Physical Review* **28** (1926) 727-63.

Nagayama, K., B. Farouk, and Y.H. Lee. "Neutral and Charged Particle Simulation of a RF Argon Plasma." *Plasma Sources Sciences and Technology* **5** (1996) 685-95.

Nairn, C., B.M. Annaratone, and J.E Allen. "On the Theory of Spherical Probes and Dust Grains." *Plasma Sources Sciences and Technology* **7** (1998) 478-90.

Nanbu, K. and Y. Kitatani. "An Ion-Neutral Species Collision Model for Particle Simulation of Glow Discharge." *Journal of Physics D: Applied Physics* **28** (1995) 324-30.

Nitter, T. and O. Havnes. "Dynamics of Dust in a Plasma Sheath and Injection of Dust into the Plasma Sheath above Moon and Asteroidal Surfaces." *Earth, Moon and Planets* **56** (1992) 7-34.

Nitter, T., T.K. Aslaksen, F. Melandsø, and O. Havnes. "Levitation and Dynamics of a Collection of Dust Particles in a Fully Ionized Plasma Sheath." *IEEE Transactions on Plasma Science* **22**(2) (1994) 159-72.

Nitter, T. "Levitation of Dust in RF and DC Glow Discharges." *Plasma Sources Sciences and Technology* **5** (1996) 93-111.

Northrop, T.G. and T.J. Birmingham. "Plasma Drag on a Dust Grain Due to Coulomb Collisions." *Planetary Space Sciences* **38** (1990) 319-26.

Nunomura, S., T. Misawa, N. Ohno, and S. Takamura. "Instability of Dust Particles in a Coulomb Crystal due to Delayed Charging." *Physical Review Letters* **83**(10) (1999) 1970-73.

Phelps, A.V. "The Application of Scattering Cross Sections to Ion Flux Models in Discharge Sheaths." *Journal of Applied Physics* **76** (2) (1994) 747-53.

Piet, S.J., A. Costley, G. Federici, F. Heckendorn, and R. Little. "ITER Tokamak Dust – Limits, Production, Removal, Surveying." *27th IEEE/NPSS Symposium on Fusion Engineering* (1997).

Press, W.H., S.A. Teuklosky, W.T. Veterling, and B.P. Flannery. *Numerical Recipes in C: The Art of Scientific Computing.* 2nd edition. Cambridge: Cambridge University Press, 1992.

Procassini R.J. and C.K. Birdsall. "Particle Simulation Model of Transport in a Bounded, Coulomb Collisional Plasma." *Physics of Fluids B* **3**(8) (1991) 1876-91.

Riemann, K.-U. "The Bohm Criterion and Sheath Formation." *Journal of Physics D: Applied Physics* **24** (1991) 493-518.

Riemann, K.-U. "The Validity of Bohm's Sheath Criterion in RF Discharges." *Physics of Fluids* **4** (9) (1992) 2693-95.

Riemann, K.-U. "The Influence of Collisions on the Plasma Sheath Transition." *Physics of Plasmas* **4** (11) (1997) 4158-66.

Salem, M.M. and J.F. Loiseau. "Experiments to Sort out Theoretical Models Concerning the Area Ratio Law for Plasma Reactors." *Journal of Physics D: Applied Physics* **29** (1996) 1181-7.

Schottky, W. "Diffusionstheorie der Positiven Säule." *Physikalische Zeitschrift* **25** (1924) 635-40.

Selwyn, G.S. "Particulate Contamination Control in Plasma Processing: Building-In Reliability for Semiconductor Fabrication." *International Integrated Reliability Workshop Final Report, Lake Tahoe, California, USA* (1996) 122-129.

Skorik, M and J.E. Allen. "Modelling of Low Pressure RF Glow Discharges." *Proceedings of the 21st International Conference on Phenomena in Ionized Gases, Bochum, Germany* (1993) 113-14.

Slatterly, W.L. and G.D. Doolen. "Improved Equation of State of the Classical One-Component Plasma." *Physical Review A* **21** (1980) 2087-95.

Smirnov, B.M. *Physics of Weakly Ionized Gases: Problems and Solutions.* Moscow: Mir, 1981. p. 217.

Stangeby, P.C. and J.E. Allen. "Transonic Plasma Flow Past an Obstacle." *Journal of Plasma Physics* **6**(1) (1971) 19-32.

Steel, W.A., D.A. Law, B.M. Annaratone, and J.E. Allen. "Laser Induced Motion of Micrometer Size Particles in RF Plasma Sheaths." *Proceedings of the 23rd International Conference on Plasmas and Ionized Gases, Toulouse, France* (1997) I:194-195.

Sternberg, N., and V.A. Godyak. "Solving the Mathematical Model of the Electrode Sheath in Symmetrically Driven RF Discharges." *Journal of Computational Physics* **111** (1994) 347-53.

Stoffels, E., W.W. Stoffels, G.M.W. Kroesen, and F.J. de Hoog. "Dust in Plasmas – Fiend or Friend." *Electron Technology* **31**(2) (1998) 255-74.

Stoffels, W.W., E. Stoffels, G.H.P.M. Swinkels, M. Boufnichel, and G.M.W. Kroesen. "Etching a Single Micrometer-Size Particle in a Plasma." *Physical Review E* **59**(2B) (1999) 2302-04.

Swift, J.D. and M.J.R. Schwar. *Electrical Probes for Plasma Diagnostics*. London: Iliffe Books, 1970.

Swinkels, G.H.P.M., E. Stoffels, W.W. Stoffels, N. Simons, G.M.W. Kroesen, and F.J. de Hoog. "Treatment of Dust Particles in an RF Plasma Monitored by Mie Scattering Rotating Compensator Ellipsometry." *Pure and Applied Chemistry* **70**(6) (1998) 1151-56.

Talbot, L., R.K. Cheng, R.W. Schefer, and D.R. Willis. "Thermophoresis of Particles in a Heated Boundary Layer." *Journal of Fluid Mechanics* **101** (1980) 737-58.

Thomas, H., G.E. Morfill, V. Demmel, J. Goree, B. Feuerbacher, and D. Mohlmann. "Plasma Crystal: Coulomb Crystallization in a Dusty Plasma." *Physical Review Letters* **73** (1994) 652-55.

Thomas, H.M. and G.E. Morfill. "Solid/Liquid/Gaseous Phase Transitions in Plasma Crystals." *Journal of Vacuum Science and Technology A* **14**(2) (1996) 501-05.

Tomme, E.B., D.A. Law, W.H. Steel, B.M. Annaratone, and J.E. Allen. "Dust Oscillations in a Plasma Sheath." *Proceedings of the 14th European Conference on the Atomic and Molecular Physics of Ionised Gases* (Malahyde, Ireland), in *Europhysics Conference Abstracts*, edited by D. Riley, C.M.O. Mahoney, and W.G. Graham, Volume **22H** (1998) 334-5.

Tonks, L. and I. Langmuir. "A General Theory of the Plasma of an Arc." *Physical Review* **34** (1929) 876-924.

Trottenberg T., A. Melzer, and A. Piel. "Measurement of the Electric Charge on Particulates forming Coulomb Crystals in the Sheath of a Radiofrequency Plasma." *Plasma Sources Sciences and Technology* **4** (1995) 450-58.

Tsytovich, V. "Plasma Dust Crystals, Plasma-Dust Liquid Drops, and Plasma-Dust Clouds." *Uspekhi Fizicheskikh Nauk* **167** (1997) 57-100.

Valentini, H.-B. "Modeling of the Field Reversal in a Capacitively Coupled High Frequency Sheath." *Journal of Applied Physics* **86**(12) (1999) 6665-72.

Van Dyke, M. *Perturbation Methods in Fluid Mechanics*. London: Academic Press, 1964, Chapter V.

Vender, D. and R.W. Boswell. "Numerical Modeling of Low-Pressure RF Plasmas." *IEEE Transactions on Plasma Science* **18**(4) (1990) 725-32.

Waldmann, L. and K.H. Schmitt. "Thermophoresis and Diffusiophoresis of Aerosols." Chapter 7 in *Aerosol Science*. C.N. Davies, ed. London: Academic Press, 1966.

Weast, R.C., D.R. Lide, M.J. Astle, and W.H Beyer, eds. *CRC Handbook of Chemistry and Physics*. Boca Raton, Florida, USA: CRC Press, 1989.

Whipple, E.C., T.G. Northrop, and D.A. Mendis. "The Electrostatics of a Dusty
        Plasma." *Journal of Geophysical Research* **90**(A8) (1985) 7405-13.

Yukawa, H. "On the Interaction of Elementary Particles I." *Journal of the Physical and
        Mathematical Society of Japan* **17** (1935) 48-57.